



UNIVERSIDAD MIGUEL HERNÁNDEZ

**SLOW AND FAST LIGHT IN MULTIPLE-
BEAM INTERFEROMETERS, MONO- AND
MULTI-LAYER SYSTEMS**

AIDA SÁNCHEZ MEROÑO

TESIS DOCTORAL

Programa de Doctorado en Tecnologías Industriales y de
Telecomunicación

Directoras: Dra. María del Mar Sánchez López

Dra. M^a Julia Arias Rodríguez

Elche, marzo 2015



M^a DEL MAR SÁNCHEZ LÓPEZ, Titular de Universidad de Física Aplicada de la Universidad Miguel Hernández de Elche, y

M^a JULIA ARIAS RODRÍGUEZ, Titular de Universidad de Tecnología Electrónica de la Universidad Miguel Hernández de Elche.

HACEMOS CONSTAR

Que el presente trabajo, titulado “Slow and Fast Light in Multiple-beam Interferometers, Mono- and Multi-layer Systems”, ha sido realizado bajo nuestra dirección y recoge fielmente la labor realizada por Doña Aida Sánchez Meroño, Ingeniera de Telecomunicación, para optar al grado de Doctor. Las investigaciones reflejadas en esta Tesis se han desarrollado en el laboratorio de Fotónica del Instituto de Bioingeniería, así como en el Laboratorio de Tecnología Electrónica del Departamento de Ciencia de Materiales, Óptica y Tecnología Electrónica de la Universidad Miguel Hernández de Elche.

Las que suscriben consideran que el trabajo reúne las condiciones de originalidad y rigor metodológico necesario para memoria de Tesis Doctoral, y de este modo puede ser presentado a la lectura y discusión ante tribunal en la Universidad Miguel Hernández de Elche.

Elche, de de 2015

Firma:

Firma:

Dra. M^a del Mar Sánchez López

Dra. M^a Julia Arias Rodríguez



Departamento de Ciencia de Materiales, Óptica y Tecnología Electrónica
Universidad Miguel Hernández
Campus de Elche- Edificio Torrevallo.
Avda. Universidad, s/n- 03202 Elche (Alicante) ESPAÑA
Tel.: +34 96 665 8498 Fax: +34 96 665 8497
E-mail: cytmat@umh.es

M^a JULIA ARIAS RODRÍGUEZ, Directora del Departamento de Ciencia de Materiales, Óptica y Tecnología Electrónica de la Universidad Miguel Hernández de Elche.

INFORMA

Que la Tesis Doctoral titulada “Slow and Fast Light in Multiple-beam Interferometers, Mono- and Multi-layer Systems”, ha sido realizada por Doña Aida Sánchez Meroño, Ingeniera de Telecomunicación, bajo la inmediata dirección y supervisión de la Dra. M^a del Mar Sánchez López y la Dra. M^a Julia Arias Rodríguez, y da su conformidad para que sea presentada ante la Comisión de Doctorado.

Para que conste y surta los efectos oportunos, firma el presente informe.

Elche, de de 2015

Firma:

Dra. M^a Julia Arias Rodríguez

Acknowledgements

Here are my sincere thanks to those who have helped me in all stages of this work, directly and indirectly.

First of all, I express my sincere gratitude to my thesis supervisors, Dra. María del Mar Sánchez and Dra. Julia Arias for your patience and understanding with all of my questions and problems during my Ph.D. I am especially grateful for their confidence and the freedom they gave me to do this work. Their guidance and advice were invaluable throughout the whole work. Without their coherent instructions, this thesis would not have reached its present form. I will always remain indebted. Thank you very much.

Furthermore, thank very much Dr. Ernesto Ávila for helping me with the VNA and offering me valuable suggestions and advices. I am also very grateful to Juan Pedro Espinosa, laboratory technician, who kindly helped me with a great efficiency in the assembly and fabrication of the experimental structures construction. I extend my sincere thanks to all members of the Area de Tecnología Electrónica.

I am deeply grateful to all members of the jury for agreeing to read the manuscript and to participate in the evaluation of this thesis.

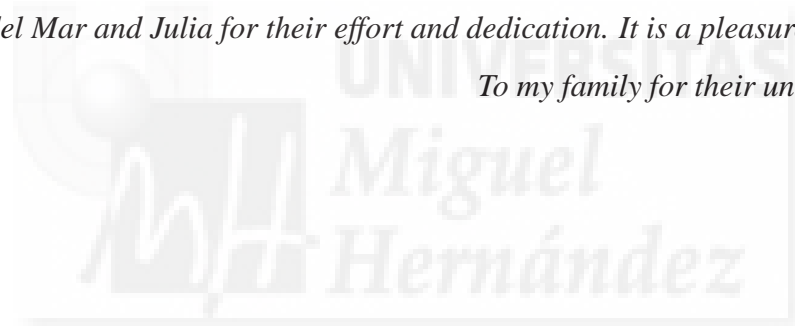
Last but not least, very special thanks go to to my parents and my sister for their moral support and understanding over the last few years. Your love and sacrifices for me have transcended all the difficulties. A particular thank you goes especially to Juanvi for his patience, sacrifice, understanding and his belief in me. Without the support of all members of my family, I would never have finished this thesis. Thank you very much! This thesis is dedicated to you!

This work has been supported by Ministerio de Educaciencia through Project No. FIS2009-13955-C02-02 and Ministerio de Econom Competitividad and Fondos FEDER through Project No. FIS2012-39158-C02-02. Financial support from Conselleria d'Educacieneralitat Valenciana through research contracts No. FPA/2008/065, FPA/2009/096 and BAF/2010/016 are also acknowledged.



To María del Mar and Julia for their effort and dedication. It is a pleasure to work with them.

To my family for their unconditional support.



Abstract

This Thesis lies within the field of Slow and Fast Light (SFL) technologies, which are currently receiving much attention because of their interesting applications, ranging from optical information processing to enhanced precision sensing and interferometry. These technologies are based on systems that exhibit steep positive dispersion to propagate a light pulse at group velocity well below the speed of light in vacuum (*slow light*) or steep negative dispersion to achieve pulse propagation at superluminal or even at negative group velocity (*fast light*). SFL effects thus arise in a myriad of materials exhibiting spectral resonances. Current efforts in this field are mainly focused on the manipulation of material gain or absorption resonances by nonlinear optical processes (*material SFL*) or on the optimization of photonic band-gap structures, without substantial material dispersion, but where structural dispersion comes as a result of the coupling between the light wavelength and the characteristic length of the system (*structural SFL*).

This Thesis focuses on the theoretical and experimental analysis of electromagnetic pulse propagation with abnormal group velocities in two kind of linear and passive devices. In the first part of the Thesis a new system exhibiting structural SFL is demonstrated. It deals with multiple-beam interferometers and provides a comprehensive study of the arising of SFL in this system devoid of photonic band gaps. A theoretical model that fully describes the allowed pulse propagation regimes and its performance in terms of both the interferometer's and the pulse characteristics is developed. Considering amplitude modulated pulses, the capabilities and limitations of SFL effects in this kind of system are retrieved by quantifying typical figures of merit like fractional delay, pulse distortion and Delay-Bandwidth Product. The theoretical framework is valid for any frequency region and the model predictions are probed by performing

experiments in the radiofrequency range and through exact numerical simulations in the optical range. The simplest interferometer, with only two branches, is first considered since it is widely used in actual communication systems. It is analytically demonstrated that slow light cannot possibly be sustained and that the total attenuation drives the changes in the pulse propagation regimes. By increasing the number of branches, group delay tuning from slow to fast light regimes occurs if the optical length of one of the branches is slightly changed.

In the second part of the Thesis, the ability of mono- and multilayer structures to speed up or slow down electromagnetic pulses is investigated, with special emphasis on their reflection properties. Namely, Distributed Bragg Reflectors (DBRs) and Fabry-Perot filters, common in today's communication systems, are examined. These structures were fabricated to operate in the microwave and in the radiofrequency range with the aim of confirming theoretical predictions. Experimental results of their frequency- and time-domain characterization are compared with simulations. An advantage of operating in these frequency ranges is that the transmission and reflection phase function can be measured with a two port vector network analyzer. Such a simple measurement of this key function that determines the pulse propagation regime cannot be directly performed in the optical range. Moreover, microstrip DBRs were designed and their potential application as a negative group-delay circuit to improve the efficiency of feedforward amplifiers, which are commonly used for cancelling inherent distortion in microwave amplifiers, is explored.

List of abbreviations and symbols

ABBREVIATIONS

ADS	Advanced design system
BER	Bit error ratio
CPO	Coherent population oscillations
DBP	Delay-bandwidth product, delay-bit-rate product
DBR	Distributed Bragg reflector
EPA	Error power amplifier
EIT	Electromagnetically induced transparency
FBG	Fiber Bragg grating
FP	Fabry-Perot
FWHM	Full width at half maximum
GVD	Group velocity dispersion
HWHM	Half width at half maximum
IMD	Intermodulation distortion
KKR	Kramers-Kronig Relations
LCLV	Liquid-Crystal light valves
MZI	Mach-Zehnder interferometer
MPA	Main power amplifier
NGD	Negative group delay
OSA	Optical spectrum analyzer
PC	Photonic crystal
PBG	Photonic band gap
PGD	Positive group delay
SBS	Stimulated Brillouin scattering
SFL	Slow and fast light
SRS	Stimulated Raman scattering
WCDMA	Wideband code-division multiple-access

SYMBOLS

α	Attenuation coefficient
β	Phase associated to the refractive index difference
δ	Loss tangent
Δ	Nominal length difference
$\hat{\epsilon}_r$	Complex relative permittivity
\hat{n}	Complex refractive index
κ	Absorption index
λ	Wavelength
Λ	Length of the mirror period
μ_r	Relative magnetic permeability
ν	Magnetic permeability
ω	Angular frequency
ω_0	Angular central frequency
ϕ	Phase
ϵ_{eff}	Effective dielectric constant
ϵ_r	Relative permittivity
σ	Conductivity
$\hat{\epsilon}$	complex dielectric permittivity
c	Speed of light in a vacuum
E_s	Signal or Stokes-Field
E_0	Wave amplitude
\vec{E}	External field
\vec{D}	Field in the medium
f	Frequency
f_B	Bragg frequency
f_c	Carrier frequency
f_m	Modulation frequency
f_p	Pump frequency
f_s	Stokes frequency, signal frequency
h	thickness of the dielectric layer
k	Wavenumber, loss-gain-bandwidth ratio
$k(\omega)$	Complex wave number as a function of the frequency

l	Medium length
L	Length
L_{eff}	Effective length
m_{eff}	Effective number of mirror periods
n	Refractive index
n_g	Group index
Q	Q-factor
S	Scattering parameters
t	Thickness of the microstrip line, time
T_{in}	Pulse duration
τ_g	Group delay
τ_d	Excess pulse delay
v_g	Group velocity
v	Phase velocity
w	Width of the microstrip line



Contents

Abstract	v
List of abbreviations and symbols	vii
1 Introduction	1
1.1 State of the art in slow and fast light systems	2
1.2 Motivation and work objectives	7
1.3 Thesis outline	10
2 Fundamentals on SFL systems	13
2.1 Wave propagation in dispersive media	13
2.1.1 Dispersive media	14
2.1.2 Phase, group and energy velocities	16
2.1.3 Subluminal, superluminal, and negative group velocities	22
2.1.4 Does fast light violate the causality principle?	24
2.2 Figures of merit of an SFL system	26
2.3 Physical processes leading to slow- and fast- light	28
2.3.1 Media with material resonances	29
2.3.2 Photonic bandgap structures	42
2.3.3 Conversion-Dispersion	48
2.3.4 Electronic circuits	49
3 SFL in multiple-beam interferometers	53
3.1 Interference pattern of multiple-beam interferometers	54
3.2 Fast light in Mach-Zehnder interferometers	61

3.2.1	Analytical model	62
3.2.2	Analysis considering the optical path difference	69
3.2.3	Transmission coefficient and group delay	71
3.2.4	Propagation of sinusoidally modulated signals	73
3.2.5	Experimental results and discussion in the RF range	77
3.2.6	Simulation results in the optical range	86
3.3	Slow- and fast- light in three-beam interferometers	89
3.3.1	Analytical model	91
3.3.2	Analysis considering the optical path difference	101
3.3.3	Transmission coefficient and group delay	104
3.3.4	Propagation of sinusoidally modulated signals	106
3.3.5	Experimental results and discussion in the RF range	108
3.3.6	Simulation results in the optical range	116
3.4	Exploring four-beam interferometers	117
3.5	Conclusions	124
4	SFL in mono- and multi-layer systems	129
4.1	Introduction	130
4.2	Transfer matrix method	131
4.2.1	TMM applied to a single layer	134
4.2.2	TMM applied to a DBR filter	138
4.2.3	TMM applied to a Fabry-Perot with DBR mirrors	140
4.3	NGDs of reflected pulses in microstrip slabs	142
4.3.1	Slab design	142
4.3.2	Results and discussion in the MW range	145
4.4	NGDs of reflected pulses in Bragg reflectors	148
4.4.1	Bragg reflector design	148
4.4.2	Results and discussion in the frequency domain	149
4.4.3	Results and discussion in the time domain	154
4.4.4	Hartman effect	156
4.4.5	Slow light in mismatched DBRs	159

4.5	SFL of reflected pulses in asymmetric Fabry-Perot filters	161
4.5.1	Asymmetric Fabry–Perot filter design	161
4.5.2	Results and discussion in the frequency domain	163
4.5.3	Results and discussion in the time domain	168
4.6	Conclusions	172
5	Efficiency enhancement of feedforward amplifiers based on DBRs	175
5.1	Feedforward amplifier description	176
5.2	Bragg reflectors design	179
5.3	Feedforward topology with DBR	184
5.4	Results	186
5.5	Conclusions	189
6	Conclusions and future work	191
6.1	Conclusions	191
6.2	Future work	195
	Publications related to this thesis	197
	Appendix A Scattering parameters	199
	Appendix B Design of RF and MW structures	205
B.1	Coaxial transmission lines	206
B.1.1	Design	206
B.2	Microstrip lines	209
B.2.1	Design	209
	Appendix C Experimental techniques	211
C.1	Setup in the frequency domain	211
C.2	Smoothing of the phase function	213
C.2.1	Savitzky–Golay filter	213
C.3	Setup in the time domain	217
C.3.1	Transmission	217

C.3.2 Reflection	219
C.4 Design and fabrication of a 3-dB splitter	220
Bibliography	225



Chapter 1

Introduction

Slow and fast light technologies (SFL) are of much interest in actual photonics because of their relevant applications in optical communications, sensing, metrology and high-resolution interferometry. They constitute a field in rapid evolution, where recent applications include aspects at the frontiers of science, like the development of quantum memories, temporal cloaking or ultraprecise optical gyroscopes for detecting gravitational waves.

The group velocity (v_g) of a pulse is the velocity at which the peak of its envelope propagates, and is related to the frequency variation of the medium's refractive index $n(\omega)$. Thus, SFL effects rely on steep slopes of the dispersion function. A positive dispersion can be used to slow the pulse propagation down to group velocities well below the light's speed in vacuum ($v_g \ll c$, *slow light*). Similarly, a negative dispersion can lead to *fast light*, where pulses propagate at superluminal ($v_g > c$) or even at negative (pulse *tunnelling*) group velocity.

Although the possibility for propagating a light pulse in dispersive media at unusually slow or fast group velocity is been known for many decades, interest in this phenomenon was triggered by the publication of outstanding experimental reports on the tunneling of optical pulses, and of pulses slowed-down to a bicycle or even to a snail's pace. It is now well established that any system exhibiting marked spectral features can sustain such abnormal pulse propagation regimes. Therefore, SFL systems are classified in two main categories: material SFL and structural SFL. The former ones have substantial material dispersion (media with gain

or absorption resonances), while in the latter case the material dispersion is negligible, but structural dispersion arises from the coupling between the light wavelength and the system's characteristic length (photonic crystals or fiber Bragg gratings).

Hence, these abnormal pulse propagation regimes occur in a myriad of systems, ranging from ultracold atomic gases to room temperature solid crystals, optical fibers, non-linear media and photonic band-gap structures. They have also been reported for electromagnetic pulses at microwave, radiofrequency or even at acoustic frequencies. Thus, research on SFL techniques is certainly a multidisciplinary field that benefits from experts of very varied disciplines, like quantum optics, semiconductors, fiber optics, non-linear optics, and microoptics.

In this chapter an overall introduction to the state-of-the art in SFL systems is given, from which several niches not yet studied are identified. The exploration of these niches are set as the objectives of this thesis and the steps made to confront their study are described. Finally, the chapter presents the organization of this Ph. D. essay.

1.1 State of the art in slow and fast light systems

Early research on abnormal electromagnetic wave propagation was conducted by Sommerfeld and Brillouin in the 1910s, and it was summarized in Brillouin's seminal book *Wave Propagation and Group Velocity* [Bri-1960] published in 1960. In this book, wave propagation through abnormal dispersion media described by a Lorentzian dielectric model is studied, and it is frequently referenced in pertinent publications to this day. A series of publications in the 1970s and 1980s followed this fundamental work, mostly dealing with propagation of more complex waveforms such as a Gaussian pulse modulated carrier waveform, through abnormally dispersive media [Gar-1970, Chu-1982]. Furthermore, a useful analogy between wave propagation in abnormal media and particle tunnelling was studied in several publications in the early 1990s [Mar-1992, Bal-1997].

Bolda, *et al.* [Bol-1993] presented the mathematical proof that anomalous dispersion phenomena not only do not violate the relativistic causality requirements, but they must exist

within some frequency bands for all dispersive media. This is a consequence of the Kramers-Kronig relations which are applicable to all physically realizable, linear causal media. Kramers-Kronig relations provide a link between the attenuation and dispersion characteristics in linear causal media, as presented in the classic book by Jackson [Jac-1998], and discussed by Waters *et al.* [Wat-2005]. Because of the Kramers-Kronig relations, such abnormal pulse propagation regimes are associated to sharp spectral features in the transmission spectrum [Boy-2007].

Renewed interest in these phenomena was triggered by the experimental reports of ralentization of an optical pulse down to group velocities as low as that of a bicycle in Bose-Einstein condensates [Hau-1999], and to superluminal group velocities in atomic vapors [Wan-2000]. Since then, SFL effects have been also shown at room temperature in solid crystals [Tur-2001, Big-2003], semiconductor waveguides [Mor-2005], semiconductor wells and quantum dots [Nar-2010, Su-2006], and through nonlinear wave mixing in optical fibers [Dah-2005, Gon-2005, Sch-2006] or liquid-crystal light valves [Res-2008]. They have also been reported in systems exhibiting structural resonances (photonic band-gap systems, PBG), like photonic crystals [Gal-2007] and fiber Bragg gratings [Lon-2003, Lon-2005], where the dispersion is due to coupling between the incident wavelength and the system's characteristic length. For such PBG systems, experimental evidence of SFL has been provided also in the microwave [Nim-2003, Moj-2000] and radio-frequency (RF) [Hac-2002, Mun-2003] range. In fact, lower frequency setups have been relevant to clarify important issues, like the puzzling advancement of the outgoing pulse peak with respect to the incident pulse in tunnelling experiments, which corresponds to negative group delay (NGD), and hence negative group velocity [Kit-2003]. They have been also used to explore quasiperiodic structures (Fibonacci or Thue-Morse) [Ayn-2005], and Fano-like resonances [Mou-2013] exhibiting strong normal/anomalous dispersion.

Many different SFL systems are currently being investigated in order to achieve optimal performances for specific applications. For instance, external tuning of the pulse propagation regime is very interesting for the synchronization of optical wave-packets in communication networks or for sensing purposes. Such tuning has been reported in non-linear systems, [Gon-2005, Jar-2012] in lossy nanowaveguides [Gov-2006], and in active FBGs [Lon-2005].

In all these cases, the gain mechanism played a key role in assisting the tuning. One of the key applications is optical data buffering. The key goal in this area is to develop a practical and compact system capable of producing a significant and controllable delay for high bandwidth optical data. An initial challenge in this endeavor was the perceived constraint imposed by a limited delay-bandwidth product [Khu-2009]. However, various clever ideas have been investigated theoretically and experimentally to pave the way for overcoming this constraint [Sha-2014]. Another arena of interest is the use of slow light for enhancing the sensitivity of interferometers [Mur-2012] and the use of fast light to develop super-sensitive optical gyroscopes for precision inertial navigation [Sha-2007, Nas-2012] or sensitivity-enhanced gravitational wave detectors [Sal-2010]. Other applications include the development of more compact and efficient nonlinear components [Bab-2008] and LIDARs [Sch-2012], remote sensing of very slowly moving objects by means of precision Doppler measurements [Bor-2013] and enhanced rotary photon drag for image rotation [Fra-2011]. The intense research in SFL technologies encompasses aspects at the frontiers of science, like quantum information processing [Lyo-2009, Cla-2014], and temporal cloaking [Fri-2012].

Let us note that the aforementioned SFL technologies are based on systems that are either active (they respond to the interaction with light by generating narrow, gain or absorption-spectral bands) [Big-2003, Hau-1999, Mor-2005, Su-2006, Tur-2001, Wan-2000], exhibit non-linear effects [Dah-2005, Gon-2005, Jar-2012, Bor-2010] or are periodically structured [Ayn-2005, Gal-2007, Lon-2003, Lon-2005, Nim-2003, Moj-2000, Mun-2003]. However, to our knowledge, few results have been reported for SFL effects in passive, linear and non-periodical structures. One of the objectives of this thesis is to fill this gap. Related to this issue, an interesting work was reported by El Boudouti *et al.* [Bou-2004] on series loop structures sustaining superluminal and subluminal regimes. These structures may be regarded as Mach-Zehnder interferometers (or asymmetric loops) connected in series through segments. Like PBG systems, they exhibit bandgaps, and defect modes appear inside the transmission gaps if one of the segments connecting the loops is somehow changed (in length, for example). The situation resembles that of a doped photonic crystal, with superluminal propagation for a pulse with center frequency in the bandgap and subluminal propagation for a pulse with center frequency at the defect mode. But unlike photonic crystals, an outstanding characteristic

of this serial loop structure is the existence of bandgaps in a totally homogeneous material, without the need of refractive index contrast (or impedance contrast, if the system operates in the RF range as it is the case in [Bou-2004]). Taking into account these results, in this thesis we investigate SFL effects in linear and passive multiple-beam interferometers, i.e. in Mach-Zehnder interferometers with two or more branches.

On another front, whereas most of the studies on superluminality deal with *transmitted* pulses, fewer results have been reported concerning the superluminal propagation of *reflected* pulses. This topic is of interest since common devices in actual communication systems, like dielectric multilayer-based devices, host reflected waves and (not only) transmitted waves. In this context, reported studies on superluminal propagation of reflected pulses include Bragg gratings, Fabry-Perot like photonic barriers and dielectric slabs.

Namely, superluminal peak advancement of reflected pulses was predicted in asymmetric photonic band gap structures where a transmission window inside the gap is opened [Lon-2001]. These predictions were soon confirmed experimentally with the measurement of negative group delays (NGDs) for picosecond optical pulses at $1.5 \mu\text{m}$ in fiber Bragg gratings adequately synthesized to have a double-Lorentzian spectral reflectivity function [Lon-2002]. Also, superluminal reflection of microwave pulses in a Fabry-Pérot photonic tunnelling barrier was reported in a time-domain experiment [Nim-2002]. In this case, and although the reflected microwave pulse arrived earlier than the reference pulse, no NGDs were measured. An ulterior theoretical work [Rao-2004] demonstrated that NGDs for reflected pulses in Fabry-Pérot barriers can be indeed achieved if the cavity contains resonant atomic absorbers. In a similar system, consisting of a dielectric slab doped with dispersive two-level or three-level atoms, superluminal reflected pulses with NGDs were obtained for specific slab thickness conditions [Wan-2004]. Let us remark that in all the works cited above reporting NGDs in reflection [Lon-2001, Lon-2002, Rao-2004, Wan-2004], the system is either asymmetric or doped with active or absorbing atoms. The study of abnormal propagation regimes for pulses reflected on linear and passive multilayer structures will thus be another objective of this thesis.

Let us emphasize that the interest in SFL technologies is not only due to its fundamental physics, their potential applications have fostered intense research on this field. As it was

mentioned above, in fiber sensors, the development of optical buffers, switches and delay lines, and the use of slow and fast light in high-resolution spectral interferometers and gscopes have been reported [Sha-2007]. In the field of fiber sensors, FBGs are widely used to sense a number of perturbations, especially strain and temperature. When a strain change is applied to a FBG, some FBG parameters change. These changes result in a shift in the Bragg wavelength. This shift can be detected with an optical spectrum analyzer (OSA), or using a Mach-Zehnder interferometer to convert the wavelength shift to an amplitude shift, where the sensitivity is proportional to the path difference between the two arms of the interferometer. Structural SFL can improve this resolution record. The phase shift induced by a perturbation applied to a device is proportional to the reciprocal of the group velocity. When the group velocity is reduced, this phase shift is therefore increased. Wen *et al.* [Wen-2012] demonstrated a strain sensor with a sensitivity of $3.14 \times 10^5 \text{ strain}^{-1}$ and a minimum detectable strain of $880 f\varepsilon/\sqrt{Hz}$, the world record for a passive FBG strain sensor at the time of writing.

Regarding delay lines, their applications also extend to the microwave range. A negative group delay synthesizer operating at microwave frequencies was first proposed by Lucyszyn *et al.* [Luc-1993] in 1993. This device operates in reflection mode and it is built with lumped components. The achieved negative group delay is tunable and relatively high over a narrow-band centered at 1 GHz, but accompanied with high losses. Applications such as antenna fed networks can benefit from a simultaneous NRI¹) [Sid-2003, Sid-2004] and NGD effect. The first such design was synthesized by Siddiqui *et al.* consisting of a transmission line circuit periodically loaded with RLC resonators (responsible for NGD) and series capacitors and shunt inductors (responsible for NRI. In order to compensate for loss associated with NGD circuits, active components can be employed. A very low bandpass amplifier exhibiting NGD was proposed by Mitchell *et al.* [Mit-1997, Mit-1998]. Kitano *et al.* synthesized a baseband active NGD circuit [Nak-2002, Kit-2003], using the circuit approach to derive equations describing the NGD phenomenon. Simultaneous negative refractive index and NGD effect in a coplanar waveguide design was reported by Ibraheem *et al.* [Ibr-2008]. Ravelo *et al.* proposed the first active gain-compensated NGD circuit operating at microwave frequency. This design consists

¹Negative refractive index (NRI) is a property not found in any known natural material but which occurs in artificially engineered structures. In a NRI structure the refractive index in the Snell's law is negative, hence, an incident wave experiences a negative refraction at the interface between this medium and a regular one.

of a field-effect transistor based amplifier with a shunt RLC resonator at the amplifier output [Rav-2007c]. A broadband version of this circuit was proposed, synthesized by cascading several stages of the original circuit, each tuned at different frequencies [Rav-2007]. Ravelo *et al.* also proposed several applications for their active circuit [Rav-2007b, Rav-2008, Rav-2010].

Inspired in these previous works, in this thesis we study the use of DBRs, which are linear and passive devices, for introducing positive and negative group delays and its application for improving the efficiency of feedforward amplifiers. Traditional feedforward amplifier designs are commonly used for cancelling inherent distortion in amplifiers by comparing the distorted waveform at the amplifier output to the delayed original input waveform. The input waveform needs to be delayed in time by the same amount as the delay introduced by the amplifier, for a correct identification of the amplifier distortion. Hence, a delay line needs to be employed, which can have a considerable physical length relative to the amplifier circuit dimensions. Noto *et al.* proposed a passive NGD circuit for reducing the physical length of delay lines in feedforward amplifiers [Not-2007], by cascading an NGD circuit with the amplifier, the overall group delay can be reduced and thus the length of the required delay lines gets reduced as well. Choi *et al.* recently reported another NGD circuit application in feedforward amplifiers [Cho-2010].

1.2 Motivation and work objectives

Research on SFL systems can therefore be considered as one of the hot topics in actual photonics, with fundamental and technological interest. The research presented in this thesis focuses on some points that seem to be lacking in the current state of the art in this field. These points have been taken as work objectives and are listed below.

I. Study of SFL effects in linear, passive, non-periodical structures: multiple-beam interferometers.

While SFL effects have been extensively studied in either non-linear, active, or in linear and passive periodical structures (like photonic crystals and fiber Bragg gratings) as mentioned in section 1.1, the possibility of having such abnormal pulse propagation

regimes in linear, passive non-periodical systems, which exhibit no photonic bandgap, has not been reported yet. Multiple-beam interferometers (also called generalized Mach-Zehnder interferometers) are an example of this kind of systems.

As a first objective, the plain Mach-Zehnder interferometer (MZI) is considered and an **analytical model is developed to determine abnormal group velocity regimes**. The study is extended to generalized Mach-Zehnder interferometers. Instead of considering the series loop structures of [Bou-2004] exhibiting bandgaps (series connection of MZI), we increase the number of arms in the MZI, keeping constant the length difference between adjacent arms. SFL transitions are studied by slightly modifying the length of one of the interferometer's branch. A major goal at this point is to **develop a full analytical description** of such transitions in the pulse propagation regime by **deriving an expression for the group delay at the minima**. For that purpose, a three-beam interferometer is considered because it is the simplest interferometer (least number of arms) where a length detuning in a branch implies a change in the otherwise constant length difference between adjacent arms. A consequent objective is to **experimentally proof this model** by building the interferometers with coaxial cables and RF wave splitters.

II. Study of SFL effects for pulses reflected in mono- and multi-layer structures.

Multilayer structures are linear, passive, periodical structures (1D photonic crystals) where, as mentioned in section 1.1, SFL effects have been well reported mainly for transmitted pulses. The second goal of this work focuses then on the analysis of these effects for reflected pulses. The starting point we have considered is based on a previous theoretical study that predicted large negative group delays (NGD) for reflected pulses in symmetric, non-doped, weakly absorbing dielectric slabs [Wan-2006]. It was shown that NGDs should occur for narrowband reflected pulses with center frequency in the minima of the slab's spectral reflective curve, where the reflective phase function had a large negative slope.

Therefore, an objective of this work is to **provide experimental evidence of these theoretical predictions** by building the structures to operate in the microwave range, where the phase function can be directly measured with a vector network analyzer.

Microstrip technology is used to fabricate the microwave analogs to dielectric slabs and our study is extended also to Bragg reflectors. In addition to the frequency-domain characterization of these structures, time-domain characterization can also be performed to explicitly show the advancement of pulses reflected on these structures. Other goals of this work are related to interesting issues regarding these systems. For example, **obtaining scaling laws** for key characteristics (which are useful in order to reproduce a specific device in another frequency range of operation), the **study of the Hartman effect** (the saturation of the group delay with increasing structure length), and the debated question on whether 1D multilayer structures can sustain tunnelling on transmission.

III. Group delay tuning of pulses reflected in Fabry-Perot filters.

Fabry-Perot filters are particularly interesting for communications and sensing applications. As stated in section 1.1, their performance as SFL systems for transmitted pulses has been already reported. In this thesis we study their capabilities and limitations to sustain abnormal propagation regimes for reflected pulses, focusing in an important question: the possibility of achieving **group velocity control**. Group velocity control (or group delay tunability) is of utmost interest for optical delay line applications. Various techniques to drive a change in the pulse propagation regime, from subluminal to superluminal or tunnelling, are considered in this work, either by changing the mirror spacings or by modifying the attenuation in the filter.

IV. Application of microwave DBRs to feedforward amplifiers.

Circuits capable of advancing or delaying a microwave signal must be kept in mind when a feedforward technique is chosen to linearize power amplifiers in actual communications. As mentioned in section 1.1, several architectures have been proposed, in particular the use of NGD circuits to reduce the delay lines, which can have a considerable physical length relative to the amplifier [Not-2007, Cho-2010]. The NGD circuits proposed in literature thus far are all single-directional, in transmission or reflection. We study a **novel design**, where microstrip **Bragg reflectors** are used simultaneously in **transmission and reflection** to induce positive and negative group delays, respectively, with the aim of **reducing or even cancelling the two delay lines** present in a feedforward amplifier.

1.3 Thesis outline

The thesis is organized as follows:

After this first chapter introducing the state of the art, motivations and objectives of the work, in chapter 2, the fundamentals on abnormal wave propagation is briefly reviewed since it is a necessary background for subsequent chapters, and an overview of the different systems and techniques to generate slow and fast light is provided. Furthermore, fundamental limits and figures of merit of SFL systems are presented, which are important issues regarding applications.

Chapters 3, 4 and 5 contain the results of the investigations of this thesis.

Chapter 3 is devoted to the study of SFL effects in multiple-beam interferometers. We begin by considering the simplest case, i.e. a linear and passive Mach-Zehnder interferometer (MZI), where we demonstrate, both theoretically and experimentally, superluminal and negative group velocities and no subluminal propagation. Next, with the aim of generating also subluminal regime, we increase the number of arms and consider the simplest interferometer (three-beam interferometer) where a length detuning in a branch implies a change in the otherwise constant length difference between adjacent arms. A model that fully describes SFL effects in such a three-beam interferometer is developed and a proof-of-model experiment is performed in the RF range by using coaxial cables and wave splitters. Finally, the study is extended to a 4-beam interferometer.

In chapter 4, SFL effects are studied for reflected pulses on multilayer structures. First, weakly absorbing dielectric slabs and distributed Bragg reflectors (DBRs) are considered. Experimental evidence of negative group delays (NGDs) on these linear and passive structures is provided through frequency- and time-domain characterization. Although our structures operate in the microwave range, these devices excellently scale to their analogous optical structures, and confirm previous theoretical predictions. A scaling law for the group delay of a weakly absorbing dielectric slab is derived and the Hartman effect on DBRs is analyzed both in reflection and transmission. To conclude this chapter, symmetric and asymmetric Fabry-Perot

filters with Bragg mirrors are analyzed, in which the group velocity can change from subluminal to superluminal by changing the mirrors spacing or the filter's attenuation. These transitions are experimentally proved in the radiofrequency range on structures made of coaxial cables assemblies.

In Chapter 5, group delay control in DBRs is analyzed and applied to improve the efficiency of feedforward amplifiers. Simulations of a feedforward amplifier based on DBRs are performed and we demonstrate the feasibility of this idea.

In Chapter 6 the main conclusions of this work with highlighted original contributions are given. Open lines and proposed future work is outlined at the end of this chapter.

Finally, the appendices provide valuable additional information. In appendix A, the S-parameters (scattering parameters) are described, which are commonly used to obtain the performance of radiofrequency and microwave devices. The design and fabrication of linear and passive structures operative in the radiofrequency and in the microwave range is described in appendix B. Finally, in appendix C, the vector network analyzer setup used in the frequency measurements is explained. An experimental technique for accurately tuning the carrier frequency of a sinusoidally modulated signal and measuring the group delay in time domain was developed and a detailed description of the setup is also given

Chapter 2

Fundamentals on SFL systems

In this chapter we summarize the basic concepts of slow- and fast-light (SFL) systems. Such pulse propagation regimes occur in media with strong normal dispersion (slow light) or with strong anomalous dispersion (fast light), this is why the first section is devoted to the main concepts dealing with wave propagation in dispersive media. Definitions of different velocities concerning the propagation of an electromagnetic pulse in a dispersive medium are recalled (phase, group and energy velocity), and the physical interpretation of SFL as an interference effect (pulse reshaping) of the pulse spectral components inside the medium is explained. Finally, we discuss the apparent contradiction of fast light with Einstein's causality principle according to which, no information can be transmitted at rates exceeding that of light in vacuum. The most important metrics to evaluate the efficiency of an SFL system is defined in the second section of this chapter. In the last section, a brief description of the different physical processes leading to slow- and fast-light and the main achievements reached by the scientific community are given.

2.1 Wave propagation in dispersive media

The physics of wave propagation at a speed exceeding c has been a subject of discussion for many decades since the beginning of the 20th century. The distinction between signal and

group velocities was considered in the early research of Voigt and Ehrenfest on elementary dispersive waves, and by Laue who first considered dispersive wave propagation in a region of anomalous dispersion where the absorption is large and strongly frequency dependent [Bri-1960]. Sommerfeld considered the distinction between front and signal velocities, and proved that no signal can travel faster than the vacuum speed of light c and that the signal front advanced with the velocity c in a Lorentz dielectric model. Then Brillouin provided a description of the signal evolution in a single resonance Lorentz dielectric model. Later, in the 70s Garrett and McCumber [Gar-1970] were the first to analytically estimate that a Gaussian pulse can travel in an anomalous and linear dispersive medium at a group velocity (the velocity of the Gaussian's envelope) greater than c or even be negative, i.e., the transmitted peak exits the medium before the incident peak enters it. Therefore, in this first section we show the main concepts of pulse propagation in dispersive media, including the definitions of different velocities involved in the propagation of an electromagnetic pulse.

2.1.1 Dispersive media

All media except vacuum are dispersive. The degree of dispersion depends on the specific spectral range and may be negligible in some frequency region (transparency region). Dispersion is due to the delay in the response of the medium to the incident electromagnetic wave, as a consequence of the interaction between the wave and the particles of the medium.

A dispersive medium is characterized by a complex dielectric permittivity, $\hat{\epsilon}$, that depends on the frequency and relates the external electric field (\vec{E}) to the field in the medium (\vec{D}) according to $\vec{D} = \epsilon_0 \hat{\epsilon} \vec{E}$, and can be written as:

$$\hat{\epsilon}(\omega) = \epsilon'(\omega) + i\epsilon''(\omega) \quad (2.1)$$

The fact that a non-zero $\epsilon''(\omega)$ is directly associated to the delay in the response of the medium can be shown very easily [Cab-2002]. For simplicity, let's consider an isotropic medium and let $E(t) = E_0 e^{j\omega t}$ be a Fourier component of the incident electromagnetic wave. The field inside

that medium will be out of phase with it due to the delay in the response to \hat{E} , then we can write $D(t) = D_0 e^{j(\omega t + \delta)}$.

By developing the above equation, and comparing the real and imaginary parts at both sides of $\vec{D} = \epsilon_0 \hat{\epsilon} \vec{E}$, the following relation between the imaginary part of the dielectric permittivity and the phase δ is found: $\delta = \text{atan} \frac{\epsilon''}{\epsilon'}$. This explicitly shows that $\delta \neq 0$ only if $\epsilon'' \neq 0$ (i.e. \vec{D} is delayed with respect to \vec{E}).

On the other hand, a delay in the response of the medium implies that the value of the internal field \vec{D} at given time t depends only on the value that the external field \vec{E} takes a prior time ($t' < t$). In other words, “times ulterior to the cause do not contribute to the effect”. This is the situation in a linear and causal medium. This causality property is contained in the Kramers-Kronig relations that link the real (ϵ') and imaginary (ϵ'') parts of the dielectric function. We will come back to this point later, since this is a key issue in the arising and interpretation of SFL effects.

The ω -dependent complex dielectric function leads to a ω -dependent complex refractive index $\hat{n} = \sqrt{\mu \hat{\epsilon}}$, (μ is the magnetic permeability) expressed as:

$$\hat{n}(\omega) = n(\omega) + i\kappa(\omega) \quad (2.2)$$

where n is the real part of the refractive index and κ is the absorption index, also called the extinction coefficient. For active media (exhibiting gain) $\kappa < 0$, while it is positive for absorptive materials. These quantities depend on the material constants $\hat{\epsilon}$, μ and conductivity σ (see for instance Chap. 6 in [Cab-2002]).

Similarly to the real (ϵ') and imaginary (ϵ'') part of the dielectric function, $n(\omega)$ and $\kappa(\omega)$ are also related by Kramers–Kronig relations:

$$n(\omega) = 1 + \frac{2}{\pi} P \int_0^\infty \frac{\omega' \kappa(\omega')}{\omega'^2 - \omega^2} d\omega' \quad (2.3a)$$

$$\kappa(\omega) = -\frac{2\omega}{\pi} P \int_0^\infty \frac{n(\omega') - 1}{\omega'^2 - \omega^2} d\omega' \quad (2.3b)$$

Eqs. 2.3 allows retrieving the values of the refractive index in a specific frequency range from measurements of the absorption in the medium. But most relevant here, it shows that a resonance in $\kappa(\omega)$ will lead to abrupt slopes in the refractive index, i.e. to strong dispersion around the resonance.

As it will be discussed in the next section, the key point to obtain SFL effects is to find some physical processes that can provide resonances showing the necessary spectral features, namely a narrow bandwidth and a strong amplitude.

2.1.2 Phase, group and energy velocities

Let us discuss how strong dispersion in the medium affects the wave propagation. Any real wave can be considered as a superposition of sine waves (Fourier components), each with a certain frequency and amplitude. The propagation of a real wave through a dispersive medium is not straightforward, since each Fourier component travels at different phase velocity. The phase velocity (v_p) is the speed at which the planes of equal phase (phase front) of a monochromatic wave propagate through a medium of refractive index n . In the time corresponding to a period T , the phase front propagates the distance of a wavelength (λ). Hence, $v_p = \lambda/T = \omega/k$ where ω is the angular frequency and k is the wavenumber, defined as $k = 2\pi/\lambda = \omega n/c$.

It must be pointed out that the phase velocity tells nothing about the process of propagation. Since a sine wave is uninterminated (it has infinite duration, it does not start nor finishes at any time), one cannot strictly define a velocity of propagation. The phase velocity only represents how the phase of the wave is delayed by the interaction of the medium (forced oscillations of the ions or electrons) but tells nothing about the process of wave propagation in the medium, since the light excitation at any point in the medium is present forever for an infinitely long sine wave.

On the other hand, every Fourier component of the real (time-limited) wave will be more or less absorbed, depending on the value of the absorption index $\kappa(\omega)$. The consequence of both

processes is the distortion of the wave as it travels through the dispersive medium. If the wave is strongly distorted, one cannot define a wave propagation velocity.

A simpler and usual case, which in fact is of interest to us, is that of a wave-packet or narrow band pulse. The pulse propagation velocity, or group velocity, is the velocity at which the peak of its envelope (with center frequency ω_0) travels, and it is defined as [Bri-1960]

$$v_g = \left. \frac{d\omega}{d\kappa} \right|_{\omega_0} \quad (2.4)$$

where $\omega(\kappa)$ is the dispersion relation. Following [Cab-2002] this definition can be retrieved from the following physical consideration. The peak of the pulse envelope occurs at time and space points where all the spectral components of the pulse are in phase. Let $t = 0$ be the instant when all the components are in phase at $z = 0$ (propagation along the z -axis is assumed). After a certain time interval Δt , all the spectral components will be again in phase at point Δz . The velocity of the peak propagation is thus $v_g = \Delta z / \Delta t$.

$E(z, t) = E_{0,\omega} e^{i(\kappa z - \omega t + \phi_0)}$ is the Fourier component of frequency ω , wavenumber κ and initial phase ϕ_0 . Hence, the phase ϕ of this component at a later instant Δt and point Δz of the medium is:

$$\phi = \kappa \Delta z - \omega \Delta t + \phi_0 \quad (2.5)$$

If all the Fourier components are to be in phase again at Δz and Δt , it means that the phase given by (2.5) cannot depend on the frequency that characterizes each component. Thus:

$$\frac{\partial \phi}{\partial \omega} = 0 = \Delta z \frac{\partial \kappa}{\partial \omega} - \Delta t \rightarrow v_g = \frac{\Delta z}{\Delta t} = \left. \frac{\partial \omega}{\partial \kappa} \right|_{\omega_0}$$

To obtain v_g , the function $\kappa(\omega)$ is usually used instead of $\omega(\kappa)$, since the system's characteristics are often characterized as a frequency function. For media that respond linearly to the applied field $\kappa(\omega) = n\omega/c$ (linear media), the group velocity can be written as:

$$v_g = \left(\frac{\partial \kappa}{\partial \omega} \right)^{-1} = \frac{c}{n(\omega) + \omega \frac{\partial n}{\partial \omega}} = \frac{c}{n_g} \quad (2.6)$$

where n_g is the group index. In analogy with the refractive index, the group index (or group refractive index) is defined as the ratio of the group velocity in vacuum to the group velocity in the medium.

In a non-dispersive medium ($\partial n / \partial \omega = 0$), the pulse propagates without distortion, since all components travel at the same speed $v_p = c/n$. According to Eq. (2.6), the group index reduces to the refractive index, consequently the pulse propagates at the phase velocity, $v_g = v_p$.

In a dispersive medium, where $\partial n / \partial \omega \neq 0$, the group velocity can vary noticeably with frequency over the pulse bandwidth, an effect that is known as group velocity dispersion. Physically, this means that the pulse will begin to experience distortion effects due to higher-order dispersion that may degrade or change the pulse's shape. Generally, the concept of group velocity is used as long as the pulse distortion is not too great, though there is no agreed-upon quantitative benchmark for this limit [Geh-2008]. However, if the distortion is not large enough, the group velocity can still be used to describe the wave propagation in the medium [Poz-2012].

According to Eq. (2.6), in a dispersive medium, the slope of $n(\omega)$ determines the pulse propagation regime. A steep positive spectral variation of the refractive index ($\partial n / \partial \omega \gg 0$) can lead to a very small group velocity $v_g \ll c$ (*slow light* or also subluminal pulse propagation), while a steep anomalous dispersion ($\partial n / \partial \omega < 0$), leads to superluminal group velocity (it is larger than c) or even negative (pulse tunnelling).

The normalized group velocity (v_g in units of c) as a function of $\omega \partial n / \partial \omega$ is shown in Fig. 2.1. In a spectral region of normal dispersion where $\partial n / \partial \omega > 0$, the group velocity decreases. It is less than the phase velocity and can take on very low values. Since the pulse is slowed down, this corresponds to slow light. If the refractive index slope is negative (anomalous dispersion), the group velocity increases. Therefore, the pulse travels at a speed faster than the phase velocity. For strong anomalous dispersion the group velocity can exceed c . This corresponds to fast light regime. In section 2.3, the physical processes leading to strong dispersion are summarized.

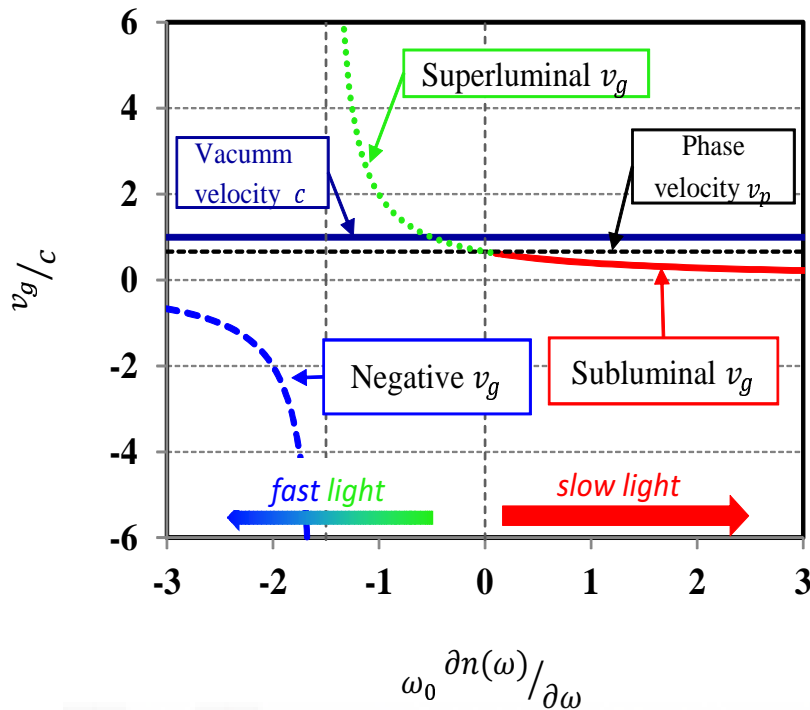


Figure 2.1: Group velocity as a function of $\omega_0 \frac{\partial n(\omega)}{\partial \omega}$ for $n(\omega_0) = 1.5$.

The group velocity can be related to the velocity of energy propagation of all carriers (*energy velocity*, v_E), which is defined as the ratio of the Poynting vector and the energy density [Bri-1960]. In a low-dispersive medium, the wave propagates with little distortion and $v_g = v_E$. By contrast, in presence of strong dispersion these velocities may be very different.

Figure 2.2 shows schematically the variation –around a material resonance– of the refractive indices for the three speeds introduced in this section, i e., phase, group, and energy speeds. Although v_p and v_g exceed the value of c in the vicinity of the resonance, the velocity v_E , which has real physical meaning in these dispersive regions does not exceed it. So, it does not contradict the theory of relativity, as it will be discussed in more detail below.

Let us now consider the wave propagation in engineered media without substantial material dispersion, like photonic crystals [Joa-2011]. These systems consist of a periodic refractive index distribution and exhibit *structural* dispersion due to coupling between the incident wavelength and the characteristic length of the structure. This structural dispersion can be

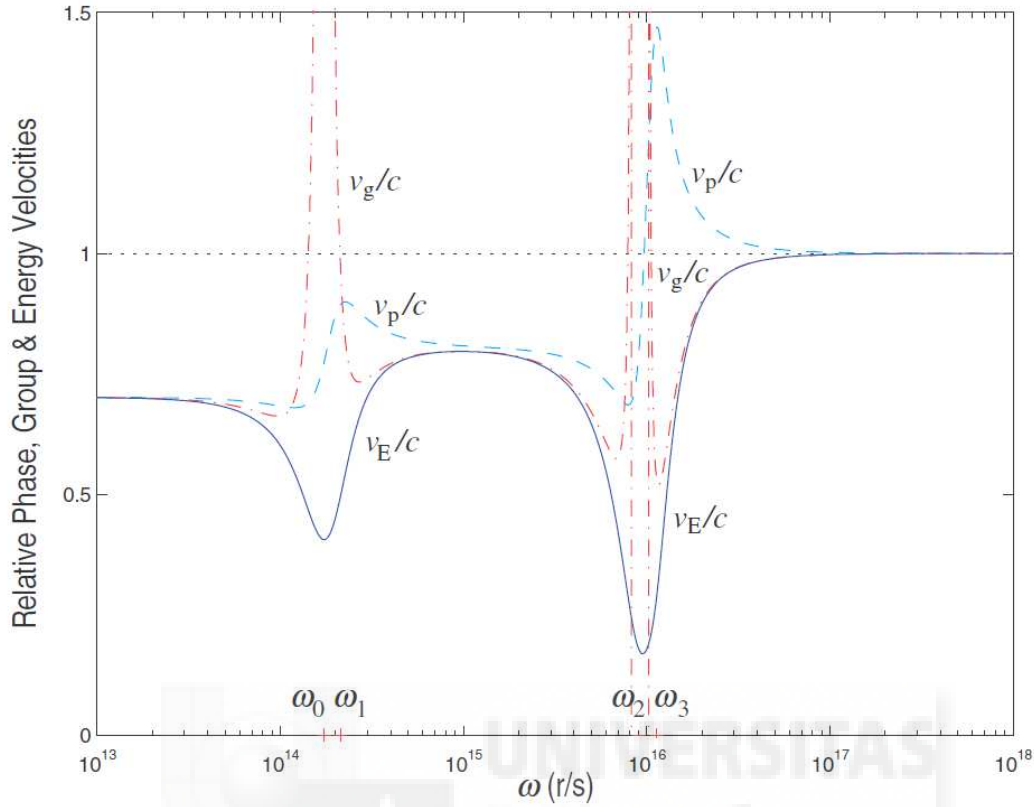


Figure 2.2: (Extracted from [Oug-2005]). Frequency dispersion of the relative phase velocity v_p/c (dot-dashed curve), relative group velocity v_g/c (dashed curve) and relative energy velocity v_E/c (solid curve) in a double resonance Lorentz dielectric model.

modelled [Cen-1999] by an effective refractive index $n_{eff}(\omega)$ that is obtained from the phase acquired upon transmission, $\phi_t(\omega)$, through the system of length d , $n_{eff}(\omega) = \frac{c}{\omega d} \phi_t(\omega)$.

For propagation in such a finite photonic band-gap structure, it has been shown [D'Ag-2001] that the group and the energy velocities are related by the module of the transmission coefficient $t(\omega)$ of the medium in the form:

$$v_E(\omega) = |t(\omega)|^2 v_g(\omega) \quad (2.7)$$

Equation (2.7) is a surprisingly simple result that makes clear that for finite structures, the group velocity, v_g , and the energy velocity, v_E , are equal only in the region (or regions) of unit transmittance and can be very different in the other regions, especially in those of very low

transmittance (the photonic band gap region). If we consider that the energy velocity can never take values greater than c , from eq. (2.7), it follows directly that the group velocity must satisfy the following inequality: $v_g \leq c/|t(\omega)|^2$. That is, the requirement that the energy velocity must be subluminal does not forbid the possibility of superluminal v_g . Rather, in regions with low transmittance, this inequality imposes an upper limit on v_g that it can be achieved without violating the requirement that the energy velocity remains subluminal [D'Ag-2001]. For example, in the region of the photonic gap, where the transmission can be as low as 10^{-5} , superluminal group velocities around $5c$ can be reached. This value is below the upper limit (10^5) imposed by the condition that v_E remains subluminal. Numerical simulations of space and time evolution of one-dimensional photonic crystals confirm that v_E never exceeds c in any place and time [Liu-2002].

Especially when describing superluminal pulse propagation, one often uses the more versatile concept of group delay (τ_g), instead of group velocity, to both spatially extended ($L \gg$ wavelength) and spatially negligible ($L \ll$ wavelength) systems. The *group delay* is the time delay of the pulse envelope as it propagates through a medium [Bri-1960]. For a spatially extended medium of length L_{eff} , the group velocity and the group delay are related according to

$$\tau_g = \frac{L_{eff}}{v_g} \quad (2.8)$$

Here the length of the medium was named as an effective length L_{eff} in order to include the case of engineered photonic band-gap structures.

Note that Eq. (2.8) is only valid for narrowband pulses, though it serves as an upper bound to the delay if higher order distortion becomes important.

Following the usually adopted phase–time approach [Nim-2003, Moj-2003, Ste-1993] the group delay of a transmitted (or reflected) narrowband pulse, with center frequency ω_0 , is obtained by frequency deriving the transmission (or reflection) phase coefficient as:

$$\tau_g = \frac{\partial \phi}{\partial \omega} \quad (2.9)$$

Negative group delays (NGDs) are puzzling, since the peak of the outgoing pulse precedes the peak of the input pulse. Although this phenomenon challenges common intuition, several works [Kit-2003, Moj-2003, Wan-2000] demonstrate that it does not violate the causality principle. In particular, lumped systems have offered a clear insight on this controversial aspect of superluminal phenomena. This issue is discussed in the next section.

2.1.3 Subluminal, superluminal, and negative group velocities: Physical interpretation

Figure 2.3 illustrates the propagation of a pulse at subluminal, superluminal and negative group velocity, where the corresponding pulse delay is compared to that of a reference pulse travelling the same distance in vacuum (air). A medium of length l through which an ideal Gaussian pulse propagates is considered.

A reference pulse propagates through free space (pulse C) with a group velocity $v_g = c$ and takes a time $\tau_g = l/c$ to traverse the medium. Under normal circumstances, the group delay of a medium of length l is positive and greater than l/c since $v_g < c$. Therefore, strictly speaking the normal situation is subluminal propagation. In this work, as it is widely used in the field of SFL effects, the term subluminal refers to the situation where $v_g \ll c$. Slow light occurs when a propagating pulse is slowed down by the interaction with the medium in which the propagation takes place (pulse D).

Pulse B traverses the medium in a time span less than the time required to travel the same distance in vacuum (l/c), since it is advanced with respect to the reference pulse C. Hence it travels superluminally with $v_g > c$. Under strong anomalous dispersion, the pulse peak can leave the medium before even entering it (pulse A), i.e. the peak of the output pulse precedes the peak of the input pulse. This results in a negative group delay and correspondingly a negative group velocity ($v_g < 0$). We speak of pulse tunnelling in this situation.

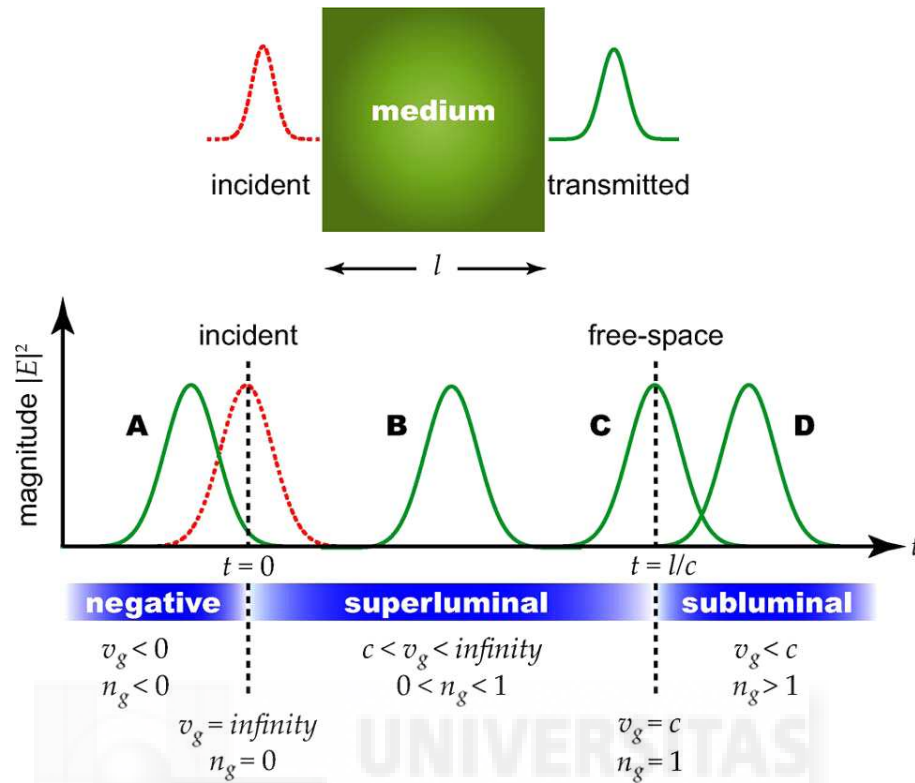


Figure 2.3: (Extracted from [Wit-2010]). Diagram of group velocity. An incident pulse travelling through a medium experiences different delay and attenuation depending on the medium's response. The normalized transmitted pulses labeled A, B, and D with negative, superluminal, and subluminal group velocity, respectively, are shown relative to the referent free-space pulse, labeled C.

Although an ideal case was assumed here, in reality the medium's dispersion not only affects the group delay, but also the attenuation (which produces a distortion of the pulse too). For a passive medium, subluminal, superluminal or negative group velocity is accompanied by reduction of the output pulse amplitude relative to the input pulse, though the envelope retains its basic shape. In other words, for such a medium, the pulses depicted in Fig. 2.2 are considered to be normalized to their respective maximum values. However, as it will be discussed in section 2.3, such attenuation is not a necessary condition in every SFL medium. In fact, it has been shown that an inverted medium (a medium with gain) displays abnormal group velocities without attenuation [Bol-1993, Bol-1994, Ste-2003, Wan-2000]. Furthermore, the effects of reflection on the interfaces air/medium have been ignored. These reflections produce standing waves in the section and, thus, cause a further reduction in the transmitted pulse amplitude; however, they do not affect the location of the pulse peaks.

The mechanism behind these large pulse delays or advancements can be explained in terms of pulse reshaping due to coherent interference of the pulse frequency components [Guo-2006, McD-2001, Pev-2008]. We can study the time evolution of a pulse by considering the spatio-temporal amplitude distributions of the individual Fourier components, and by Fourier analysis, this waveform can be decomposed into many single-frequency sinusoidal components. The peak of the pulse is formed at the position where these individual frequency components interfere constructively, and the nulls of the pulse are formed where these components interfere destructively.

In a normal medium where $0 < v_g \leq c$ the shift is negative; the pulse appears to have been delayed during its passage through the medium. But after traversing a negative group velocity medium, the pulse appears to have been advanced. This advance is possible because in the Fourier view, each component wave extends over all space, even if the pulse appears to be restricted. The unusual “*reshaping*” in a negative group velocity medium shifts the phases of the frequency components of the wave train in the region ahead of the nominal peak such that the phases all coincide, and a peak is observed, at times earlier than expected at points beyond the medium.

2.1.4 Does fast light violate the causality principle?

The existence of dispersion regions (of material or of structural origin) capable of sustaining superluminal group velocities leads immediately to an apparent paradox and has led to misinterpretations. In the first measurements of the group velocity, carried out by Lord Rayleigh on sound waves, the group velocity was identified with the energy and signal velocities [Bri-1960]. Obviously, this theory clashed with Einstein’s relativity, which states that no signal or particle can travel at velocity faster than light in vacuum, c .

Sommerfeld’s work, among others, contributed fundamentally to clarify these issues by comparing the signal propagation theory with Einstein’s relativity. Sommerfeld showed¹ that

¹A. Sommerfeld, “Über die Fortpflanzung des Lichtes in disperdierenden Medien”, Ann. Phys. 44, 177-202 (1914).

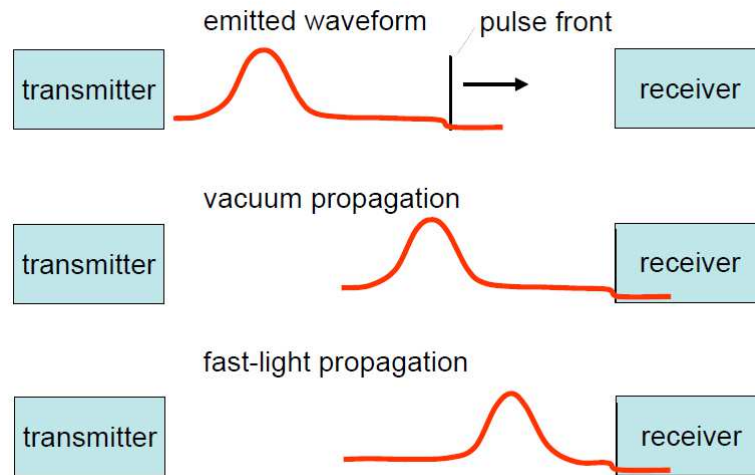


Figure 2.4: (Extracted from [Mug-2009]). Pulse propagation through a fast-light medium. In superluminal propagation experiments, the peak of the pulse moves at superluminal velocity, but the front of the pulse moves at velocity c . Because the information content of the pulse is contained in the front, no information is transmitted at a velocity exceeding c .

the group velocity is not the velocity at which a signal propagates, especially in regions with strong anomalous dispersion. Sommerfeld introduced the concept of front signal velocity, and showed that the front advances at velocity less or equal than c , under any circumstance (see Fig. 2.4). The front velocity represents the speed at which information travels. Recent measurements of superluminal group velocities in photonic crystals and optical gain media or media with intense absorption bands have revived these issues and the apparent conflict with the causality principle [Moj-2000, Moj-2003, Sid-2004].

The group velocity can take on any value. However, the information always travels slower than c . It is based on the concept of causal signals (with a well-defined front) that are propagated by causal media. A causal medium is defined as one for which the effect cannot precede the cause. The mathematical formalization of these concepts are detailed in [Bri-1960, Moj-2000] where it is shown that it is not possible to detect a signal at some point x at a time instant less than x/c . From a purely theoretical point of view, it states that the information carried by an electromagnetic pulse is associated with the front of the pulse ($t = 0$) and the oscillations of the field immediately following the front, i.e. the Sommerfeld *forerunner*. Every causal signal has a starting point in time, before which the signal does not exist. This starting point

($t = 0$) is marked by a discontinuity in the pulse envelope or in higher-order derivatives of the envelope, where the pulse is no longer analytic. These points of nonanalyticity are conveyers of *genuine information* and can be shown to propagate at exactly the speed of light c under all circumstances, and thereby fulfill the requirements of the relativistic causality. In short, for a smoothly varying pulse, presented by an analytical function, there is no more information in the pulse peak than in its earliest parts.

It is important to note that while theoretical evidences and simulations of microwave pulse propagation [Moj-2003] demonstrate the causal propagation of information in the points of nonanalyticity, the amplitudes associated with these fronts are particularly small, making their experimental detection a challenging task. This difficulty is the reason that the detected "signal" is not the pulse front, but the maximum or half–maximum of the pulse envelope, which, in turn, can be made to propagate superluminally or with negative velocities [Sid-2004].

2.2 Figures of merit of an SFL system

The efficiency of SFL systems is evaluated through some metrics or figures of merit [Geh-2008]. The group index was already mentioned as a possible metric. However, the group index by itself is not sufficient to fully characterize a SFL system. In the following paragraphs the main figures of merit are defined

I. Group index (n_g), group velocity (v_g), or group delay (τ_g):

The group index and the group velocity are equivalent measures since they are connected by the speed of light in vacuum, $v_g = c/n_g$. In a frequency domain experiment v_g can be obtained from Eq. (2.6) when the refractive index function is known in the spectral range of interest. A simpler method consists in retrieving v_g from the characterization of the system's phase function $\phi(\omega)$ (transmission phase or reflection phase), and use Eqs. (2.8) and (2.9) to obtain $v_g = l(\partial\phi/\partial\omega)^{-1}$, where l is the length of the medium. Since a frequency–domain characterization of $\phi(\omega)$ is difficult to perform in the optical range (complicate interferometric techniques must be used), in practice, it is usually determined in a time–domain experiment by measuring the propagation time of the pulse (τ_{pulse})

through the medium, hence $v_g = l/\tau_{pulse}$. Let us point out that the pulse delay τ_{pulse} is generally different from the group delay τ_g due to pulse widening or compression upon propagation. Unfortunately, these simple parameters can be the least useful measures for some applications. A delay of 10 ns is large for a pulse of 1 ns duration, but insignificant for a pulse of 10 μ s. Hence, the group delay is usually accompanied by a measure of the achievable bandwidth or bit rate in order to present a more meaningful analysis.

The group index (also sometimes referred to as the *slowdown factor*) is a common metric used to describe an SFL system too. For a pulse whose bandwidth is considerably smaller than the region of linear dispersion, the group index is directly proportional to the delay experienced during propagation since $n_g = \frac{c}{v_g} = (c/l) \cdot \tau_{pulse}$.

II. Fractional Delay (*FD*):

It is defined as the ratio between the excess pulse delay (which is the difference between the pulse delay and the phase delay $\tau_d = \tau_{pulse} - \tau_p$ and the input pulse duration, T_{in} , i.e.,

$$FD = \frac{\tau_d}{T_{in}} = \frac{\tau_{pulse} - \tau_p}{T_{in}} \quad (2.10)$$

T_{in} is most commonly defined as the pulse full-width at half-maximum (FWHM), though authors occasionally use other measures of the pulse duration. Conceptually, the fractional delay is more adequate when evaluating the delay because it is related to the pulse duration to give more accurate information of delays.

Therefore, for the above example, fractional delays of 10 and 0.001, respectively, are achieved. Note that for the same absolute pulse delay of 10 ns, the corresponding fractional time delay shows a significant difference in the case of a pulse duration of 1 ns or of 10 μ s. Unfortunately, the fractional delay cannot stand alone as the unique metric; a fractional delay does not provide information on the pulse delay or the pulse width, only on their ratio. Hence, this metric is usually accompanied by a bandwidth measurement.

III. Delay-Bandwidth or Delay-Bit-Rate Product:

Very similar to the fractional delay, the delay-bandwidth product or delay-bit-rate product (DBP) combines a pulse delay measurement with the pulse bandwidth or bit rate.

In general, “bandwidth” refers to the optical spectral width of a data channel, whereas bit rate refers to the bits per second (bits/s) of transmitted data. The expression for DBP product is

$$\Delta_{DBP} = \tau_{pulse} \cdot B \quad (2.11)$$

where τ_{pulse} is the pulse delay and B denotes the FWHM bandwidth or bit rate. In most SFL systems, the DBP is a valuable parameter since large absolute time delays might be accompanied by low bit-rate channel, but this might correspond to only an insignificantly small fractional delay. Moreover, higher bit-rate channels are presently of high interest in terms of potentially performing digital signal processing. Therefore, small delays for extremely small bit times might be of significance [Geh-2008].

IV. Q-Delay Product:

One opportunity to quantify the data distortion after the pulse transmission is the Q factor which is directly related to the signal-to-noise-ratio, the bit error ratio (which indicates the ratio of the received numbers of bit errors over the total number of bits within a certain time interval) and the eye diagram opening. It decreases with an increasing distortion. The Q-delay product combines the amount of distortion with the delay and thus, provides an insight into the optimal design of the SFL system. Thus, the Q-factor product can be used to find a tradeoff between the delay and the distortion [Khu-2009].

V. Other Metrics:

There are other metrics that can be used to evaluate SFL systems. Many familiar figures of merit can be applied seamlessly, including bit error rate, power penalty, and eye opening. Each application imposes its own metrics that must be met.

2.3 Physical processes leading to slow- and fast- light

As it was discussed in Section 2.1, fast light is observed when a pulse propagates in a medium with a steep anomalous dispersion at the pulse center frequency, whereas steep positive spectral variation of the refractive index can lead to slow light. Now, the physical processes that originate such a strong dispersion are addressed. Experimental evidence of SFL has been reported for a

myriad of systems exhibiting *material resonances* (gain or absorption), like Bose–Einstein condensates [Hau-1999], atomic vapors [Wan-2000], solid crystals [Big-2003, Tur-2001], semiconductor waveguides [Mor-2005], semiconductor quantum wells and dots [Nar-2010, Su-2006], and in doped optical fibers [Dah-2005, Gon-2005, Sch-2006]. The reason why gain or absorption resonances lead to strong dispersion relies on the Kramers–Kronig relations between the real (n) and imaginary (κ) part of the complex refractive index (see 2.1.1). SFL effects have also been reported in systems exhibiting *structural resonances* (photonic band-gap systems, PBG), like photonic crystals [Gal-2007], fiber Bragg gratings [Lon-2001, Lon-2005] and coupled resonators [Mou-2013], where the dispersion is due to coupling between the incident wavelength and the system’s characteristic length. Material SFL and structural SFL are then two standard methods for controlling the group velocity, whose differences and similarities renders one of them more appropriate depending on the application [Boy-2011]

This section presents an overview about the most common mechanisms through which SFL propagation can be achieved in different systems.

2.3.1 Media with material resonances

A rapid frequency variation of the refractive index is associated with an absorption or gain resonance. For absorption resonances fast–light appears on the line center and slow light in the nearby frequency. For a gain resonance, instead the group velocity is subluminal within the gain line and superluminal on both sides of the line. The left–hand column of figure 2.5 shows an absorption resonance profile, where slow light is expected in the wings of an absorption line and fast light is expected near the line center. The right–hand column shows that just the opposite situation is expected for a gain line [Boy-2007].

It shows that a spectrally narrow absorption tends to induce a sharp transition of the refractive index in the material, which in turn leads to a strong anomalous dispersion ($\partial n/\partial\omega \ll 0$) associated with signal advancement or fast light. On the contrary, a peak or gain band will create a strong normal dispersion ($\partial n/\partial\omega \gg 0$) in the material, resulting in signal delay or slow light. The steep linear variation of the refractive index, making $\partial n/\partial\omega$ large in absolute

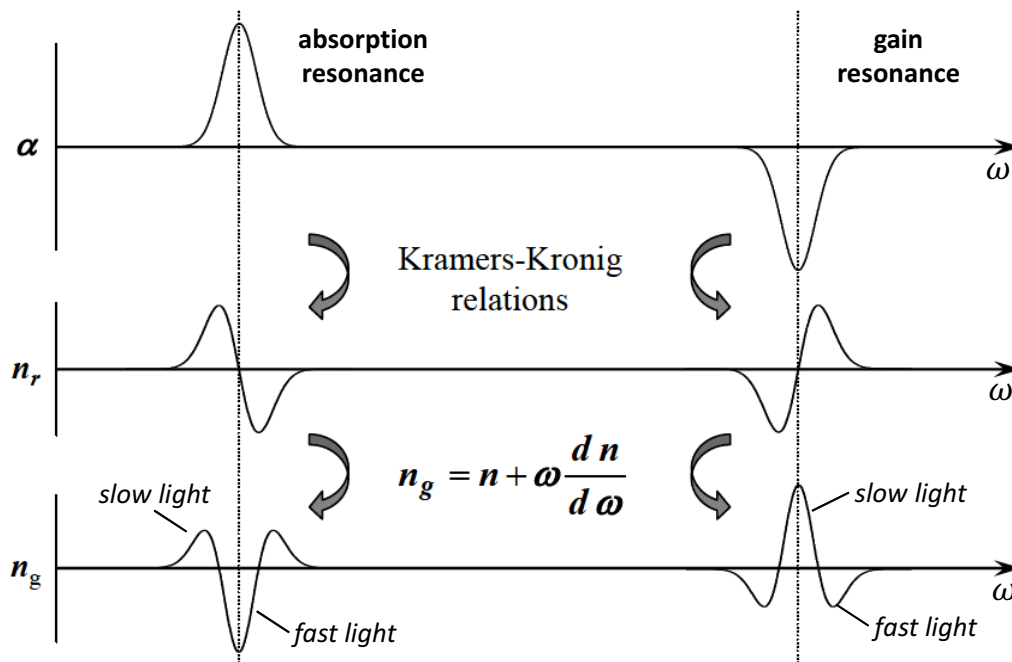


Figure 2.5: Origin of slow- and fast-light for an absorption and gain resonance. The top panel shows absorption coefficient, middle panel shows the dispersion profiles of the refractive index n , and bottom panel shows the group index n_g .

value, induces in turn a strong change of the group index. Thereby, a large change of the relative time delay for a pulse can be observed after the pulse propagates through the material.

Because of the large attenuation that light experiences at the center of a strong absorption resonance, it is difficult, but not impossible, to observe fast light under these circumstances. As a resonance occupies a narrow spectral band, abnormal group velocity can be observed only when the spectral width of the incident pulse is sufficiently small.

The first experimental evidence of abnormally fast and abnormally slow group velocities were obtained in systems with material resonances. In 1993, Chiao demonstrated numerically superluminal phase, group, and energy velocities for a Gaussian wavepacket tuned to a transparent spectral region far below the resonance of an inverted two-level atomic medium [Chi-1993]. A similar effect was achieved by sending a pulsed probe beam through a Xe gas cell exhibiting a gain line, as proposed by Bolda *et al.* [Bol-1994]. Wang *et al.* [Wan-2000] used gain-assisted linear anomalous dispersion to demonstrate superluminal light propagation in atomic caesium gas. They applied two strong continuous-wave pump light beams that propagate

through the atomic medium to exhibit a long steady-state gain doublet. In the middle of the two gain lines, a lossless anomalous dispersion region occurs and causes a pulse advancement shift of 62 ± 1 ns, its advancement gives an effective group-velocity index of $n_g = -310 \pm 5$. Agarwal *et al.* [Aga-2001] controlled the dispersion profile of gaseous rubidium atoms by applying a laser coupling field with tunable intensity. They were able to change the group velocity of a probe pulse from subluminal to superluminal and even to negative values by controlling the pump field intensity.

In the following sections several SFL techniques to render or modify material resonances are briefly described.

a. Electromagnetically induced transparency

Electromagnetically induced transparency (EIT) is a technique that renders an atomic medium transparent over a narrow spectral range within an absorption band. By using the coherent quantum interference effect of EIT, the attenuation due to the absorption resonance present in resonance media (see section 2.3.1) can be canceled while the slow- and fast- light effect is preserved [Fle-2005]. The effect of EIT was first discovered by Harris *et al.* in a gas of atoms with three energy levels [Har-1997]. It has been observed in atomic media [Liu-2001], Bose-Einstein condensates [Hau-1999], solid crystals [Tur-2001], and hollow-core photonic-bandgap fibers [Gho-2006]. Applications of EIT include ultraslow light, stored light and enhancement of nonlinear optical effects.

Via EIT a narrow transparency window within the absorption profile can be created, as shown in Fig. 2.6(a). A pulse within this window experiences little or no absorption and is associated with a change of its group velocity. According to the Kramers–Kronig relations the transparency window leads to a rapid positive variation of the refractive index and therefore, to a large normal dispersion, as can be seen in Fig. 2.6(b). Hence, the magnitude of the group velocity change and time delay depends on the efficiency of the transparency and on the slope of the dispersion, respectively.

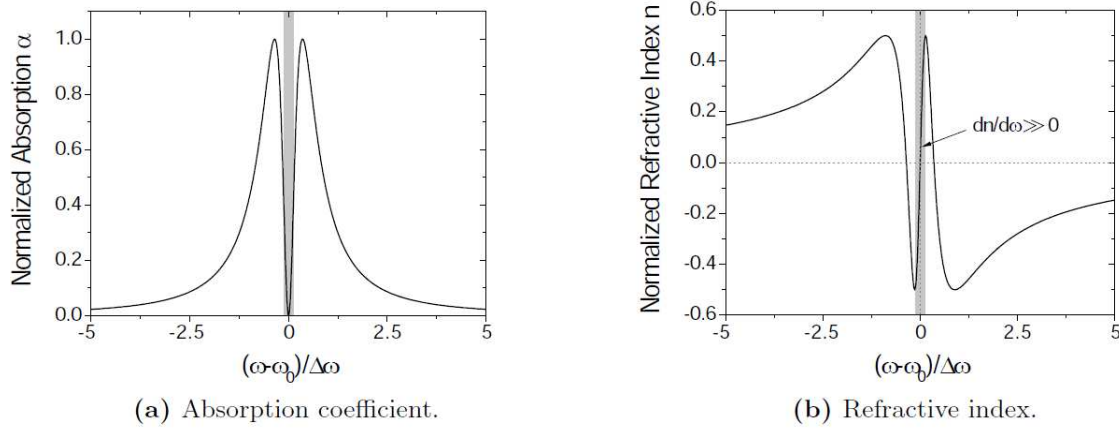


Figure 2.6: (Extracted from [Hen-2010]). Absorption coefficient and refractive index as a function of the frequency detuning from the center of the absorption band (ω_0) for an EIT scheme. The shadowed area shows the narrow transparent spectral range with normal dispersion.

In practice, EIT can take place in a three-level atomic system as shown schematically in Fig. 2.7. A weak probe field (ω_p) is tuned near the $|1\rangle \leftrightarrow |3\rangle$ transition frequency that originates the absorption resonance and is used to measure the absorption spectrum of the transition, while a much stronger coupling field (ω_c) is tuned near the $|3\rangle \leftrightarrow |2\rangle$ transition frequency. The $|1\rangle \leftrightarrow |2\rangle$ transition is dipole forbidden. Quantum interference between the $|1\rangle \leftrightarrow |3\rangle$ and $|2\rangle \leftrightarrow |3\rangle$ transition amplitudes results in a cancellation of the probability amplitude for exciting state $|3\rangle$, thereby reducing the probe beam absorption. If state $|2\rangle$ has a long lifetime, the above mentioned quantum interference leads to a narrow transparency window completely contained within the $|1\rangle \leftrightarrow |3\rangle$ absorption line. The rapid positive change in refractive index in the narrow transparency window (see Fig. 2.6) produces an extremely low group velocity for the probe field, which leads to slow light [Zhu-2008].

Slow light based on EIT has been demonstrated in various material systems. In 1999 Hau *et al.* slowed down light pulses to a velocity of 17m/s in a Bose–Einstein condensate [Hau-1999]. In that experiment, they applied a strong coupling field to an ultra cold atomic cloud in the form of a Bose–Einstein condensate to create the narrow transparency window within the absorption resonance, a diagram of the sophisticated experimental setup is shown in Fig. 2.8. Later, in 2002, Turukhin *et al.* demonstrated the propagation of slow light with a velocity of 45 m/s, corresponding to a group delay of 66 μ s through a solid crystal at a cryogenic temperature of 5 K [Tur-2001]. Liu *et al.* [Liu-2001] demonstrated experimentally that coherent optical

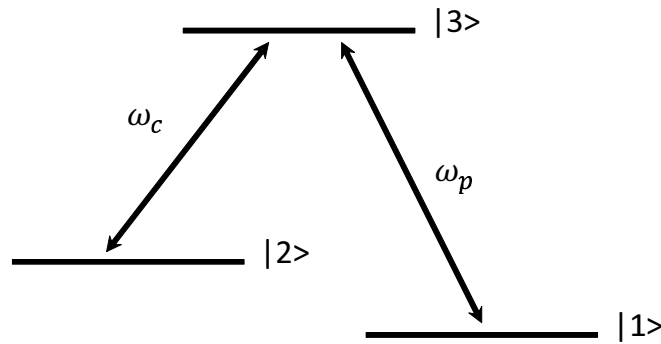


Figure 2.7: EIT in a three-level Λ system. To produce EIT, a strong probe beam (ω_p) is applied between levels $|1\rangle \leftrightarrow |3\rangle$. This effectively splits level $|3\rangle$ so that a control beam (ω_c) sees reduced absorption over a very narrow spectral range.

information can be stored in an atomic medium and subsequently read out by inducing EIT in a magnetically trapped, cold cloud of sodium atoms. They experimentally verified that the storage and read-out processes are controlled by stimulated photon transfers between two laser fields.

While the above results are truly impressive, there has been increased interest in less sophisticated systems, as hollow-core photonic-bandgap fiber (HC-PBF). These fibers are of great interest because the light can be confined and guided with low loss in a hollow core surrounded by a photonic crystal structure that localizes light in the core. By filling the hollow core with desirable gases, resonant optical interactions, such as EIT, can be achieved over a long interaction length. Such a HC-PBF gas cell is compact and can be integrated with existing fiber-based technologies. EIT-based slow-light propagation has recently been demonstrated experimentally by propagating a 19-ns-long probe pulse through an acetylene-filled hollow-core fiber [Gho-2005]. The delay measured in the presence of the control beam is 800 ps. This was the first demonstration of EIT slow light at telecommunication wavelengths. Besides acetylene, alkali atomic vapors such as Rubidium have also been injected into a HC-PBF to achieve ultra-low power level optical interactions [Gho-2006]. Recently, Safaeni-Naeini *et al.* [Saf-2011] demonstrated EIT and tunable optical delays in a nanoscale optomechanical crystal, using the optomechanical nonlinearity to control the velocity of light by way of engineered photon-phonon interactions. At low temperature (8.7 kelvin), they

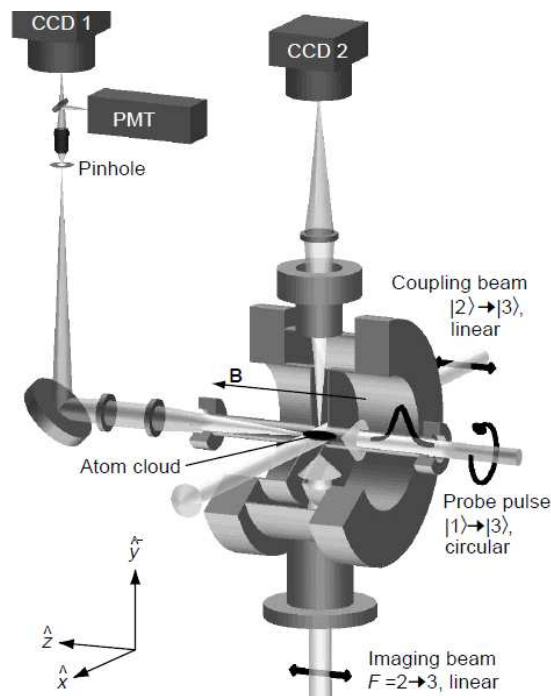


Figure 2.8: (Extracted from [Hau-1999]). Experimental setup. With a flipper mirror in front of camera CCD 1, the probe beam is directed either to the camera or to the photomultiplier (PMT). For pulse delay measurements, a pinhole is placed in an external image plane of the imaging optics and a small area of the probe beam centered on the atom clouds is selected. Pulse delays are measured with the PMT. The imaging beam propagating along the y axis is used to image atom clouds onto camera CCD 2 to the length of the clouds along the pulse propagation direction (z axis) for determination of light speeds.

report an optically tunable delay of 50 nanoseconds with near unity optical transparency, and superluminal light with a $1.4 \mu s$ signal advance.

Although the majority of works focus in the production of slow light because of its applications, there are also considerable efforts in the production of fast light. Akulshin *et al.* have observed a negative group velocity of $-c/23000$ using electromagnetically induced *absorption* (as opposed to EI *transparency*) [Aku-1999]. More recently, Wheeler *et al.* [Whe-2010] have developed an all-fiber system where they generate electromagnetically induced transparencies in a $20 \mu m$ acetylene-filled photonic microcell. Using this system, pulses of probe light were delayed and advanced by up to 5 and 1 ns, respectively.

Although the results of EIT are noticeable, EIT suffers from significant disadvantages. First, the pulse wavelength has to be adjusted exactly to the wavelength of the material absorption resonance. In most cases, these wavelengths are not used in optical communications.

Furthermore, the resonances and hence, the transparency windows are extremely narrowband. Therefore, it is not possible to cover today's common bandwidths of tens of Gbit/s. Another major problem for practical applications of EIT-based systems is their not so large slow-down factor and their difficult handling because the exotic materials need extremely low temperatures to avoid any disturbance of the quantum interference. For these reasons, alternative methods have been requested which work in solids at room temperatures and at wavelengths or frequencies used in optical communications [Zhu-2008].

b. Coherent population oscillations

A method which has a similar behaviour like EIT but works in solids at room temperature is coherent population oscillations (CPO). It leads also to a narrow spectral window inside an absorption profile and therefore, it causes a change of the group index. However, while EIT involves a quantum mechanical interference effect between the electronic state wave functions, the coherence for CPO is assured by the interference of two external laser beams [Ohm-2006].

The great advantage of CPO is that it can be realized in a variety of materials at room temperatures and at wavelengths used in optical communications. Ultra slow- and fast-light and even negative group velocities have been shown in crystals, such as alexandrite [Big-2003] and ruby [Big-2003b], as well as in erbium-doped fibers [Geh-2006, Sch-2006, Jar-2012]. Furthermore, CPO-based SFL was achieved in semiconductor waveguides [Mor-2005, Ohm-2006], and quantum dots [Su-2006].

Coherent population oscillations (CPO) are a quantum effect that creates a narrow dip (or spectral hole) in an absorption profile (slow light) or in a gain profile (fast light). The rapid variation of refractive index in the neighborhood of the spectral hole leads to slow- or fast- light propagation. The idea behind CPO is illustrated in Fig. 2.9. CPO occurs when the ground-state population of a saturable medium oscillates at the beat frequency between a pump wave and a probe wave. The population oscillations are appreciable only for $\delta T_1 \sim 1$, where δ is the beat frequency and T_1 is the ground state recovery time. When this condition is met, the pump wave can efficiently scatter off of the temporally modulated ground-state population into the probe wave, resulting in reduced absorption of the probe wave. In the frequency domain, this leads to

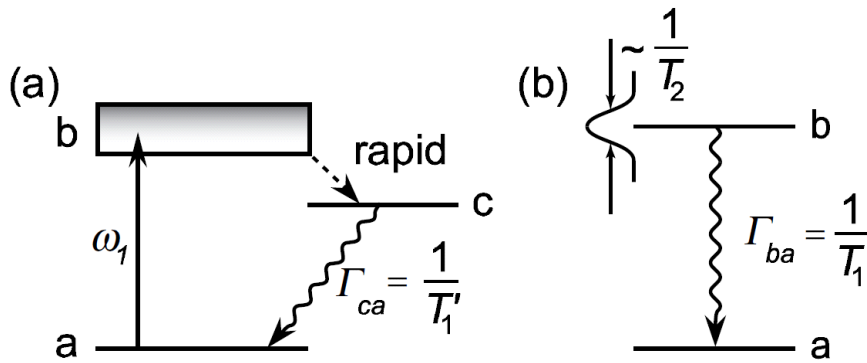


Figure 2.9: (Extracted from [Big-2003b]). Coherent population oscillations (CPO) realized in a simple two-level system. (a) A simplified version of the energy levels in ruby. Because of the rapid decay into level c, we can model this system as the two-level atom shown in (b). ω_1 is the population inversion, T_1 is the ground state recovery time, T_1' is the lifetime of level c, and T_2 is the dipole moment dephasing time.

a narrow spectral hole in the absorption profile, and the hole has a line-width on the order of the inverse of the excited-state lifetime [Boy-2009].

In CPO slow light experiments, the pump and probe need not be separate beams; a single beam with a temporal modulation can experience slow light delay. However, the modulation frequency or the pulse spectral width should be narrow enough to essentially fit within the spectral hole for the slow light effect to be appreciable with minimum pulse distortion. This means that the slow light bandwidth is limited by the width of the spectral hole created by CPO. In addition to an absorbing medium, CPO can also occur in an amplifying (population inverted) medium. In this case, a spectral hole is created in a gain feature, and the resulting anomalous dispersion can lead to superluminal or negative group velocities.

Slow light using CPO was first demonstrated by Bigelow *et al.* [Big-2003b], where v_g as low as 58 m/s was observed in a 7.25-cm-long ruby crystal at room temperature. Slow light and fast light propagation was demonstrated in a 4-cm-long alexandrite crystal at room temperature using CPO [Big-2003], and group velocities as slow as 91 m/s to as fast as $-800 m/s$ were measured. In 2004, Ku *et al.* [Ku-2004] demonstrated for the first time slow light via CPO in semiconductor quantum-well structures. A group velocity as low as 9600 m/s was inferred from the experimentally measured dispersive characteristics, the transparency window exhibited a bandwidth as large as 2 GHz. These systems reach the highest group index values ($n_g \sim 10^6$),

but their operation is limited to the very narrow gain or absorption lines which are given by the electronic and optical properties of the material.

A key aspect for many practical applications is the tunability of abnormal group delays. Tunable SFL effects were recently demonstrated at room temperature in erbium-doped fibers where the absorption or gain could be controlled by a pump laser that creates a population inversion [Geh-2006, Sch-2006]. In one experiment [Sch-2006], modulated or pulsed light at a wavelength of 1550 nm was delayed or advanced through an erbium-doped fiber with varying powers of a 980 nm pump. The degree of signal delay or advancement is found to depend significantly on the pump intensity. A maximum fractional advancement of 0.124 and a maximum fractional delay of 0.09 were achieved. A theoretical model of such a system was recently developed [Jar-2012] which shows the role not only of the pump power but also of its phase with regard to the signal phase. Fractional delays/advancements near $FD = 0.5$ are obtained. Superluminal light propagation with negative group velocity due to CPO was observed in an Erbium-doped fiber where the signal pulse appears to propagate backwards [Geh-2006], which demonstrates that “backwards” propagation is a realizable physical effect.

During the last years, other systems have attracted much interest. For example, Mørk *et al.* [Mor-2005] reported slow-down of light by a factor of three in a 100 μm long semiconductor waveguide at room temperature and at a record-high bandwidth of 16.7 GHz. Group velocity controlled all-optically as well as through an applied bias voltage were shown. Su *et al.* [Su-2006] proposed a room temperature optically and electrically-tunable group delay using population oscillation in a quantum-dot semiconductor optical amplifier. A reduction of the group index up to 10% with a bandwidth of 13 GHz was achieved.

Like other SFL techniques, CPO-based SFL propagation also suffers from pulse distortion. Shin *et al.* observed that pulse distortion caused by these effects depends on the input pulse width, pump power, and background-to-pulse power ratio. They reduced pulse distortion through an erbium-doped fiber amplifier by a proper choice of these parameters [Shi-2007]. In their experiment, with a 10 ns pulse length fractional advancement $FD \sim 0.17$ and minimal distortion was obtained.

Although CPO seems to be a very promising slow- and fast-light technique it still suffers from a narrow bandwidth which is set by the inverse of the population recovery time. For crystal and erbium structures it is restricted to a few kHz as a consequence of the long population relaxation times of these materials, implying that the materials can be used to delay pulses not much shorter than 1 ms. CPO slow light in semiconductors exhibits bandwidths on the order of a few GHz, which can be used to delay pulses as short as hundred ps [Gau-2006]. This large bandwidth, together with mature semiconductor processing techniques, makes CPO in semiconductor structures an important route to achieve chip-scale SFL devices [Khu-2009].

c. Nonlinear wave mixing

Nonlinear wave mixing processes rely on the coherent coupling between two or more optical beams, which induces a nonlinear excitation in the medium. As it was discussed in section 2.1.2, because of the Kramers–Kronig relations, the gain features of the wave mixing process are associated to dispersion and ultimately with a nonlinear phase change. For example, in the coupling of an intense pump beam and a much weaker probe beam at the exit of the medium the probe not only has been amplified but it has also undergone a nonlinear phase shift. The variations of the phase shift with the frequency detuning between the pump and probe usually leads to strong dispersion, in the same way as absorption and refractive index are related in EIT and CPO.

Therefore, nonlinear wave mixing has been exploited for controlling the group velocity of light pulses [Bor-2010]. These processes usually operate at room temperature and can be encountered in different types of nonlinear media. Namely, Bragg diffraction in photorefractive crystals, stimulated Brillouin (or Raman) scattering in optical fibers, and two-wave mixing in liquid-crystal light valves. Some of them are described below.

– Stimulated scattering

SFL effects induced by means of stimulated scattering have been reported in optical fibers. Usually, stimulated light scattering processes are considered harmful to fiber communications,

since they impose a limit on the power or the transmission distance of an optical signal [Agr-2004]. However, in a carefully designed system, stimulated Brillouin scattering (SBS) or stimulated Raman scattering (SRS) processes can be harnessed to generate slow- or fast-light.

In stimulated scattering processes the photons of a light wave interact with the medium. Sufficiently strong light waves induce a material excitation or resonance which is coupled to the light fields if their frequency difference is equal to the frequency of the excitation. This gives rise to nonlinear coupling between the pump and probe waves and the energy can flow from one to another. Hence, a probe wave can be amplified or absorbed. Additionally, according to the Kramers–Kronig relations, this leads to a change of the refractive index with the frequency and therefore, to slow- or fast-light.

Stimulated Brillouin Scattering (SBS) process can be described classically as a nonlinear interaction between the pump field applied (at frequency ω_L) and a vibrational (acoustic) wave (at frequency Ω). This interaction causes some light from the pump field to be scattered into a counterpropagating Stokes sideband at frequency $\omega_s = \omega_L - \Omega$ (see Fig. 2.10(a)). The beating between the pump and the Stokes fields enhances the acoustic wave through a process called electrostriction, or the tendency of a material to compress in the presence of an applied electric field. The enhanced acoustic wave causes stronger scattering of the pump into the sideband, reinforcing the effect. As a result, the Stokes wave experiences exponential gain upon propagation through the material. It should be noted that the same effect causes exponential loss (absorption) for the anti–Stokes sideband at frequency $\omega_s = \omega_L + \Omega$ [Boy-2003]. Efficient SBS occurs when both energy and momentum are conserved, which is satisfied when the pump and probe waves counterpropagate [Geh-2008].

During the last years, SBS has become a very promising fiber–based technique to realize slow- and fast-light [Son-2005, Gon-2010, Cab-2008, The-2008, Sch-2012]. This is due to its crucial advantages over the other methods. With SBS it is possible to tune the group velocity continuously in an extremely wide range. Slow- and fast-light via SBS was first demonstrated by Song *et al.* [Son-2005]. In Song’s experiment 100 ns pulses were continuously delayed between -10 ns and $+30$ ns with a slope of 0.97 ns/dB gain in a single mode fiber (SMF), and changes in the group index of 10^{-3} were measured. In short SMF of 2 m group

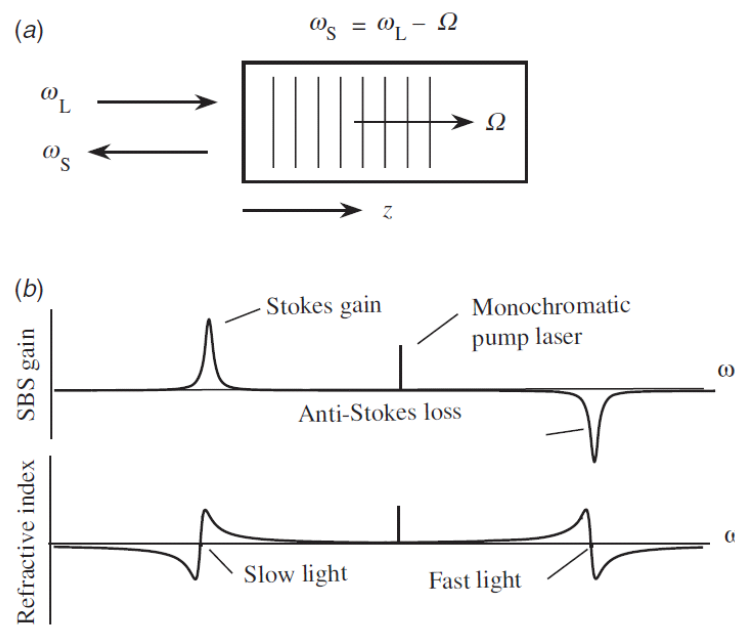


Figure 2.10: (Extracted from [Boy-2009]). (a) Schematic representation of the SRS process, where ω_L is the pump field applied frequency, Ω is the vibrational wave frequency and ω_s is the Stokes sideband frequency. (b) Origin of slow and fast light through SRS and a monochromatic pump field.

velocities of less than 71000 km/s up to superluminal and even negative group velocities were achieved [Gon-2005]. Furthermore, just small pump powers are necessary to achieve very high time delays. The systems are very easy to implement and can be built using standard telecommunications components [Cab-2008].

On the other hand, SRS has some disadvantages which limits the performance of the slow- and fast-light systems. The maximum delayable data rate is restricted by the narrow natural full width at half maximum (FWHM) Brillouin bandwidth. Furthermore, the maximum achievable time delay is limited by the saturation of the Brillouin amplifier. Another problem is that the time delay of the pulses is accompanied by a distortion of the pulse shape which primarily manifests itself in a temporal broadening of the pulse width [Cab-2008].

Slow light via stimulated Raman scattering (SRS) can also be achieved in optical fibers, but over much larger bandwidths than SRS and hence it can be used with pulses of much shorter duration [Khu-2009]. In SRS, scattering arises from the interaction between the pump wave and exciting vibrational motions or oscillations of the individual particles, also known as phonons.

With SRS wide bandwidth slow–light has been shown where 430 fs pulses were delayed by up to 85% of the pulse width [Sha-2005]. In [Dah-2005] a Raman-assisted fiber optical parametric amplification in a fiber with a length of 2 km was used to achieve negative delays as well as large positive delays and delay tuning ranges, in the order of 160 ps for a 70 ps wide pulse.

– Two-wave mixing in liquid-crystal light valves (LCLV)

This technique is based on the nonlinear mixing of a pump laser beam and a much weaker signal pulse, both impinging on a nematic liquid-crystal (LC) cell on which a photoconductive layer is deposited. The process is shown in Fig. 2.11 [Bor-2010]. The signal pulse and the pump beam interfere creating a fringe pattern on the photoconductive layer, which modulates the effective voltage across the LC cell. As a result, the LC molecules reorient and, because of their birefringence, a refractive-index grating is induced which diffracts the signal pulse. Associated with each output order there is a gain and a dispersion spectral function, thus leading to slow or fast light regimes in each diffracted order. These gain curves are a consequence of the photon transference from one beam into the other, whereas the dispersion curves originate via the Kramers-Kronig relations. The SFL regimes achieved on each diffracted order depend on the frequency detuning between the signal and the pump frequency, and they can be tuned by varying the voltage amplitude applied to the cell or by changing the intensity of the probe beam.

The response time of the LCLV is the time needed to build up the photo-induced grating, which is dictated by the time the LC molecules spent in reorientating over the whole thickness of the nematic layer. For typical thickness of about 15 micrometers, the response time is of the order of 100 ms. Therefore, this technique works for pulses with a minimum temporal width of 100 ms. Gaussian pulses of width 140 ms and 180 ms were advanced by -65 ms and delayed by 110 ms, respectively; which correspond to fractional delays of $FD = -0.46$ and $FD = 0.60$. This technique has been proved successful at delaying images by 80 ms, at increasing the spectral sensitivity of a Mach-Zehnder interferometer [Bor-2010] and at measuring with great accuracy Doppler shifts as low as 1 microhertz of very slow-moving objects [Bor-2013], which have all

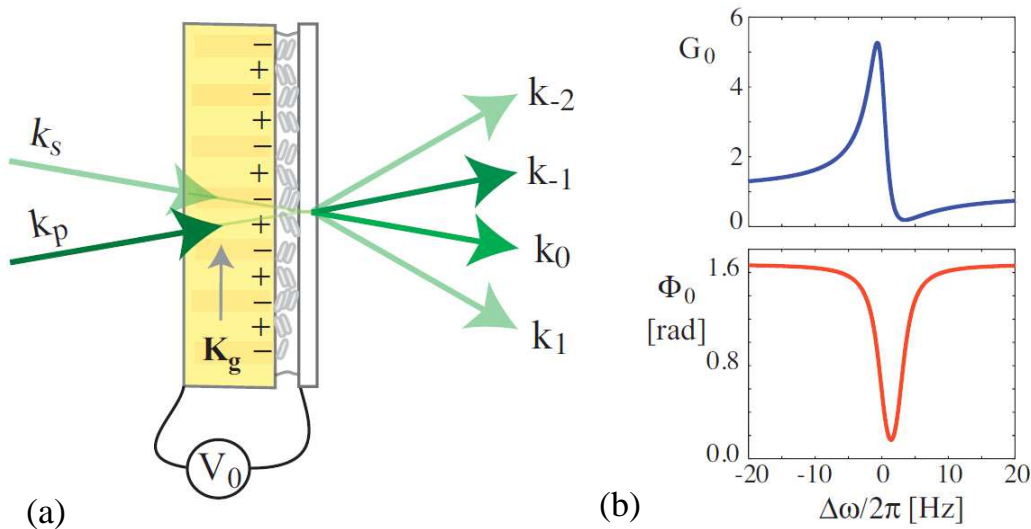


Figure 2.11: (Extracted from [Bor-2010]). (a) The liquid crystal light valve (LCLV) and the two-wave mixing in the Raman-Nath regime of diffraction. (b) Gain G_0 and phase shift Φ_0 for the $m = 0^{th}$ output order beam as a function of the frequency detuning $\Delta\omega$ between the pump and signal; $\beta = 30$.

interesting applications for the detection of conformational changes in material structures or in biological samples.

2.3.2 Photonic bandgap structures

As it was mentioned earlier, SFL effects also arise in systems with structural resonances with a different behavior. By structural resonances, one means that the propagation of light pulses is significantly modified by the (typically periodic on distances of the order of an optical wavelength) spatial modulation of the optical properties of a material system. Unlike the case of material resonances, there is a true increase of the electric field strength within structural resonances. This increase can lead to direct enhancement of nonlinear optical interactions because the light bounces back and forth many times in its passage through the structure. Also, because there are both forward- and backward-going waves within the structure, each of which carries power, the total energy stored within the structure is larger than the energy stored in a wave propagating freely through a medium of the same mean refractive index. There will thus be an increase in electric field strength within the structure, which can lead to enhanced nonlinear optical effects [Boy-2011].

A well-known example of such a behaviour is that of photonic band-gap (PBG) systems, where the dispersion is not of material origin (the media are in fact fairly dispersion less) but an “effective” dispersion arises due to coupling between the incident wavelength and the characteristic length of the system. PBG devices are especially attractive for generating slow- and fast-light, as they are compatible with on-chip integration and room temperature operation, and can offer wide-bandwidth and dispersion-free propagation [Bab-2008]. As opposed to the systems with material resonances described in the previous sections, SFL occurs in entirely linear and passive structures where the wider bandwidth operation comes at the expense of much lower group index values ($n_g \sim 10^2$).

A PBG structure, also known as a photonic crystal, is made of two or more materials with different refractive indices arranged in an alternating fashion. As a consequence, the light is scattered at the index interfaces and if the periodicity of the structure is right (around half the operation wavelength) the multiply-scattered waves interfere destructively, thus yielding a photonic gap. Hence, the structure is designed to influence the propagation of electromagnetic waves in the same way as the periodic potential in semiconductor crystals influences the electron motion by defining allowed and forbidden energy bands. The absence of allowed propagating electromagnetic modes inside the structure in a range of wavelengths is called a photonic bandgap. This stopband is connected with anomalous dispersion and thus gives rise to superluminal group velocity, whereas at the stopband edges subluminal group velocity is supported.

The simplest form of photonic crystal is a one-dimensional periodic structure such as a multilayer film or Bragg mirror. Electromagnetic wave propagation in these structures was first studied by Rayleigh in 1887 [Yeh-1988], who showed that any such one-dimensional system has a band gap. Although 1D-periodic systems continued to be studied extensively over the following century, and appeared in applications from reflective coatings to distributed feedback (DFB) devices, it was not until 100 years later, when Yablonovitch and John in 1987 joined the tools of classical electromagnetism and solid-state physics, that the concepts of omnidirectional photonic band gaps in two and three dimensions was introduced, and such structures have since seen growing interest by a number of research groups around the world.

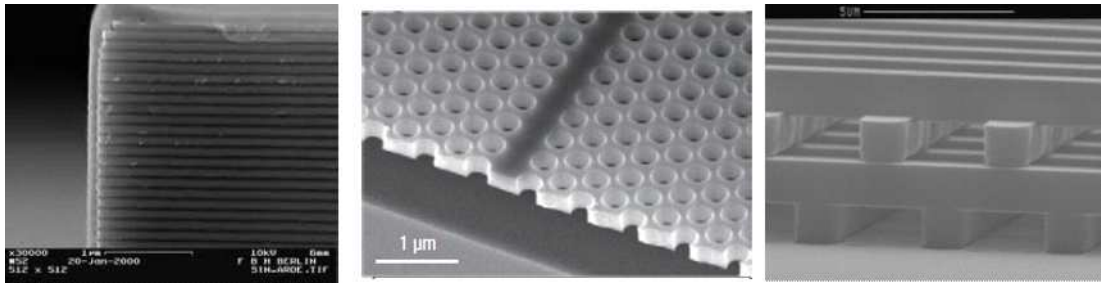


Figure 2.12: (Extracted from [Bab-2008] and [Lin-1998]). Examples of one-, two-, and three-dimensional photonic crystals. (a) 1D Bragg reflector, (b) 2D silicon photonic waveguide. (c) 3D photonic crystal.

Figure 2.12 shows examples of photonic crystals with one- (1D), two- (2D) and three-dimensional (3D) periodicity. Another kind of 2D PBG structure, different to the one illustrated in Fig. 2.12(b), is the photonic crystal fiber [Kni-1998]. In 3D, PBG applications in the optical regime have remained elusive until very recently due to the difficulties associated with the controlled fabrication or growth of structures with lattice constants only a few hundreds of nanometers in length [Ish-2013]. This is why the first demonstrations of the potential of these structures were made in the microwave regime, with the development of a PBG metal substrate for antenna applications [Qia-1999].

Although a few works report SFL in 2D [Bab-2008] and 3D [Gal-2007] photonic crystals, most of the research has been devoted to 1D structures, like multilayer dielectric stacks and fiber Bragg gratings. One-dimensional photonic crystals have a wide range of applications such as stop-band filters, high-reflection mirrors, antireflection coatings, and cavities for distributed feedback lasers. One-dimensional photonic crystals are well known for several decades, and experiments related to anomalous propagation have been carried out in various spectral ranges. Some key work in the area is summarized below.

Centini *et al.* [Cen-1999] discuss the linear dispersive properties of finite 1D photonic band gap structures. They introduce the concept of a complex effective index for structures of finite length, derived from a generalized dispersion equation that identically satisfies the Kramers–Kronig relations.

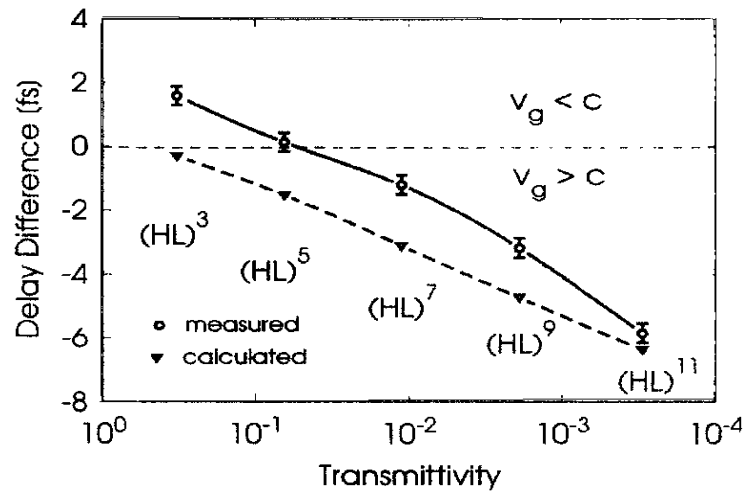


Figure 2.13: (Extracted from [Spi-1994]). Measured and calculated difference between the tunnelling time and the corresponding vacuum time for multilayer dielectric coatings of various thicknesses.

Steinberg *et al.* [Ste-1993] employed a two-photon interferometer to measure the time delay for a photon to tunnel across a barrier consisting of a multilayer dielectric mirror, composed of six titanium oxide layers alternated with five fused silica layers, with its stopband residing between 600 and 800 nm. The measurement showed that the peak of the photon wave packet appeared on the far side of the barrier 1.47 ± 0.21 fs earlier than it would if it were to travel at the vacuum speed of light c , corresponding to a group velocity of $(1.7 \pm 0.2)c$. Spielmann *et al.* [Spi-1994] used femtosecond optical wave packets for the tunnelling experiment instead of a single photon, extending the experiment of [Ste-1993] to measure the tunnelling time for multilayer dielectric mirrors of different thicknesses. It was shown that the group velocity linearly increases with the barrier thickness and becomes superluminal for sufficiently thick barriers (see Fig. 2.13).

Existence of slow and fast light regimes was predicted for pulses reflected on asymmetric photonic band gap structures with a transmission window inside the gap [Lon-2001]. These predictions were confirmed experimentally by reflecting picosecond optical pulses in fiber Bragg gratings adequately synthesized to have a double-Lorentzian spectral reflectivity function [Lon-2002]. Tunable group delays can also be obtained with these structures. Namely, transition from subluminal to negative group delay was achieved by tuning the pulse spectrum over the band gap. Superluminal pulse reflection for a pulse tuned off resonance, with a peak

pulse advancement of $\simeq 60$ ps, was observed without appreciable distortion. Conversely, for a pulse spectrum tuned at one of the two Lorentzian peaks, the group delay was positive and reflection was subluminal, with a peak pulse delay of $\simeq 90$ ps. A theoretical work presented a similar system, consisting of a dielectric slab doped with dispersive two–level or three–level atoms, where by adjusting the thickness or background dielectric constant of the slab, the reflected pulse can be controlled from superluminal to subluminal or viceversa [Wan-2004]. Also, a gain-driven transition from superluminal to subluminal group velocities was predicted for pulses reflected in active fiber Bragg gratings with asymmetric profile [Lon-2005] with fractional delays in the range $FD = [0.3 - 0.5]$.

Because of the scalability, flexibility and simplicity of 1D PBG structures, experimental evidence of structural SFL has been provided for lower frequency ranges, like radiofrequency (RF) [Hac-2002, Hac-2004, Mun-2003, Poi-2001] and microwave (MW) [Moj-2000, Moj-2003, Nim-2003, Tir-1999]. For instance, electrical analogs of one–dimensional photonic crystals, operative in the RF range, have been constructed using low– and high–impedance coaxial cables with a specific cascading arrangement. Impurities can be introduced into these crystals by inserting cable segments to break the crystal symmetry. This system provides a simple way to study 1D photonic band structure effects with complete control over impurities in the lattice [Sch-2001].

For the first time to our knowledge, Poirier and Haché [Poi-2001] devised a 1D PBG structure made of coaxial segments with periodic impedance to create a stop band in transmission near 10 MHz due to impedance mismatch, and within the stopband a pulse travels with a group velocity three times faster than light in vacuum [Hac-2002]. They also demonstrate that large-scale photonic crystals can be used to simulate nonlinear optical effects occurring in real photonic crystals. Munday and Robertson [Mun-2003] observed subluminal group velocity ($v_c = 0.3c$) through a narrow transmission band of a simple coaxial photonic crystal. The narrow transmission band was formed by creating a defect in a periodic coaxial cable filter which resulted in a narrow–frequency passband within an otherwise forbidden band stop region. Haché and Essiambre [Hac-2004] achieved a tunable group velocity from subluminal to superluminal in a completely passive system by connecting a pair of diodes to a coaxial crystal

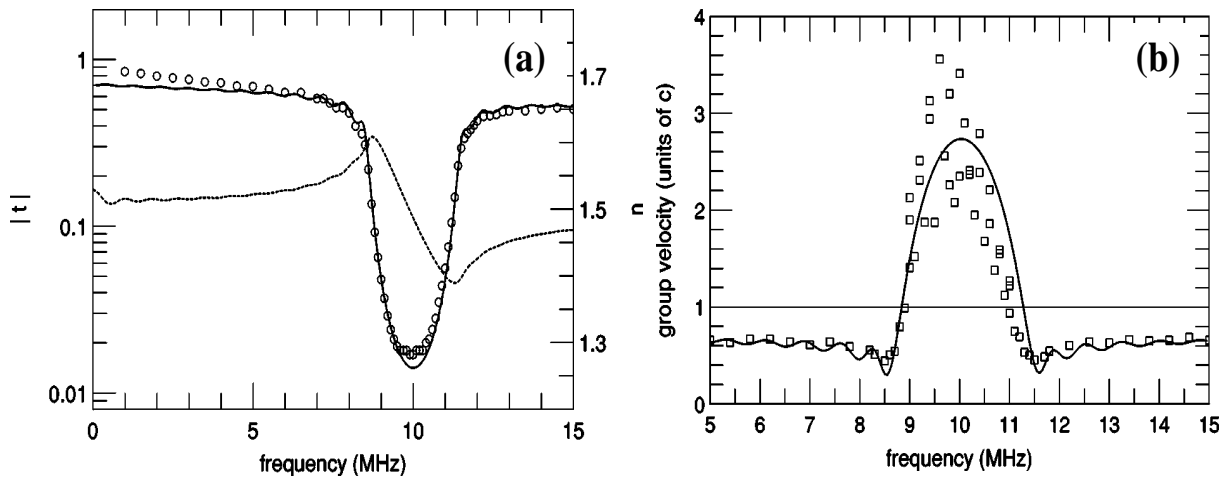


Figure 2.14: (Extracted from [Hac-2004]). Simulations (lines) and experimental (circles) results of the following quantities of a coaxial photonic crystal: (a) the transmission and the effective refractive index (dashed curve) extracted from $n = c/\omega d\phi_t(\omega)$ and (b) group velocity.

(see Fig. 2.14). The diodes exhibit a nonlinear response depending on the signal frequency and amplitude and thus create the nonlinearity in the system. As a consequence, the resulting amplitude-dependent phase shift enables to control the dispersion and the propagation velocity at the stop band frequency in much the same way as the dispersion control in material SFL systems by manipulation of gain or absorption lines through EIT or CPO techniques.

Controversial issues like the superluminal tunnelling of optical pulses through photonic band gaps [Spi-1994] have also been addressed by using their analogs in the microwave range [Nim-2002, Nim-2003]. In general, these PBG structures operative at frequencies well below the optical range provide an easy experimental way to probe theories and phenomena of their optical analogs. In the microwave range, SFL effects were reported too, for the first time to our knowledge, by Tirapu *et al.* [Tir-1999] who provided experimental evidence of tunable group velocity in a photonic bandgap microstrip structure.

Recent advancements on structural SFL for applications in the optical region consider nonlinear effects in photonic-crystal waveguides, leading to enhancement of slow light [Ham-2009] in green-light emission through slow-light enhanced third harmonic generation [Cor-2009]. Another major achievement is based on coupled resonators to expand the bandwidth and to get tunable pulse buffering [Khu-2009] or the engineering of losses caused by technical imperfections to enhance slow light effects [Fao-2010].

2.3.3 Conversion-Dispersion

A simple method for controlling the velocity of light is to make use of transmission through a medium with a large dispersion in the group velocity [Sha-2005]. Conversion-dispersion (C/D) refers to a novel technique that generates tunable delay without relying on absorption or gain resonances nor in engineered PBG systems. It consists of three stages: wavelength conversion, dispersive delay and wavelength reconversion (see Fig. 2.15). By varying the carrier frequency of the signal, the time delay can thereby be controlled directly. In practice, the incident signal pulses are converted to another carrier frequency via a wavelength conversion device, propagate through a length of highly-dispersive waveguide (with large group velocity dispersion), and the delayed pulses are converted back to the original wavelength via a second wavelength conversion device. Tunable group delay of the pulses are then obtained because of the frequency dependence of the group velocity in the dispersive waveguide. Although C/D is not really a true SFL technique, it is often included in discussions of SFL because it is related to slow light by its reliance on highly dispersive materials and because it is useful under many of the same conditions for which SFL is useful [Boy-2009].

This technique was first demonstrated in an optical fiber by Sharping et al. [Sha-2005]. Tunable pulse delays that operate in the 1.5 μm telecommunication window and that can be varied by as much as 800 ps were demonstrated by varying the pump wavelength of the fiber-based parametric amplifier, yielding a relative delay of 80 pulse-widths. Okawachi *et al.* recently simplified the fiber-based wavelength-conversion-and-dispersion technique and delayed 3.1 ps pulses up to 4 ps, corresponding to a fractional delay of $FD = 1200$ [Oka-2007].

Compared with resonance-based and structural-based SFL techniques, the conversion-dispersion method has several advantages: a highly controllable span of tunable delays from ps to ns and large fractional delay (which by the other techniques hardly reaches $FD = 0.5$), it can support broad bandwidths suitable for data rates exceeding 10 Gb/s [Oka-2007], and the delayed pulses can have identical wavelength and bandwidth. Still, the reconfiguration rate is limited by the tuning speed of the filters or of the pump laser frequencies. Also, care

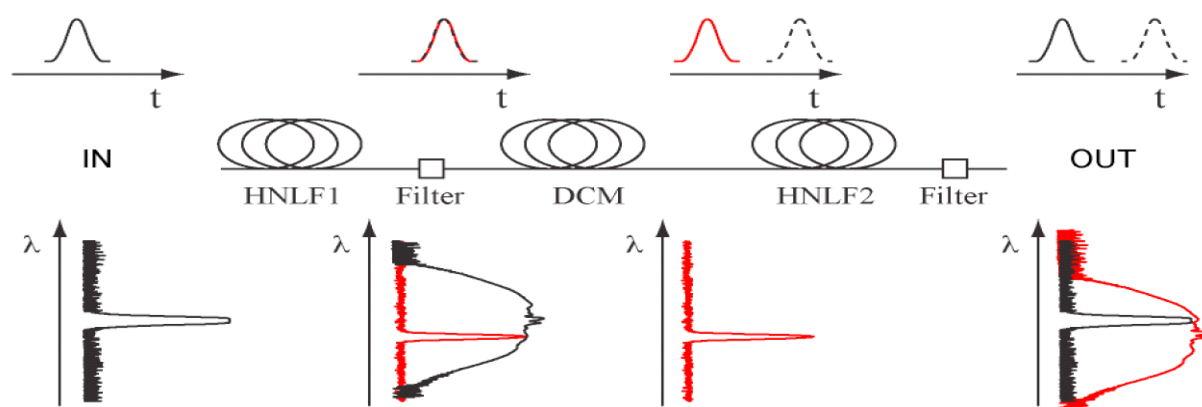


Figure 2.15: (Extracted from [Oka-2007]). Conversion–Dispersion scheme. It shows the original pulse (dashed) and the delayed pulse (solid). The top and bottom set of plots show the pulse position and spectrum, respectively, at various stages. The pulse is spectrally broadened and filtered in the first stage, sent into a dispersive medium to generate the delay in the second stage, and again broadened and filtered to return to the original wavelength in the third stage.

must be used in choosing the dispersive element and wavelength conversion range to minimize dispersive pulse broadening and maximize slow light delay [Khu-2009].

2.3.4 Electronic circuits

Experimental evidence of superluminal and negative group delays in electronic circuits has been reported. The reason why these effects are encountered in some electronic circuits relies on the fact that the magnitude–phase relation of an electronic circuits transfer-function is analogous to the Kramers–Kronig relation which links the real part to the imaginary part of the dielectric constant of a physical (i.e. causal) medium (or, equivalently, that links the refractive index to the absorption index of a medium). In an electronic circuit the real and imaginary part of its transfer function (i.e. the transfer function’s magnitude and phase) are also related via the Hilbert transform on the basis of causality [Wit-2010].

Mitchell and Chiao [Mit-1997, Mit-1998] were the first to implement a bandpass amplifier with a very low passband (51 Hz), shown in Fig. 2.16(a), to study the superluminal effect. The circuit basically emulates an optical gain medium which shows anomalous dispersion in off-resonant region (see its transfer function in Fig. 2.16(b)). Kitano *et al.* [Kit-2003] presented a simple electronic circuit which provides negative group delays for band–limited baseband pulses and

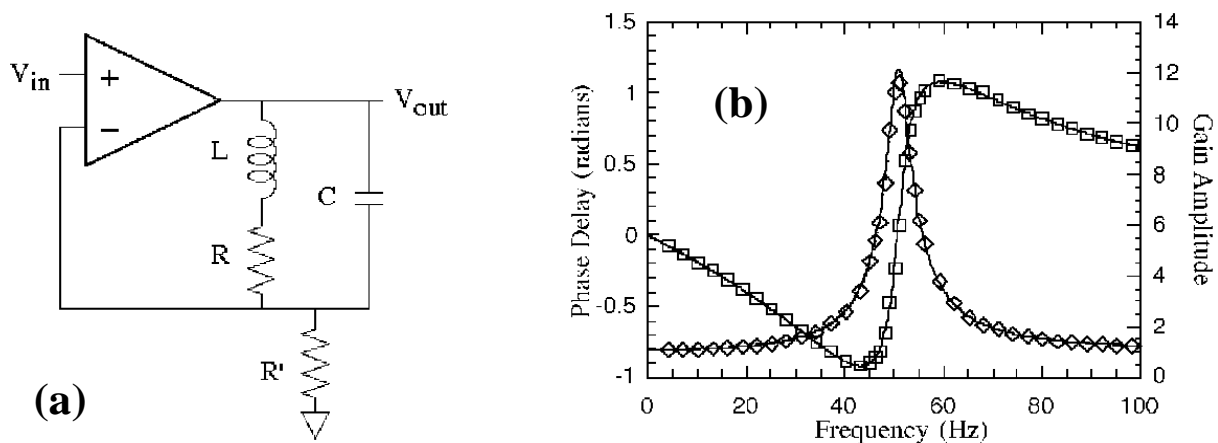


Figure 2.16: (Extracted from [Mit-1997, Mit-1998]). (a) A simple bandpass amplifier consists of an operational amplifier in a non-inverting feedback configuration with a resonant element (LRC circuit) in the feedback loop. (b) Transfer function amplitude (diamonds) and phase (squares) for the amplifier proposed by Mitchell and Chiao.

demonstrated that large time advancement comparable to the pulse width can be achieved with appropriate cascading of negative-delay circuits. Cao *et al.* [Cao-2004] implemented a dual-band electronic amplifier and extended the system in [Mit-1997, Mit-1998] by using two LC resonators to study the pulse advance and pulse compression of light propagation through a transparent, anomalous dispersive medium. At the middle of two gain peaks the frequency dependence of the amplitude response is compensated and the pulse distortion can be minimized. This leads to linear anomalous dispersion between these two gain lines, and thus results in a negative group delay.

Operating in low frequency ranges, as electronic and microwave range, offers some advantages over higher frequency ranges. For example, Gaussian pulses can be generated easily and a resulting pulse advance of the order of milliseconds can be unmistakably displayed on a standard oscilloscope. The transmission and reflection phase function can be measured with a vector network analyzer. Such a simple measurement of this key function that determines the pulse propagation regime cannot be directly performed in the optical range.

Moreover, by applying filter theory Withayachumnankul and Abbott [Wit-2010] have modelled an anomalous dispersive medium and systematically describe the superluminal propagation of a Gaussian pulse through the system. Since the condition for superluminal propagation is

modeled in the basis of filter theory, it is applicable to all types o media. Similarly, Nakanishi *et al.* [Nak-2002] provide an enlightening analysis for the tunnelling of pulses and its agreement with relativistic causality using filter theory in a simple electronic circuit.



Chapter 3

SFL in multiple-beam interferometers

In this chapter slow and fast light (SFL) generation in linear and passive multiple-beam interferometers is studied. First, we show their characteristic transmission pattern. We discuss the abnormal values (subluminal, superluminal and negative) that the group velocity can reach in these structures over narrow frequency intervals within the interferometer's transmission minima. A model that fully describes SFL effects in linear and passive Mach-Zehnder and three-beam interferometers is developed in the second and third section, respectively, and an analytical approximate expression for the group delay at the minima is derived and relevant figures of merit which are intrinsic to the system are determined. The propagation of sinusoidally modulated pulses through these systems is described. As a proof of model, simulations in the optical range and experimental results in the radiofrequency range are performed by using coaxial cables and 1xN radiofrequency wave splitters. We demonstrate that slow light can arise if the length difference between every pair of adjacent branches of the interferometer is not a constant. The simplest interferometer where this condition on the arms length holds is a three-beam interferometer. A brief extension of the results to four-beam interferometers is presented in the fourth section. Finally, the conclusions of the chapter are given in the fifth section.

3.1 Interference pattern of multiple-beam interferometers

Previous studies of the transmission pattern of multiple-beam interferometers [Dav-2006] seem to indicate the possibility that these systems present frequency regions with abnormal group velocity associated to the sharp features of their transmission spectrum. In this section we focus on multiple-beam interferometers with the same phase shift between every pair of adjacent branches. The origin of this constant phase shift is a constant optical length difference between adjacent arms, due to either physical length difference, Δ , or refractive index difference, Δ_n .

The multi-beam interferometer considered is depicted in figure 3.1(a). An input beam enters a $(1 \times N)$ splitter that divides it into N plane waves, they travel through separate paths with different optical lengths, and finally they reach an $(N \times 1)$ coupler that combines them producing an interference. One can modify the optical path of the i^{th} branch, ($\ell_i = n_i L_i$), by altering either its refractive index, n_i , or its physical length, L_i . For an ideal interferometer of this kind, we assume that the optical length difference between adjacent branches, δ , is a constant, i.e., $\ell_i = \ell_{(i-1)} + \delta$, for $i = 2$ to N . In order to have a clear idea of the origin of SFL effects in such interferometers, in this work we focus on the optical path difference due to either a physical length difference, Δ , alone or a refractive index difference, Δ_n , alone, always avoiding the mixing of both for simplicity. In the former case, we will refer to them as **asymmetric** interferometers.

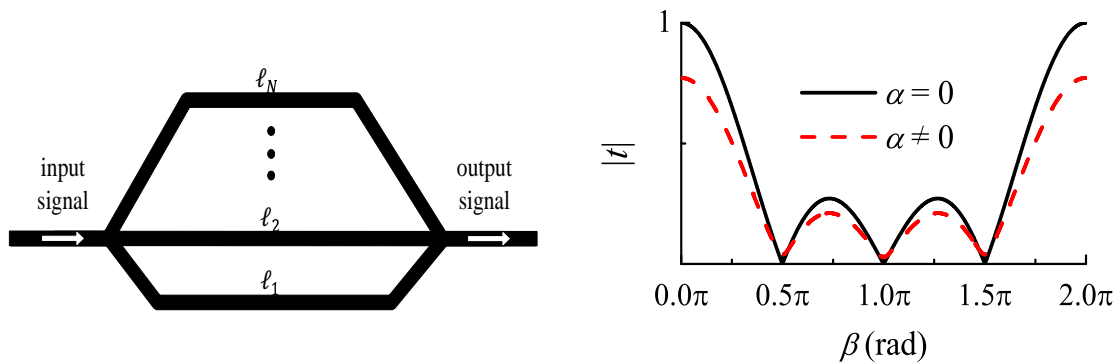


Figure 3.1: (a) Schematic of a multi-beam interferometer consisting of a $(1 \times N)$ splitter and an $(N \times 1)$ coupler connected by branches of different optical length. (b) Typical transmission spectrum of a 4-beam interferometer with (dashed line) and without (solid line) attenuation, α is the attenuation coefficient of the medium in the branches.

Constant optical length difference leads to a characteristic interference pattern with sharp spectral features (see figure 3.1(b)). From this pattern, and recalling the origin of SFL effects discussed previously (see Chapter 2, Section 2.3), we can expect anomalous regimes around the transmission minima. Such regimes are not expected around the maxima because they are too wide. As it is shown in Fig. 3.1(b), the interference pattern reduces its contrast (the spectral features are less sharp) if the attenuation is considerable. Therefore, SFL effects are not expected to be sustained for large enough attenuation.

Assuming that the divider splits the input signal's amplitude into N equal parts ($|t_0|/N$), we can express the output complex amplitude resulting from the interference of N sinusoidal beams as follows:

$$\hat{t} = \frac{t_0}{N} \sum_{i=1}^N e^{j\hat{\phi}_i} \quad (3.1)$$

where $\hat{\phi}_i$ is the phase of the wave after propagating through branch i . This phase depends on the frequency, ω , the optical and physical lengths of the branch, and the attenuation coefficient of the medium, α , **which, for simplicity, is assumed to be uniform and the same for all arms.** The following expression contains this dependency:

$$\hat{\phi}_i = \frac{\omega \ell_i}{c} + j\alpha L_i \quad (3.2)$$

By writing the phase in the i_{th} branch in terms of that in the first arm and the optical length difference (δ) and physical length difference (Δ) between adjacent branches,

$$\hat{\phi}_i = \frac{\omega}{c}[\ell_1 + (i-1)\delta] + j\alpha[L_1 + (i-1)\Delta] \quad (3.3)$$

and using Eq. (3.3) into (3.1) the latter can be written as:

$$\hat{t} = \frac{t_0}{N} e^{j\hat{\phi}_1} \sum_{m=0}^{N-1} e^{jm(\frac{\omega\delta}{c} + j\alpha\Delta)} \quad (3.4)$$

Finally, solving the summation in Eq. (3.4), the complex amplitude resulting from the interference of N sinusoidal waves is obtained:

$$\hat{t} = \frac{t_0}{N} e^{j\phi_1} \times \frac{1 - e^{-N\alpha\Delta} \cdot e^{jN\omega\delta/c}}{1 - e^{\alpha\Delta} \cdot e^{j\omega\delta/c}} \quad (3.5)$$

Usually, in interference experiments, the magnitude detected is power, $P = |\hat{t}|^2$. Therefore, calculating the complex conjugate of Eq. (3.5) and normalizing the power expression, we obtain the total normalized power in the coupler:

$$P = \frac{|t_0|^2}{N^2} e^{-2\alpha L_1} \times \frac{1 + e^{-2N\alpha\Delta} - 2e^{-N\alpha\Delta} \cos(N\beta)}{1 + e^{-2\alpha\Delta} - 2e^{-\alpha\Delta} \cos(\beta)} \quad (3.6)$$

where β is defined as the phase associated to the optical length difference, i.e. $\beta = \omega\delta/c$.

In order to identify the most relevant aspects of the transmission pattern, now we consider the ideal case in which there is no attenuation ($\alpha = 0$). In this situation, the transmitted complex amplitude of Eq. (3.5) can be written as:

$$\hat{t} = \frac{t_0}{N} e^{j(\omega L_1 + (N-1)\frac{\beta}{2})} \frac{\sin(N\frac{\beta}{2})}{\sin(\frac{\beta}{2})} \quad (3.7)$$

and the total power reads:

$$P = \frac{|t_0|^2}{N^2} \frac{\sin^2(N\frac{\beta}{2})}{\sin^2(\frac{\beta}{2})}, \quad (3.8)$$

which is analogous to the intensity expression of N coherent optical oscillators [Hec-2002]. Analyzing Eq. (3.8), the numerator oscillates rapidly, while the denominator oscillates more slowly. The combination of both terms results in maxima (main peaks) and minima (zero-transmission) of the N -beam interference pattern located at the following phase position β :

$$\beta_{max} = 2\pi m \quad (3.9a)$$

$$\beta_{min} = 2\pi m + \frac{2\pi}{N}, 2\pi m + \frac{4\pi}{N}, \dots, 2\pi m + \frac{(N-1)2\pi}{N} \quad (3.9b)$$

where the integer number m is the order of the principal maximum. In the interval $\beta = 0 - 2\pi$, zero-transmission appears at $\beta = 2\pi/N, 4\pi/N, \dots, (N-1)2\pi/N$. Therefore, between two adjacent absolute maxima there are $N - 2$ smaller local peaks and $N - 1$ minima. Table 3.1 summarizes the phase positions of the minima located between the zero and the first-order ($m = 0, 1$) principal peaks in interferometers with $N=2, 3, 4$ branches. The frequency positions of these maxima and minima are deduced from the relationship between the phase β and the frequency parameter ($\beta = \omega\delta/c$), leading to:

$$\omega_{max} = 2\pi m \frac{c}{\delta} \quad (3.10a)$$

$$\omega_{min} = \left(m + \frac{1}{N}\right) \frac{2\pi c}{\delta}, \left(m + \frac{2}{N}\right) \frac{2\pi c}{\delta}, \dots, \left(m + \frac{(N-1)}{N}\right) \frac{2\pi c}{\delta} \quad (3.10b)$$

Let us remark that these positions are obtained for a lossless system ($\alpha = 0$) but they also hold for lossy MZI and also for lossy multiple-beam interferometers in which δ is due to refractive index difference Δ_n alone. All in all, as we shall see, it is a good approach to consider Eqs. (3.9) as the phase position for the maxima and minima for lossy interferometers too. In particular, if the optical path difference is only due to a refractive index difference, Δ_n , by using $\Delta = 0$ in Eq. (3.6), the following expression for the output power is obtained:

$$P = \frac{|t_0|^2}{N^2} e^{-2\alpha L_1} \times \frac{2 - 2 \cos(N\beta)}{2 - \cos(\beta)} \quad (3.11)$$

It follows that since the branches are of the same length, the attenuation plays no role whatsoever in the value of the power detected at the minima. The role of the attenuation coefficient is only relevant if there is a physical length difference between arms. Namely, using Table 3.1 and evaluating Eq. (3.11) at the minima leads to $P_{min} = 0$ no matter the value of the attenuation coefficient. As it will be discussed later, no SFL effects arise in this situation.

Following [Shi-2007] one can define the degree of visibility (or contrast) of the interference pattern as:

$$\nu \equiv \frac{P_{max} - P_{min}}{P_{max} + P_{min}} \quad (3.12)$$

where $P = |\hat{t}|^2$ is the detected power and the subindex indicates maximum or minimum power. Considering Eq. (3.6), the power at β_{max} and β_{min} is evaluated for an interferometer with general number of branches N :

$$P_{max} \propto \frac{1 + e^{-2N\alpha\Delta} - 2e^{-N\alpha\Delta}}{1 + e^{-2\alpha\Delta} - 2e^{-\alpha\Delta}} \quad (3.13a)$$

$$P_{min} \propto \frac{1 + e^{-2N\alpha\Delta} - 2e^{-N\alpha\Delta} \cos(N\beta_{min})}{1 + e^{-2\alpha\Delta} - 2e^{-\alpha\Delta} \cos(\beta_{min})} \quad (3.13b)$$

A common factor in P_{max} and P_{min} was neglected in the previous equation. Since $\cos(N\beta_{min}) = 1$ for all N , but $\cos(\beta_{min})$ changes with N , no general expression can be obtained for the degree of visibility of an N -branch interferometer (ν_{N-beam}), and different expressions will be derived for the interferometers studied in this work.

Using the values of Table 3.1, the power at the minima for the two main interferometers studied in this work can be evaluated:

$$P_{min} = \begin{cases} \sim \frac{1 + e^{-4\alpha\Delta} - 2e^{-2\alpha\Delta}}{1 + e^{-2\alpha\Delta} + 2e^{-\alpha\Delta}} & N = 2, \\ \sim \frac{1 + e^{-6\alpha\Delta} - 2e^{-3\alpha\Delta}}{1 + e^{-2\alpha\Delta} + e^{-\alpha\Delta}} & N = 3, \end{cases} \quad (3.14a)$$

$$(3.14b)$$

and their degree of visibility be obtained.

Number of branches	β_1	β_2	β_3
$N = 2$	π	-	-
$N = 3$	$2\pi/3$	$4\pi/3$	-
$N = 4$	$\pi/2$	π	$3\pi/2$

Table 3.1: Phase positions of the minima (β_{min}) located between the zero and first-order principal peaks in interferometers with $N = 2, 3$ and 4 branches. Note the different number of minima in each case.

By using Eq. (3.13a) and Eq. (3.14a) into Eq. (3.12), the fringe visibility of the Mach-Zehnder interferometer ($N = 2$, MZI) is found to depend solely on the attenuation along the length difference between branches ($\alpha\Delta$):

$$\nu_{MZI} = \frac{1}{\cosh(\alpha\Delta)} \quad (3.15)$$

Therefore, $\nu_{MZI} = 1$ for a lossless MZI ($\alpha = 0$) whereas $\nu_{MZI} < 1$ for a lossy interferometer ($\alpha \neq 0$), thus corroborating the well-known fact that the larger the losses are, the lower the fringe visibility is. Since SFL effects require sharp spectral features, a visibility of at least $\nu = 0.65$ is required [Shi-2007], and this implies that the amplitude ratio of the combining waves at the end of the MZI, $e^{-\alpha\Delta}$, should be less than $1/e$, that is, $\alpha\Delta < 1$.

$$\nu_{\alpha\Delta \leq 1} = \frac{2e^{-\alpha\Delta}}{1 + e^{-2\alpha\Delta}} \geq \frac{2e^{-1}}{1 + e^{-2}} = 0.65 \quad (3.16)$$

Similarly, the degree of visibility of the three-beam ($N = 3$) interferometer is obtained:

$$\nu_{3-beam} = \frac{3}{4 \cosh(\alpha\Delta) - 1} \quad (3.17)$$

where if $\alpha\Delta < 1$ the contrast is at least $\nu_{3-beam} = 0.58$.

$\alpha\Delta$	ν_{MZI}	ν_{3-beam}
0.01	0.99995	0.99993
0.1	0.995	0.993
0.5	0.887	0.854
0.75	0.772	0.718
0.99	0.653	0.585

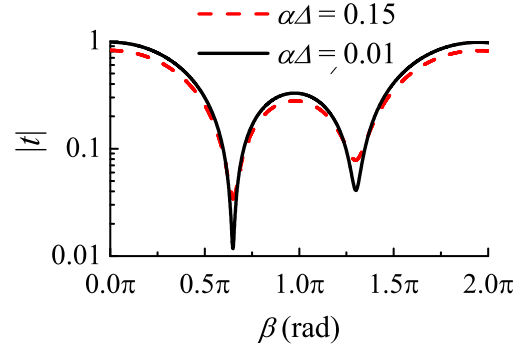


Table 3.2: Fringe visibility for various values of $\alpha\Delta$ for MZI and three-beam interferometers. Blurring of the transmission spectrum of a three-beam interferometer as $\alpha\Delta$ increase.

It can be checked that for the same value of $\alpha\Delta$, the contrast of the interference pattern decreases as the number of branches in the system increases. As an example, the fringe visibility for various values of $\alpha\Delta$ is given in Table 3.2 for the two systems, and the blurring of the interference pattern for large enough $\alpha\Delta$ is illustrated.

We conclude that for small enough $\alpha\Delta$, the degree of visibility is good enough to preserve the characteristic sharp features of the interference pattern around the minima. Therefore small $\alpha\Delta$ ($\alpha\Delta < 0.5$) will be assumed in order to study analytically the arising of SFL in these systems.

Of course, interferometers where the optical path difference is only due to a refractive index difference Δ_n (i.e. $\Delta = 0$ in Eq. (3.15) and (3.17)) have a perfect fringe contrast $\nu = 1$, since the attenuation plays no role.

In the next sections multiple-beam interferometers with constant length difference between every pair of adjacent branches ($\Delta \neq 0$) will be considered. Nevertheless if this is not the case, i.e., if this length difference is not the same, there are other mechanisms, different than attenuation, which can give rise to SFL effects. The simplest interferometer where this may occur is the one with three branches, which is analyzed in section 3.3.

3.2 Fast light in Mach-Zehnder interferometers

In this section, we consider the simplest multiple-beam interferometer (least number of arms, $N = 2$). Superluminal and negative group delay will be demonstrated in weakly absorbing asymmetric Mach-Zehnder interferometers (MZI), where the difference in the optical path is due to the different length of the branches. It will be shown that anomalous dispersion in a narrow frequency region around the interferometer's transmission minima is strong enough to hold fast light without the need of microstructuring, doping or using non-linear media in the interferometer's arms. It will be demonstrated that a difference in the refractive index of the branches alone cannot possibly induce these effects i.e. fast light is not sustained in a MZI of equal branch lengths.

Figure 3.2 illustrates the concept of a lossless asymmetric Mach-Zehnder interferometer and shows its typical transmission spectrum. For each wave component, the length of the branches are defined as: $L_1 = L - \Delta/2$ and $L_2 = L + \Delta/2$, where the length difference (Δ) between the arms yield a phase shift (β) (see Fig. 3.2(a)). As a result, the interference spectrum shows one minimum between every pair of adjacent peaks. As it was discussed in section 3.1 (see Eq. (3.9)) and it is depicted in figure 3.2(b), for the lossless MZI the maxima lie at even multiples of π and the minima lie at odd multiples of π .

An analytical expression of the transmission spectrum (magnitude and phase) and group delay of the MZI as a function of frequency, attenuation and system's size is developed.

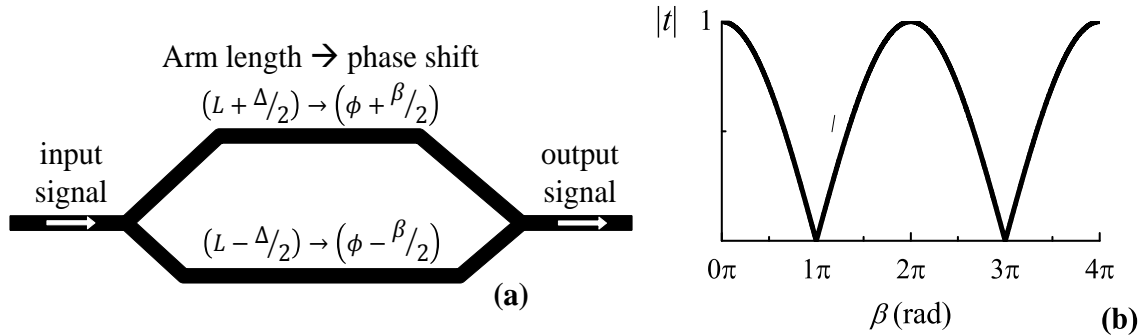


Figure 3.2: (a) Schematic of a lossless asymmetric Mach-Zehnder interferometer and (b) its typical transmission spectrum.

3.2.1 Analytical model

We consider a plane wave, with unit amplitude, impinging on a Mach-Zehnder interferometer of different branch length. A 1×2 splitter divides the wave in two equal components that travel along each arm and are recombined by a 2×1 coupler. The transmitted complex amplitude at the end of the interferometer is:

$$\hat{t} = \frac{1}{2} \sum_{i=1}^2 e^{j\hat{\phi}_i} \quad (3.18)$$

The complex phase along the i^{th} branch which was defined in Eq. (3.2) is written as:

$$\hat{\phi}_i = \frac{\omega}{v} L_i + j\alpha L_i \quad (3.19)$$

where ω is the frequency, v is the phase velocity in the medium, and L_i is the length of the specific branch. For simplicity, **the refractive index and the attenuation coefficient (α) of the medium in the branches, are assumed to be constant over the whole frequency range.**

The effective length of the MZI is the average length of the branches since the field amplitude in both arms is the same, thus:

$$L_{eff} = \frac{L_1 + L_2}{2} = \frac{(L - \Delta/2) + (L + \Delta/2)}{2} = L \quad (3.20)$$

where Δ is the length difference between them.

The magnitude and phase of the transmission coefficient can be expressed as:

$$|t| = e^{-\alpha L} \sqrt{Re^2 + Im^2} \quad (3.21a)$$

$$\phi_t = \frac{\beta L}{\Delta} + \arctan\left(\frac{Im}{Re}\right) \quad (3.21b)$$

where β is the phase associated to the physical length difference between branches, Δ , i.e. $\beta = \omega\Delta/v$, and parameters Re and Im are related to the real and imaginary parts of the transmission coefficient and are given by:

$$Re = \cosh(\alpha\Delta/2)\cos(\beta/2) \quad (3.22a)$$

$$Im = -\sinh(\alpha\Delta/2)\sin(\beta/2) \quad (3.22b)$$

Let us note that the ω -dependency of the above quantities is contained in β .

The propagation of an electromagnetic pulse through the interferometer is described in terms of the group delay, which is the time taken by the pulse envelope to propagate through the system [Bri-1960]. Following the usually adopted phase-time approach [Kit-2003, Nim-2003], the group delay is obtained from the frequency derivative of the transmission coefficient phase:

$$\tau_g = \frac{\partial\phi_t}{\partial\omega} = \frac{L}{v} + \frac{Re\frac{\partial Im}{\partial\omega} - Im\frac{\partial Re}{\partial\omega}}{Re^2 + Im^2} \quad (3.23)$$

After some algebraic calculations and recalling that the phase velocity v and the attenuation coefficient α are considered to be constant, we obtain:

$$Re' = \frac{\partial Re}{\partial\omega} = -\frac{\Delta}{2v} \sin(\beta/2) \cosh(\alpha\Delta/2) \quad (3.24a)$$

$$Im' = \frac{\partial Im}{\partial\omega} = -\frac{\Delta}{2v} \cos(\beta/2) \sinh(\alpha\Delta/2) \quad (3.24b)$$

And also,

$$Re^2 + Im^2 = \cos^2(\beta/2) + \sinh^2(\alpha\Delta/2) \quad (3.25a)$$

$$Im' \cdot Re = -\frac{1}{2} \frac{\Delta}{v} \cos^2(\beta/2) \sinh(\alpha\Delta/2) \cosh(\alpha\Delta/2) \quad (3.25b)$$

$$Re' \cdot Im = \frac{1}{2} \frac{\Delta}{v} \sin^2(\beta/2) \sinh(\alpha\Delta/2) \cosh(\alpha\Delta/2) \quad (3.25c)$$

Therefore, using Eqs. (3.25) into Eq. (3.23), the exact expression of the group delay through the MZI with constant attenuation α as a function of β is retrieved:

$$\frac{\tau_g}{\tau_p} = 1 - \frac{\Delta \sinh(\alpha\Delta/2) \cosh(\alpha\Delta/2)}{2L \cos^2(\beta/2) + \sinh^2(\alpha\Delta/2)} \quad (3.26)$$

In Eq. (3.26), the group delay has been normalized to the phase delay over the system's effective length, $\tau_p = L/v$.

Group delay at the transmission minima

With the aim of obtaining an analytical expression for the group delay at the transmission minima, the position of the minima must be first derived. For lossless interferometers the intensity at the minima is exactly zero. Therefore, requiring $|\hat{t}| = 0$ in Eq. (3.21a) with $\alpha = 0$ leads to condition $Re^2 + Im^2 = \cos^2(\beta/2) = 0$ which is accomplished for phase values $\beta = (2m + 1)\pi$, where m is the order of the principal maximum below the minimum. As it should be expected, it agrees with the general result in Eq. (3.9) if $N = 2$.

If a lossy MZI is considered ($\alpha \neq 0$), the transmission at the minima is not exactly zero ($|\hat{t}| \neq 0$) and their phase position must be obtained from the necessary condition $\partial|\hat{t}|/\partial\beta = 0$. When this is satisfied, the more easier to calculate condition $\partial|\hat{t}|^2/\partial\beta = 0 = 2|\hat{t}|(\partial|\hat{t}|/\partial\beta)$ is also accomplished. Considering Eqs. (3.21a) and (3.22), it reads $\partial|\hat{t}|^2/\partial\beta = 2e^{-2\alpha L} \sin(\beta)$ and holds for phase values $\beta = (2m + 1)\pi$ or $\beta = 2\pi m$ with $m = 0, 1, 2, \dots$. The former values correspond to the minima and the latter to the maxima of the transmission function $|\hat{t}(\beta)|$.

Therefore, the remarkable result is obtained where the position of the minima in a MZI does not change with attenuation at all, as far as constant α is assumed.

Considering $\beta = (2m + 1)\pi$ in Eq. (3.26) an exact expression of the group delay at the minima is obtained:

$$\tau_g = \tau_p \left[1 - \frac{\Delta}{2L} \coth\left(\frac{\alpha\Delta}{2}\right) \right], \quad (3.27)$$

In the following analysis small values of $\alpha\Delta$ will be considered. As it was discussed in section 3.1, $\alpha\Delta \ll 1$ corresponds to a high contrast of the interference pattern and, consequently, to a situation where SFL effects can be expected. For small enough $\alpha\Delta$ we have $(\Delta/2) \coth(\alpha\Delta/2) \approx 1/\alpha$ which substituted into Eq. (3.27) leads to an approximate expression for the group delay at the minima:

$$\tau_g \approx \tau_p \left(1 - \frac{1}{\alpha L} \right) = \tau_p - \frac{1}{\alpha v}. \quad (3.28)$$

Interestingly, if we now apply the relationship between the attenuation coefficient and the imaginary part of the complex refractive index, n_i , ($\alpha = n_i\omega/c$) into Eq. (3.28), the group delay at ω_{min} can also be approximated as:

$$\tau_g \approx \tau_p - \frac{n}{n_i} \frac{1}{\omega_{min}}. \quad (3.29)$$

The above expression brings an interesting point into attention. It sets a scaling law for the group delay; since it indicates that the product $\omega_{min} \times (\tau_g - \tau_p)$ does not depend on the interferometer's operative frequency range, but only on the ratio between the real and imaginary parts of the complex refractive index of the medium in the branches (n/n_i).

Following the discussion, we now focus on a system with a given refractive index and take Eq. (3.28) to analyze the possible propagation regimes at the minima.

a. Lossless MZI ($\alpha = 0$)

In this case, Eq. (3.27) leads to $\tau_g/\tau_p = 1$, in other words, the group delay at the minima is equal to the phase delay. This is expected in a linear and lossless system, where the phase relation between the pulse components is not changed. Thus, the pulse peak travels at the phase speed

and no anomalous propagation regimes can be sustained. Let us point out that since for $\alpha = 0$, $Re = \cos(\beta/2)$ (which is zero at the minima) and $Im = 0$, Eq. (3.21a) yields $|t| = 0$. As it will become clear later, the absence of anomalous propagation regimes in the lossless MZI is directly associated to the fact of having exactly null transmission at the minima.

b. Lossy MZI ($\alpha > 0$)

Here we provide theoretical argumentation to show that tunnelling and superluminal regimes can arise at the minima by properly choosing the interferometer effective length for a given attenuation coefficient.

Eq. (3.28) justifies the impossibility of getting slow light (τ_g cannot be larger than τ_p) in a lossy MZI, since α is positive by definition. Only in the case of an active MZI ($\alpha < 0$) could subluminal regime be sustained. Namely, in the hypothetical case of constant gain, τ_g/τ_p would always be larger than 1 and, consequently, the only possible pulse propagation regime at the minima would be subluminal. This is, however, an unphysical situation since no real medium displays gain over the whole frequency range. Practical situations, like considering a MZI with a medium in one of the branches that exhibits a narrow gain resonance, are discussed in the literature [Shi-2007]. Since this work focuses on passive systems, this analysis is not regarded.

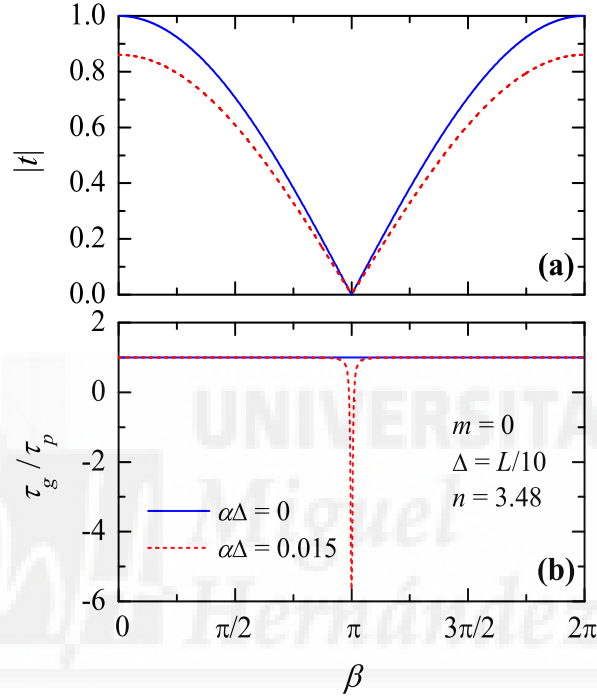
The interferometer will sustain tunnelling at the minima ($\tau_g < 0$) if the effective length is chosen so that:

$$\alpha L < 1 \tag{3.30}$$

The above condition holds for most of the interferometers one might envisage. Therefore, tunnelling is the expected propagation regime for a narrowband pulse with carrier frequency tuned at a transmission minimum. Nevertheless, superluminal regime will arise ($0 < \tau_g < L/c$) if the interferometer's effective length satisfies the following condition:

$$1 < \alpha L < \frac{n}{n-1} \tag{3.31}$$

Condition	$\alpha L < 1$	$1 < \alpha L < \frac{n}{n-1}$	$\alpha L > \frac{n}{n-1}$
$\alpha > 0$	Tunnelling	Superluminal	Normal

Table 3.3: Possible propagation regimes of a lossy MZI.**Figure 3.3:** (a) Coefficient magnitude and (b) group delay in units of the phase delay through a Si-based Mach-Zehnder interferometer with length difference between arms $\Delta = L/10$, and refractive index $n = 3.48$, for two values of the attenuation coefficient α .

where n is the real part of the medium's refractive index. Note that Eqs. (3.30) and (3.31) do not depend on Δ , which only determines the frequency position of the minima, namely $\omega_{min} = (2m + 1)\pi v/\Delta$, being m and integer. Table 3.3 summarizes the possible propagation regimes at the minima as a function of αL .

The above analysis shows that the mechanism responsible for anomalous group velocity in a lossy MZI is the total attenuation of the system, αL , which can be modified by either changing the attenuation coefficient α and/or the interferometer's effective length L . This is illustrated by performing numerical simulations on a Si-based MZI with refractive index $n = 3.48$. Figure

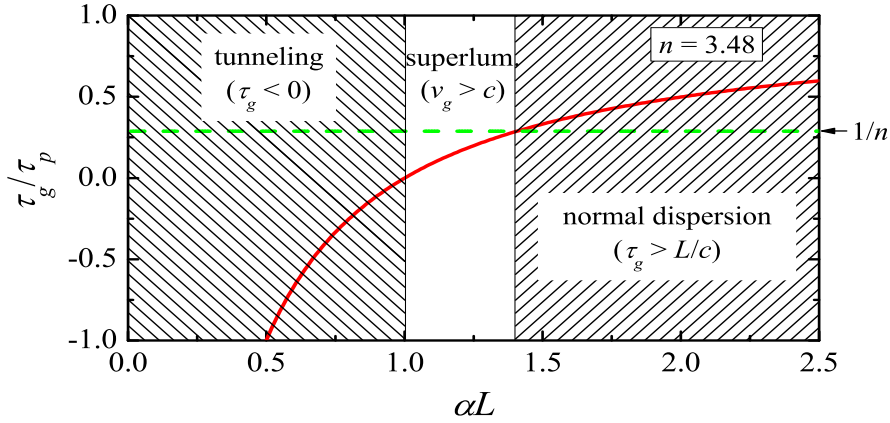


Figure 3.4: Pulse propagation regimes at the transmission minima of a Si-Based MZI with $\alpha\Delta = 0.015$ as a function of the total system's attenuation αL . Group delay plotted from Eq. (3.27) (solid line) and phase delay through vacuum (dashed line). The delays are given in units of the phase delay over the system's effective length, $\tau_p = L/v$.

3.3 shows, for two attenuation values and $\Delta = L/10$, the transmission coefficient magnitude calculated using Eq. (3.21a) and the exact expression of the group delay as a function of β given in Eq. (3.26). In agreement with our previous discussion, no anomalous propagation regimes occur in the lossless interferometer, while if losses with $\alpha\Delta = 0.015$ are considered, tunnelling appears around each minimum with negative group delays of almost $-6\tau_p$.

Figure 3.4 shows how the system's total attenuation determines the pulse propagation regime. The group delay at the minima (normalized to the phase delay) is plotted as a function of αL for a Si-based MZI with $\alpha\Delta = 0.015$. Together with Eq. (3.27), the straight line $1/n$ corresponding to the propagation through vacuum is represented. In agreement with Eq. (3.30), the system exhibits tunnelling for small enough attenuation ($\alpha L < 1$). For values of αL ranging between 1 and 1.4, superluminal propagation is sustained, in agreement with expression (3.31), whereas the system presents normal dispersion for too high attenuation, ($\alpha L > 1.4$). To conclude, Figs. 3.3 and 3.4 clearly show that fast light is achieved in a MZI for small enough total attenuation, while it disappears if it is either too high ($\alpha L > n/(n-1)$) or zero.

3.2.2 Analysis considering the optical path difference

One can generalize the situation and consider a MZI where both the length and/or the refraction index of the branches are different. The optical path in the i^{th} arm is $\ell_i = n_i L_i$ where, as before, the attenuation coefficient, is considered to be constant and equal in every arm and the branch lengths are defined as $L_1 = L - \Delta/2$ and $L_2 = L + \Delta/2$ but where now the refractive index in each branch is $n_1 = n - \Delta_n/2$ and $n_2 = n + \Delta_n/2$.

The effective optical path $\ell_{\text{eff}} = (\ell_1 + \ell_2)/2$, can be written in terms of the effective refractive index $n = (n_1 + n_2)/2$, the effective physical length $L_{\text{eff}} = (L_1 + L_2)/2 = L$ and the refractive index difference Δ_n as:

$$\ell_{\text{eff}} = nL + \frac{\Delta_n}{4} \Delta \quad (3.32)$$

An optical path difference occurs if the branches differ in length ($\Delta \neq 0$) and/or if their refractive index is different ($\Delta_n \neq 0$). For the sake of simplicity, the situation where both causes are concomitant will not be regarded. One thus distinguishes two cases:

- (a) Δ -induced fringe pattern ($\Delta_n = 0$, $\Delta \neq 0$): the interference pattern is due to the difference in the length of the branches. It is the situation previously analyzed and corresponds to an asymmetrical MZI (also called unbalanced MZI) [Por-1999].
- (b) Δ_n -induced fringe pattern ($\Delta_n \neq 0$, $\Delta = 0$): the branches are of the same length L and the interference pattern arises because of the different refractive index in each branch $n_1 \neq n_2$. This is usually called symmetrical MZI [Por-1999].

It is straightforward to find that in case (a), the effective optical path is the effective physical path $L_{\text{eff}} = (L_1 + L_2)/2 = L$ multiplied by the (common) refractive index, while in case (b), ℓ_{eff} is the effective refractive index times the (common) branch length. In both cases, $\ell_{\text{eff}} = nL$.

Let us now analyze whether SFL effects arise in case (b), in other words, whether there can be Δ_n -induced SFL in a symmetrical MZI. This situation is worth being studied because for

practical purposes, one might consider the possibility of inducing the optical path difference in the MZI not by means of a physical length difference Δ , but through a difference in the refractive index of the branches Δ_n . We could then envisage a MZI with equal branch lengths and fabricated using an electro-optic material such as Lithium Niobate, where Δ_n is tuned upon the application of voltage [Sin-2012]. As we shall now demonstrate, though, SFL effects cannot occur in such a device.

The analysis goes along similar lines as that of the previous section. Since now $L_1 = L_2 = L$ the phase of the wave upon propagation through the i^{th} branch (see Eq. (3.2)) reads:

$$\hat{\phi}_i = \frac{\omega}{c} n_i L + j\alpha L \quad (3.33)$$

The complex transmission coefficient in Eq. (3.18) can then be written as:

$$\hat{t} = e^{-\alpha L} (e^{j\frac{\omega}{c}n_1L} + e^{j\frac{\omega}{c}n_2L}) = e^{-\alpha L} e^{j\frac{\omega}{c}nL} \cos(\omega\Delta_n L/2c) \quad (3.34)$$

The magnitude and phase of the transmission coefficient is thus given by:

$$|\hat{t}| = e^{-\alpha L} \sqrt{Re^2 + Im^2} = e^{-\alpha\Delta} \cos(\beta/2) \quad (3.35a)$$

$$\phi_t(\omega) = \frac{\omega}{c} nL \quad (3.35b)$$

where β is the phase associated to the optical length difference ($\beta = \omega\Delta_n L/c$).

The group delay of a pulse centered at frequency ω is then:

$$\tau_g = \frac{\partial\phi_t}{\partial\omega} = \frac{nL}{c} = \frac{\ell_{\text{eff}}}{c} = \tau_p \quad (3.36)$$

Two important consequences can be extracted from the above expressions. First, **the transmission is exactly zero at the minima** (occurring at $\beta = (2m + 1)\pi$) **whatever the attenuation value is**. This is easy to understand. Because the branches have the same length

and attenuation coefficient, the plane waves travelling along each branch reach the end with the same amplitude. In addition, the refractive index difference between branches, Δ_n , makes the phase shift (β) between each plane wave an odd multiple of π for certain frequencies. As a result, the interference of such plane waves is completely destructive.

Second, **the group delay corresponds to normal pulse propagation, i.e. there are no Δ_n -induced SFL effects in a MZI with equal branch lengths.** The group delay obtained is that of a pulse travelling at the average phase velocity $v = c/n$ along a distance L , or, equivalently, it corresponds to the average phase delay of the propagation along the two branches $(\tau_1 + \tau_2)/2 = (Ln_1 + Ln_2)/2 = nL/c$.

In other words, the reason for the absence of SFL effects in symmetric MZIs is that the transmission is exactly zero at the minima, independently of the attenuation. No degree of freedom is left to yield anomalous propagation regimes. This situation resembles that of the *lossless asymmetric* MZI discussed in section 3.2.1a., which displays zero transmission at the minima and the group delay was equal to the phase delay. In contrast, for the *lossy asymmetric* system discussed in section 3.2.1b., the attenuation provides the degree of freedom necessary to yield fast light, and (for equal attenuation coefficient in every arm) this only can occur if the branches differ in length.

3.2.3 Transmission coefficient and group delay around the transmission minima

In the previous section the requirement of a physical length difference between the branches of the MZI in order to get fast light effects was assessed. Therefore, only this case will be considered onwards.

The scope of this section is to derive approximate analytical expressions of the magnitude and phase of the transmission coefficient ($|\hat{t}(\omega)|$ and $\phi_t(\omega)$) and of the group delay, $\tau_g(\omega)$, valid for frequencies close to a transmission minimum. The expressions obtained will be used in the next section to analyze the propagation of sinusoidally modulated pulses through asymmetric MZIs.

The complex transmission coefficient in Eq. (3.21) is considered. The term $\beta/2$ that appears as argument of the trigonometric functions involved (see Eqs. (3.22)) is now written in terms of β_{min} . Recalling the phase values for the minima, $\beta_{min} = (2m + 1)\pi$, and after applying the trigonometric relations for complimentary angles, the following equations are obtained, where m is the order of the minimum:

$$\sin(\beta/2) = \sin\left(\frac{\beta - \beta_{min}}{2} + \frac{\beta_{min}}{2}\right) = (-1)^m \cos\left(\frac{\beta - \beta_{min}}{2}\right) \quad (3.37a)$$

$$\cos(\beta/2) = \cos\left(\frac{\beta - \beta_{min}}{2} + \frac{\beta_{min}}{2}\right) = (-1)^{m+1} \sin\left(\frac{\beta - \beta_{min}}{2}\right) \quad (3.37b)$$

The above expressions are used in Eqs. (3.21) to get:

$$|\hat{t}| = e^{-\alpha L} \sqrt{\sin^2\left(\frac{\beta - \beta_{min}}{2}\right) + \sinh^2\left(\frac{\alpha\Delta}{2}\right)} \approx e^{-\alpha L} \sqrt{\left(\frac{\beta - \beta_{min}}{2}\right)^2 + \left(\frac{\alpha\Delta}{2}\right)^2} \quad (3.38a)$$

$$\frac{Im}{Re} = \frac{\tanh(\alpha\Delta/2)}{\tan(\beta - \beta_{min}/2)} \approx \frac{\alpha\Delta}{\beta - \beta_{min}} \quad (3.38b)$$

where the approximation valid for small angles $(\beta - \beta_{min})$ and small $\alpha\Delta$ (good visibility of the fringes) was considered. Recalling that $\beta = \omega\Delta/v$ and defining a new parameter: $\gamma = -\alpha v$, leads to the following approximate equations for the magnitude and phase of the transmission coefficient around the minima ω_{min} :

$$|\hat{t}(\omega)| \approx e^{-\alpha L} \frac{\alpha\Delta}{2} \sqrt{1 + \left(\frac{\omega - \omega_{min}}{\gamma}\right)^2} \quad (3.39a)$$

$$\phi_t(\omega) \approx \omega\tau_p + \arctan\left(\frac{\omega - \omega_{min}}{\gamma}\right) + \frac{\pi}{2} \quad (3.39b)$$

with $\tau_p = L/v$ being the phase delay over the system's effective length. Note that the result of null transmission at the minima is recovered for the lossless case ($\alpha = 0$).

The approximate expression for the group delay around each minimum is retrieved through an ω -derivation of the phase function in Eq. (3.39b):

$$\tau_g(\omega) \approx \tau_p + \frac{\gamma}{(\omega - \omega_{min})^2 + \gamma^2}, \quad (3.40)$$

Equation (3.40) shows that the *excess* group delay ($\tau_g - \tau_p$) around the minima is a Lorentzian function with half-width at half maximum (HWHM) $|\gamma|$, and excess group delay at the transmission minima $1/\gamma$. Since γ is directly proportional to the attenuation coefficient ($\gamma = -\alpha v$), one concludes that the larger the losses, the wider will be the group delay curve and the smaller (in absolute value) will be the group delay at ω_{min} . Hence, the softening of the anomalous group delay regimes in the case of notable losses is demonstrated, in agreement with the discussion in section 3.1. Finally, let us note that the approximate expression of the group delay at ω_{min} (normalized to τ_p) given in Eq. (3.28) is recovered.

3.2.4 Propagation of sinusoidally modulated signals

The propagation of a sinusoidally modulated pulse through the MZI is now modeled. A sinusoidally modulated wave-packet with carrier frequency ω_c and modulation frequency ω_m is considered, $E_{in}(t) = E_c \sin(\omega_c t)[1 + M_{in} \cos(\omega_m t)]$, where the modulation index M_{in} is the amplitude ratio of the modulating and carrier signal. As it is well known, together with the carrier component, this kind of modulation generates two sidebands of amplitude $E_{\pm s} = M_{in} E_c / 2$ and frequency $\omega_{\pm s} = \omega_c \pm \omega_m$, where the plus sign corresponds to the upper sideband and the minus sign to the lower sideband.

By setting the carrier frequency at one of the transmission minima ($\omega_c = \omega_{min}$) and considering a carrier signal with unit amplitude, Fourier theory is applied to retrieve the output field from the effect of the system's complex transmission function on each spectral component, reading:

$$E_{out}(t) = |\hat{t}_{min}| \sin(\omega_{min} t - \phi_{min}) + \frac{M_{in}}{2} [|\hat{t}_{+s}| \sin(\omega_{+s} t - \phi_{+s}) + |\hat{t}_{-s}| \sin(\omega_{-s} t - \phi_{-s})] \quad (3.41)$$

The amplitude and phase of the central band and the side bands are obtained from Eqs. (3.39) and are given by:

$$|\hat{t}_{min}| = e^{-\alpha L} \frac{\Delta}{2v} |\gamma| \quad (3.42a)$$

$$|\hat{t}_{\pm s}| = \frac{|\hat{t}_{min}|}{|\gamma|} \sqrt{\omega_m^2 + \gamma^2} \quad (3.42b)$$

$$\phi_{min} = \omega_{min} \frac{L}{v} + \frac{\pi}{2} \quad (3.42c)$$

$$\phi_{\pm s} = \phi_{min} \pm \left[\omega_m \frac{L}{v} + \arctan \left(\frac{\omega_m}{\gamma} \right) \right] \quad (3.42d)$$

Using the above equations into Eq. (3.41), and after some algebraic calculations, the outgoing pulse reads:

$$E_{out}(t) = |\hat{t}_{min}| \sin(\omega_{min}t - \phi_{min}) \times \left[1 + M_{in} \frac{\sqrt{\omega_m^2 + \gamma^2}}{|\gamma|} \cos(\omega_m t - \omega_m L/v - \arctan(\omega_m/\gamma)) \right] \quad (3.43)$$

An inspection of the above expression suggests defining an output modulation index (M_{out}) and a pulse delay (τ_{pulse}) such that Eq. (3.43) can be written as:

$$E_{out}(t) = |\hat{t}_{min}| \sin(\omega_{min}t - \phi_{min}) [1 + M_{out} \cos(\omega_m(t - \tau_{pulse}))] \quad (3.44)$$

with

$$M_{out} = M_{in} \sqrt{1 + (\omega_m/\gamma)^2} \quad (3.45)$$

and

$$\tau_{pulse} = \tau_p + \frac{1}{\omega_m} \arctan(\omega_m/\gamma) \quad (3.46)$$

where as pointed out earlier $\tau_p = L/v$ and $\gamma = -\alpha v$.

Let us now discuss the implications of the above analysis. The pulse delay in Eq. (3.46) is the time that a sinusoidally modulated pulse of modulation frequency ω_m and carrier frequency tuned at a minimum ω_{min} takes in travelling through a MZI. In the limit of extremely narrow pulse bandwidth $\omega_m \rightarrow 0$, $\tau_{pulse} \rightarrow \tau_p + 1/\gamma$, thus recovering the value of the group delay at ω_{min} which was discussed in section 3.2.1. In other words, this analysis shows that the narrower the spectral pulse-width is, the more the *pulse delay* measured in a time-domain propagation experiment approaches the value of the *group delay* given by Eq. (3.28) at the transmission minima.

Figures of merit

A widely used figure of merit of SFL systems is the fractional (or relative) delay [Geh-2008], FD, defined as the ratio between the excess pulse delay and the duration of the incident pulse, T_{in} :

$$FD = \frac{\tau_{pulse} - \tau_p}{T_{in}} \quad (3.47)$$

This quantity is equal to the excess number of pulses that can be contained at any time within the system with respect to the number that would be contained if the pulses travelled at the phase velocity. It is hence a measure of how much the information storage capacity of the system is enhanced due to SFL effects.

A common definition when dealing with optical pulses is to take the pulse duration (T_{in}) as the FWHM of the detected pulse power. For sinusoidally modulated pulses of modulation index M , the corresponding pulse duration is $T = (2/\omega_m) \arccos((1 - \sqrt{2} + M)/\sqrt{2}M)$ and consequently, FD reads:

$$FD = \frac{\arctan\left(\frac{\omega_m}{\gamma}\right)}{2 \arccos\left(\frac{(1 - \sqrt{2} + M_{in})}{\sqrt{2}M_{in}}\right)} \quad (3.48)$$

Note that in this case the fractional delay is a fractional advancement, $|FD|$, because of the negative sign of γ .

Figure 3.5(a) shows that $|FD|$ increases with modulation frequency. Also, Eq. (3.48) predicts $|FD| = 34\%$ if modulation is performed with $\omega_m = |\gamma|$, i.e. if the pulse spectral components lie within the FWHM of the group delay function in Eq. (3.40). For higher modulation frequencies, however, the pulse will undergo a certain degree of distortion, which is larger as ω_m increases.

According to Eq. (3.44) the outgoing pulse envelope evolves as $E_{out}(t) \propto 1 + M_{out} \cos[\omega_m(t - \tau_{pulse})]$ and its duration is $T_{out} = (2/\omega_m) \arccos\left(\frac{1 - \sqrt{2} + M_{out}}{\sqrt{2}M_{out}}\right)$. According to (3.45), the modulation index of the transmitted pulse is larger than that of the input pulse and, consequently, the duration of the output pulse (T_{out}) will always be smaller, thus leading to a pulse compression, b , whose value can be calculated by:

$$b = 1 - \frac{T_{out}}{T_{in}} = 1 - \frac{\arccos\left(\frac{1 - \sqrt{2} + M_{out}}{\sqrt{2}M_{out}}\right)}{\arccos\left(\frac{1 - \sqrt{2} + M_{in}}{\sqrt{2}M_{in}}\right)} \quad (3.49)$$

Figure 3.5(a) shows (dashed line) the relation between pulse compression and modulation frequency (normalized to $|\gamma|$). Comparing it to the fractional delay curve it is found that, for not too high values of ω_m , the compression factor b goes roughly quadratic with the fractional delay, $b \approx K(FD)^2$. Considering $M_{in} = 1$, the proportionality constant K is 0.74 if $\omega_m \rightarrow 0$ and it is 0.71 if $\omega_m = |\gamma|$. This relation is illustrated in Fig. 3.5(b); it implies that, in order to keep the pulse compression below 5%, the fractional delay cannot exceed 27%, and to keep it below 10%, the fractional delay cannot exceed 38%.

In addition to pulse compression, distortion of the pulse amplitude also appears, similarly to what is observed for fast light in systems with material resonances [Boy-2007]. In the case of $M_{in} = 1$ this amplitude distortion acts as a pulse breakup, giving rise to a main peak (lying at $t = \tau_{pulse}$) and a secondary peak (lying at $t = \tau_{pulse} + \pi/\omega_m$). The secondary-to-main power amplitude ratio is given by $(1 - M_{out})^2/(1 + M_{out})^2$, which increases with increasing modulation frequency or, equivalently, with increasing fractional advancement, as shown in Fig. 3.5(b). Thus, in order to maintain the secondary peak amplitude below 10% of the main peak amplitude, the fractional delay may not exceed 45%.

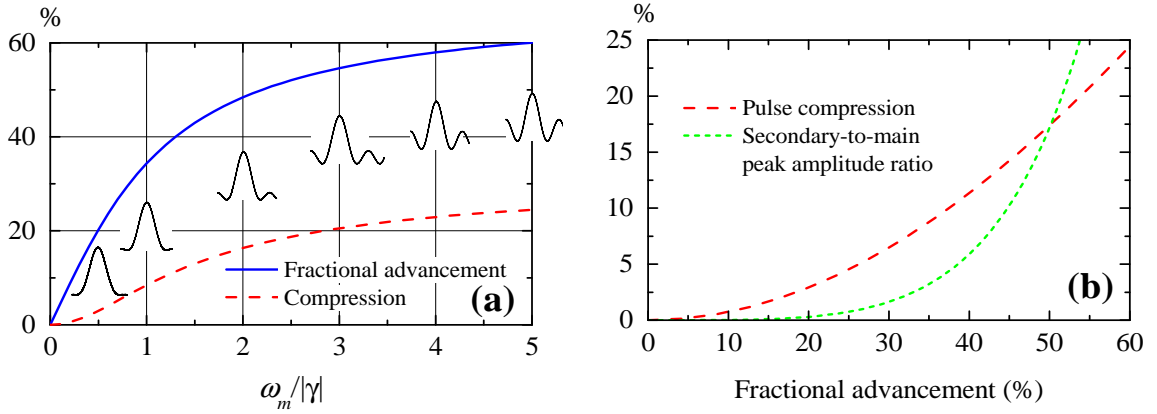


Figure 3.5: (a) Fractional advancement (solid line) and pulse compression (dashed line) versus normalized modulation frequency, and (b) pulse compression (dashed line) and secondary to main peak amplitude ratio (short-dashed line) as a function of the fractional advancement, for a 100% sinusoidally modulated pulse train with carrier frequency tuned at one of the transmission minima.

Another relevant figure of merit of SFL systems is the delay-bandwidth product (DBP) (see section 2.2), defined as the product of the delay and bandwidth of the signal transmitted through the system. This quantity can be estimated in various units depending on which magnitude the bandwidth is given. Choosing once again a modulation frequency $f_m = |\gamma|/2\pi$ so that the spectral components of the signal here considered lie within the FWHM of the Lorentzian group delay curve in Eq. (3.40), the expected DBP is $(\tau_{pulse} - \tau_p) \times 2f_m = 25\%$.

It is worth noticing that the above features and figures of merit are entirely applicable to MZIs operating at any frequency range. In this context, we shall recall the simple scaling law for the excess group delay that was previously obtained (see Eq. (3.29)), which is useful to transform a device originally designed to operate at a specific frequency range into another operative range.

3.2.5 Experimental results and discussion in the RF range

The previous analytical model is checked experimentally in a linear and passive asymmetric MZI operative in the radiofrequency (RF) range. Evidence of superluminal and negative group delays is provided over a narrow frequency interval within the interferometer's transmission minima. Propagation of RF sinusoidally modulated pulses is characterized and pulse delay measurements (τ_{pulse}) are compared to the model predictions given in section 3.2.4.

[h!]	$L(m)$	$\Delta(m)$	$\alpha(Np/m)$	$\alpha\Delta$	n
	8	12	0.014	0.168	1.5

Table 3.4: Characteristics of the fabricated MZI operative in the RF range with branches $L_1 = L - \Delta/2$ and $L_2 = L + \Delta/2$.

a. Interferometer design

The interferometer consists of two coaxial cables lines (50 Ω , RG-58C/U), of 2 and 14 m length, respectively, connected by a 1 \times 2 RF power splitter and a 2 \times 1 RF coupler (both PE2000, Pasternack). Hence, after Eq. (3.20) the system's effective length is $L = 8$ and $\Delta = 12$ m is the difference between branches. Since the wave velocity in the cables is $v = 0.67c$ the refractive index of the system is $n = 1.5$. The phase delay of the system is thus $\tau_p = 40$ ns. The characterization of the attenuation coefficient in the cables as a function of frequency, $\alpha(\omega)$, is given in Appendix B.1. For the frequency range under study (20-100 MHz) an average value $\alpha = 0.014$ Np/m was obtained, which is considered as the constant loss coefficient in the model equations when comparing it to the experimental results.

Therefore, the model parameters take the values $\alpha\Delta = 0.014 \times 12 = 0.168$ and $\gamma^{-1} = -1/\alpha v = -357.14$ ns. Considering Table 3.3 and the fact that $\alpha L = 0.014 \times 8 = 0.112 < 1$, tunnelling is the predicted group delay regime at the transmission minima. This regime is expected to be clearly noticeable since the degree of visibility of the fringes calculated from Eq. (3.15) is $\nu_{MZI} \sim 99\%$. In Table 3.4 the characteristics of the coaxial MZI are summarized.

b. Results in the frequency domain

The coaxial cable MZI described above is characterized in the frequency domain by means of a two-port vector network analyzer (Agilent model E8363B) (see Appendix B.1). The S_{21} scattering parameter (the transmission coefficient) was recorded in the 20-100 MHz range every 112.500 kHz with an average of 64 to suppress the random noise. The splitters were characterized in order to properly compare the experimental response to the numeral simulations and model predictions, which do not include the effect of the splitters.

The phase of S_{21} is the transmission phase function $\phi_t(\omega)$, which is derived versus frequency to obtain the experimental group delay function $\tau_g(\omega)$. The measured S_{21} data contains a small amount of noise that is amplified upon derivation of the phase data curve, leading to spurious effects on the experimental τ_g curve. To avoid them, a 17-point smoothing algorithm is applied to the measured phase curve prior to differentiating it.

To get a complete picture, the real part of the system's effective refractive index $n_{eff}(\omega)$ and the group velocity $v_g(\omega)$ are also determined. The former is obtained from the overall phase accumulated on transmission through the structure of effective length $L_{eff} = L$. Within this picture [Cen-1999], the interferometer behaves as a homogeneous medium with dispersion given by $n_{eff}(\omega)$.

$$n_{eff}(\omega) = \frac{c\phi_t(\omega)}{\omega L} \quad (3.50)$$

while the latter is given by:

$$v_g(\omega) = \frac{L}{\tau_g(\omega)} = \frac{L}{\frac{\partial \phi_t}{\partial \omega}} \quad (3.51)$$

Together with the experimental results, numerical simulations are performed considering the actual (frequency dependent) attenuation coefficient of the cables $\alpha(\omega)$. The system's transmission spectrum (magnitude and phase) is numerically calculated using Eqs. (3.18) and (3.19). The numerical phase function $\phi_t(\omega)$ is then used in Eqs. (3.50) and (3.51) to obtain the effective refractive index $n_{eff}(\omega)$ and the expected group velocity $v_g(\omega)$. Finally, the same smoothing algorithm as that applied to the experimental phase data is applied to the simulated phase function (prior differentiation) to calculate the group delay $\tau_g(\omega)$.

In Fig. 3.6, experimental and simulation results are shown. The agreement between simulation and experiment is very good, thus assessing the accuracy of the procedure to subtract the effect of the splitters from the experimental data. The transmission $|t|(\omega)$ shows an oscillatory behavior at the frequencies of the transmission minima. The slope of the transmission phase function $\phi_t(\omega)$ becomes negative, and this causes the anomalous dispersion regions in the effective refraction index curve $n_{eff}(\omega)$. These regions of negative slope in $n_{eff}(\omega)$ lead to

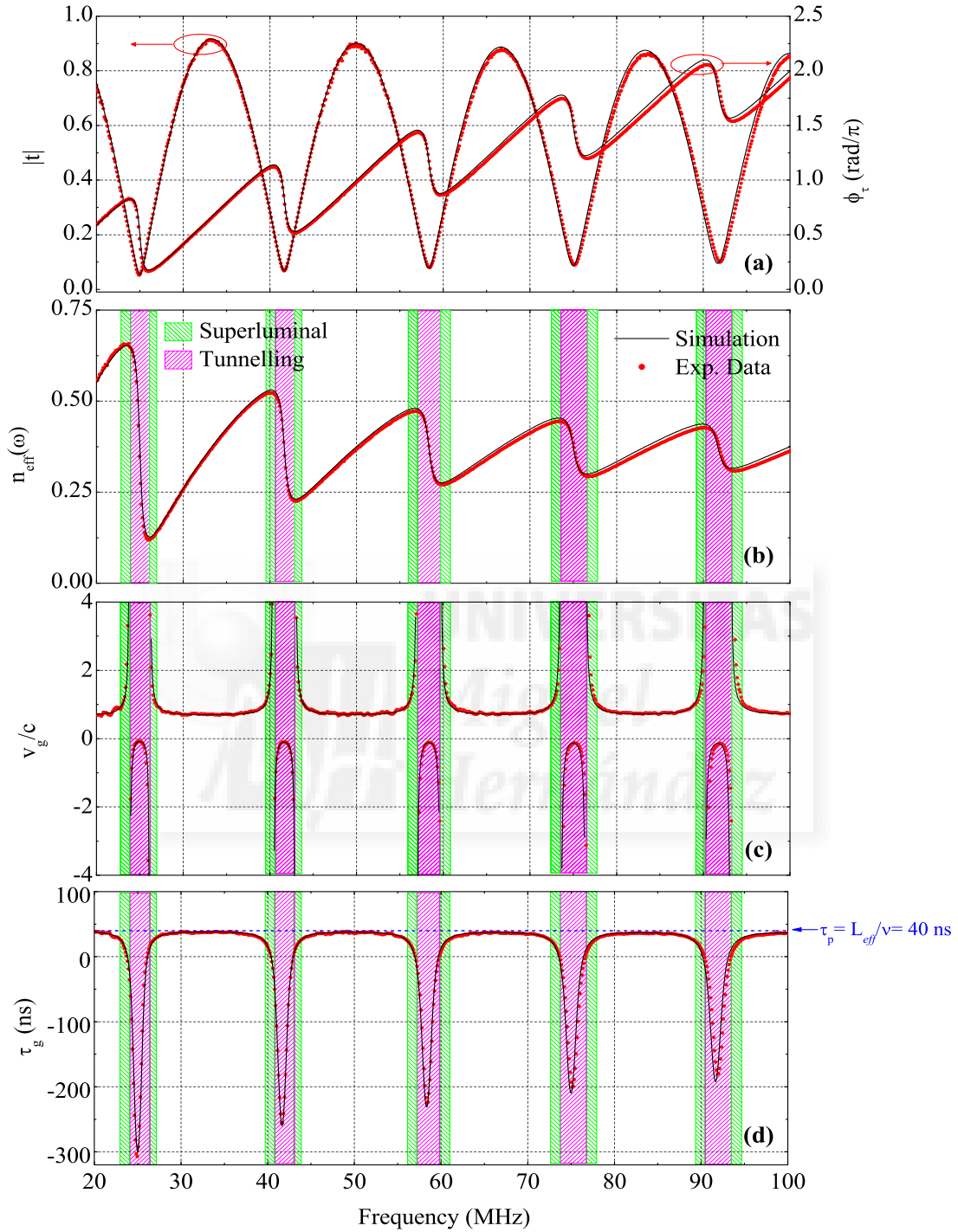


Figure 3.6: Simulation (lines) and experimental (symbols) results of the following quantizes of a MZI operative in the RF range:(a) transmission coefficient, magnitude and phase, (b) effective refractive index using Eq. (3.50), (c) group velocity using Eq. (3.51) and (d) group delay. Simulation results consider the frequency–dependent attenuation coefficient of the cables $\alpha(f)$. The interferometer arms are 2 and 14 m long.

superluminal or negative group velocities, depending on the slope's magnitude. It should be emphasized that such anomalous dispersion in n_{eff} is of structural origin; it is not due to material dispersion of the medium in the branches (whose refractive index was in fact considered constant) but to the features in the spectral transmission. This is also the situation in photonic band-gap systems. Anomalous dispersion is stronger at lower frequencies because of the lower attenuation in the cables. In the normal dispersion region, the group velocity equals the phase velocity in the cables ($0.67c$).

Accordingly to the steep negative slope of $\phi_t(\omega)$ in a narrow region around the minima, tunnelling and superluminal regimes can arise at these frequencies. In agreement with the model predictions for $\alpha L < 1$, the results in Fig. 3.6 corroborate that tunnelling is the expected pulse propagation regime at the minima, leading to negative group delay values of about -200 ns. Panels (c) and (d) in the figure show that for a pulse with center frequency very close to the minima, very small group delays ($\tau_g \sim 10$ ns) corresponding to superluminal group velocities larger than $4c$ are expected.

Once the results in the frequency domain have been described, we compare the experimental results with our theoretical model. As Fig. 3.7(a) shows, the constant loss coefficient $\alpha = 0.014Np/m$ considered in the model fits very well the experimental $|t|$ and ϕ_t curves in the displayed frequency range, which is centered at the transmission minimum where pulse propagation experiments will be later performed. The experimental transmission minimum lies at 58.3625 MHz i.e. 62.5 KHz above the theoretical f_{min} . The agreement was found to be also good in a broader spectral range (20 – 100 MHz), with the only effect of a lowering of the measured transmission peaks for larger frequencies because of the frequency-dependence of the actual coefficient loss.

As shown in Fig. 3.7(b), the experimental group delay function is reasonably well accounted for by the theoretical model. The experimental and theoretical group delay at the minimum takes the values $\tau_g^{exp}(f_{min}) = -292.81$ ns and $\tau_g^{theo}(f_{min}) = -316.46$ ns. The error in the experimental value is estimated to be ± 30 ns considering the data experimental dispersion and the frequency discretization. Let us note that the frequency derivation of the phase data amplifies the small amount of noise that is contained in the measured S_{21} parameter; this

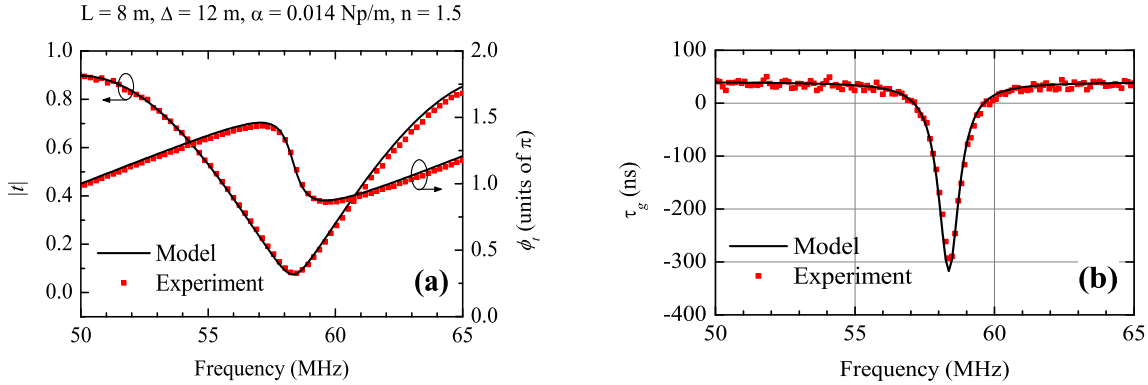


Figure 3.7: Experimental and model results of a RF MZI with the indicated parameters. (a) Magnitude and phase of the transmission coefficient, and (b) group delay around the transmission minimum at 58.3 MHz.

is why the experimental τ_g^{exp} curve exhibits significant dispersion. The theoretical prediction of -316.46 ns lies within the experimental range of $\tau_g^{exp}(f_{min}) = -292.81 \pm 30 \text{ ns}$. It is worthwhile mentioning that the Lorentzian approximation of Eq. (3.40) with model parameter $\gamma^{-1} = -357.14 \text{ ns}$ almost perfectly fits the experimental function $\tau_g^{exp}(f)$.

Comparison with a coaxial photonic crystal of the same effective length shows that the MZI achieves three times larger superluminal velocities and presents regions of negative group delay which are not expected in one-dimensional photonic crystals [Poi-2005].

c. Results in the time domain

The experimental setup is similar to the one proposed by Munday and Robertson [Mun-2002] and it is accurately described in Appendix C.3.1. The 500 kHz sinusoidal output of generator-1 is used to amplitude modulate the sinusoidal signal of generator-2. This produces a train of sinusoidally modulated wave packets with carrier frequencies (f_c) in the megahertz range and $2\mu\text{s}$ width that traverse the MZI and is recorded at the oscilloscope (Agilent DSO-6032A). The choice of the modulating frequency was a compromise between narrow-enough bandwidth to avoid pulse distortion, and large-enough bandwidth to get appreciable pulse delays in comparison to the pulse duration. This modulation frequency is only by $\approx 50 \text{ kHz}$ larger than

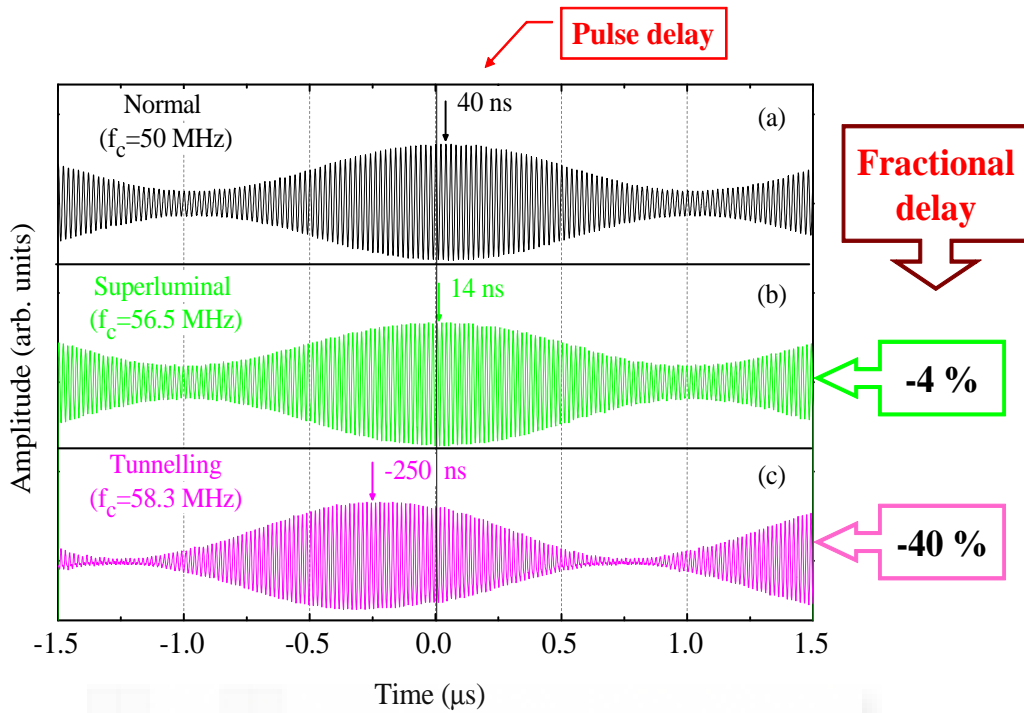


Figure 3.8: Wave-packet traces at the three different propagation regimes, with carrier frequencies (a) 50 MHz (normal), (b) 56.5 MHz (superluminal), and (c) 58.3 MHz (tunnelling). Each trace is normalized to its maximum amplitude.

$|\gamma|/2\pi$. Consequently, the side spectral components of the pulse lie only slightly beyond the FWHM of the Lorentzian group delay curve.

Figure 3.8 shows three wave-packet traces obtained at different carrier frequencies f_c . The size of the transmitted signal (10 V in amplitude) decreases sharply as the frequency approaches the transmission minima. Accordingly, the amplitudes have been rescaled to make the analysis easier to discuss. Since the signals were largely attenuated, a direct observation of the pulse peak on the oscilloscope was not accurate enough to measure the pulse delay. Hence, the pulse peak position was obtained from a numerical analysis of the data by finding the best fit to the pulse envelope.

The arrows in Fig. 3.8 indicate the time spent by the pulse center in propagating through the interferometer and it is explained in Appendix C.3.1. The τ_{pulse} values agree reasonably well with those found in the frequency-domain characterization. Fig. 3.8(a) shows the wave packet

at a carrier frequency of $f_c = 50$ MHz corresponding to the normal dispersion region in Fig. 3.6. This signal is delayed by 40 ns as expected from the group velocity of $0.67c$. This is also the time delay measured for this wave packet after propagating along a single coaxial cable of 8 m length, thus proving that the interferometer's effective length L is indeed the average length of the two interferometer arms. Fig. 3.8(b) shows the wave packet at a carrier frequency of $f_c = 56.5$ MHz corresponding to the superluminal region in Fig. 3.6. The amplitude of the signal was reduced to 4 V. The propagation time is reduced to 14 ± 6 ns denoting a superluminal group velocity of $1.9c \pm 0.8c$, close to the expected group velocity of $1.4c$. Fig. 3.8(c) shows the wave packet at a carrier frequency of $f_c = 58.3$ MHz and is advanced to negative values of τ_{pulse} . The amplitude of the signal was reduced to 1 V. Its center exits the MZI 250 ± 40 ns before the center of the input pulse has entered the structure, i.e., it tunnels through the interferometer with a negative group velocity of $-0.11c \pm 0.02c$, which is in good agreement with the expected group velocity ($-0.09c$). This counterintuitive effect is a direct result of the interference of the different frequency components and is not in conflict with relativistic causality [Moj-2000]. By considering the pulse duration T_{in} as the period of the modulating signal ($2\mu s$), the fractional advancement achieved is 0.12, the same value as the one reported with an erbium-doped optical fiber [Sch-2006]. The fractional delay FD obtained by taking T_{in} as the FWHM of the pulse power is indicated in the figure.

Let us now interpret this interesting tunnelling results in the framework of the model developed in section 3.2.4. For that purpose the pulse *power* traces are required. They are obtained by squaring the wave-packet traces shown in the previous figure. Figure 3.9 shows thus the experimental pulse power traces (normalized to their maximum value) and their fitted envelopes for carrier frequencies corresponding to the normal regime (panel (a)) and the tunnelling regime (panel (b)). As pointed earlier the pulse with $f_c = 50$ MHz propagates at the phase velocity and it is hence delayed by 40 ns. Since its propagation is equivalent to that of a pulse with $f_c = 58.3$ MHz traversing a coaxial cable of 8 m (the MZI effective length), we take the pulse in panel (a) as the reference (or input) pulse in our model. The envelopes fitting the experimental power captures have modulation index $M_{in} = 0.65$ (Fig. 3.9(a)) and $M_{out}^{exp} = 0.95 \pm 0.05$ (Fig.3.9(b)). Let us remark that because of the higher distortion of the tunnelled pulse (due to the sharp decrease of the transmitted signal at the minima) a rough error of ± 0.05 was estimated in its

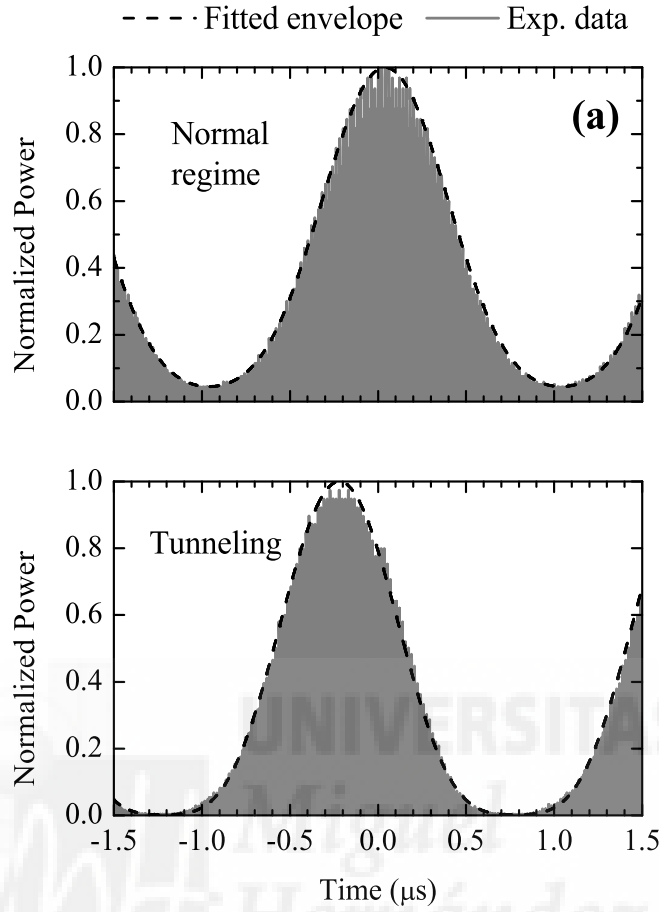


Figure 3.9: Experimental pulse power traces and their fitted envelopes for two different carrier frequencies (a) 50 MHz (normal regime), and (b) 58.3 MHz (tunnelling). Each trace is normalized to its maximum amplitude. The fitted envelopes have modulation index $M = 0.65$ (a) and $M = 0.95$ (b).

modulation index. Using the above values of the modulation index, the pulse duration (FWHM) for the reference and tunnelled pulse are $T_{in} = 835$ ns and $T_{out}^{exp} = 739.5 \pm 11.5$ ns.

In Table 3.5 the comparison between the model predictions and the experimental results for the following quantities of the tunnelled pulse is summarized: output modulation index M_{out} , pulse delay τ_{pulse} , fractional delay FD and compression factor b . The theoretical predictions were obtained using $\omega_m = 2\pi \times 500$ kHz and the model parameter $\gamma^{-1} = -357.14$ ns into Eq. (3.45), Eq. (3.46), Eq. (3.48) and Eq. (3.49), respectively. The experimental value of FD was obtained from Eq. (3.47) using $\tau_{pulse}^{exp} = -250 \pm 40$ ns since the error estimated in the pulse capture measurements of Fig. 3.8 is of ± 40 ns. The experimental figures of merit bear a good

Results	M_{out}	$\tau_{pulse}(ns)$	$ FD $	$b\%$
Experiment	0.95 ± 0.05	-250 ± 40	0.35 ± 0.05	11.4 ± 1.3
Theory	0.98	-228	0.32	12.2

Table 3.5: Comparison between the model predictions and the experimental results for the following quantities of the tunnelled pulse: pulse delay τ_{pulse} , output modulation index M_{out} , fractional delay FD and compression factor b .

agreement with the model predictions. Since the output modulation index is $M_{out} \leq 1$ (as a consequence of having $M_{in} = 0.65$) no peak breakup is observed, in accordance to the theory.

3.2.6 Simulation results in the optical range

The predictions of the model developed in the previous sections (3.2.1-3.2.4) are here illustrated through simulations on a MZI designed to operate in the optical range.

A silicon-based MZI of attenuation coefficient 6.5 dB/cm and refractive index $n = 3.48$ is considered. It is designed to have a fixed branch length difference $\Delta = 200 \mu m$ that sets the minima 430 GHz apart. Therefore, the model parameters take the values $\alpha\Delta = 0.015$ and $\gamma^{-1} = -155$ ps. The conditions summarized in Table 3.3 yield the range of values that the system's effective length L must take in order to sustain tunnelling, superluminal or normal group delay at the minima. Consequently, three such MZIs of the following lengths are considered: $L = 2$ mm (tunnelling), $L = 1.5$ cm (superluminal) and $L = 2$ cm (normal).

The transmission magnitude $|\hat{t}|$ and group delay τ_g of the three MZIs are calculated according to Eqs. (3.21a) and Eq. (3.26) in a frequency range of 450 GHz centered at the transmission minimum located at $f_{min} \approx 193$ THz; the results are plotted in Fig. 3.10(a). As L increases, the attenuation of the transmission spectra is stronger and the group delay curves are shifted upwards because of the positive contribution of a larger phase delay ($\tau_p = Ln/c$). The group delay value at f_{min} , namely $\tau_g \approx -131$ ps, 19 ps and, 77 ps, corresponds to tunnelling, superluminal and normal regime respectively, in agreement with the model predictions. For

each interferometer, the excess group delay curve, $\tau_g(f) - \tau_p$, fits excellently to a Lorentzian function of HWHM $|\gamma|/2\pi = 1$ GHz and -155 ps excess delay at the minimum.

Now, an optical pulse train travelling through each interferometer is numerically simulated. The optical carrier is tuned at $f_{min} \approx 193$ THz ($\lambda = 1.55\mu m$) and it is sinusoidally modulated with frequency $f_m = |\gamma|/2\pi$ and 100% modulation index to generate a train of pulses of width $T_{in} = 364$ ps at a repetition rate of 1 GHz. Fig. 3.10(b) shows the pulse traces corresponding to a propagation through the interferometers of $L = 2$ mm (pulse #1), $L = 1.5$ cm (pulse #2) and $L = 2$ cm (pulse #3). All traces were normalized to its peak value for an easier comparison.

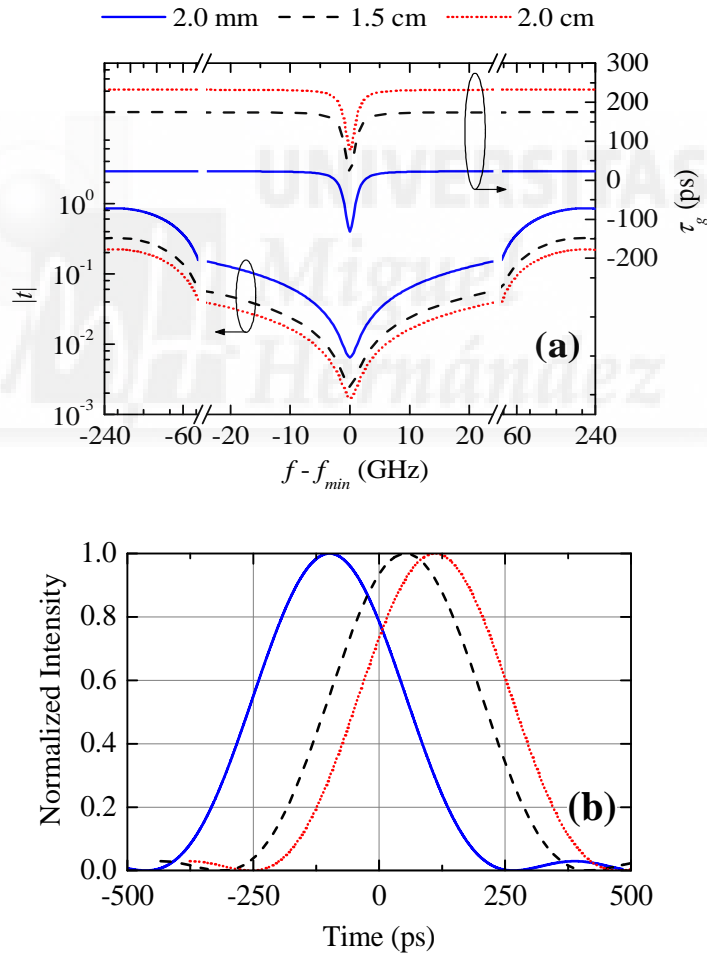


Figure 3.10: Numerical simulation of a Si-based MZI with parameters $\Delta = 200 \mu m$, $\alpha = 6.5$ dB/cm, and $n = 3.48$, for three values of the effective length: $L = 2$ mm (solid line), $L = 1.5$ cm (dashed line) and $L = 2$ cm (dotted line). (a) Magnitude of the transmission coefficient and group delay; (b) Normalized traces of pulses with carrier frequency tuned at f_{min} and transmitted through each interferometer. The incident pulse has its peak at $t = 0$.

The peak position of each envelope is the time that the pulse takes in travelling through the system, i.e. the pulse delay. These delays are, respectively, ≈ -98 ps, 52 ps and, 110 ps and they agree very well with the values predicted by Eq. (3.46). Since the incident pulse (not depicted) has its peak at $t = 0$; pulse #1 clearly tunnels through the system, pulse #2 propagates almost superluminally (superluminal delay should be less than $L/c = 50$ ps) whereas pulse #3 corresponds to a normal propagation. For the three pulses shown in the figure, a fractional delay $|FD| = 34\%$ was observed, in agreement with Eq. (3.48).

The case of pulse #2 is a neat example that Table 3.3 provides an *estimation* of the propagation regime for narrowband pulses tuned at the minima. The actual regime depends indeed on the pulse spectral width, as it is contained in Eq. (3.46) for τ_{pulse} . It was checked that by decreasing the modulation frequency slightly below 1 GHz, the resulting pulse does propagate superluminally through the MZI of $L = 1.5$ cm.

Figure 3.11 shows the normalized traces of two pulses transmitted through the shortest MZI ($L = 2$ mm) and tuned at two different frequencies: $f_{min} \approx 193$ THz (pulse #1) and the next transmission maximum $f_{max} = f_{min} + 215$ GHz. The phase delay of the system is $\tau_p = 23$ ps. Since the pulse with carrier frequency at f_{max} travels at the phase velocity, pulse #1 is advanced 122 ps with respect to it. A slight compression of pulse #1 is revealed by looking at the widths of both pulses. Such a compression also occurs for pulse #2 and pulse #3 shown in the previous figure. In the three cases a compression factor $b = 8\%$ is observed, in agreement with Eq. (3.49). In physical terms, this behaviour can be ascribed to spectral reshaping of the input pulse due to the transmission feature at the minimum. Namely, the center pulse frequency is transmitted with less intensity than its side components, thus causing spectral broadening and consequently, pulse shrinking in time. This situation has also been reported for fast light based on material resonances [Boy-2007].

Figure 3.11 also shows the pulse #1 breakup, with a discernible secondary peak at 388 ps and power amplitude of 2.9% of the main peak power amplitude, in excellent agreement with the predicted values given that $M_{out} = \sqrt{2}$.

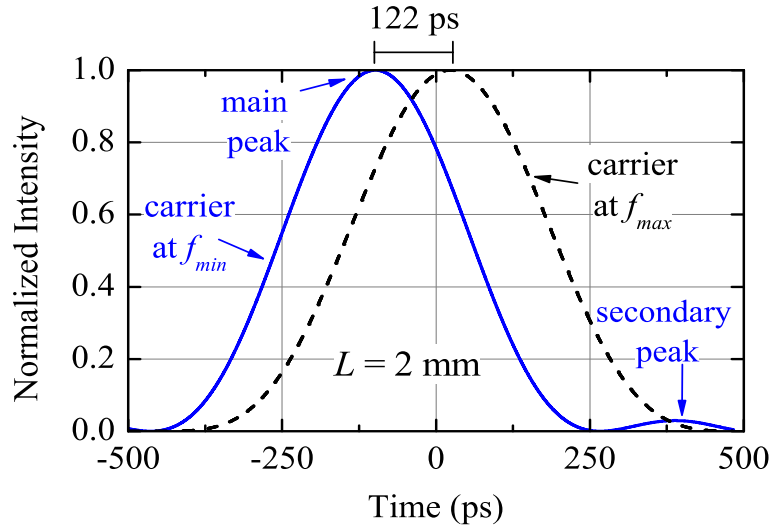


Figure 3.11: Normalized traces of pulses transmitted through the interferometer of $L = 2$ mm with two different carrier frequencies: tuned at f_{min} (solid line) and tuned at f_{max} (dashed line). The incident pulse has its peak at $t=0$.

It is worth emphasizing that the above numerical simulations regard an *ideal* waveguide silicon-based MZI. Real waveguide integrated interferometers usually have power imbalance on the nominal 3 dB couplers. Interestingly, power imbalance can play the role of total losses αL in changing the propagation regime, as it can be deduced from the results of [Cua-2008]. In that work, the author analyzes the performance of a MZI with variable power splitting ratios. The softening of the phase jump in the phase spectral function for splitting ratios detuning from 3 dB is similar to the effect of total losses.

3.3 Slow- and fast- light in three-beam interferometers

A model that describes fast light in a linear and *lossy asymmetric* MZI was presented in section 3.2, however, it was demonstrated that slow light cannot arise in this system. Slow light is particularly interesting since it improves the spectral sensitivity of interferometers [Shi-2007] and can enhance light-matter interaction and hence non-linear effects [Kra-2008].

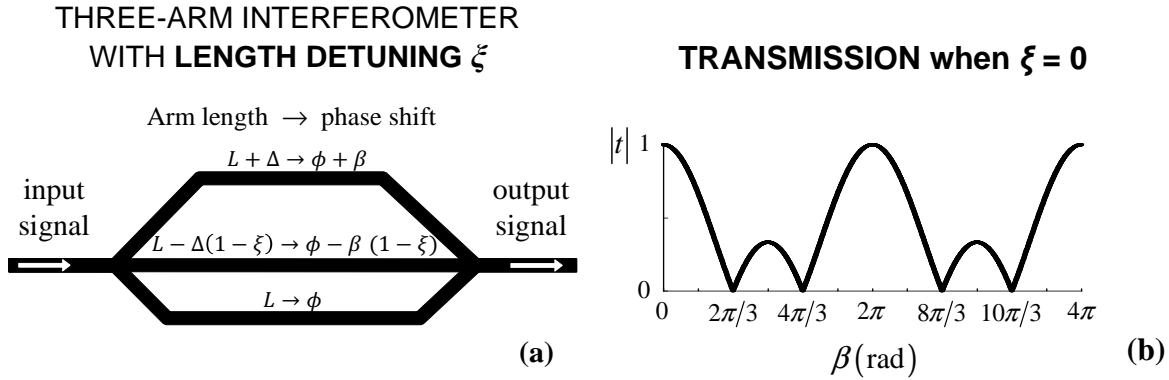


Figure 3.12: (a) Schematic of a lossless asymmetric three-arm interferometer and (b) its typical transmission spectrum.

Interestingly, the series loop structures studied by El Boudouti *et al.* in [Bou-2004] do present subluminal regime when defects are introduced. These structures may be regarded as MZIs (asymmetric loops) connected in series through segments. Like PBG systems, they exhibit bandgaps, and defect modes appear inside the transmission gaps if one of the segments connecting the loops is somehow changed (in length, for example). The situation resembles that of a doped photonic crystal, with superluminal propagation for a pulse with center frequency in the bandgap and subluminal propagation for a pulse with center frequency at the defect mode. But unlike photonic crystals, an outstanding characteristic of this serial loop structure is the existence of bandgaps in a totally homogeneous material, without the need of refractive index contrast (or impedance contrast, if the system operates in the RF range as it is the case in [Bou-2004]).

With the aim of generating not only fast light but also slow light in an asymmetric interferometer, we have explored another alternative. Instead of connecting in series several MZIs, we increase the number of arms of a single interferometer. We consider the simplest interferometer (least number of arms N) where a length detuning in a branch implies a change in the otherwise constant length difference between adjacent arms (Δ). Note that this condition holds only for $N \geq 3$. Subluminal propagation will be demonstrated to occur if the length of any of the interferometer's arms is changed in a very small fraction (ξ) of the nominal length difference Δ , otherwise the pulse propagation regime is tunnelling or superluminal.

Figure 3.12 illustrates the concept of a lossless asymmetric three-beam interferometer and shows its typical transmission spectrum. For each wave component, the length of each branch is defined as: $L_1 = L - \Delta(1 - \xi)$, $L_2 = L$ and $L_3 = L + \Delta$, which leads to a nominal length difference (Δ) between adjacent arms. A small length detuning ($\xi \ll 1$) in the first arm is introduced to explore the induced transitions in the pulse propagation regimes at the transmission minima (see Fig. 3.12(a)). The interference spectrum shows two minima between every pair of adjacent peaks. As it was discussed in section 3.1 (Eq. 3.9) and it is depicted in figure 3.12(b), for the lossless three-beam interferometer, the maxima lie at even multiples of π and the minima at $\beta_{0_1} = 2\pi(m + 1/3)$ and $\beta_{0_2} = 2\pi(m + 2/3)$.

The study goes along the steps followed for the MZI in the last section. An analytical expression of the transmission spectrum (magnitude and phase) and group delay of the three-arm interferometer as a function of frequency, attenuation and length detuning is developed. An approximate equation of the group delay at the minima is derived, and the allowed pulse propagation regimes are discussed. In particular, the critical length detuning needed to get slow light is deduced. The propagation of a sinusoidally modulated pulse through the system is modeled, and experiments in the RF range using coaxial cable three-beam interferometers are performed as a proof of model.

3.3.1 Analytical model

We consider a plane wave, with unit amplitude, impinging on a three-arm interferometer. A 1×3 splitter divides the wave in three equal components that travel along each arm and are recombined by a 3×1 coupler. The transmitted complex amplitude at the end of the interferometer is:

$$\hat{t} = \frac{1}{3} \sum_{i=1}^3 e^{j\hat{\phi}_i} \quad (3.52)$$

The complex phase along the i^{th} branch $\hat{\phi}_i$ that was defined in Eq. (3.2) is written as

$$\hat{\phi}_i = \frac{\omega}{v} L_i + j\alpha L_i \quad (3.53)$$

where ω is the frequency, v is the phase velocity in the medium of refractive index n , and L_i is the length of the specific branch. Once again, for simplicity, **the refractive index and the attenuation coefficient** through the medium, α , **is assumed to be constant and the same for all arms.**

The effective length of the three-arm interferometer is the average length of the branches since the field amplitude in all arms is the same, thus:

$$L_{eff} = \frac{L_1 + L_2 + L_3}{3} = L + \frac{\Delta\xi}{3} \quad (3.54)$$

where Δ is the nominal length difference between adjacent arms and ξ is a small length detuning ($\xi \ll 1$) that is introduced in the first arm to explore the induced transitions in the pulse propagation regimes at the transmission minima.

The magnitude and phase of the transmission coefficient can be expressed as:

$$|t| = e^{-\alpha L} \sqrt{Re^2 + Im^2} \quad (3.55a)$$

$$\phi_t = \frac{\beta L}{\Delta} + \arctan\left(\frac{Im}{Re}\right) \quad (3.55b)$$

where β is the phase associated to the physical length difference, Δ , i.e. $\beta = \omega\Delta/v$, and parameters Re and Im are related to the real and imaginary parts of the transmission coefficient and are given by:

$$Re = \frac{1}{3}[1 + e^{-\alpha\Delta} \cos(\beta) + e^{\alpha\Delta(1-\xi)} \cos(\beta(1-\xi))] \quad (3.56a)$$

$$Im = \frac{1}{3}[e^{-\alpha\Delta} \sin(\beta) - e^{\alpha\Delta(1-\xi)} \sin(\beta(1-\xi))] \quad (3.56b)$$

Let us note that the ω dependency of the above quantities is contained in β .

Following the usually adopted phase-time approach [Kit-2003, Nim-2003], the group delay is obtained from the frequency derivative of the transmission coefficient phase:

$$\tau_g = \frac{\partial \phi_t}{\partial \omega} = \frac{L}{v} + \frac{Re \frac{\partial Im}{\partial \omega} - Im \frac{\partial Re}{\partial \omega}}{Re^2 + Im^2} \quad (3.57)$$

Therefore, the exact expression of the group delay through the interferometer as a function of frequency (through β) and length detuning ξ is:

$$\begin{aligned} \frac{\tau_g}{\tau_p} &= 1 + \frac{\Delta}{L} \times \\ &\times \frac{e^{-2\alpha\Delta} - (1-\xi)e^{-2\alpha\Delta(1-\xi)} + e^{-\alpha\Delta} \cos \beta - (1-\xi)e^{\alpha\Delta(1-\xi)} \cos[\beta(1-\xi)] + \xi e^{-\alpha\Delta\xi} \cos[\beta(2-\xi)]}{1 + e^{-2\alpha\Delta} + e^{-2\alpha\Delta(1-\xi)} + 2e^{-\alpha\Delta} \cos \beta + 2e^{\alpha\Delta(1-\xi)} \cos[\beta(1-\xi)] + 2e^{-\alpha\Delta\xi} \cos[\beta(2-\xi)]} \end{aligned} \quad (3.58)$$

where the group delay has been normalized by $\tau_p = L/v$, that is, the phase delay in the medium over length L . Next, we analyze particular cases of attenuation and detuning.

a. Interferometer without detuning ($\xi = 0$)

Let us first consider the case where the length difference between adjacent arms is a constant ($\xi = 0$), and thus the interferometer effective length is $L_{eff} = L$.

a.1. Lossless media ($\alpha = 0$)

In this situation, $Re = (1 + 2 \cos \beta)/3$ and $Im = 0$. This implies that transmission minima are located where $\cos \beta = -1/2$, i. e., the first and second transmission minima after a principal maximum of order m lie at $\beta_{0_1} = 2\pi(m + 1/3)$ and $\beta_{0_2} = 2\pi(m + 2/3)$, respectively. From expression (3.58) it is then trivial to obtain the group delay at the minima as $\tau_g/\tau_p = 1$. The group delay is identical to the phase delay and, consequently, the group velocity equals the phase velocity. Therefore, a lossless interferometer with $\xi = 0$ cannot sustain anomalous propagation regimes. This is not surprising, since in a linear system with nothing altering the phase relation

between the pulse components, the pulse peak cannot be shifted and hence it travels at the phase speed.

a.2. Lossy media ($\alpha > 0$)

If we consider a certain level of losses ($\alpha > 0$), the transmission minima are located where:

$$\cos \beta = -\frac{\cosh(\alpha\Delta)}{2} \quad (3.59)$$

Taking this into account, the group delay at the transmission minima according to Eq. (3.58) will be:

$$\frac{\tau_g}{\tau_p} = 1 - \frac{\Delta}{L} \coth(\alpha\Delta) \quad (3.60)$$

As the \coth function is always positive for positive argument values, τ_g/τ_p is always smaller than 1 and, consequently, the system will never sustain subluminal regime. However, tunnelling and superluminal regimes can arise at the minima by properly choosing the interferometer effective length for a given attenuation coefficient.

Within the assumption of a good visibility of the interference pattern (see section 3.1), we consider small values of $\alpha\Delta$, for which the transmission minima can be taken to lie at $\beta_{1,2}^0$ and Eq. (3.60) can be approximated by:

$$\frac{\tau_g}{\tau_p} \approx \left(1 - \frac{1}{\alpha L}\right) \quad (3.61)$$

This is exactly the same expression encountered for a lossy MZI (see section 3.2.1 Eq. (3.28)), therefore it leads to the same propagation regimes at the transmission minima, which are summarized once again in Table 3.6.

As it was the case for the lossy MZI a proper change in the attenuation range (either by changing α and/or the interferometer's effective length L) changes the propagation regime at the transmission minima. This behaviour is illustrated by numerical simulations on an interferometer with refractive index $n = 1.5$. Figure 3.13 shows the transmission coefficient

Condition	$\alpha L < 1$	$1 < \alpha L < \frac{n}{n-1}$	$\alpha L > \frac{n}{n-1}$
$\alpha > 0$	Tunnelling	Superluminal	Normal

Table 3.6: Possible propagation regimes at the minima of a lossy three-beam interferometer without detuning ($\xi = 0$).

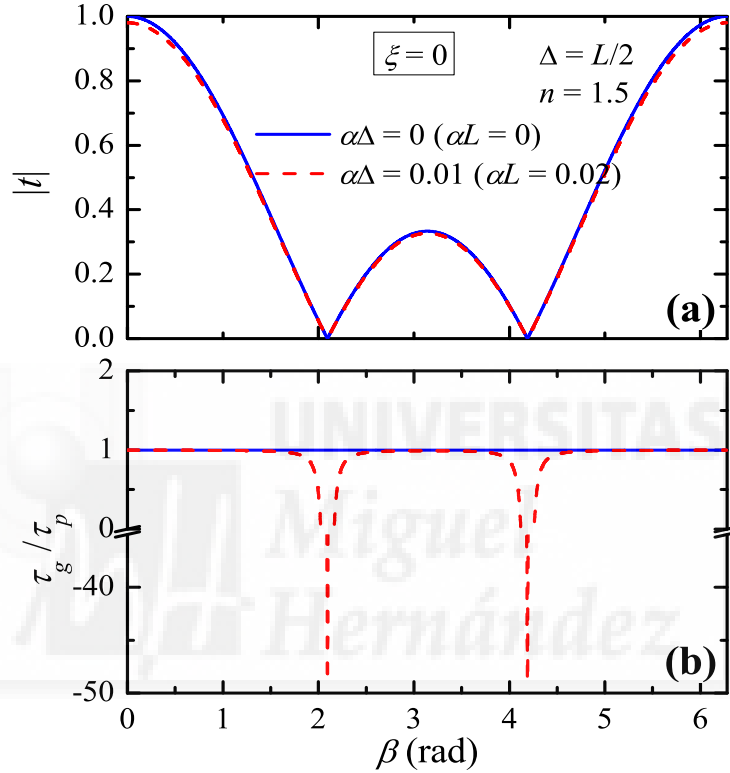


Figure 3.13: (a) Transmission coefficient magnitude and (b) group delay (Eq. (3.58)) in units of the phase delay through the medium of a three-beam interferometer with length difference between adjacent arms $\Delta = L/2$, length detuning $\xi = 0$ and refractive index $n = 1.5$, for two values of the attenuation coefficient α .

magnitude calculated using Eq. (3.55a) and the group delay obtained from Eq. (3.58), for two attenuation values and $\Delta = L/2$. The transmission curve $|t|$ displays the typical three-beam interference pattern, with principal peaks at $\beta = 2\pi m$ (m is the order of the peak) and two minima located in between [Dav-2006]. In agreement with our previous discussion, no abnormal propagation regimes occur in the lossless interferometer, while in the case of losses with $\alpha\Delta = 0.01$, tunnelling appears around the two minima and negative group delays of almost $-50\tau_p$ can be reached.

The evolution of the pulse propagation regime at the minima, as a function of the total system's attenuation $\alpha\Delta$ was described in Fig. 3.4 for a MZI. For the three-beam interferometer we obtain the same evolution. Hence, the total attenuation in the system determines the pulse propagation regime. Fast light is achieved with small enough attenuation while it disappears if it is either too high ($\alpha L > n/(n-1)$) or zero.

b. Interferometer with detuning ($\xi \neq 0$)

We now consider the case where a small length detuning ($\xi \ll 1$) is introduced in the first branch of the interferometer. If $\alpha\Delta$ and $|\xi|$ are small, it can be shown that the transmission minima move with ξ according to:

$$\beta_{1,2} \approx \beta_{0,2} \left(1 + \frac{\xi}{2} \right), \quad (3.62)$$

where $\beta_{0,2}$ corresponds to the first and second minima when $\xi = 0$ and $\alpha = 0$, given in Eq. (3.9)

It should be remarked that the position of the minima changes with attenuation, as opposed to the situation in a MZI.

b.1. Lossless media ($\alpha = 0$)

In a lossless medium, following Eq. (3.58), the group delay at the first and second transmission minima can be approximated by:

$$\frac{\tau_{g1}}{\tau_p} \approx 1 - \frac{\Delta}{L} \frac{2\sqrt{3}}{\xi\beta_{01}}, \quad (3.63a)$$

$$\frac{\tau_{g2}}{\tau_p} \approx 1 + \frac{\Delta}{L} \frac{2\sqrt{3}}{\xi\beta_{02}}, \quad (3.63b)$$

respectively. Consequently, by setting $\xi \neq 0$, one can always obtain slow light at one of the minima. More specifically, these are the possible cases: i) If $\xi < 0$, the system sustains

slow light at the 1st minimum. At the 2nd minimum, the possible pulse propagation regime is tunnelling if

$$L < -\frac{2\sqrt{3}}{\beta_{0_2}\xi}\Delta, \quad (3.64)$$

and superluminal ($0 < \tau_g < L_{\text{eff}}/c$) if

$$-\frac{2\sqrt{3}}{\beta_{0_2}\xi}\Delta < L < -\left(\frac{n}{n-1}\right)\frac{2\sqrt{3}}{\beta_{0_2}\xi}\Delta, \quad (3.65)$$

Otherwise, only normal propagation will be possible at the 2nd minimum.

ii) If $\xi > 0$, slow light occurs at the 2nd minimum, whereas at the 1st minimum, the system will sustain tunnelling if

$$L < \frac{2\sqrt{3}}{\beta_{0_1}\xi}\Delta, \quad (3.66)$$

and superluminal propagation if

$$\frac{2\sqrt{3}}{\beta_{0_1}\xi}\Delta < L < \left(\frac{n}{n-1}\right)\frac{2\sqrt{3}}{\beta_{0_1}\xi}\Delta, \quad (3.67)$$

Otherwise, only normal propagation occurs at the 1st minimum. The above expressions set restrictions on the length L of the second branch, which is very close, but not equal, to the system's effective length (see Eq. (3.54)).

This behaviour is observed in Fig. 3.14, for a three-arm interferometer where its first branch has been increased or decreased according to $\xi = \pm 5\%$. Exact expression (3.58) was used to simulate the group delay as a function of β in a system with $\Delta = L/2$ and refractive index $n = 1.5$. The transmission's minima shift with ξ is manifest in the group delay curves. According to the approximation in Eq. (3.63), for a detuning of +5%, the group delay should be $-15.5\tau_p$ and $9.3\tau_p$ at the first and second minima of zero-order, respectively. Whereas if $\xi = -5\%$, the expected group delay at the zero-order first and second minimum is $17.5\tau_p$ and $-7.3\tau_p$, respectively. These approximate values of the group delay at the minima are in excellent agreement with the exact results shown in the figure.

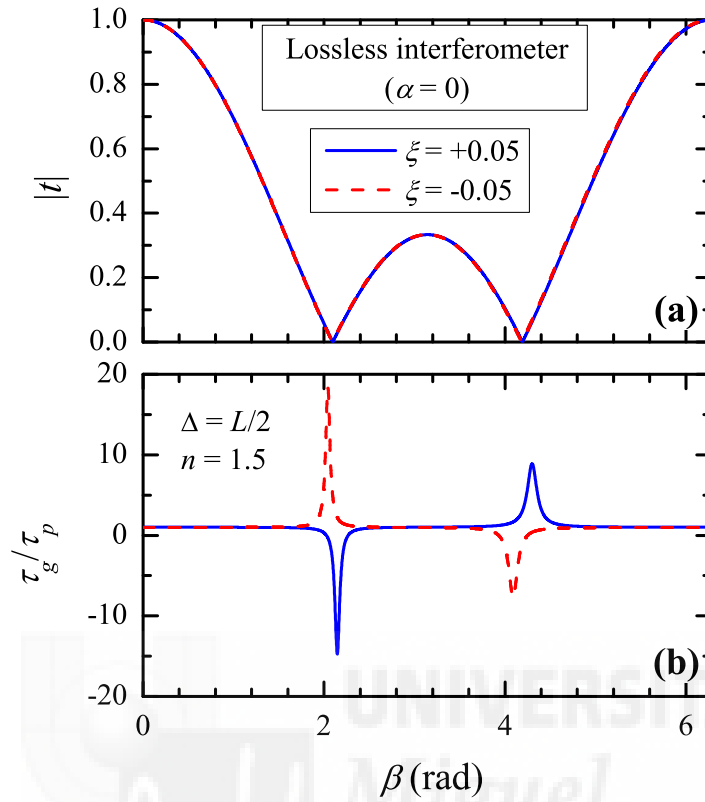


Figure 3.14: (a) Transmission coefficient magnitude and (b) group delay of a lossless three-beam interferometer with nominal length difference between adjacent arms $\Delta = L/2$ and refractive index $n = 1.5$, for two values of length detuning ξ .

b.2. Lossy media ($\alpha > 0$)

In the most general case, where both detuning and a certain attenuation level are considered, and under the conditions of small $\alpha\Delta$ and $|\xi|$, Eq. (3.58) can be approximated at the transmission minima as:

$$\frac{\tau_{g1}}{\tau_p} \approx 1 - \frac{\Delta}{L} \frac{2\sqrt{3}}{\beta_{01}(\xi - \xi_{c1})}, \quad (3.68a)$$

$$\frac{\tau_{g2}}{\tau_p} \approx 1 + \frac{\Delta}{L} \frac{2\sqrt{3}}{\beta_{02}(\xi - \xi_{c2})}, \quad (3.68b)$$

Condition	Regime @ 1 st min	Regime @ 2 nd min
$\xi < \xi_{c1}$	Slow	Tun/Super/Normal
$\xi_{c1} < \xi < \xi_{c2}$	Tun/Super/Normal	Tun/Super/Normal
$\xi > \xi_{c2}$	Tun/Super/Normal	Slow

Table 3.7: Possible propagation regimes at the transmission minima of a lossy three-beam interferometer.

where the critical detuning lengths ξ_{c1} and ξ_{c2} are approximately:

$$\xi_{c1} = -\frac{2\sqrt{3}\alpha\Delta}{\beta_{01}}, \quad (3.69a)$$

$$\xi_{c2} = +\frac{2\sqrt{3}\alpha\Delta}{\beta_{02}}, \quad (3.69b)$$

For lossless media, $\xi_{c1} = \xi_{c2} = 0$ and Eqs. (3.68) reduce to Eqs. (3.63); thus recovering the situation discussed before. The role of the attenuation is then to increase the magnitude of the critical detuning needed to obtain slow light at the minima. Table 3.7 summarizes the possible propagation regimes at both minima. If $\xi < \xi_{c1}$, the system only sustains slow light at the 1st minimum. If $\xi > \xi_{c2}$, the system only sustains slow light at the 2nd minimum. For $\xi_{c1} < \xi < \xi_{c2}$ the allowed pulse propagation regimes at the minima can be either tunnelling, superluminal or normal, depending on the length L .

Table 3.8 summarizes the possible propagation regimes at the 1st minimum. If $\xi > \xi_{c2}$ there is a maximum value of L to obtain tunnelling at the 1st minimum:

$$L_{t1} = \left(\alpha + \frac{\beta_{01}\xi}{2\sqrt{3}\Delta} \right)^{-1} \quad (3.70)$$

For lengths L greater than L_{t1} and smaller than $\left(\frac{n}{n-1}\right)L_{t1}$, superluminal propagation is sustained at the 1st minimum. Finally, when L exceeds the value $\left(\frac{n}{n-1}\right)L_{t1}$ the normal regime is attained.

Condition	$L < L_{t1}$	$L_{t1} < L < \left(\frac{n}{n-1}\right) L_{t1}$	$L > \left(\frac{n}{n-1}\right) L_{t1}$
$\xi < \xi_{c1}$	Slow	Slow	Slow
$\xi > \xi_{c1}$	Tun	Super	Normal

Table 3.8: Possible propagation regimes at the 1st transmission minimum of a lossy three-beam interferometer.

Condition	$L < L_{t2}$	$L_{t2} < L < \left(\frac{n}{n-1}\right) L_{t2}$	$L > \left(\frac{n}{n-1}\right) L_{t2}$
$\xi < \xi_{c2}$	Tun	Super	Normal
$\xi > \xi_{c2}$	Slow	Slow	Slow

Table 3.9: Possible propagation regimes at the 2nd transmission minimum of a lossy three-beam interferometer.

Similarly, the possible propagation regimes at the 2nd minimum are shown in Table 3.9. For $\xi < \xi_{c2}$ there is a maximum value of L to get tunnelling at the 2nd minimum:

$$L_{t2} = \left(\alpha - \frac{\beta_{02}\xi}{2\sqrt{3}\Delta} \right)^{-1} \quad (3.71)$$

For lengths greater than L_{t2} and smaller than $\left(\frac{n}{n-1}\right) L_{t2}$, superluminal propagation occurs at the 2nd minimum. Once again, when L exceeds the value $\left(\frac{n}{n-1}\right) L_{t2}$ the normal regime is attained. In the case $\xi = 0$, lengths $L_{t1} = L_{t2} = 1/\alpha$, and the conditions for a lossy interferometer with a constant length difference Δ between adjacent branches are recovered. Let us remark that, as opposed to that case, Δ does now influence the conditions that determine the propagation regime.

We have checked the validity of the approximated Eqs. (3.68) and (3.69) for estimating the group delay at the transmission minima. The approximated value has been compared with the exact result obtained from Eq. (3.58), as a function of the detuning ξ and for an attenuation level of $\alpha\Delta = 0.01$. The results in Fig. 3.15 reveal the following features: i) the agreement between the approximated and the exact value of τ_g is excellent for ξ up to $\pm 5\%$; ii) the group delay increases in magnitude as the detuning approaches the critical value; and iii) the SFL transition

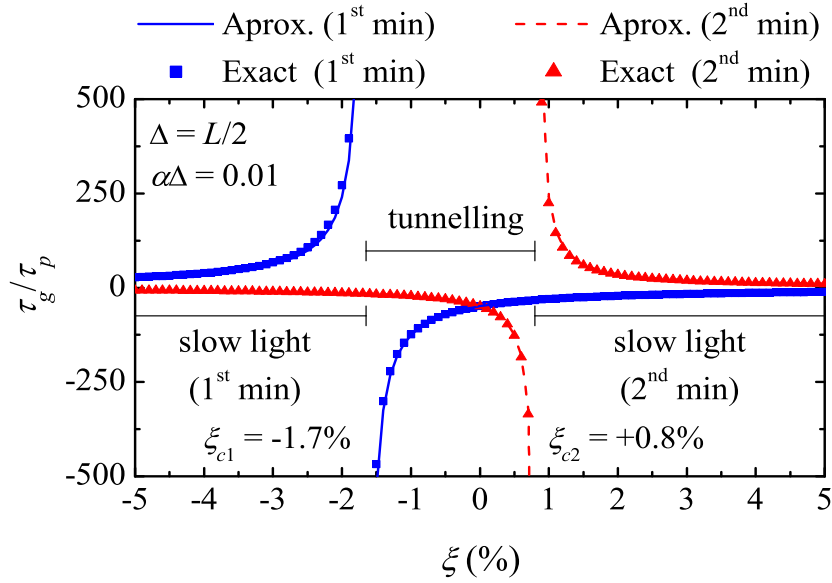


Figure 3.15: Dependence with length detuning of the group delay at the minima for a three-beam interferometer with nominal length difference between adjacent arms $\Delta = L/2$ and attenuation $\alpha\Delta = 0.01$. The approach in Eqs. (3.68) (line) is compared to the exact result of Eq. (3.58) (symbols) for each minima.

when reaching the critical detuning is extremely abrupt. Namely, the absolute value of τ_g at each minimum approaches infinity when the length detuning equals exactly the corresponding ξ_c . This behaviour is understood from Eqs. (3.55)–(3.57): for a given $\alpha\Delta$ value, the critical detuning is the one that makes $Re^2 + Im^2 = 0$ at the corresponding minimum. Therefore, this abrupt SFL transition is achieved through a passage from a zero transmission condition. We would like to draw the attention here to the similarity of this mechanism with that reported by Longhi in active fiber Bragg gratings with asymmetric profile [Lon-2005]. In that work, an abrupt superluminal to subluminal transition of reflected pulses near to a local minimum of the reflection spectrum was achieved by increasing the gain level.

3.3.2 Analysis considering the optical path difference

Similarly to the analysis performed in section 3.2.2 for the MZI, one can generalize the situation and consider a three-beam interferometer where both the length and/or the refraction index of the branches are different. The attenuation coefficient, α , is considered to be constant and equal

in every arm. The optical path in the i^{th} arm is $\ell_i = n_i L_i$ with the branch lengths defined as in Fig. 3.12(a), namely: $L_1 = L - \Delta(1 - \xi)$, $L_2 = L$ and $L_3 = L + \Delta$ but where now the refractive index in each arm is:

$$\begin{aligned} n_1 &= n - \Delta_n(1 - \xi_n) \\ n_2 &= n \\ n_3 &= n + \Delta_n \end{aligned} \tag{3.72}$$

with Δ_n being the nominal refractive index difference between adjacent branches and ξ_n a small detuning from the nominal refractive index value.

The effective optical path, $\ell_{\text{eff}} = (\ell_1 + \ell_2 + \ell_3)/3$, can be written in terms of the effective refractive index $n = (n_1 + n_2 + n_3)/3$, the nominal refractive index difference Δ_n , and the length and index detuning (ξ and ξ_n) as:

$$\ell_{\text{eff}} = nL + \frac{n_1 \xi}{3} \Delta + \frac{\Delta_n(2 - \xi_n)}{3} \Delta \tag{3.73}$$

An optical path difference occurs if the branches differ in length ($\Delta \neq 0$) and/or if their refractive index is different ($\Delta_n \neq 0$). For the sake of simplicity, we will consider each cause separately.

a. Δ -induced fringe pattern ($\Delta_n = 0$, $\Delta \neq 0$)

This is the situation analyzed in subsection 3.3.1, and here we will simply remark the main conclusion. The interference pattern is due to the different length of the branches. Let us draw attention to the fact that by adding one branch we are increasing a key degree of freedom of the three-beam interferometer that is not present in the MZI, namely, the possibility of detuning the nominal length difference between a pair of adjacent branches with respect to its nominal value Δ . It is the situation previously analyzed, where it is this detuning, ξ , what makes slow light arise in the three-beam interferometer. Such a fast to slow light transition occurs by the passage

through zero transmission ($|\hat{t}| = 0$) at one of the minima. The length detuning provides the degree of freedom necessary to completely cancel the transmission at a given frequency and for a given attenuation coefficient. Let us emphasize that this structural transition cannot be driven solely by the attenuation, which takes the transmission at the minima away from zero. This is why the MZI, where no length detuning is possible, does not sustain slow light.

It is straightforward to find that in this case, the effective optical path in Eq. (3.73) is the effective physical path $L_{eff} = (L_1 + L_2 + L_3)/3 = L + \Delta\xi/3$ multiplied by the (common) refractive index.

b. Δ_n -induced fringe pattern ($\Delta_n \neq 0, \Delta = 0$)

The branches are of the same length L and the interference pattern arises because of their different refractive index. Unlike the previous case, here, the effective optical path is the effective refractive index times the (common) branch length, $\ell_{eff} = nL = (n + \Delta_n\xi_n/3)L$.

It is straightforward to see from Eq. (3.5) (setting $\Delta = 0$) that the attenuation plays no role on the phase of the transmission coefficient but only on its magnitude, and hence has no influence on the group delay. Moreover, for a constant Δ_n between adjacent branches, the analysis is similar to a MZI in subsection 3.2.2, i.e., the symmetric three-beam interferometer with constant refractive index difference exhibits zero transmission minima and does not sustain slow nor fast light.

On the other hand, if Δ_n is not constant between adjacent branches ($\xi_n \neq 0$), no analytic derivation is necessary. One can readily foresee (based on our previous study of the asymmetric three-beam interferometer with length detuning) that **slow and fast light will indeed arise in the symmetric three-beam interferometer if a detuning ξ_n from the otherwise constant refractive index difference is introduced**. The reason is that ξ_n provides the degree of freedom necessary to make the complex transmission coefficient go through zero, thus changing the sign of its phase. For lossless systems ($\alpha = 0$) one expects to get analogous results in the symmetric and in the asymmetric interferometer, i.e. equivalent expressions of the critical index detuning and critical length detuning to yield slow or fast light at each minima. For lossy systems ($\alpha \neq 0$)

the attenuation plays no role whatsoever in the symmetric interferometer: the waves travelling along each branch reach the end equally attenuated, their interference is governed only by the real part of the complex phase $\hat{\phi}_i = (\omega/c)n_iL + j\alpha L$, and hence the critical index detuning does not depend on α . In the asymmetric interferometer, however, the attenuation does affect the critical length detuning, as it was discussed in section 3.3.1 (see Eqs. (3.69)).

Therefore, in the symmetric three-beam interferometer (lossless or lossy), expressions (3.63) for the group delay at the 1st and 2nd transmission minima can be rewritten as:

$$\frac{\tau_{g1}}{\tau_p} \approx 1 - \frac{\Delta_n}{n} \frac{2\sqrt{3}}{\xi_n \beta_{01}}, \quad (3.74a)$$

$$\frac{\tau_{g2}}{\tau_p} \approx 1 + \frac{\Delta_n}{n} \frac{2\sqrt{3}}{\xi_n \beta_{02}}, \quad (3.74b)$$

with β being the phase associated to the refractive index difference ($\beta = \omega\Delta_n L/c$) and $\tau_p = \frac{Ln}{c}$.

The propagation regimes described by Eqs. (3.64) and (3.66) are valid with the substitution:

$$L \Rightarrow n \quad (3.75a)$$

$$\Delta \Rightarrow \Delta_n \quad (3.75b)$$

$$\xi \Rightarrow \xi_n \quad (3.75c)$$

3.3.3 Transmission coefficient and group delay around the transmission minima

In the previous sections two requirements in order to get both slow and fast light in three-beam interferometer were assessed: (i) the interferometer must be symmetric (equal branch lengths) with a detuning from the nominal refractive index difference between adjacent branches; (ii) it must be asymmetric (different branch lengths) with a length detuning in one of the branches.

Because proof-of-model experiments can be readily performed for situation (ii), only this case will be considered onwards.

The scope of this section is to derive approximate analytical expressions of the magnitude and phase of the transmission coefficient ($|\hat{t}(\omega)$ and $\phi(\omega)$), and of the group delay, $\tau_g(\omega)$ valid for frequencies close to a transmission minimum of asymmetric three-beam interferometers. The expressions obtained will be used in the next section to analyze the propagation of sinusoidally modulated signals through this system.

For lossless media and in the case where the length difference between adjacent arms is a constant ($\xi = 0$), the first and second transmission minima after a principal maximum of order m lie at $\omega_{0_1} = (2\pi v/\Delta)(m+1/3)$ and $\omega_{0_2} = (2\pi v/\Delta)(m+2/3)$, respectively. In the general case, under certain conditions of small $\alpha\Delta$ and $|\xi|$, the transmission minima move with ξ according to $\omega_{1,2} \approx \omega_{0_{1,2}}(1 + \xi/2)$ and the transmission coefficient magnitude and phase (Eq. (3.55)) can be approximated around each transmission minimum, ω_{min} , as:

$$|\hat{t}(\omega)| \approx \frac{e^{-\alpha L}}{\sqrt{3}} \frac{\Delta}{v} \left[1 \mp \frac{1}{2\sqrt{3}} \frac{\Delta}{v} (\omega - \omega_{min}) \right] \sqrt{(\omega - \omega_{min})^2 + \gamma^2}, \quad (3.76a)$$

$$\phi_t(\omega) \approx \omega\tau_p + \arctan\left(\frac{\omega - \omega_{min}}{\gamma}\right) + \frac{\pi}{2} \quad (3.76b)$$

where the $-$ and $+$ signs apply to the first and second minimum, and parameters γ are

$$\gamma_1 \approx -\frac{\omega_{0_1}(\xi - \xi_{c1})}{2\sqrt{3}}, \text{ and } \gamma_2 \approx +\frac{\omega_{0_2}(\xi - \xi_{c2})}{2\sqrt{3}} \quad (3.77)$$

for the first and second minimum, respectively. Here, we have introduced the critical detuning lengths, ξ_{c1} and ξ_{c2} defined in Eq. (3.69) but now expressed in terms of the frequency:

$$\xi_{c1} = -\frac{2\sqrt{3}\alpha c}{\omega_{01} n}, \text{ and } \xi_{c2} = +\frac{2\sqrt{3}\alpha c}{\omega_{02} n}, \quad (3.78)$$

By differentiation of Eq. (3.76b), the group delay can be approximated in the vicinity of each transmission minimum as a Lorentzian function with half-width at half-maximum that equals $|\gamma|$:

$$\tau_g(\omega) \approx \tau_p + \frac{\gamma}{(\omega - \omega_{min})^2 + \gamma^2}, \quad (3.79)$$

The group delay at the considered minimum is then given by $\tau_p + 1/\gamma$ and increases in magnitude as the detuning approaches the critical value. The SFL transition when reaching the critical detuning is extremely abrupt. Namely, the absolute value of τ_g at each minimum approaches infinity when the length detuning equals exactly the corresponding ξ_c . For a given $\alpha\Delta$ value, the critical detuning is the one that makes $|t| = 0$ at the corresponding minimum. Therefore, this abrupt SFL transition is achieved through a passage from a zero transmission condition.

Note that the sign of parameter γ at each minimum and, consequently, the positive or negative delay at the minimum, is in agreement with the propagation regimes discussed in section 3.3.1 and summarized in Tables 3.8 and 3.9. Let's remark too that if zero length detuning ($\xi = 0$) is considered, Eqs. (3.77) and (3.78) lead to $\gamma_1 = \gamma_2 = -\alpha v$ which is the result obtained in the case of the MZI, thus showing the equivalency between the three-beam interferometer with constant length difference and the MZI, where only fast light is sustained.

3.3.4 Propagation of sinusoidally modulated signals

As it was performed for the MZI (see section 3.2.4), we consider an incident sinusoidally modulated wave-packet with carrier frequency at a transmission minimum, ω_{min} and modulation index M_{in} . Such a signal has spectral components at ω_{min} , $(\omega_{min} - \omega_m)$, and $(\omega_{min} + \omega_m)$, being ω_m the modulation frequency, and the amplitude of the central frequency

is twice that of the side bands. The module of the incident field envelope is $E_{in}(t) \propto 1 + M_{in} \cos(\omega_m t)$.

Applying Fourier theory and proceeding like in section 3.2.4, one can obtain the module of the field envelope of the transmitted signal through the interferometer:

$$E_{out}(t) \propto 1 + M_{out} \cos[\omega_m(t - \tau_{pulse})] \quad (3.80)$$

where $M_{out} = M_{in} \sqrt{1 + (\omega_m/\gamma)^2}$ and the pulse delay, τ_{pulse} , depends on the modulation frequency through the following equation:

$$\tau_{pulse} = \tau_p + \frac{1}{\omega_m} \arctan\left(\frac{\omega_m}{\gamma}\right) \quad (3.81)$$

As one might expect, Eq. (3.81) reduces to $\tau_p + 1/\gamma$ when $\omega_m \rightarrow 0$, where γ is γ_1 or γ_2 defined in Eq. (3.77) depending on which minimum the sinusoidal pulse is centered.

Figures of merit

The analysis of the propagation of a sinusoidally modulated pulse through the three-beam interferometer leads to formally the same results as those obtained for the MZI with the only difference in the definition of γ_1 and γ_2 . But this difference is crucial since now, instead of having a single and negative parameter γ that always leads to fast regime, there are two parameters, γ_1 and γ_2 , of opposite signs for a certain range of detuning values ξ . As a consequence, slow light can be held at one minimum while fast light is held at the other minimum. Therefore, the evolution of the fractional delay (FD) (its absolute value) and pulse compression (b) versus normalized modulation frequency for a sinusoidally modulated pulse with carrier frequency tuned at one of the transmission minima are exactly the same as those presented in section 3.2.4 for the MZI (see Fig. 3.5).

As described in section 3.2.4, the absolute FD values increases with modulation frequency (see Eq. (3.48)) and values greater than $\pm 35\%$ can be obtained for modulation frequencies greater than γ . However, pulse distortion also increases with ω_m . As M_{out} is always greater than 100%,

the transmitted pulses suffer certain distortion. Therefore, either pulse delay or advancement is accompanied by a certain degree of pulse compression, defined in Eq. (3.49). The above features are entirely applicable to three-arm interferometers operating in any frequency range.

Since the pulse delay (or advancement) will only be effective for signals centered at the transmission minima and with spectral components within the Lorentzian function in Eq. (3.79), the product $[\tau_g - \tau_p] \times \gamma = 1$ gives an estimation of the maximum delay-bandwidth product (DBP) achieved by this system for any frequency range the interferometer may operate. As it was the case for the MZI, a more realistic estimation should consider the pulse delay in Eq. (3.81) (not the group delay), which yields an expected DBP of $(\tau_{pulse} - \tau_p \times 2f_m = 25\%)$.

3.3.5 Experimental results and discussion in the RF range

A proof-of-model experiment based on coaxial-cable three-beam interferometers is designed. The experimental setup and fabricated RF interferometers are presented. Frequency and time-domain measurements were performed on these systems and are compared to the model predictions.

a. Interferometer design

We have designed a nominal interferometer consisting of a 1×3 RF power splitter, a 3×1 RF coupler (both PE2002, Pasternack) and three coaxial cables (50Ω , RG-58C/U). The designed effective length of the system is 2 m and the intended length difference between adjacent cables is 1 m. In practice, every branch of the interferometer comprises the cable itself, the connectors between cable and splitters, and a small track inside the splitters. After measuring all these elements, the actual branch lengths of the starting interferometer were found to be $L_1 = 1.049$ m, $L_2 = 2.066$ m, and $L_3 = 3.088$ m, yielding $\Delta = 1.022$ m, and $\xi = +0.5\%$, according to our definitions in Fig. 3.12(b). In addition, four coaxial cables were prepared to substitute the L_1 cable of the starting interferometer. The actual first arm lengths are 0.989, 1.008, 1.086

and 1.103 m. Therefore, we have five interferometers to be characterized in frequency and time domain, each with $\Delta = 1.022$ m, and a set of values for ξ of -5.4% , -3.5% , $+0.5\%$, $+4.1\%$, and $+5.8\%$. This set of ξ values allows checking the evolution from fast to slow light at the minima as L_1 varies.

All the cables available for the branches were cut out of the same long coaxial cable whose attenuation coefficient as a function of frequency, $\alpha(\omega)$, had been previously determined as explained in Appendix B. Note that in order to estimate the critical length detuning through Eq. (3.78), the system's attenuation must be known so that we could prepare the cables with adequate values of ξ to display the SFL transition. From the characterization of $\alpha(\omega)$ we obtained an attenuation of $\alpha = 0.015$ Np/m (0.13 dB/m) at 65.2 MHz (first transmission minimum of the nominal interferometer) and $\alpha = 0.022$ Np/m (0.19 dB/m) at 130.4 MHz (second transmission minimum of the nominal interferometer). These attenuation values yield a critical length detuning of $\xi_{c1} = -2.5\%$ and $\xi_{c2} = +1.9\%$ for the first and second minimum, respectively. The characteristics of the fabricated RF three-beam interferometers are summarized in Table 3.10.

The frequency characterization of these interferometers was performed by means of a two-port vector network analyzer (PNA series, Agilent E8363B) (see Appendix C.1). The scattering parameter S_{21} (the transmission coefficient) was recorded in the 10-200 MHz range every 59.375 kHz with an average of 64 to help suppress the random noise. The splitters were also fully characterized and this measurement was used to correct the interferometer experimental response for a proper comparison with simulation, which does not include the effect of the splitters. The two splitters directly interconnected introduce an overall group delay of 1.8 ns and an attenuation of 1 dB, approximately, in the transmission response.

The experimental data contain a small amount of noise which is not very apparent in the S_{21} parameter itself. To obtain the experimental group delay, the phase data curve is differentiated and this amplifies the noise leading to spurious effects. For this reason, the network analyzer was configured to smooth the phase curve by averaging 17 adjacent points. The selected averaging algorithm preserves the key features of the group delay at the transmission minima.

Interferometer	$L_1(\text{m})$	$\xi(\%)$
L1-99	0.989	-5.4
L1-101	1.008	-3.5
L1-105	1.049	+0.5
L1-109	1.086	+4.1
L1-110	1.103	+5.8

Table 3.10: Fabricated three-beam RF interferometers with $L = 2.066$ m, $\Delta = 1.022$ m.

Additionally, time-domain pulse propagation experiments were performed on each interferometer (see Appendix C.3.1). The sinusoidal signal of generator-2 (IntraAction VFE-604A4), whose frequency can be varied between 40-80 MHz, was 100% amplitude modulated by the 300 kHz sinusoidal output of generator-1 (Tektronix CFG-253). This produces a train of sinusoidally modulated wave packets with 300 kHz repetition rate and carrier frequencies in the MHz range. The pulse train transmitted through the interferometer was recorded at the oscilloscope (Agilent DSO-6032A) with a resolution of 0.5 ns (10 kSamples/5000 ns).

b. Results in the frequency domain

Figures 3.16 and 3.17 show the transmission (magnitude $|t|$ and phase ϕ_t) and group delay (τ_g), of our five three-beam RF interferometers whose parameters are summarized in Table 3.10. Experimental and simulation results are shown. Namely, we include two experimental curves. One corresponds to the whole system measured with the vector network analyzer (labeled *uncorrected experimental data*) –including the splitters–, while the other (labeled *corrected experimental data*) is the result of subtracting the effect of the splitters. For each interferometer, the simulated $|t|$ and ϕ_t curves were obtained from Eqs. (3.52) and (3.53), by numerically calculating the interference of three sinusoidal RF waves propagating through coaxial cables of the lengths given in Table 3.10, including the frequency-dependent attenuation in the cables shown in Appendix B.1. The τ_g curves were obtained by differentiating the corresponding

numerical phase curve with respect to the frequency. The same 17-point smoothing algorithm as that applied to the measured τ_g curve was used for the simulated group delay. The agreement between simulations and the corrected experimental results is very good, thus assessing the accuracy of the procedure employed to subtract the effect of the splitters. From the figures, it is obvious that the splitters introduce losses (the peaks in transmission are less pronounced for the raw data) and also they add an additional phase (the raw data phase function is above the numerical one). Their effect on the group delay is hardly noticeable, for this reason only the corrected experimental τ_g curve is shown in the figures.

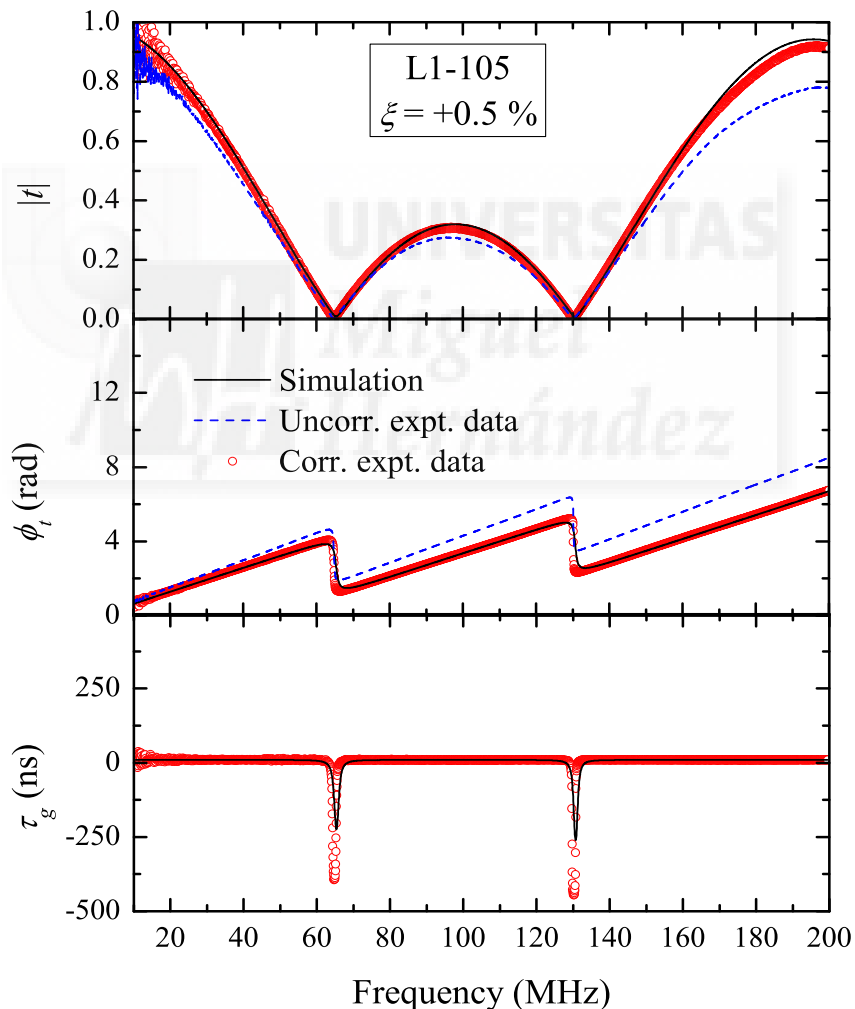


Figure 3.16: Numerical simulation (solid curve) and experimental frequency-domain characterization of the starting interferometer L1-105. The dashed curve corresponds to the whole system measured with the vector network analyzer -including the splitters-, and the symbols refer to the result of subtracting the effect of the splitters. (a) Magnitude of the transmission coefficient, (b) phase of the transmission coefficient, and (c) 17-point averaged group delay.

We analyze in the first place the starting interferometer L1-105 which is displayed in Fig. 3.16. The $|t|$ curves exhibit absolute maxima every 200 MHz and two minima between the zero and the first-order principal peak that lie close to the expected positions $f_{01} = 65.4$ MHz and $f_{02} = 130.8$ MHz (see Eq. (3.62)). Negative group delay around -400 ns are reached at both minima, accordingly to the steep negative slope of the phase function at these frequencies. These results agree with our model predictions, since the interferometer's length detuning ($+0.5\%$) satisfies the condition $\xi_{c1} < \xi < \xi_{c2}$ (with $\xi_{c1} = -2.5\%$, and $\xi_{c2} = 1.9\%$), and the length of the second branch ($L = 2.066$ m) is well below the limiting values ($L_{t1} = 55.7$ m and $L_{t2} = 62.2$ m) above which tunnelling regime disappears.

Figure 3.17 shows how the situation changes when the interferometer's length is slightly changed. According to theory, a reduction of at least $2.5\%\Delta$ in branch length L_1 fulfills the condition to generate slow light at the 1^{st} minimum. On the contrary, an increase of at least $1.9\%\Delta$ would generate slow light at the 2^{nd} minimum. Figures 3.17(a)-(d) correspond to samples L1-99, L1-101, L1-109 and L1-110, respectively. In the two samples with shorter L_1 , the system exhibits positive τ_g at the 1^{st} minimum while negative τ_g is retained at the 2^{nd} minimum. The opposite situation occurs for samples L1-109 and L1-110.

These results are justified within our model, considering the length detuning ξ of each sample (Table 3.10), the critical detuning lengths (ξ_{c1} , ξ_{c2}), and the model conditions summarized in Tables 3.8 and 3.9. Namely, $\xi < \xi_{c1} = -2.5\%$ for the system in Figs. 3.17(a) and 3.17(b) and $\xi > \xi_{c2} = +1.9\%$ for the system in Figs. 3.17(c) and 3.17(d), which explains the occurring of slow light at the 1^{st} minimum in one case, and at the 2^{nd} minimum in the other. Also, a quick estimation using Eq. (3.71) shows that only tunnelling can be sustained at the 2^{nd} minimum for interferometers L1-99 and L1-101, since L (2.066 m) is for both systems smaller than L_{t2} (11.6 m and 15.8 m, respectively). A similar result occurs by using Eq. (3.70) to obtain the value of L_{t1} for systems L1-109 and L1-110; we find $L < L_{t1}$ (25.5 m, and 20.3 m, respectively) and this is why these samples exhibit tunnelling at the 1^{st} minimum.

From Fig. 3.17 it is obvious the link between the strength of the group delay peaks and the steepness in the slope of the phase function. Such steepness is ultimately linked to the attenuation in the system (for higher attenuations the slopes are less pronounced) and to how

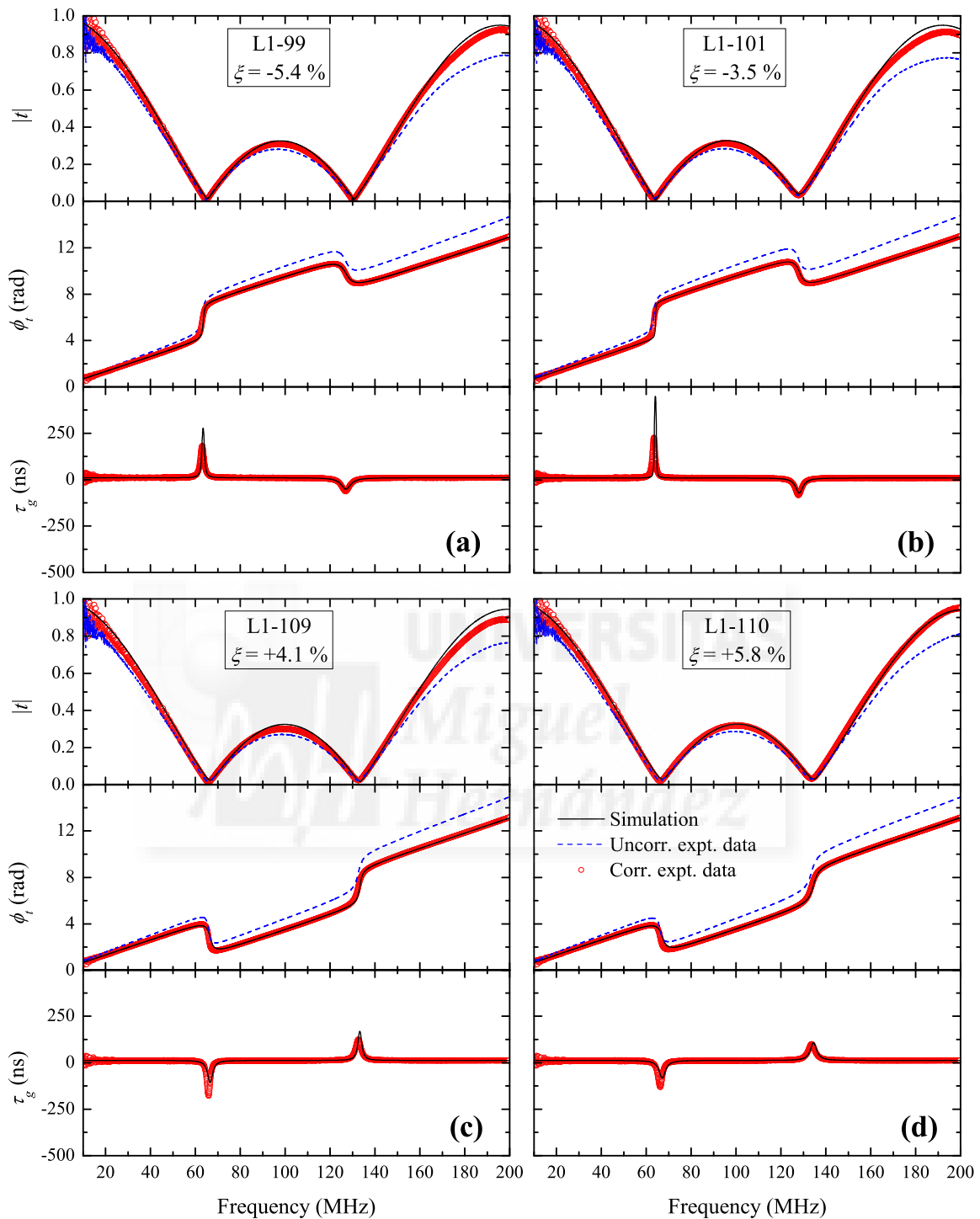


Figure 3.17: Numerical simulations (solid curve), uncorrected (dashed curve) and corrected (symbols) experimental results for the frequency-domain characterization of three-beam RF interferometers. Top panel shows magnitude of the transmission coefficient, middle panel shows phase of the transmission coefficient, and bottom panel shows the 17-point averaged group delay for samples (a) L1-99, (b) L1-101, (c) L1-109, and (d) L1-110.

much ξ approaches the critical detuning ξ_{c1} or ξ_{c2} . Samples L1-101 and L1-105 are the ones with ξ closer to one of the critical values, thus leading to the highest and narrowest τ_g peaks. Finally, the frequency shift of the minima as the length detuning varies is evident in Fig. 3.17. The minima move towards higher frequency as ξ increases, just like the theoretical model predicts.

c. Results in the time domain

Pulse propagation experiments were carried out using the experimental setup described in Appendix C.3.1 (Fig. C.5). The modulating signal was a 300 kHz sinusoidal wave, which results in a 3.3 μ s-wide pulse. This choice of the modulating frequency was a compromise between narrow-enough bandwidth to avoid pulse distortion, and large-enough bandwidth to get appreciable pulse peak advancements (or delays) in comparison to the pulse length. For each interferometer, the carrier frequency was selected to coincide with the first transmission's minimum. Since the signals were largely attenuated, a direct observation of the pulse peak on the oscilloscope was not accurate enough to measure the group delay. Hence, the pulse peak position was obtained from a numerical analysis of the data by finding the best fit to the pulse envelope.

Figure 3.18 shows the pulse captures for the five RF interferometers. The arrow indicates the time spent by the pulse peak in propagating through the interferometers and it is obtained as explained in Appendix C.3.1. The SFL transition in the pulse propagation regime is evident in these captures. The τ_g values agree reasonably well with those found in the frequency-domain characterization. The pulse propagates with negative group delay of -302 , -147 , and -115 ns in samples L1-105, L1-109, and L1-110, respectively. Whereas positive group delays of $+248$ and $+308$ ns occur in samples L1-99, and L1-101, respectively. As it is clearly demonstrated in [Guo-2006, Pev-2008, Wan-2004], such peak advancements and delays arise from the coherent interference of the pulse frequency components. Each component travels at phase velocity $2/3c$ in the cables, but their relative phases are modified after the pulse's transmission through the system; as a result, the peak of the output pulse (where the frequency components are all in phase) is shifted backwards (or forwards) and the pulse appears to travel at superluminal (or

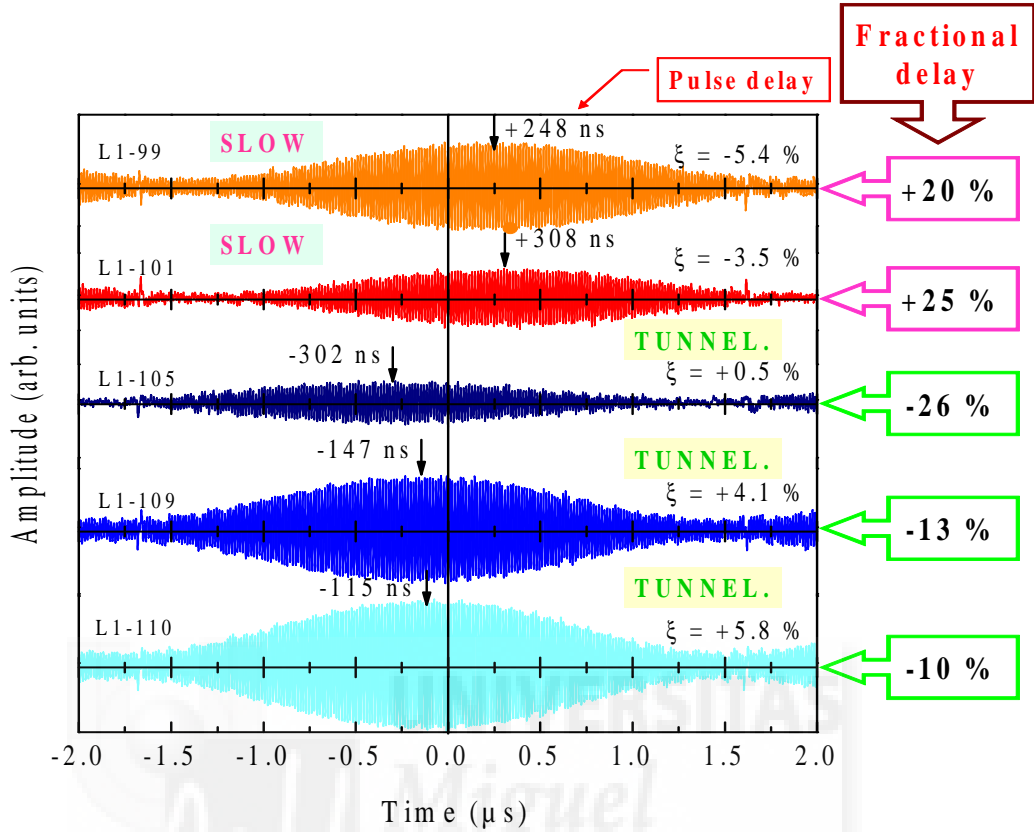


Figure 3.18: Wave-packet traces of the RF interferometers (from top to bottom) L1-99, L1-101, L1-105, L1-109 and L1-110. In each case, the pulse carrier frequency is that of the first transmission minimum. The arrow indicates the pulse propagation time through the interferometer and it is obtained as mentioned in Appendix C.3.1. The fractional delay is calculated from Eq. (3.47) taking T_{in} as the FWHM of the pulse power.

subluminal) speed. As it is argued in several works [Guo-2006, Pev-2008], these abnormal propagation regimes occur only if the spatial length of the pulse (L_{pulse}) greatly exceeds that of the system. This condition is nicely satisfied here, since $L_{pulse} = 3.3\mu s \times 2/3c = 400$ m is much longer than the interferometer's length ($L_{eff} \approx 2$ m).

In our time-domain experiments, we have measured a maximum relative pulse delay of $\sim \pm 300$ ns ($\tau_p \sim 10$ ns is almost negligible in comparison). Various definitions of the pulse duration are considered by the authors. For our sinusoidally modulated wavepackets and by considering T_{in} as the period of the modulating signal ($3.3\mu s$), we obtain a fractional delay of $\sim 9\pm\%$. Instead, if we take T_{in} as the FWHM of the pulse amplitude signal, this parameter becomes $\sim \pm 18\%$.

Furthermore, by regarding T_{in} as the FWHM of the pulse power signal, the measured fractional delay becomes $\sim \pm 25\%$.

3.3.6 Simulation results in the optical range

Leaving the free-space configurations aside, there are several technologies to realize a wave-guided three-arm interferometer operating in the optical range, namely, all-fiber and channel waveguide structures. For practical purposes, it would be desirable to induce the SFL transitions by changing the optical path without affecting the physical length of the arms, i. e., by changing the refractive index. With this idea, Lithium Niobate (LN) is an excellent candidate material, being an established choice for electro-optic applications such as the realization of Mach-Zehnder optical modulators [Woo-2000]. Optical waveguides can be fabricated, among other techniques, by in-diffusion of Titanium into an X- or Z-cut LN crystal. A precise control of the phase shift in one arm can be achieved by applying an electric field through the metallic electrode above the corresponding waveguide which induces a refractive index change due to the electro-optic properties of this material.

Fig. 3.19 shows a schematic of a Z-cut LN asymmetric three-arm interferometer with added phase-shift control in one arm. Although it seems more adequate to place the drive electrode above one of the outer arms, the drive electrode has been placed above the middle arm in order to directly extrapolate our previous analysis with length detuning ξ . Therefore, an external voltage applied to the drive electrode will produce a phase shift, $\delta\phi_1$, in the shortest arm, which is equivalent to introducing a length detuning of $\xi = c\delta\phi_1/(n_{eff}\omega\Delta)$, where n_{eff} is the waveguide effective refractive index.

As an example, let us consider the case of a LN interferometer with $L = 5$ cm, nominal Δ of $935\mu m$, and a phase shift $\delta\phi_1 \approx 0.08\pi$ rad (equivalent to a length detuning of $\xi = 3 \times 10^{-5}$). This value of Δ is chosen so that the separation between transmission minima of the same order is 50 GHz. Fig 3.20(a) shows the transmission coefficient and the group delay in a frequency range of 150 GHz centered at the middle frequency between a pair of minima of the same order

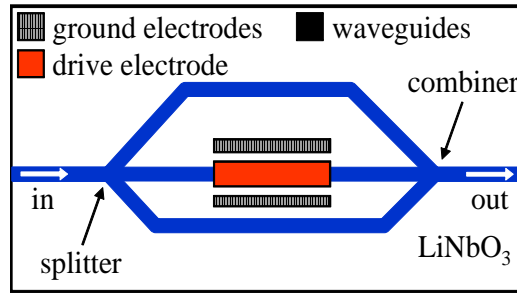


Figure 3.19: Schematic of a Lithium Niobate three-arm interferometer.

at ~ 193 THz. Considering $n_{eff} = 2.14$ the phase delay in this system is $\tau_p \approx 356$ ps. Fast light regime is sustained at the first transmission minimum whereas slow light appears at the second minimum. As indicated in the figure, pulses of bandwidth smaller than 3.4 GHz and 3.2 GHz, will experience such peak advancement or delay, respectively, without too much distortion. We have simulated the propagation of an optical pulse train through this interferometer. An optical carrier of ~ 193 THz ($\lambda = 1.55 \mu m$) is sinusoidally modulated in order to produce a train of pulses with pulse duration $T_{in} = 214$ ps at a repetition rate of 1.7 GHz. Fig 3.20(b) shows the pulse traces corresponding to propagation at both transmission minima together with a pulse trace propagating at the central frequency, for which the group delay is τ_p . The relative group delays at the first and second minima are ~ -73 ps and $+76$ ps, respectively, yielding fractional delays of -34% and $+36\%$, with pulse compression of 8 and 9 %, respectively. These values are larger than those reported in passive fiber Bragg gratings [Lon-2001], where fractional delays/advancements of 17% were measured when tuning a picosecond optical pulse spectrum through the grating band gap. Our results are also similar to the ones reported in [Lon-2005] for active fiber Bragg gratings when keeping the pulse compression in our system below 13%.

3.4 Exploring four-beam interferometers

In the preceding sections the feasibility of getting fast light in a MZI and both slow and fast light in a three-beam interferometer was assessed. Following intuition, the same phenomena

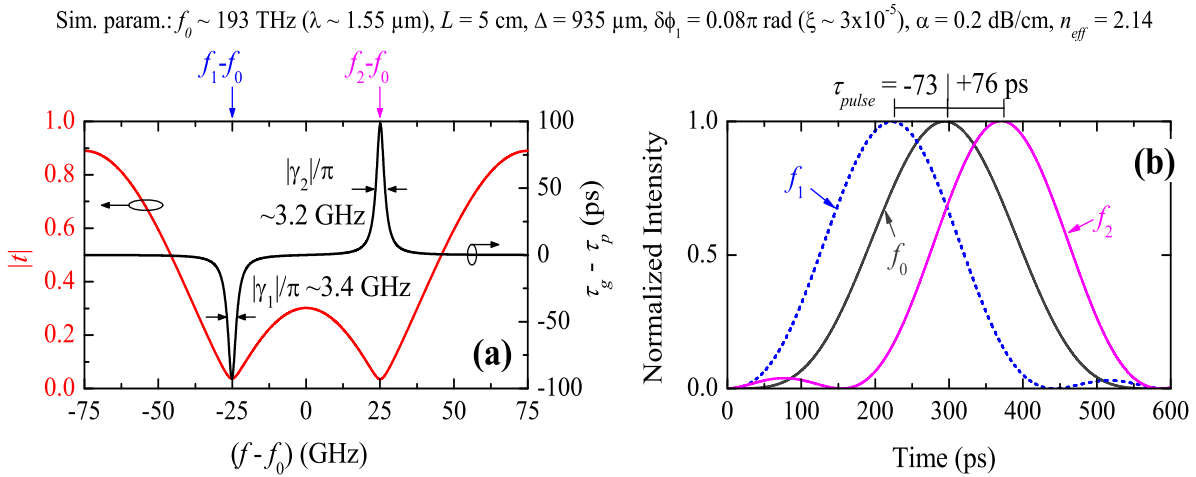


Figure 3.20: Numerical simulation of a LN interferometer with the indicated parameters. (a) Magnitude of the transmission coefficient and group delay, and (b) pulse traces of transmitted pulses with the indicated carrier frequencies corresponding to different propagation regimes.

might be encountered if one further increases the number of branches and allows for length detuning. For practical purposes, though, the simplest system would be used. Nevertheless, just for checking and since 1×4 splitters are available, SFL effects in four-beam RF interferometers are explored in this section.

a. Interferometer design

Figure 3.21(a) illustrates the designed interferometer. It consists of a 1×4 RF power splitter, a 4×1 coupler (PE2001, Pasternack) and four coaxial cables (50Ω , RG-58C/U). Two small length detunings in the first (ξ_1) and fourth (ξ_4) branches are considered. The nominal ($\xi_1 = \xi_4 = 0$) effective length of the system is $L_{\text{eff}} = 40$ m and the nominal length difference between adjacent arms is $\Delta = 4$ m. The actual branch lengths are: $L_1 = 33.93$ m ($\xi_1 = 0.0175$), $L_2 = 38$ m, $L_3 = 42$ m and $L_4 = 45.9$ m ($\xi_4 = -0.0125$). The cables in the branches were cut out of the same long coaxial cable whose attenuation coefficient as a function of frequency, $\alpha(\omega)$, had been previously determined following the procedure described in Appendix B.1.

Figure 3.21(b) shows the typical transmission spectrum of a lossless four-beam interferometer with no length detuning. The interference pattern exhibits three minima between every pair of principal peaks. As it was discussed in section 3.1 the maxima lie at even multiples of π

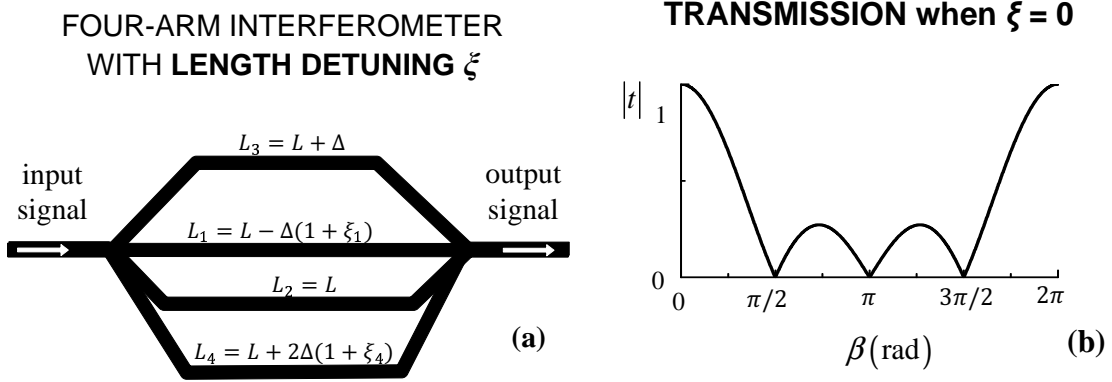


Figure 3.21: (a) Schematic of a lossless asymmetric four-arm interferometer and (b) its typical transmission spectrum.

and the minima at $\beta_1^0 = 2\pi(m + 1/4)$, $\beta_2^0 = 2\pi(m + 2/4)$ and $\beta_3^0 = 2\pi(m + 3/4)$ where $\beta = \omega\Delta/v$ is the phase associated to the nominal length difference between adjacent branches. This fabricated coaxial-cable interferometer is characterized in the frequency and time-domain.

b. Results in the frequency domain

The frequency characterization of this interferometer was performed by means of a two-port vector network analyzer (PNA series, Agilent E8363B). The scattering parameter S_{21} (the transmission coefficient) was recorded in the 10-200 MHz range every 59.375 kHz with an average of 64 to help suppress the random noise.

Figure 3.22 shows the transmission (magnitude $|t|$ and phase ϕ_t) and group delay (τ_g), of such four-beam RF interferometer. Experimental and simulation results are shown. The simulated $|t|$ and ϕ_t curves were obtained by numerically calculating the interference of four sinusoidal RF waves, including the frequency-dependent attenuation in the cables. The τ_g curves were obtained by differentiating the corresponding numerical phase curve with respect to the frequency. The same 11-point smoothing algorithm as that applied to the measured phase curve was used for the simulated phase function prior calculating the group delay.

The agreement between simulations and experimental results is very good because the effect of the splitters was subtracted from the raw data as it is explained in Appendix C.4. It is obvious that the splitters introduce losses (the peaks in transmission are less pronounced for the raw

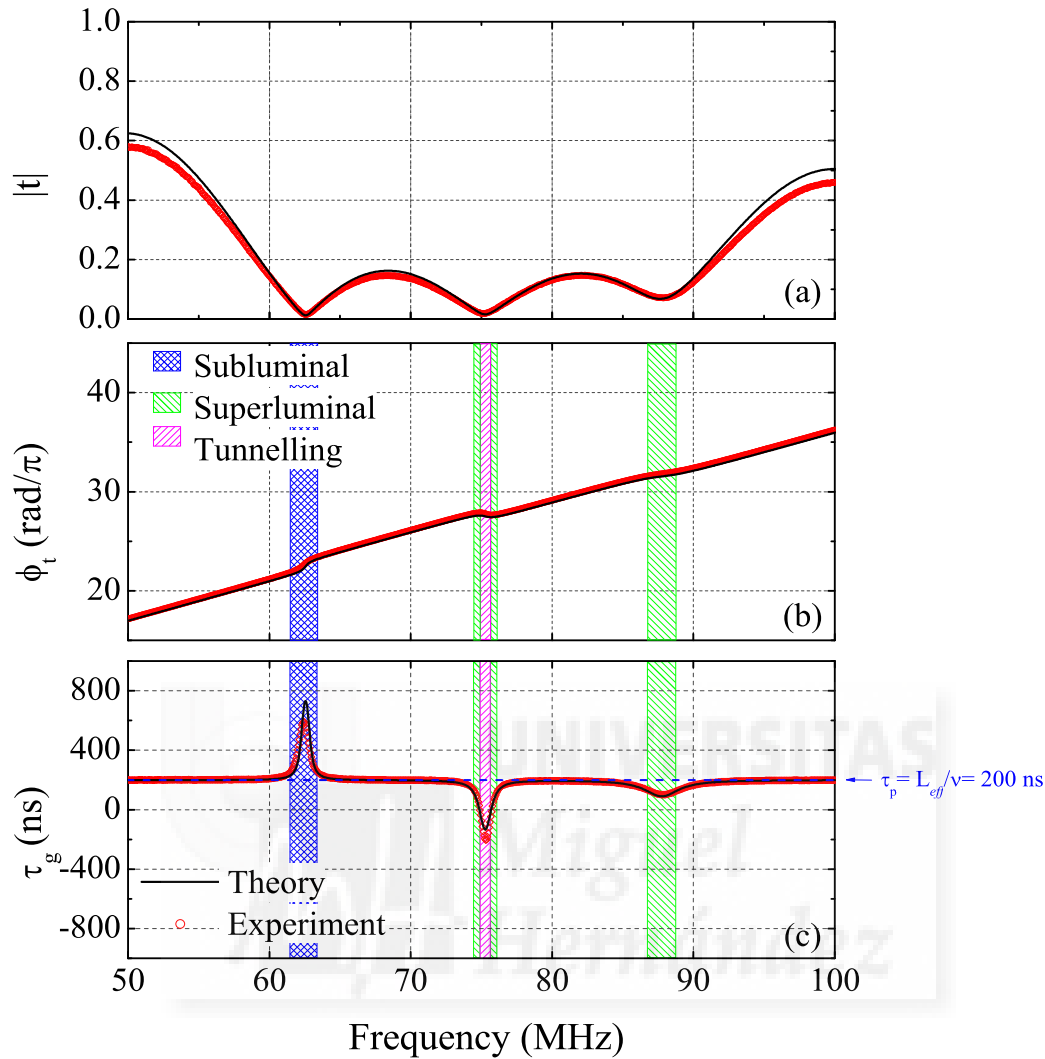


Figure 3.22: Theoretical (solid lines) and experimental (symbols) results of: (a) magnitude of the transmission coefficient, (b) phase of the transmission coefficient, and (c) group delay of a four-beam interferometer with $L_1 = 33.93$ m, $L_2 = 38$ m, $L_3 = 42$ m and $L_4 = 45.9$ m.

data) and also they add an additional phase (the raw data phase function is above the numerical one). Their effect on the group delay is hardly noticeable.

Figure 3.22 shows the typical interference pattern of an $N = 4$ interferometer, with $N - 1$ minima and $N - 2$ local maxima located between two absolute maxima. A subluminal region occurs around the first transmission minima where the phase has a strong positive slope whereas fast light regime occurs around the second and third minima due to the negative slope of the phase function around these frequencies. Anomalous dispersion is less pronounced at higher frequencies because of the larger attenuation in the transmission line, this is why the third

minimum only exhibits superluminal regime while negative group delay is achieved in the second minimum. Consequently, the group delay function in terms of the frequency (Fig. 3.22(c)) presents four different propagation regions: normal pulse propagation, corresponding to the normal dispersion region where the group delay is that of a pulse travelling at the phase velocity along a distance L_{eff} , and three abnormal propagation regimes: subluminal, superluminal and tunnelling. These results predict negative group delay as negative as -150 ns and large group delay as positive as $+670$ ns that lead to slow group velocities of $0.2c$.

The superluminal and tunnelling regions are considerably narrower than in the MZI and three-beam (compare Figs. 3.6(d) and 3.16(c) with Fig. 3.22(c)). This is only a consequence of the longer effective length of the four-beam interferometer, which is five times longer than the MZI.

We have observed that the subluminal region only appears if the length difference Δ between adjacent arms of the interferometer slightly varies from its expected constant value. This behaviour was explained in section 3.3.1 for a three-beam interferometer and can be extended to this case. It is reflected in Fig. 3.23, where theoretical results are shown for the fabricated four-beam interferometer ($L_1 = 33.93$ m, $L_2 = 38$ m, $L_3 = 42$ m, $L_4 = 45.9$ m) and for an ideal one with $L_1 = 34$ m, $L_2 = 38$ m, $L_3 = 42$ m and $L_4 = 46$ m. Note that for the latter structure (with $\xi_1 = \xi_4 = 0$) the slope of the effective refractive index, $n_{eff}(\omega)$, –obtained as in Eq. (3.50)– at 62.5 MHz is negative, as opposed to the positive slope displayed by the fabricated structure with detuning. Numerical simulations show that by changing slightly the length of any of the interferometer’s arms, the transition from tunnelling to subluminal regime occurs at different transmission minima.

c. Results in the time domain

Pulse propagation experiments were carried out using the experimental setup described in Appendix C.3.1 (Fig. C.5). The modulating signal was a 200 kHz sinusoidal wave, which results in a $5 - \mu s$ wide pulse. This choice of the modulating frequency was a compromise between narrow-enough bandwidth to avoid pulse distortion, and large-enough bandwidth to get appreciable pulse peak advancements (or delays) in comparison to the pulse length. The carrier frequency was selected to coincide with the transmission’s minimum. Since the signals were

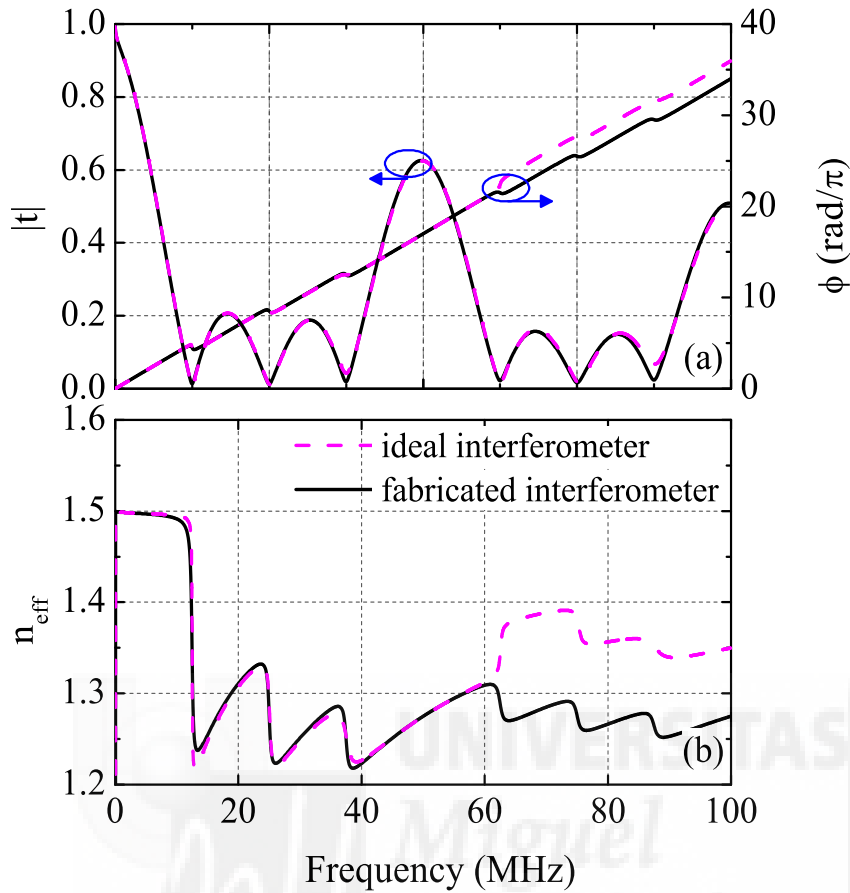


Figure 3.23: Theoretical results for: (a) magnitude and phase of the transmission coefficient, (b) refractive index of an interferometer without detuning ($\xi = 0$) (solid line) and $L_1 = 34$ m, $L_2 = 38$ m, $L_3 = 42$ m and $L_4 = 46$ m, and an interferometer with detuning ($\xi \neq 0$) (dashes) and $L_1 = 33.93$ m, $L_2 = 38$ m, $L_3 = 42$ m and $L_4 = 45.9$ m.

largely attenuated, a direct observation of the pulse peak on the oscilloscope was not accurate enough to measure the group delay. Hence, the pulse peak position was obtained evaluating numerically the best fit to the pulse envelope.

Fig. 3.24 shows the pulse captures for the four-beam interferometer. The arrow indicates the time spent by the pulse peak in propagating through the interferometer and it is obtained as explained in Appendix C.3.1. The SFL transition in the pulse propagation regime is evident in these captures. In panel (a) the pulse carrier frequency is $f_c = 50$ MHz, corresponding to the normal dispersion region of Fig. 3.22. The measured group delay is around 200 ns, which corresponds to a group velocity of $0.67c$ that coincides with the phase velocity. For $f_c = 62.5$ MHz, the measured group delay is 419 ns, that is, the pulse takes about twice the time to travel

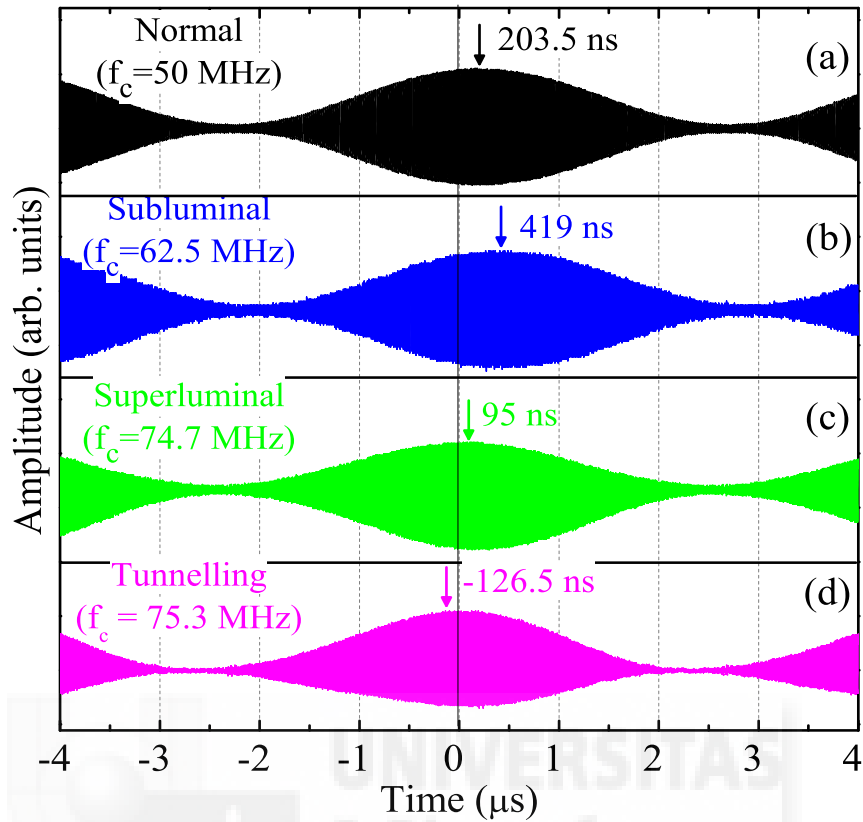


Figure 3.24: Pulse captures after traversing the four-beam interferometer with $L_{eff} = 40$ m and $L_1 = 33.93$ m, $L_2 = 38$ m, $L_3 = 42$ m, $L_4 = 45.9$ m (right panel). From top to bottom, the different propagation regions sustained by this interferometer are shown. The arrow indicates the pulse centre.

through the interferometer than to travel along a coaxial cable of the same effective length ($L_{eff} = 40$ m). The group velocity obtained in this regime is only $0.32c$, similar to that achieved by doping a coaxial photonic crystal [Mun-2003]. In panel (c) superluminal propagation is observed, with positive delay less than half the delay in the normal regime. Finally, Fig. 3.24(d) shows the pulse at $f_c = 75.3$ MHz (tunnelling region in Fig.3.22), where the steep negative slope of the refractive index leads to a negative group velocity and, therefore, the pulse centre moves to negative times. The pulse centre leaves the interferometer 126.5 ns before the centre of the incident pulse has even entered the structure. Such effect is due to the interference of the different frequency components of the pulse and does not contradict the causality principle [Moj-2000].

In summary, four-beam interferometers present both fast and slow regimes around their minima if small length detunings are considered in some of the branches. For practical purposes, one would of course use the simplest three-arm interferometer.

3.5 Conclusions

In this chapter slow and fast light generation in linear and passive multiple-beam interferometers was studied. The conclusions are the following:

- I. We have demonstrated the arising of fast light in linear and passive Mach-Zehnder, three-beam and four-beam interferometers for frequencies close to the transmission minima. In the case of interferometers with more than two branches, slow light regime is also achieved if the length difference between adjacent arms slightly varies from its expected constant value. These abnormal pulse propagation regimes are possible because of the abrupt slopes of the transmission phase function occurring in a narrow frequency region around the transmission minima. As opposed to other systems, anomalous dispersion in a narrow frequency region around the interferometer's transmission minima is strong enough to hold such propagation regimes without the need of microstructuring, doping, or using nonlinear media in the interferometer's arms. As in photonic band-gap systems, this anomalous dispersion is of structural origin i.e. it is not due to dispersion of the medium in the branches of the interferometer, but to the features in the spectral transmission. Such structural anomalous dispersion is stronger than in one-dimensional photonic crystals, where negative group delays are not predicted.
 - II. An approximate analysis is performed within the condition of good fringe visibility (small $\alpha\Delta$) and in a narrow spectral region around the transmission minima, where anomalous regimes are observed. The intensity of SFL regimes depends on how much the group delay differs from the phase delay, i.e. the excess group delay. For MZI structures, it is highlighted that the magnitude of the excess group delay at the transmission minima scales with frequency by a proportionality constant which is the ratio between the real and the imaginary parts of the complex refractive index of the branch media.
-

- III. Transitions in the pulse propagation regime at these frequencies in terms of the system's characteristics (attenuation and length detuning) were theoretically analyzed. We proved that slow light is not possible when the length difference between adjacent arms (Δ) is a constant. This is always the case for an asymmetric MZI. In this situation, fast light is achieved only if the system has attenuation (α), while for a lossless interferometer the group delay equals the phase delay. The total attenuation drives the group delay transitions at the transmission minima, where tunnelling is the expected regime for low total attenuation, whereas superluminal and eventually normal propagation are attained as total attenuation further increases. The same conditions limiting each regime were obtained for the lossy MZI and the lossy three-beam interferometer with constant Δ . It was demonstrated that no abnormal regimes can be sustained in symmetric MZI (equal branch lengths).
- IV. By introducing a small length detuning (ξ) in a branch of the three-beam interferometer, we have demonstrated that slow light can arise. Analytical expressions for the group delay τ_g at the transmission minima in the approximation of good visibility of the fringes (small $\alpha\Delta$) and small length detuning were obtained, and a critical length detuning (ξ_c) beyond which slow light appears was determined. We found that in the case of lossless media ξ_c is zero, being the role of the attenuation to increase the magnitude of ξ_c . For every pair of minima located between absolute peaks of the transmission spectra of the three-beam interferometer, only one minimum may support slow light at a time, whereas the other minimum will sustain either tunnelling, superluminal or normal dispersion depending on the system's length. Let us remark that such length-detuning driven SFL transition stems from a structural change in the system's dispersive properties at the transmission minima. This change is triggered by the passage through a local zero transmission when the critical detuning value is reached. This is in formal analogy to previously reported group delay tuning mechanism for pulses reflected on active Bragg gratings by changing the gain. But unlike it, here the SFL transition is attained in an entirely passive system.
- V. Approximations of the transmission coefficient around the transmission minima were developed to analyze the propagation of sinusoidally modulated wavepackets through MZI and three-beam interferometers. The field's envelope module of the transmitted
-

signal with carrier frequency tuned at one transmission minimum was obtained and an approximate expression for the pulse delay, τ_{pulse} , was derived in terms of the modulation frequency and the HWHM (γ) of the group delay function $\tau_g(\omega)$ around the minima. We explicitly show that in both systems, pulse delay reduces to group delay as the modulation frequency tends to zero. Figures of merit like fractional delay, pulse distortion, and delay-bandwidth product were discussed by performing numerical simulations on pulse propagation. Taking the pulse duration as the FWHM of the detected power pulse, we found that fractional delay increases with modulation frequency and values greater than $\pm 35\%$ can be obtained for modulation frequencies greater than $|\gamma|$. However, we demonstrated that pulse delay (or advancement) is accompanied by a certain degree of pulse compression and also peak-breakup. A roughly quadratic relation between fractional delay and pulse compression was deduced for sinusoidally modulated wavepackets and we showed that in order to maintain the pulse compression below 8%, and a secondary-to-main peak amplitude ratio of about 3%, the fractional delay cannot exceed 27%, and to keep it below 10%, the fractional delay cannot exceed 38%. These figures of merit are the same in both, the MZI and three-beam interferometer, and universal for any frequency range. Maximum delay-bandwidth product is estimated to be 32%.

- VI. An experimental demonstration of the model predictions on the pulse propagation regimes was performed in the RF range by using 50Ω coaxial cables and 1×2 and 1×3 power splitters to build MZI and three-beam interferometers, respectively. The structures were characterized in the frequency-domain, and the group delay curve around the transmission minima agreed with that predicted by the analytical expressions. Time-domain experiments were also performed on these structures. For the coaxial-cable three-beam interferometer, group delay from less than -300 ns to more than $+300$ ns was measured for a train of $3.3 \mu s$ wide sinusoidally modulated wavepacket with carrier frequency at a minimum as the length of the first branch was slightly varied. The experimental results were in good agreement with the theoretical predictions. The experimental study was extended to a four-beam interferometer, where pulse delays

greater than 400 ns and pulse advancements larger than 100 ns were measured for a train of $5\mu s$ -wide pulses.

VII. Finally, considering the characteristics intrinsic to the system, i.e. independent of the operational frequency range, that were outlined in point IV, one observes that the achievable pulse delays (keeping small pulse compression) are shorter than the pulse duration. This would be a drawback for developing practical delay lines or optical buffers based on these systems for signal processing. However, the very abrupt SFL transition when approaching the critical length detuning in the case of the three-beam interferometers opens the door for sensing applications. Similar phenomena would be expected by varying whatever changes the *optical path* in one of the arms. With this idea, a Lithium Niobate interferometer operative at $1.55\mu m$ was proposed and simulated in the frequency and time domain, where a fine control of the phase shift in a branch could be achieved by applying an electric field through a metallic electrode which induces a refractive index change on the waveguide. Fractional delays and advancements similar to those reported in active fiber Bragg gratings were obtained. We propose the use of these linear and passive three-beam interferometers as an alternative to PBG and active systems for sensing purposes and group delay tuning.

Chapter 4

SFL in mono- and multi-layer systems

In this chapter, experimental and theoretical evidence of negative group delays (NGDs) for reflected pulses in mono- and multi-layer structures is provided. First, we show the characteristic reflection pattern for multilayer systems based on Bragg mirrors. We discuss the abnormal values (subluminal, superluminal and negative) that the group velocity can reach in a narrow spectral region around specific frequencies for pulses reflected on these structures. In the third and fourth section, respectively, symmetric, linear, and passive microstrip slabs and distributed Bragg reflectors (DBRs) are analyzed together with experimental results in the MW range. These microwave operating devices excellently scale to their analogous structures in the optical range. In this context, we demonstrate a simple scaling law for the group delay at the slab's design frequency. In the case of DBRs, we show that, as opposed to transmitted pulses, NGDs do occur for pulses reflected in these linear and periodical one-dimensional (1D) structures. Additionally, new interpretation of the Hartman effect is given in terms of the Bragg reflector's effective length. Group delay tuning of pulses reflected in asymmetric Fabry-Perot filters is explored in the fifth section. In this case, our results are obtained in the radiofrequency (RF) range through frequency- and time-domain characterization of Fabry-Perot filters based on high and low impedance coaxial cables. Finally, the conclusions of the chapter are given.

4.1 Introduction

Multilayer systems have become an important field in the last years, both from the fundamental research point of view and because of their technological applications [Joa-2011]. A multilayer system consists of a periodic arrangement of dielectric media having different refractive indices. Its main characteristic is the existence of a photonic bandgap, i.e., a frequency region where light propagation is forbidden, for certain directions and/or polarizations, being completely reflected. In their 1D version, they are well known as optical multilayers of alternating dielectric/semiconductor materials. In these structures the photonic band gap arises from the constructive interference of the multiple waves reflected at the layer interfaces. Bragg mirrors are a particular case of 1D-photonic crystals.

A DBR is a periodic structure formed by several pairs of layers of two different refractive indices. Typically, the thickness of those layers is one quarter of the wavelength for which the mirror is designed ($\lambda/4$ layers). The latter condition holds for normal incidence. Increasing the number of pairs in a DBR enhances the mirror's reflectivity and increasing the refractive index contrast in the Bragg pairs increases both the reflection and the bandwidth [Yeh-1988]. DBRs are widely used in narrow linewidth lasers such as vertical-cavity surface-emitting lasers (VCSELs) due to their high attainable reflectivity.

A Fabry-Perot (FP) filter is a special case of an interference filter. A simple Fabry-Perot filter includes a pair of reflectors, typically multilayer structures, spaced a fixed distance. The structure behaves as an optical resonator that confines and stores light energy at selected frequencies. FP filters are widely used in sensor and measurement applications [Yos-1982]. They have also found applications in the design of multiplexer systems for local area network communications systems [Sal-1989].

Multilayer systems are usually analyzed by means of a compact method known as the transfer matrix method. We start by describing this technique and then we apply it to single slabs, Bragg mirrors, and Fabry-Perot cavities with Bragg mirrors. In subsequent sections, theoretical and experimental results are shown on structures fabricated to operate in the radiofrequency (RF) and microwave (MW) range. This allows to demonstrate the analogy between optical

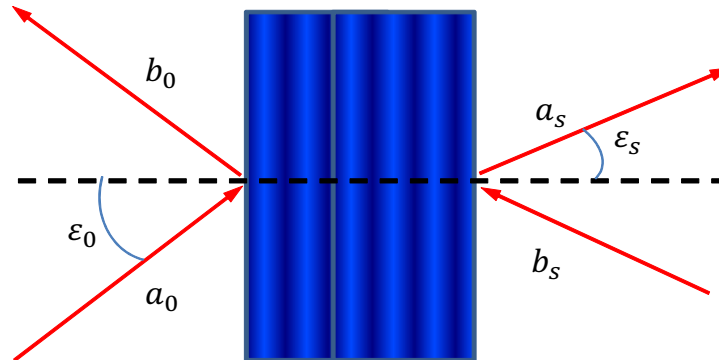


Figure 4.1: Multilayer system and nomenclature used to denote the incident and reflected waves.

multilayers and transmission lines and microstrip line-based structures. Additionally, Appendix B.2.1 describes the Hammerstad-Jensen equations that we use as a reference to design microstrip lines with frequency-dependent characteristics.

4.2 Transfer matrix method

The transfer matrix method (TMM) is useful when analyzing the reflection and transmission properties of multilayer optics [Hec-2002, Mac-2001, Yeh-1988]. The simplest DBR consisting of two media of refractive indices n_1 and n_2 is a paradigmatic case. In this section we apply the TMM to this structure.

The transmission and reflection properties of a multilayer structure can be described by a 2×2 matrix of complex elements. This array connects the complex amplitudes of the wave functions which represent the electric field on both sides of the multilayer, as shown in Fig. 4.1

In Eq. (4.1), letter a refers to the complex amplitude of the waves travelling from left to right, and letter b refers to the complex amplitude of the waves travelling from right to left. The subscript 0 indicates the incident medium of refractive index n_0 , and subscript s refers to the final medium, of refractive index n_s , which is generally the substrate where the multilayer is deposited on.

$$\begin{pmatrix} a_0 \\ b_0 \end{pmatrix} = \begin{pmatrix} A & B \\ C & D \end{pmatrix} \begin{pmatrix} a_s \\ b_s \end{pmatrix} \quad (4.1)$$

The matrix in Eq. (4.1) describes the multilayer set, and may be obtained as the product of successive 2×2 matrices that represent the path followed by the wave through the structure, where the wave propagates through various homogeneous media separated by plane interfaces of refractive index change in which the wave undergoes a partial reflection. Each of these situations is described by a propagation matrix and a matrix index change, respectively.

Assuming that the multilayer is constituted by an absorbent media, the propagation matrix is given by:

$$P = \begin{pmatrix} e^{-j\hat{\phi}} & 0 \\ 0 & e^{j\hat{\phi}} \end{pmatrix} \quad (4.2)$$

where $\hat{\phi}$ is the complex phase which acquires the wave in propagating a distance d through a medium of complex refractive index $\hat{n} = n_r + jn_i$. Assuming normal incidence, it can be written as:

$$\hat{\phi} = \frac{2\pi d}{\lambda}(n_r + jn_i) = \phi + j\alpha d. \quad (4.3)$$

In Eq. (4.3), $\alpha = (2\pi/\lambda)n_i$ is the attenuation coefficient of the wave in the medium through which it propagates, and ϕ is the real phase acquired upon propagation.

The index change matrix, assuming ideal lossless interfaces, can be written [Yeh-1988] as:

$$D_{12} = \frac{1}{t_{12}} \begin{pmatrix} 1 & r_{12} \\ r_{12} & 1 \end{pmatrix} \quad (4.4)$$

where r_{12} and t_{12} are the reflection and transmission coefficients at an interface between a medium with real refractive index n_1 and a medium with real refractive index n_2 . The Fresnel coefficients at normal incidence are defined as:

$$r_{12} = \frac{n_1 - n_2}{n_1 + n_2} \quad (4.5a)$$

$$t_{12} = \frac{2n_1}{n_1 + n_2} \quad (4.5b)$$

The transfer matrix of the multilayer, M_{ABCD} , is then obtained as a result of multiplying the successive propagation and index change matrices. It can be shown [Mol-2004] that the reflection (\hat{r}) and transmission (\hat{t}) coefficients of the entire multilayer for light incident from the medium in the left is obtained through the transfer matrix elements A, B, C and D. These coefficients are generally complex and are given by:

$$\hat{r} = \frac{b_0}{a_0} \Big|_{b_s=0} = \frac{C}{A} \quad (4.6a)$$

$$\hat{t} = \frac{a_s}{a_0} \Big|_{b_s=0} = \frac{1}{A} \quad (4.6b)$$

We can thus relate the reflection and transmission complex coefficients as:

$$\hat{r} = C \cdot \hat{t} \quad (4.7)$$

where $\hat{r} = |r|e^{j\phi_r}$ and $\hat{t} = |t|e^{j\phi_t}$. In the same way, the phases of both coefficients are related as $\phi_r = \phi_t + \phi_C$; where ϕ_C is the phase coefficient of element C .

As will be shown in the following sections, the phase function $\phi_{r,t}(\omega)$ determines the group velocity of a reflected or transmitted pulse in a mono- and multi-layer structure. The group delay is obtained using the phase-time approach explained in section 2.1.2 from the frequency derivative of the coefficient phase as:

$$\tau_{r,t} = \frac{\partial \phi_{r,t}}{\partial \omega} \quad (4.8)$$

Using Eq. (4.7), the group delays in reflection and transmission are related as:

$$\tau_r = \tau_t + \tau_C \quad (4.9)$$

where $\tau_C = \partial\phi_C/\partial\omega$.

We adapt the TMM to microstrip structures so we can compare the obtained simulations with experimental results in the radiofrequency (RF) and microwave (MW) range. In this case, the Fresnel coefficients shown in Eq. (4.5) are defined as [Sch-2001]:

$$r_{12} = \frac{Z_2 - Z_1}{Z_1 + Z_2} \quad (4.10a)$$

$$t_{12} = \frac{2Z_2}{Z_1 + Z_2} \quad (4.10b)$$

where the refractive index has been replaced by the inverse of the characteristic impedance, Z , of the transmission lines¹.

4.2.1 TMM applied to a single layer

A single layer, also known as slab, is a planar dielectric sheet or thin film of some thickness say d , as shown in Fig. 4.2. For simplicity, we assume that the media to the left and right of the slab are the same. Applying the TMM described above to the case of the single high refraction index layer (H) of Fig. 4.2, its transfer matrix can be written as the following product of propagation and index change matrices:

$$M = D_{LH}P_H D_{HL} = \frac{1}{t_{LH}} \begin{pmatrix} 1 & r_{LH} \\ r_{LH} & 1 \end{pmatrix} \begin{pmatrix} e^{-j\hat{\phi}} & 0 \\ 0 & e^{j\hat{\phi}} \end{pmatrix} \frac{1}{t_{HL}} \begin{pmatrix} 1 & r_{HL} \\ r_{HL} & 1 \end{pmatrix} \quad (4.11)$$

¹The refractive index is defined as $n = \sqrt{\mu_r \epsilon_r}$, being ϵ_r the relative permittivity of the material, and μ_r its relative electromagnetic permeability. For non-magnetic materials, μ_r is very close to 1, i.e., $n \approx \sqrt{\epsilon_r}$. For a plane electromagnetic wave the wave impedance is $Z = \sqrt{\mu_0 \mu_r / \epsilon_0 \epsilon_r} \approx 377 / \sqrt{\epsilon_r} \Omega$

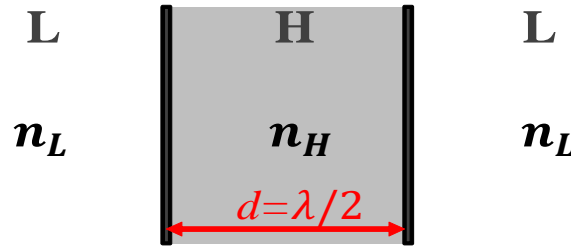


Figure 4.2: General scheme of a slab.

where r_{LH} and t_{LH} are the reflection and transmission coefficients of the interface $L \rightarrow H$ defined either in Eqs. (4.5) or (4.10) for optical and transmission line slabs, respectively. Considering the Stokes equations [Yeh-1988] that relate the $H \rightarrow L$ interface coefficients (r_{HL} and t_{HL}) to the $L \rightarrow H$ interface coefficients, the transfer matrix M_{ABCD} of the monolayer reads:

$$M = \frac{1}{t_{LH}t_{HL}} \begin{pmatrix} e^{-j\hat{\phi}} - r_{LH}^2 e^{j\hat{\phi}} & -r_{LH} (e^{-j\hat{\phi}} - e^{j\hat{\phi}}) \\ r_{LH} (e^{-j\hat{\phi}} - e^{j\hat{\phi}}) & -r_{LH}^2 e^{-j\hat{\phi}} + e^{j\hat{\phi}} \end{pmatrix} \quad (4.12)$$

Using the above matrix and Eq. (4.6), the reflectance and transmittance of a $\lambda/2$ dielectric slab operating in the MW range is simulated.

Fig. 4.3 shows the expected behaviour with zero-reflection occurring at the resonant frequencies (ω_{min} and its multiples) and maximum transmission at those frequencies. Therefore, between two adjacent absolute maxima in reflection there is a minimum.

For simplicity we rewrite r_{LH} as r and use Eq. (4.3) with $\phi = dn_H\omega/c$ into Eq. (4.12). Identifying the matrix element A and considering Eq. (4.6b), the expression defining the phase of the transmission coefficient in a slab is retrieved.

$$\phi_t = -\phi_A = \arctan \left[\frac{(e^{\alpha d} + r^2 e^{-\alpha d}) \sin \phi}{(e^{\alpha d} - r^2 e^{-\alpha d}) \cos \phi} \right] = \arctan \left[\frac{(1 + r^2 e^{-2\alpha d}) \tan \phi}{(1 - r^2 e^{-2\alpha d})} \right] \quad (4.13)$$

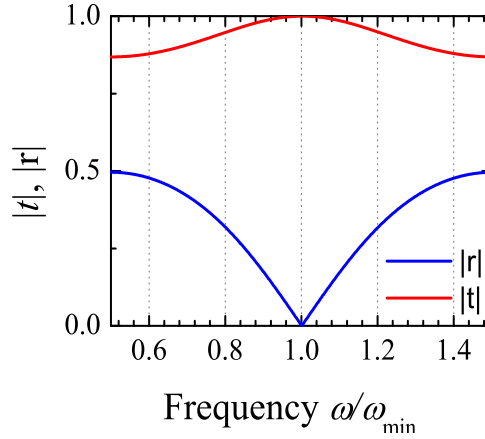


Figure 4.3: Magnitude of the transmission (red curve) and reflection (blue curve) coefficients of a $\lambda/2$ microstrip slab with attenuation. TMM numerical simulation.

The transmission group delay evaluated at the frequencies of minimum reflection (ω_{min}) is obtained from the frequency derivative of the above phase coefficient, where let us point out that the ω -dependence lays on ϕ and the reflection minima occur at $\phi = \pi$. Given these considerations, the group delay on transmission at the frequencies of the slab's reflection minima is:

$$\tau_t|_{\omega_{min}} = \left. \frac{\partial \phi_t}{\partial \omega} \right|_{\phi=\pi} = \frac{(1 + r^2 e^{-2\alpha d})}{(1 - r^2 e^{-2\alpha d})} \cdot \tau_p \quad (4.14)$$

where $\tau_p = n_H d / c$.

Likewise, by identifying element C in Eq. (4.12), the phase of the C coefficient is obtained:

$$\phi_C = -\arctan \left[\frac{\sin \phi (e^{\alpha d} + e^{-\alpha d})}{\cos \phi (e^{\alpha d} + e^{-\alpha d})} \right] = -\arctan(\tan \phi \coth \alpha d) \quad (4.15)$$

At the reflection minimum the group delay associated to this phase is:

$$\tau_C|_{\omega_{min}} = \left. \frac{\partial \phi_C}{\partial \omega} \right|_{\phi=\pi} = -\tau_p \cdot \coth \alpha d \quad (4.16)$$

The slab's group delay on reflection evaluated at ω_{min} can now be calculated by using Eq. (4.14) and Eq. (4.16) into Eq. (4.9), yielding:

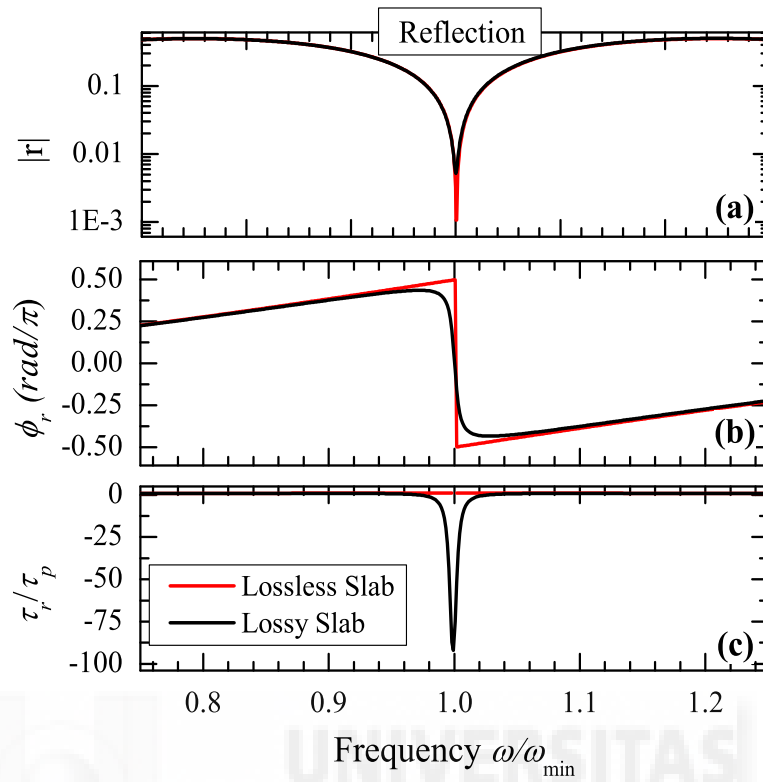


Figure 4.4: TMM numerical simulation of a $\lambda/2$ microwave slab with attenuation (black curve) and without attenuation (red curve). (a) Magnitude of the reflection coefficient -logarithmic scale-, (b) phase of the reflection coefficient, and (c) group delay on reflection.

$$\tau_r|_{\omega_{min}} = \tau_p \cdot \left[\frac{(1 + r^2 e^{-2\alpha d})}{(1 - r^2 e^{-2\alpha d})} - \coth \alpha d \right] \quad (4.17)$$

The above concepts are now illustrated by performing simulations on a microwave slab. In order to keep the first reflection minima at ω_{min} , we have considered the slab's thickness, d , to be $\lambda/2$ for a design frequency of ω_{min} . The results ($|r|$, ϕ_r and τ_r) are shown in Fig. 4.4, for two values of the attenuation coefficient α , and the frequency axis was normalized to the design frequency.

The magnitude of the reflection coefficient in Fig. 4.4(a) shows the expected behaviour of a dielectric slab, with minima at the resonant frequencies (ω_{min} and its multiples). These minima are less pronounced for the lossy slab because of its stronger attenuation. The sudden phase change at ω_{min} in the lossless slab makes the phase undefined at this frequency and τ_r has no

physical meaning since the slope is infinite. However, for the lossy slab, ϕ_r exhibits a large but finite negative slope at ω_{min} , with a nonzero, albeit small, reflection. Therefore, negative group delay (NGD) occurs at the reflection's minimum. This behaviour was first predicted by Wang and Zhu [Wan-2006] for pulses reflected on a weakly absorbing dielectric slab.

Evaluating Eq. (4.17) at the **minima**, two cases are distinguished:

- I. **Lossless slab** ($\alpha = 0$), parameter C is real and consequently $\tau_C = 0$. Therefore, the reflection group delay is equal to the transmission group delay $\tau_r = \tau_t = \tau_p \cdot [(1 + r^2)/(1 - r^2)]$. In this case, NGDs cannot be sustained, in accordance to what is observed in Fig. 4.4 (red curve).
- II. **Lossy slab** ($\alpha \neq 0$), $\tau_r = \tau_t + \tau_C$. For small attenuation values, NGDs in reflection do arise, in agreement with Fig. 4.4 (black curve). For small enough total attenuation αd , we have $\coth(\alpha d) \approx 1/\alpha d$ which tends to ∞ , thus making $\tau_r|_{\omega_{min}}$ in Eq. (4.17) a large negative number.

4.2.2 TMM applied to a DBR filter

We now consider a periodic multilayer structure of alternating high (H) and low (L) index of refraction, repeated N times to form the $(HL)^N$ structure. Typically, the thickness of these layers is equal to one quarter of the design wavelength ($\lambda/4$ layer). Often, an additional H-layer is added at the end of the structure to increase its reflectance [Hec-2002], yielding a $(HL)^N H$ structure. In this chapter we have focused on this type of DBR.

In general, the phase of a wave reflected on a Bragg filter depends on the refractive indices of the layers forming the structure, the total number of layers N , and the refractive indices of the initial and final media. For simplicity, we have considered that these media have both n_L refractive index. At each interface part of the wave is reflected and part is transmitted.

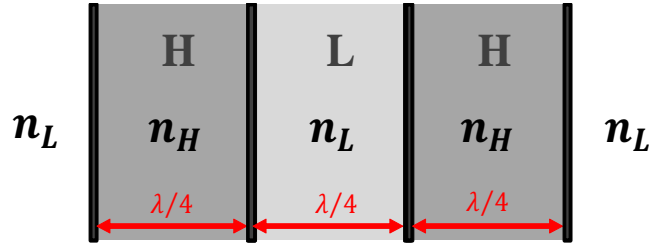


Figure 4.5: General scheme of a distributed Bragg reflector (DBR).

Applying the TMM to the case of a simple DBR formed by one and a half periods ($N = 1$), as shown in Fig. 4.5, the DBR transfer matrix can be expressed as the following product of propagation and index change matrices:

$$M = D_{LH}P_H D_{HL}P_L D_{LH}P_H D_{HL} \quad (4.18)$$

where once again, r_{LH} and t_{LH} are the reflection and transmission $L \rightarrow H$ interface Fresnel coefficients defined in Eq. (4.5) (or in Eq. (4.10) for transmission line DBRs), and the Fresnel $H \rightarrow L$ interface coefficients (r_{HL} , t_{HL}) are related to them by the Stokes relations [Yeh-1988].

Once the M_{ABCD} transfer matrix is obtained, numerical simulations are carried out in order to compare the reflection of pulses on this simple DBR structure with and without attenuation. For that purpose, a periodic $\lambda/4$ structure of the type HLH is selected. The results ($|r|$, ϕ_r and τ_r) are shown in Fig. 4.6, where the frequency axis is normalized to the Bragg frequency ω_B .

The magnitude of the reflection coefficient in Fig. 4.6(a) shows the typical Bragg oscillations, with one broad reflection peak centered at ω_B and two minima in the displayed frequency range (note the logarithmic scale). As it occurs for the simple slab structure previously analyzed, these minima are less pronounced for the lossy DBR, whose reflection phase function ϕ_r (see Fig. 4.6(b)) displays a steep but finite negative slope at the frequencies of the reflection minima, which lead to large and negative values of the group delay in Fig.4.6(c). Therefore, tunnelling of narrow band pulses centered at these frequencies and reflected on lossy DBRs is expected.

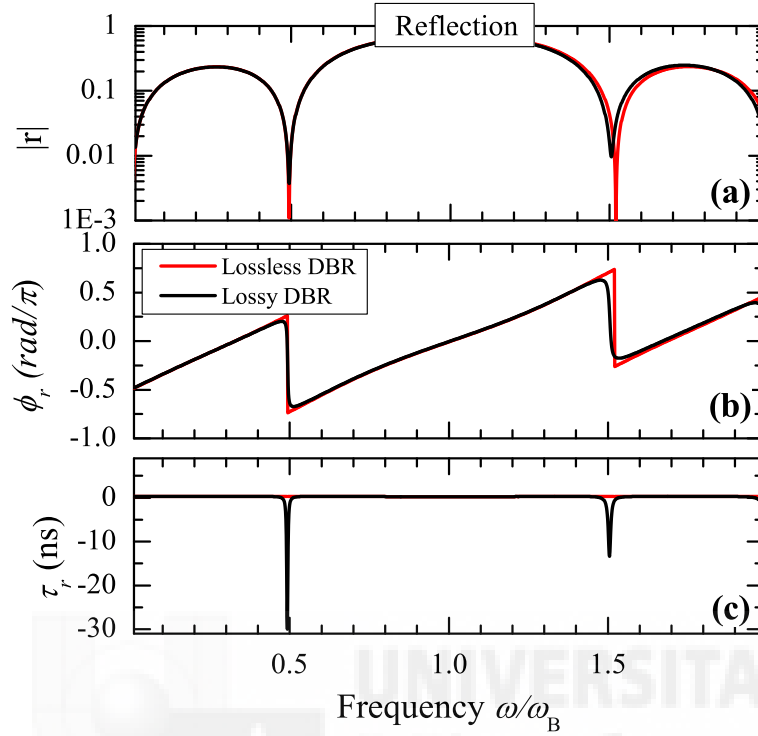


Figure 4.6: TMM numerical simulation of a simple microwave DBR formed by one and a half periods ($N = 1$, $\lambda/4$ layer for ω_B) with attenuation (black curve) and without attenuation (red curve). (a) Magnitude of the reflection coefficient -logarithmic scale-, (b) phase of the reflection coefficient, and (c) group delay on reflection.

4.2.3 TMM applied to a Fabry-Perot with DBR mirrors

To conclude this section, TMM is now applied to a Fabry-Perot (FP) filter with Bragg mirrors. We have focused on $(HL)^{N_1}H - L' - (HL)^{N_2}H$ structures (see Fig. 4.7), where L' is a spacing layer of thickness d .

Considering the simple FP with DBR mirrors formed by one and a half periods ($N_{1,2} = 1$), of Fig. 4.7, we can obtain the FP transfer matrix as the product of the following propagation and index-change matrices:

$$M = D_{LH}P_H D_{HL}P_L D_{LH}P_H D_{HL}P_{L'} D_{L'H}P_H D_{HL}P_L D_{LH}P_H D_{HL} \quad (4.19)$$

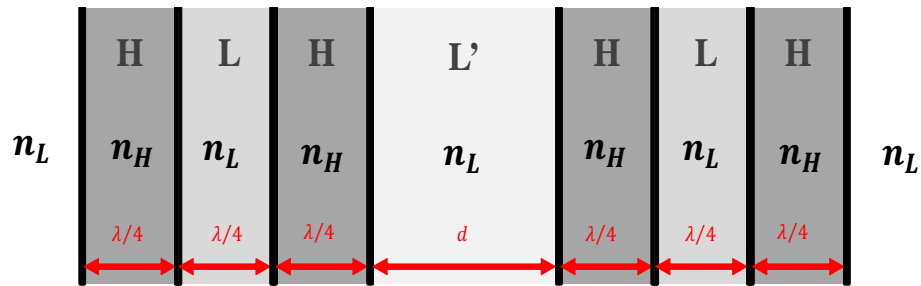


Figure 4.7: General scheme of a FP with DBR mirrors.

The M_{ABCD} transfer matrix of the FP structure is then obtained and we have compared the reflection of pulses on symmetrical ($N_1 = N_2$) and asymmetrical ($N_1 \neq N_2$) lossy FPs with $\lambda/2$ mirror spacing. The simulation results for $|r|$, ϕ_r and τ_r are shown in Fig. 4.8, where the frequency axis was normalized to the design frequency ω_B (the mirror's Bragg frequency).

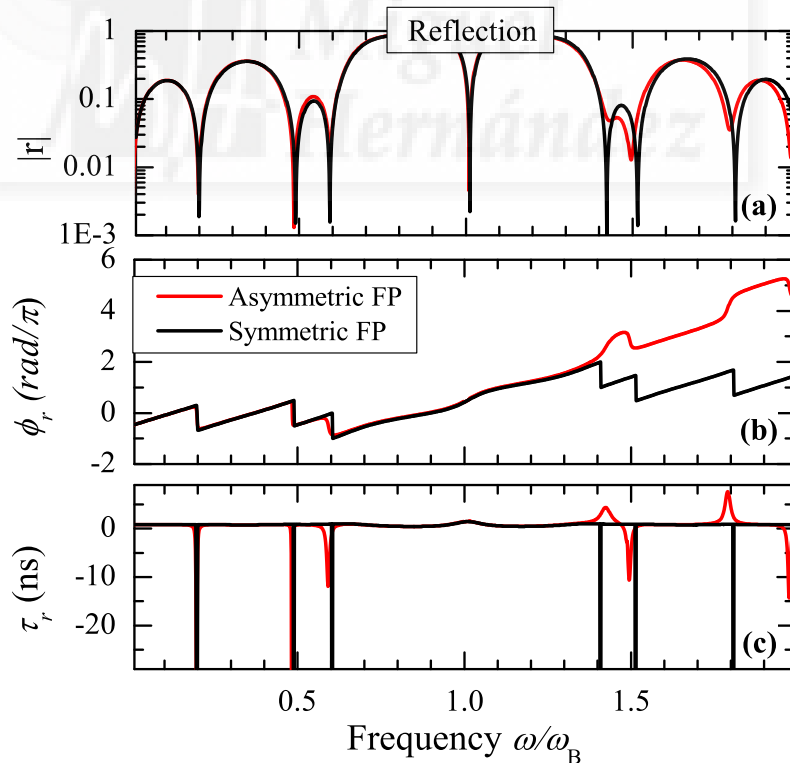


Figure 4.8: TMM numerical simulation of a simple microwave FP with DBR mirrors formed by a one and a half periods ($N = 1$, $\lambda/4$ layer for ω_0) with attenuation (black curve) and without attenuation (red curve). (a) Magnitude of the reflection coefficient –logarithmic scale–, (b) phase of the reflection coefficient, and (c) group delay on reflection.

In both cases (symmetric and asymmetric FP), the magnitude of the reflection coefficient in Fig. 4.8(a) shows an inverted peak at the Bragg frequency ω_B , which (for the considered mirror spacing) coincides with a transmission resonance at the gap center. However, the phase function features at the minima are not the same. The reflection phase function ϕ_r in Fig. 4.8(b) displays a steep negative slope in all the minima for the symmetric FP (black curve), thus leading to large and negative group delay values (see Fig. 4.8(c)), but this is not the case for the asymmetric FP (red curve), where a steep positive slope occurs at some minima.

4.3 NGDs of reflected pulses in microstrip slabs

Theoretical demonstration of the occurrence of NGDs in lossy slabs was presented in section 4.2, in agreement with previous predictions of Wang and Zhu [Wan-2006]. Here, experimental evidence of such predictions is provided. For that purpose, the optical dielectric slab considered by Wang and Zhu is scaled to the MW range and a simple scaling law for the group delay at the slab's design frequency, f_0 is derived. We describe the fabrication procedure of such a microstrip high-impedance dielectric slab, and measure NGDs by frequency-domain characterization of the microstrip slab.

4.3.1 Slab design

We have designed microstrip single lines following the Hammerstad-Jensen model [Ham-1980], which provides simple equations for the characteristic frequency-dependent impedance and the effective dielectric constant as functions of the microstrip width, substrate thickness and dielectric constant (Fig. 4.9, see Appendix B.2.1 for details). In the case of microstrip structures the attenuation coefficient α is retrieved from the contribution of both dielectric and ohmic losses.

Samples were fabricated on a high-quality substrate using a LPKF Protomat 93s circuit board milling machine with 100 μm resolution. This substrate is a high-frequency double-sided 35 μm copper-plated laminate Taconic TLC, which is a commercial microwave circuit board

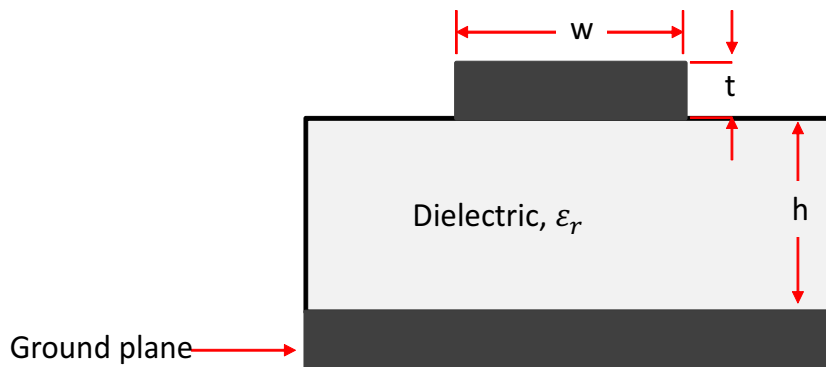


Figure 4.9: Microstrip line design.

material with a dielectric constant of 3.18 and thickness of 1.6 mm [Taconic]. The nominal loss tangent of this substrate is 0.003. However, we found that experimental structures exhibit a larger overall attenuation. A fitting procedure using a longer structure (the longest Bragg reflector where attenuation effects are larger) led to 0.0045 as a more suitable value for the loss tangent and was used for the theoretical simulations presented in the next section.

We have measured the actual values of every element width and length with an optical microscope of 100 μm resolution and checked that they lay within the experimental resolution of the milling machine.

Measurements of the scattering (S) parameters were performed by a two-port vector network analyzer (Agilent, model E8363B). The parameters S_{11} and S_{21} , which correspond to the reflection and transmission coefficient, respectively, were recorded in the range of 1 to 9 GHz every 2.5 MHz.

Experimental data contain a small amount of noise which is not very apparent in the S parameters themselves. To obtain the experimental group delay, the phase data curve must be differentiated and this amplifies the noise leading to spurious effects [Moj-2000]. For this reason, in the calculations of the group delay following the phase-time approach in Eq. (4.8), the experimental phase data were smoothed prior differentiation. Although it is well known that smoothing is an arbitrary process that may give results which vary critically with the smoothing parameters, we finally used a 17 point Savitzky–Golay algorithm based on a second-

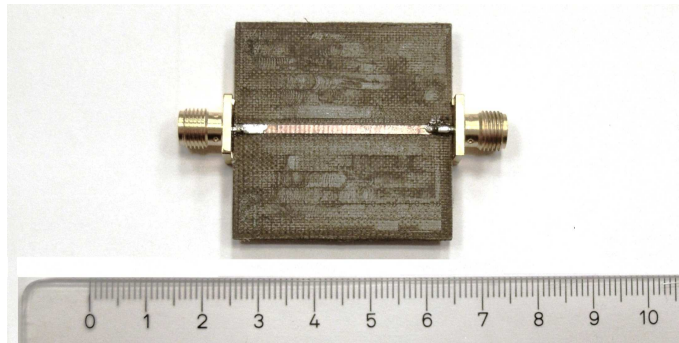


Figure 4.10: Top view of fabricated microstrip structure: 86.6 Ω dielectric slab.

degree polynomial fit [Sav-1964], which does not essentially affect the slope of the phase at the reflection maxima and is satisfactory enough to preserve the key features of the group delay trends at the reflection minima.

We have fabricated a microstrip slab of 1.377 mm nominal track width – which yields a 86.6 Ω characteristic impedance – and 39 mm nominal length. This length corresponds to $\lambda/2$ (where λ is the wavelength in the medium) for a frequency $f_0 = 2.5$ GHz. The nominal impedance contrast between the 50 Ω ports and the microstrip line corresponds to a contrast ($1 : \sqrt{3}$), which is that of the optical dielectric slab refractive index contrast considered by Wang and Zhu [Wan-2006]. Fig. 4.10 shows the fabricated sample. Actual values of line width and length are 1.35 mm and 39.1 mm, respectively.

The effective dielectric constant, ϵ_{eff} is related with the thickness h of the dielectric layer and width w of the microstrip line [Ham-1980, Get-1973]. Since the propagation through the microstrip is not purely TEM the dielectric constant varies with frequency, for the design frequency ($f_0 = 2.5$ GHz), $\epsilon_{eff} = 2.36$. The model predicts that the effective dielectric constant gradually climbs with increasing frequency in agreement with our observations.

The attenuation coefficient α of a microstrip line consists of conductor (ohmic) losses and substrate (dielectric) losses. For a frequency $f_0 = 2.5$ GHz, $\alpha = 2.52$ dB/m.

4.3.2 Results and discussion in the MW range

By means of the frequency-domain characterization performed with the vector network analyzer, we wish to compare the reflection of pulses on this microstrip slab with the behaviour predicted by Wang and Zhu for a weakly absorbing optical dielectric slab [Wan-2006].

For that purpose, we have selected one of their structures, namely a dielectric slab with refractive indexes $1 : \sqrt{3} : 1$ and dielectric constant imaginary part $\epsilon_i = 0.01$. In order to keep the frequency range shown in that reference, with the first reflection minima at 129.9 THz, we have considered the thickness, d , of this optical slab to be $\lambda/2$ for a design frequency of $f_0 = 129.9$ THz, thus yielding $d \approx 0.66 \mu\text{m}$. Consequently, our microstrip line is a scaled version, in the microwave range, of this optical dielectric slab. Following the theory explained in section 4.2.1, the standard TMM [Yeh-1988] is applied to calculate the reflection coefficient (magnitude $|r|$ and phase ϕ_r) of the optical slab as a function of frequency. For the microstrip line, these functions are measured using the network analyzer and they are also calculated numerically by TMM using the actual values of the microstrip line width and length. The corresponding group delay in reflection, τ_r , is then obtained from the frequency derivative of ϕ_r . In this calculation, the same numerical treatment (phase smoothing prior differentiation) was applied to the experimental and simulated data. The results ($|r|$, ϕ_r and τ_r) are shown in Fig. 4.11, where the frequency axis was normalized to the design frequency (2.5 GHz and 129.9 THz for the microstrip and optical slab, respectively) for better comparison.

The magnitude of the reflection coefficient in Fig. 4.11(a) shows the expected behaviour of a dielectric slab, with minima at the resonant frequencies (f_0 and its multiples). These minima are more pronounced for the optical slab because of its weaker attenuation. The second resonance of the microstrip slab is slightly shifted from $2f_0$ because of the dispersion in the effective dielectric constant, which is indeed taken into account in the simulations [Ham-1980]. The good agreement between the microstrip experimental and simulated curves probes the success of the microstrip design and fabrication. The reflection phase function ϕ_r of the optical dielectric slab has been shifted down π radians in order to directly compare it with the microstrip slab curve. The reflection phase functions ϕ_r in Fig. 4.11(b) display a steep negative slope at the resonant

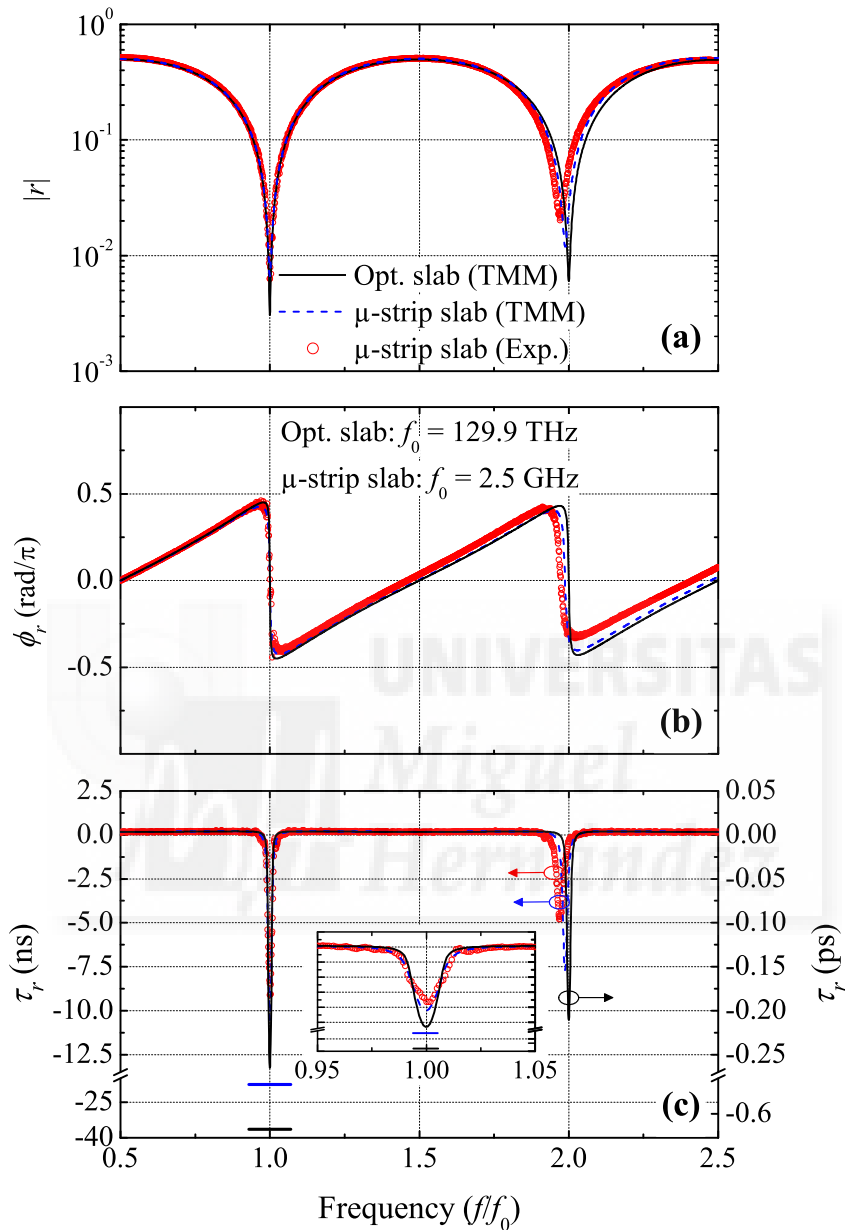


Figure 4.11: Scaling of optical (in black) and microstrip (red) slabs. TMM numerical simulation of a $\lambda/2$ optical dielectric slab for $f_0 = 129.9$ THz and thickness $d = 0.66 \mu\text{m}$ with $\tau_r = 3$ and $\epsilon_i = 0.01$ (black curve). TMM numerical simulation (dashed curve) and experimental frequency-domain characterization (circles) of a $\lambda/2$ microstrip slab for $f_0 = 2.5$ GHz and length $d = 39.1$ mm with loss tangent 0.0045. (a) Magnitude of the reflection coefficient -logarithmic scale-, (b) phase of the reflection coefficient, and (c) 17-point averaged group delay. The horizontal marks indicate the theoretical value of τ_r at f_0 when the group delay data are not averaged numerically. The inset figure shows the situation at f_0 in more detail. The reflection phase function ϕ_r of the optical dielectric slab is shifted down π radians in order to compare both curves.

frequencies, which lead to large and negative values of the group delay in Fig. 4.11(c). The results for the optical slab agree with those in [Wan-2006]. The inset shows in detail the group delays at the design frequency. We ascribe the difference in the experimental and simulated results for the microstrip to a higher attenuation of the actual slab. Group delay more negative than $\tau_r \approx -9$ ns is expected for a microwave narrowband pulse of 2.5 GHz center frequency reflected on the fabricated microstrip slab. The corresponding situation for the optical slab and an optical pulse centered at 129.9 THz is $\tau_r \approx -0.26$ ps. Therefore, microwave pulses reflected on a microstrip slab show essentially the same physics predicted in [Wan-2006] for optical pulses reflected on the equivalent dielectric slab.

Now, let us make a closer comparison. Since this $\lambda/2$ microstrip slab is a scaled version, in the microwave range, of the $\lambda/2$ optical slab, a natural question arises: is there a scaling law for the NGD at the design frequency? Using the analytical expressions of the group delay in Eq. (4.17), it can easily be obtained that for small attenuation values, the reflective group delay at f_0 can be approximated as:

$$\tau_r \approx \tau_t - \frac{1}{2\pi f_0} \frac{n_r}{n_i} \approx -\frac{1}{\omega_0} \frac{n_r}{n_i} \quad (4.20)$$

where n_r (here $n_r = n_H$) and n_i are the real and imaginary part of the refractive index, respectively. Let us point out that in the above equation, the term τ_t was finally disregarded because of its very small value. Namely, $\tau_t \approx 0.2$ ns is obtained from Eq. (4.14) for the microstrip slab and $\tau_t \approx 40$ fs is expected from [Wan-2006] for the optical slab.

The ratio n_r/n_i is 600 for the optical slab [Wan-2006], and 276 for the microstrip slab at f_0 , where $n_r = \sqrt{\epsilon_r}$ and $n_i = c\alpha/\omega_0$. Therefore, the expected group delay at f_0 for the optical slab is $\tau_r = -0.73$ ps, whereas for the microstrip slab it is $\tau_r = -17$ ns. These values are larger (absolute values) than the ones shown by the curves in Fig. 4.11(c) because of the smoothing of the group delays. The horizontal marks in Fig. 4.11(c) indicate the values reached by τ_r at f_0 when the data are not smoothed numerically. As we can see, these latter values do agree with the scaling law in Eq. (4.20).

The expression in Eq. (4.20) brings an interesting point into attention: an equivalent relation was obtained for the group delay at the transmission minima of a MZI (see Eq. (3.29), section 3.2.1). Therefore, it shows the resemblance between pulse reflection on a dielectric slab and pulse transmission through a MZI. This should not be unexpected since the reflection spectrum of a dielectric slab is in fact very similar to the MZI transmission spectrum.

Finally, let us mention that in order to compare the group delays at the resonant frequencies, the limiting numbers of the time axes in Fig. 4.11(c) were selected such that, once multiplied by its corresponding f_0 , they take the same value for both slabs. In this way, the apparent difference in τ_r for the microstrip and optical slab is due to the ratio n_r/n_i .

4.4 NGDs of reflected pulses in Bragg reflectors

Considering the typical reflectance spectrum of multilayer mirrors [Yeh-1988] and as it was shown in section 4.2.2, NGDs in reflection do occur in these structures. In this section experimental results for fabricated microstrip Bragg reflectors and various aspects of their behaviour for reflected pulses, such as the arising of NGDs and the Hartman effect, are analyzed.

4.4.1 Bragg reflector design

Microstrip single lines were designed and fabricated on a high-quality substrate (see Appendix B.2). The actual values of every element width and length were measured with an optical microscope, as it was done for the high-impedance dielectric slab of the previous section.

We have fabricated periodic $\lambda/4$ structures of the type $(HL)^N H$ containing $N + 1/2$ unit cells, where H represents a high impedance line (nominally 75Ω) with length L_H and width w_H , and L represents a low impedance line (nominally 50Ω) with length L_L and width w_L . These Bragg reflectors were designed to have the first transmittance gap at 2.5 GHz and were fabricated with

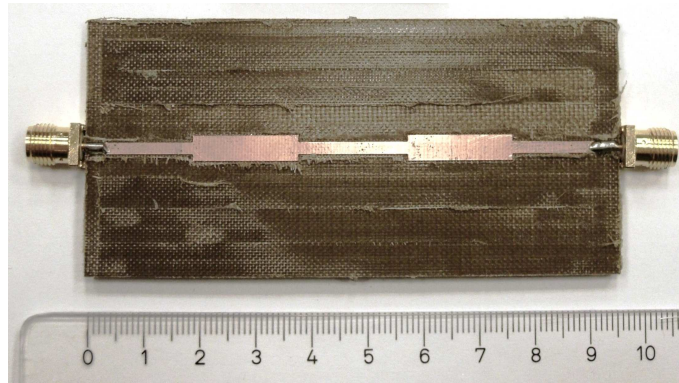


Figure 4.12: Top view of one of the fabricated microstrip structures: Bragg reflector with $2 + \frac{1}{2}$ unit cells. SMA connectors have 50Ω characteristic impedance.

$N = 2, 4, 6,$ and 8 unit cells. As an example, Fig. 4.12 shows the $N = 2$ structure. The actual values of element width and length are $L_H = 19.25$ mm, $w_H = 1.75$ mm, $L_L = 18.75$ mm, and $w_L = 3.75$ mm in the case of the Bragg reflector with $N = 6$ layers. These values were similarly enough for the other structures and were the ones considered in the theoretical simulations presented in the next subsection.

4.4.2 Results and discussion in the frequency domain

Measurements of the scattering (S) parameters and group delays were performed by means of a two-port vector network analyzer (Agilent, model E8363B). The parameters S_{11} and S_{21} , which correspond to the reflection and transmission coefficient, respectively, were recorded in the range of 1 to 9 GHz every 4.4 MHz. As it was mentioned in the previous section, as a result of the noise present in the experimental data, in the group delay calculations following the phase-time approach in Eq.(4.8), the experimental phase data were smoothed prior differentiation using a 17 point Savitzky–Golay algorithm based on a second–degree polynomial fit [Sav-1964]. The method used to smooth the phase curve is broadly described in Appendix C.2.

We now discuss the frequency-domain characterization of our fabricated microstrip Bragg reflectors $(HL)^N H$ with $N = 2, 4, 6$ and 8 in transmission and reflection. Fig. 4.13 shows the reflection coefficient's magnitude $|r|$ and phase ϕ_r (top and middle panels, respectively)

and the group delay on reflection τ_r (bottom panel) obtained from Eq. (4.8). The experimental curves correspond to the scattering parameter data S_{11} , whereas the theoretical curves (solid line) were obtained by applying the TMM [Yeh-1988], including the wave attenuation along the microstrip structure. The excellent agreement between theory and experiment is a consequence of considering the following issues.

First, for the numerical simulation of the structures, the actual values of the lengths and widths of the H and L layers are considered. The consideration of the actual values for L_H , w_H , L_L and w_L , rather than their design values, is important to avoid shifts in the positions of the resonant peaks between theory and experiment. Second, in the calculation of the group delay, the same numerical treatment (explained in Section 4.3.1 and described in detail in Appendix B) is given to the experimental and to the theoretical group delay data. Third, as explained before, instead of the nominal value of 0.003, a loss tangent of 0.0045 was considered in the TMM theoretical calculations for all the Bragg reflectors.

Let us now analyze the results. Figure 4.13(a) corresponds to the microstrip structure $(HL)^2H$. The function $|r|$ shows the typical oscillations in Bragg reflectors, with two main reflection peaks in the displayed frequency range (note the logarithmic scale). The first peak position agrees with its design value of 2.5 GHz, while the second peak is slightly shifted off 7.5 GHz in both the experimental and simulated curve because of the frequency dispersion of the microstrip effective dielectric constant. Between these peaks there are five reflection minima, and, as it occurs for the simpler microstrip slab previously analyzed, these minima are associated to large negative slopes in the reflection phase function ϕ_r , and the consequent negative values of the group delay in a narrow frequency region around the reflection minima. For instance, around 1.6 GHz, group delays of -8 ns and NGD bandwidth > 140 MHz could be reached. This value of group delay is similar to the ones obtained in coplanar waveguide left-handed media [Ibr-2008].

As the number of layers (N) increases, the number of minima between the main reflection peaks increases by the rule $2N + 1$ (see Figs. 4.13(b)–4.13(d)) so that a larger number of minima must fit inside the same frequency interval. This sharpens the minima and makes narrower the frequency region of NGDs. Also, and due to the higher attenuation as N increases, lower NGDs

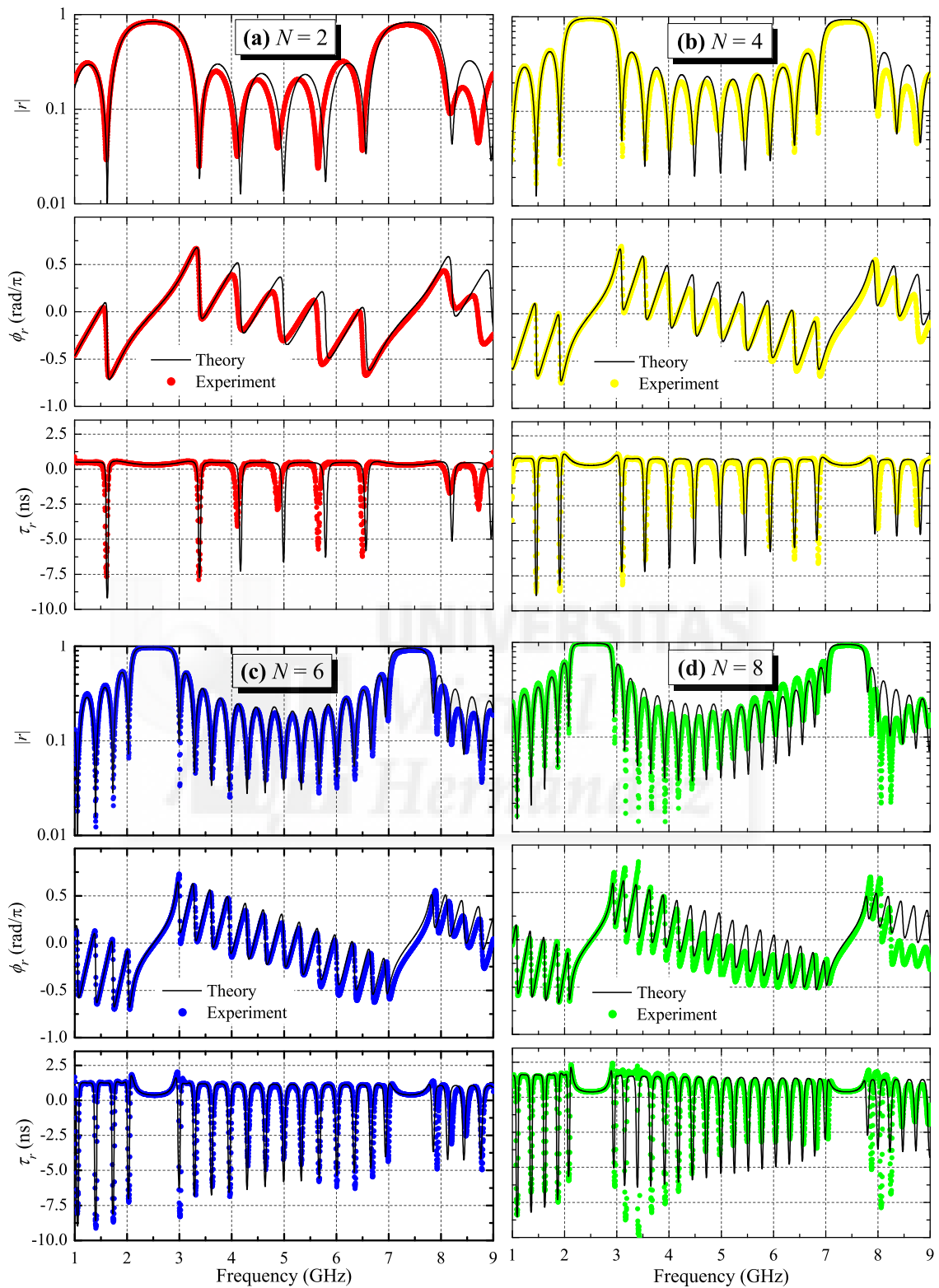


Figure 4.13: Experimental and theoretical results for the frequency–domain characterization of reflected pulses on microstrip Bragg reflectors $(HL)^N H$. Top panel shows magnitude of the reflection coefficient, middle panel shows phase of the reflection coefficient, and bottom panel shows (17-point averaged) group delay for (a) $N = 2$, (b) $N = 4$, (c) $N = 6$, and (d) $N = 8$ unit cells.

are reached. For instance, also at 1.6 GHz and for $N = 8$, the NGD is ~ -7.5 ns and the pulse bandwidth is now limited to 90 MHz.

Experiments of superluminal reflection of optical pulses have reported NGDs of -60 ps in fiber Bragg gratings specially apodized to provide a double-Lorentzian spectral reflectivity with a pronounced dip [Lon-2002]. The results of Fig. 4.13 show that NGDs should also occur for fiber Bragg gratings with an index profile like that of a quarter-wave dielectric structure.

Figure 4.14 shows the experimental, and TMM calculated, magnitude $|t|$ and phase ϕ_t of the transmission coefficient (top and middle panels, respectively) and the group delay on transmission τ_t (bottom panel) obtained from Eq. (4.8). The three considerations regarding the excellent agreement between theory and experiment which were explained above were also applied in these numerical calculations.

Fig. 4.14(a) shows the results for the $(HL)^2H$ structure. The transmission gaps at 2.5 GHz and 7.5 GHz are now the only minima in the displayed transmission spectrum where superluminal pulse propagation should be expected. Nevertheless, these minima are too wide and well above zero, and the phase on transmission ϕ_t is basically a monotonically increasing function of frequency, very much like that of a uniform waveguide. Therefore, the corresponding group delay is positive. As the number of layers N increases (see Figs. 4.14(b)–4.14(d)), the transmission gaps approach zero while keeping their width, and the slope of ϕ_t in the gap regions is smaller than outside the gaps. Therefore, τ_t becomes appreciably smaller in the gap regions as N increases, but it always remains positive. Interestingly, we found that our measured transmission coefficient data for the Bragg reflectors show that, as opposed to reflected pulses, NGDs do not occur for pulses transmitted in these linear and periodical structures. This issue is still controversial [Mun-2002, Mun-2007, Poi-2005], and in this context, our S_{21} data agree with a previous theoretical work [Poi-2005] which questioned experimental results reporting such NGDs for transmitted pulses in radiofrequency band gap structures [Mun-2002], which are a scaled version of 1D photonic crystals. Let us note, however, that NGDs do have been reported for 3D photonic crystals [Gal-2007].

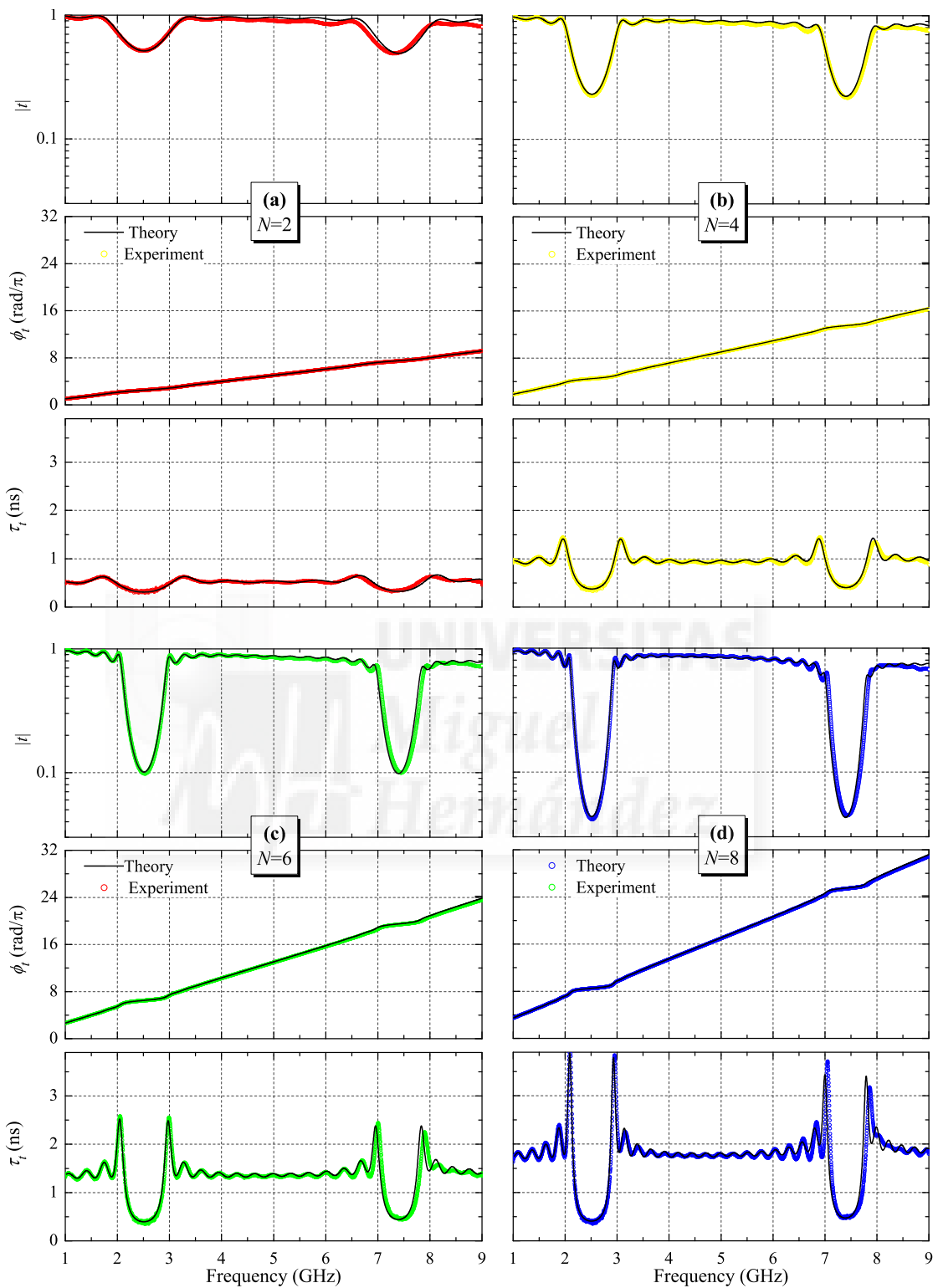


Figure 4.14: Experimental and theoretical results for the frequency-domain characterization of transmitted pulses on microstrip Bragg reflectors $(HL)^N H$. Top panel shows magnitude of the transmission coefficient, middle panel shows phase of the transmission coefficient, and bottom panel shows group delay (obtained using Eq. (4.8) after filtering the phase function) for (a) $N = 2$, (b) $N = 4$, (c) $N = 6$, and (d) $N = 8$ unit cells.

4.4.3 Results and discussion in the time domain

In order to support the previous results obtained from the frequency-domain characterization of Bragg filters, we carried out time–domain experiments for pulses reflected on these mirrors. The experimental setup is similar to the one proposed by Munday and Robertson [Mun-2002] and it is described in detail in Appendix C.3. A 20 MHz sinusoidal output of a signal generator is used to amplitude modulate the sinusoidal signal of a second generator, whose frequency can be varied up to 6 GHz. This produces a train of sinusoidally modulated wave packets with carrier frequencies (f_c) in the GHz range and 50 ns width that is reflected by the Bragg filter through a low-cost microwave power splitter. Although, a circulator should have been a more efficient way to extract the reflected wave, we decided to use a 3-dB splitter because of its simpler design and fabrication by microstrip technology. The reflected pulse train was recorded at an oscilloscope with a resolution of 12.5 ps (4 kSamples/50 ns), and the pulse delay, τ_{pulse} , is measured.

As it is mentioned, we used a microwave splitter to extract the reflected wave packets. Just as we expected (see Appendix C.3), this notably distorts the total reflection coefficient. As an example, Fig. 4.15 (lines) shows the frequency-domain characterization of the system formed by the $(HL)^4H$ Bragg filter and the splitter. In spite of this, it still exhibits the essential features of the original Bragg filter: a band pass centered at 2.5 GHz and the same number of sharp minima (but frequency shifted). Around these minima, group delays are still negative, although they are not as deep as for the Bragg filter alone. Measuring such small group delays (around -2 to 2 ns) for carrier frequencies up to 3 GHz was challenging and a very precise and systematic experimental procedure was needed.

Figure 4.15 shows (symbols) the experimental results for the reflection coefficient and pulse delay in time-domain detection. The reasonably good agreement between the results from frequency- and time-domain characterizations is a consequence of some considerations. First, the choice of 20 MHz for the modulating signal (and hence the pulse width) was made on the basis of reaching a compromise between low-distortion of the pulse and good time resolution ensuring at the same time that $\tau_{pulse} \simeq \tau_g$. And, second, since superluminal and

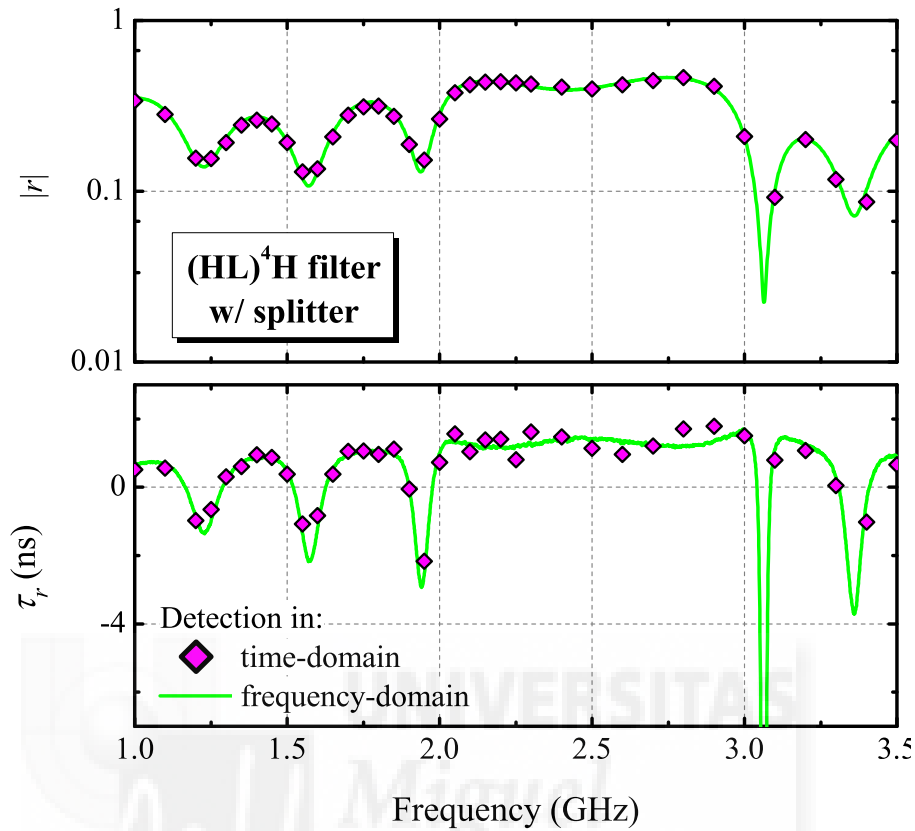


Figure 4.15: Experimental results for the frequency- and the time-domain characterization of reflected pulses on the $(HL)^4H$ Bragg reflector through a 3-dB microwave splitter. Top panel shows magnitude of the reflection coefficient, and bottom panel shows group delay (17-point-smoothed in the case of frequency-domain detection).

mostly tunnelling signals are largely attenuated, a direct observation of the pulse peak on the oscilloscope is not accurate enough in these regimes. A systematic technique to determine the pulse center, which is less vulnerable to local fluctuations than the pulse peak, is more adequate. Here, the pulse center is obtained from a numerical analysis of the data by finding the best fit to the pulse envelope.

As an example, Figure 4.16 shows the capture of pulses with very different group delays: the upper one corresponds to a carrier frequency of $f_c = 1.95$ GHz and exhibits an advancement time of around 2.2 ns, whereas the lower one corresponds to $f_c = 2.9$ GHz and exhibits a delay time of around 1.8 ns. On the other hand, negative group delay around 3.07 GHz was not measurable in time detection due to the signal low level and pulse distortion.

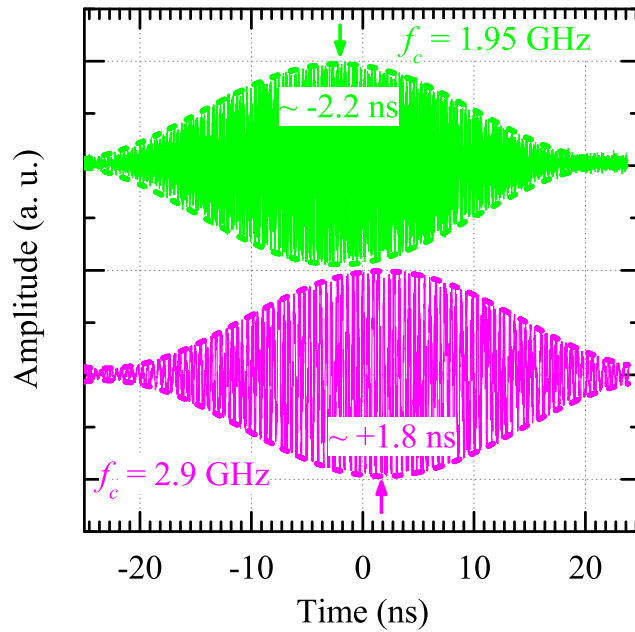


Figure 4.16: Wave-packet traces and envelopes showing two different propagation regimes, with carrier frequencies: 1.95 GHz (upper), and 2.9 GHz (lower). Each trace is normalized to its maximum value and shifted vertically for better comparison.

4.4.4 Hartman effect

The remarkable differences between the phase functions ϕ_r and ϕ_t in Figs. 4.13 and 4.14 are the origin of the differences observed in [Nim-2002] and [Doi-2007] on the Hartman effect for reflected and transmitted pulses along Bragg reflectors, as we show below. The Hartman effect is the saturation of the group delay of a pulse that propagates along a photonic barrier as the length of the barrier increases [Har-1962]. Photonic band gap structures, like Bragg reflectors, behave as such barriers for pulses with their frequency components inside the band gap. The frequency-domain characterization of our microstrip Bragg reflectors with increasing number of layers N makes possible to study the Hartman effect for reflected and transmitted pulses.

For that purpose, we consider the center frequencies of the transmission gaps (Bragg frequencies 2.5 GHz and 7.5 GHz) and we plot, as a function of length, the corresponding values for the group delay on reflection (τ_r) and on transmission (τ_t) obtained from Figs. 4.13 and 4.14. The results are shown in Fig. 4.17. The filled points in the figure correspond to the experimental values and the crossed points are the TMM calculated values for the structures with $N = 1 - 8$.

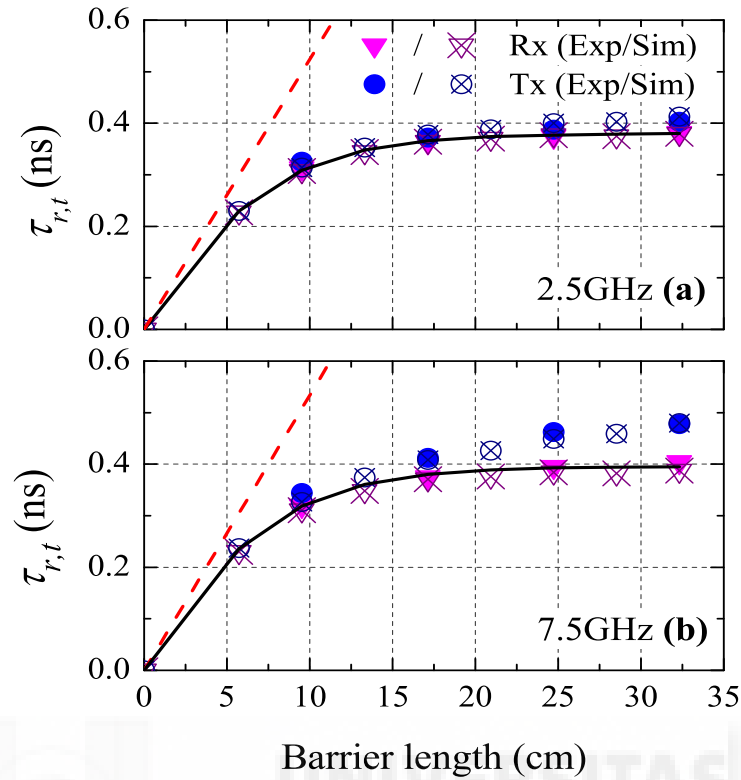


Figure 4.17: Study of the Hartman effect in microstrip Bragg reflectors. Transmission and reflection group delays as functions of the length of the $(HL)^N H$ structures at (a) 2.5 GHz, and (b) 7.5 GHz. Filled points are experimental data for $N = 2, 4, 6$, and 8 , and crossed points are TMM theoretical results for $N = 1 - 8$. The solid line is obtained using a theoretical approach for τ_r explained in the text, and the dashed line corresponds to a uniform microstrip waveguide.

The agreement between theory and experiment is very good. Also included is the calculated group delay for a uniform microstrip waveguide, τ_0 , (dashed line).

Figure 4.17(a) shows the group delays at 2.5 GHz. Reflection and transmission group delays coincide for short barriers, but as the barrier length increases, τ_r saturates for the structure with $N = 6$ layers (barrier length ~ 25 cm) whereas τ_t does not quite saturate yet. This different behaviour is more evident at 7.5 GHz (see Fig. 4.14(b)), where τ_t clearly increases with barrier length (although at a slower rate than τ_0) while τ_r takes similar values as those in Fig. 4.17(a). This behaviour was also observed in the tunnelling of radiofrequency pulses through coaxial-cable band-gap structures [Doi-2007]. It can be understood by closely examining the phase functions ϕ_r and ϕ_t as N increases: We found that the curves ϕ_r converge to the same linear function near the gap center frequency (thus yielding the same group delay), whereas the slopes of the ϕ_t curves increase slightly. This is due to the attenuation, which is higher for larger

structures and smoothes the Bragg interference in the band gap region. As a consequence, the slope of ϕ_t tends to approach the value outside the gap region.

Therefore, the results of Fig. 4.17 clearly show that the role of attenuation is much weaker for τ_r , which rapidly saturates. This result was interpreted in [Doi-2007] by regarding this kind of structures as a combination of a shortened lossless Bragg reflector and a uniform but absorptive waveguide. From this point of view, attenuation mainly affects the transmission wave and has negligible contribution to the reflected wave. Following this picture, one can attempt to estimate τ_t at f_0 for a given structure as a linear combination of τ_r and the group delay of a uniform microstrip line of the same length, τ_0 , with absorption–depending coefficients such that τ_r and τ_t coincide in the absence of attenuation. For our specific Bragg reflectors we found that a good approximation is:

$$\tau_t \approx \left(1 - \frac{A}{\sqrt{2}}\right) \tau_r + \frac{A}{\sqrt{2}} \tau_0 \quad (4.21)$$

where $A = 1 - |r|^2 - |t|^2$ accounts for the total absorption through our Bragg structures at f_0 , which can be obtained by taking into account that $r = r_0 e^{-2\alpha L_{eff}}$ and $t = t_0 e^{-2\alpha L_{eff}}$ [Col-1995], which substituted into the definition of A yields:

$$A \approx 1 - e^{-4\alpha L_{eff}} \quad (4.22)$$

The values obtained from Eq. (4.21) exactly match the TMM calculated results of τ_t shown in Fig. 4.17.

The above results point out that in the case of weak absorption, τ_r and τ_t approximately have the same value at f_0 , and a simple expression to estimate them can be very attractive. A reasonable approach considers the Bragg reflector as a discrete mirror with equal magnitude of the grating's reflection, $|r|$, but placed a distance L_{eff} away, such as it gives the proper mirror phase, ϕ_r . In this picture, τ_r , can be estimated as the propagation delay of the incident wave traversing a

distance equal to this effective mirror length L_{eff} and back:

$$\tau_r = \frac{2L_{eff}}{v_p}, \quad (4.23)$$

where the effective length of a lossless Bragg reflector can be calculated at the Bragg frequency as [Col-1995]:

$$L_{eff} = \frac{1}{2}m_{eff}\Lambda \left(\frac{1}{1+r_{HL}^2} - \frac{1}{2m_{eff}} \right), \quad (4.24)$$

where r_{HL} is the $H - L$ interface reflectivity, Λ is the length of the mirror period, and m_{eff} is the effective number of mirror periods seen by the incident field at the Bragg frequency. This number can be calculated as:

$$m_{eff} = \frac{\tanh \left[m \ln \left(\frac{1+r_{HL}}{1-r_{HL}} \right) \right]}{\tanh \left[\ln \left(\frac{1+r_{HL}}{1-r_{HL}} \right) \right]}, \quad (4.25)$$

where m is the number of mirror periods, which is $N + 1$ in our structures.

We consider a propagation velocity, v_p , as the average between the propagation velocities through 50- and 75 - Ω elements, which gives a value of approximately $c/1.57$ at 2.5 GHz. Neglecting mirror losses, L_{eff} saturates with number of mirror periods to a value of approximately 38 mm. For $N = 6$, L_{eff} is 99% of the saturation value. The calculated values of τ_r for lossless Bragg reflectors using this simple approach (see solid curve in Fig. 4.17) are in excellent agreement with the theoretical values using TMM simulations.

4.4.5 Slow light in mismatched DBRs

NGDs in reflection from slabs and Bragg reflectors were reported in the previous sections, however, no slow light regime was observed. With the aim of generating not only fast light but also slow light in a DBR, we have explored a mismatched DBR. The DBR is mismatched by

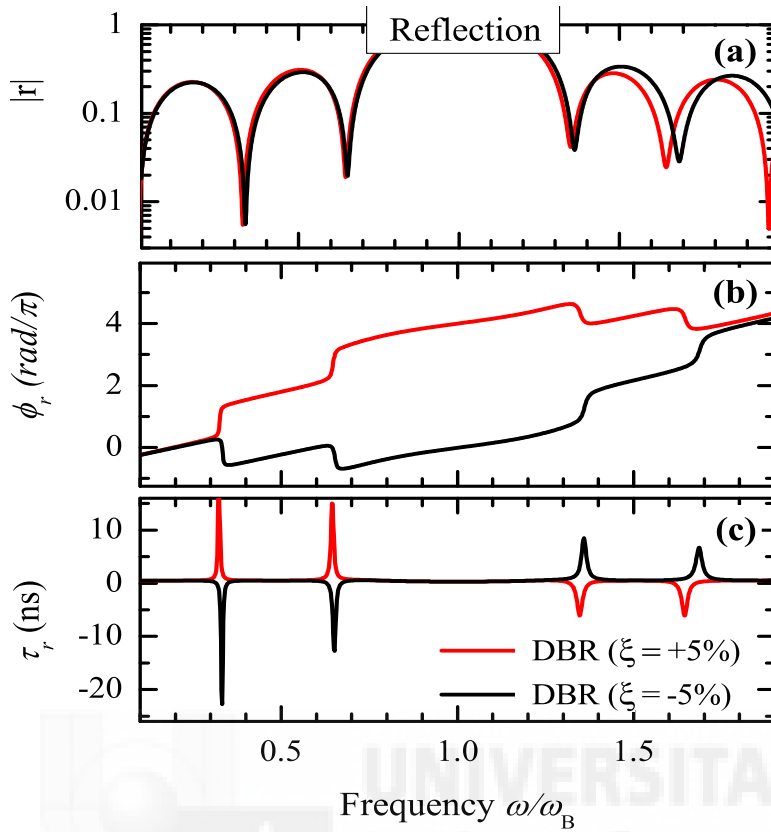


Figure 4.18: (a) Reflection coefficient magnitude (b) phase and (c) group delay of a lossy microwave DBR with $2 + 1/2$ unit cells, for two values of fractional detuning ξ ($+5\%$ (red line) and -5% (black line)).

slightly changing the length of one of its layers. We consider a DBR with $2 + 1/2$ unit cells like that of Fig. 4.12, where a length detuning in a layer implies a change in the otherwise perfect quarter wavelength layer. Subluminal propagation is demonstrated to occur if the length of any of the DBR's layer is changed in a very small fraction (ξ) of the nominal layer length.

This behaviour is observed in Figure 4.18, for a simulated Bragg reflector $(HL)^2H$ where its last layer has been increased or decreased according to $\xi = \pm 5\%$. The reflection's minima shift with ξ is clear in the group delay curves.

Let us now compare the curves in Figures 4.18 (mismatched DBR) and 4.13(a), (DBR without mismatch). Mismatch induces a change in the total length of the structure and the minima position change. For a detuning of -5% , the group delay keeps its negative value at the first and second minima, whereas large positive τ_g are achieved at the third and fourth minima. On

the other hand, if $\xi = +5\%$, the opposite effect is observed, the group delay at the first and second minima is large and positive while it is negative at the third and fourth minima.

These results resembles what was presented in Chapter 3, where asymmetric interferometers were explored and subluminal propagation was demonstrated to occur if the length of one the arms was changed in a very small fraction (ξ) of the nominal length difference Δ . As we shall see in the next chapter, mismatched DBRs can find interesting applications in digital communications systems.

4.5 SFL of reflected pulses in asymmetric Fabry-Perot filters

In this section we provide experimental evidence of group delay tuning for pulses reflected in asymmetric Fabry-Perot (FP) filters with Bragg mirrors, each one having different number of layers. We show that the group velocity can be tuned from subluminal to superluminal, and even negative values, by changing the spacing between the mirrors or the attenuation. As in the photonic band-gap systems analyzed in the previous sections, these phenomena occurs for narrowband pulses with center frequency close to the mirrors Bragg frequency, and it is associated to steep slopes of the reflection phase function at this frequency. Experiments are done in the radiofrequency range by using high and low impedance coaxial cables to build the FP filters. Also, group delays are measured in time domain by reflecting on these asymmetric FP filters a train of sinusoidally modulated wave-packets with carrier frequency in the MHz range.

4.5.1 Asymmetric Fabry–Perot filter design

Structures of the type $(HL)^{N_1}H - L' - (HL)^{N_2}H$ were assembled using coaxial cables, where H is a high impedance (75Ω , RG-59/U) cable and L and L' are low impedance (50Ω , RG-58C/U) cables. The number of bilayers in the $(HL)^N H$ Bragg mirrors are $N_1 = 1$ and $N_2 = 1, 2$ (symmetrical and asymmetrical FP filters are considered). Each layer is a quarter-wavelength cable for a design wavelength $\lambda = 4.24$ m, where λ is the wavelength

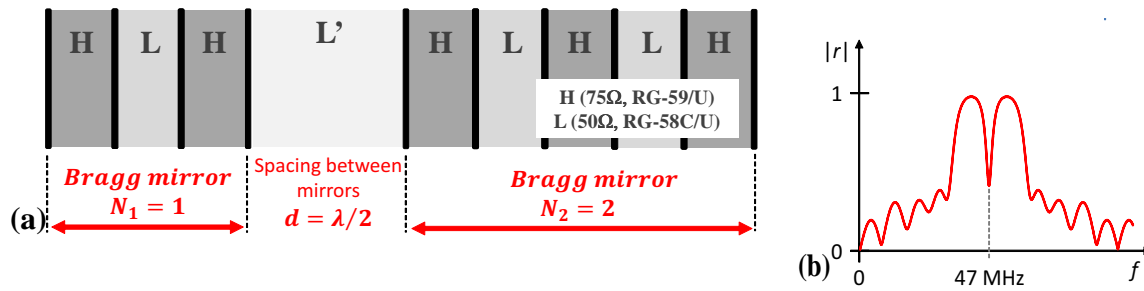


Figure 4.19: (a) Schematic of an asymmetric coaxial FP filter and (b) its ideal lossless reflection spectrum.

in the medium. Since the phase velocity in the cables is $2c/3$, the Fabry Perot filters have their first transmittance gap at a frequency of 47 MHz (Bragg frequency of the multilayer mirrors, f_B). Several such structures were fabricated with spacing d between mirrors (length of cable L') equal to $\lambda/2$, $\lambda/4$ and $3\lambda/2$. Figure 4.19 illustrates one of these RF structures, and its ideal reflection spectrum (without attenuation).

The frequency characterization of such Fabry-Perot filters was performed by means of a two-port vector network analyzer (PNA series, Agilent E8363B). The scattering parameter S_{11} (the reflection coefficient) was recorded in the range 10-100 MHz every 59.375 kHz with an average of 64 to help suppress the random noise contained in the experimental data. This noise is not very apparent in the S parameters themselves, but in order to obtain the experimental group delay $\tau_r(\omega)$, the phase data curve $\phi_r(\omega)$ is differentiated and this leads to spurious effects in $\tau_r(\omega)$. For this reason, the network analyzer was configured to smooth the phase data prior to differentiation by averaging 17 adjacent points. Although smoothing is an arbitrary process that may give results which vary critically with the smoothing parameters, we finally used a 17-point averaging algorithm that is satisfactory enough to preserve the key features of the group delay trends.

A 1×2 RF wave splitter (PE2000, Pasternack) was characterized too, since this splitter is used in the real-time pulse propagation experimental setup. The attenuation of the high and low impedance cables was determined as a function of frequency by measuring the S_{21} scattering parameter (the transmission coefficient) for each kind of cable [Dav-2006]; the

attenuation coefficients are: $\alpha_H[dB/m] = 0.0032 + 0.1\sqrt{f} + 0.00126f$ and $\alpha_L[dB/m] = 0.136 + 0.15\sqrt{f} + 0.00224f$, where the frequency is given in MHz.

Time-domain pulse propagation experiments were done on these filters. The experimental setup is shown in Appendix C.3. The 300 kHz sinusoidal output of generator–1 (Tektronix CFG-253) is used to amplitude modulate the sinusoidal signal of generator–2 (IntraAction VFE-604A4), whose frequency can be varied between 40 – 80 MHz. This produces a train of 3.3 – μs wide sinusoidally modulated wave packets with carrier frequencies in the MHz range. Although, a circulator would have been a more efficient way to extract the reflected wave, only a 3-dB 1×2 RF wave splitter (PE2000, Pasternack) was available. The reflected pulse train was recorded at the oscilloscope (Agilent DSO-6032A) with a resolution of 0.5 ns (10 kSamples/5000 ns).

4.5.2 Results and discussion in the frequency domain

We discuss here the experimental results obtained for the frequency characterization of the assembled FP structures described above. Using the phase-time approach in Eq. (4.8) the group delay as a function of frequency is obtained and compared to numerical simulations within the transfer matrix method (TMM) [Yeh-1988]. Numerical results varying the number of bilayers in the mirrors and the attenuation are also discussed.

a. Symmetric and asymmetric FP filters

Firstly, the differences between asymmetric, $(HL)H - L' - (HL)^2H$, and symmetric structures, $(HL)H - L' - (HL)H$, for pulse propagation are investigated. Figures 4.20 and 4.21 show their reflection coefficient's magnitude $|r|$, phase ϕ_r , and group delay on reflection, $\tau_r(\omega)$ obtained from the frequency derivative of the phase function $\partial\phi_r/\partial\omega$. The experimental curves correspond to the scattering parameter data S_{11} , whereas the theoretical curves (solid line) were obtained by applying the TMM, including the wave attenuation along the structure. The experimental results are excellently accounted for by the theoretical calculations because of the following issues. First, for the numerical simulation of the structures, the actual values of the H and L layers length (including the BNC connectors between the cables) are considered, which is

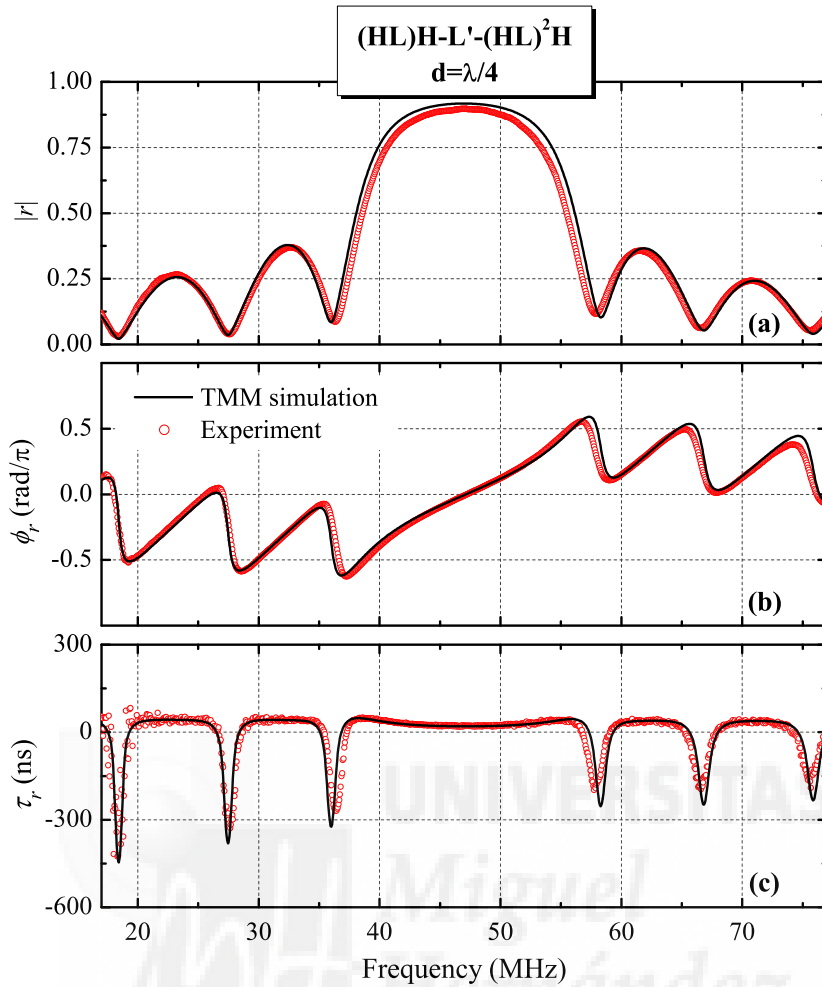


Figure 4.20: Experimental and theoretical results for the frequency-domain characterization of reflected pulses on the filter $(HL)H - L' - (HL)^2H$ with $d = \lambda/4$. Top panel shows magnitude of the reflection coefficient, middle panel shows phase of the reflection coefficient and bottom panel shows (17–point averaged) group delay.

important to avoid shifts in the positions of the resonant peaks between theory and experiment. Second, the same 17–point smoothing algorithm as that applied to the measured $\phi_r(\omega)$ curve prior to differentiation was used to calculate the group delay.

Figure 4.20 corresponds to the structure $(HL)H - L' - (HL)^2H$ with mirror spacing $d = \lambda/4 = 1.06$ m. Since all the layers are quarter-wavelength, this structure is in fact a Bragg mirror $(HL)^4H$. Its reflection coefficient's magnitude $|r|$, (top panel) shows the typical oscillations or sidelobes in Bragg reflectors discussed in 4.2.2, with one main reflection peak in the displayed frequency range laying at the Bragg frequency $f_B = 47$ MHz. Steep negative slopes in the reflection phase function ϕ_r (middle panel) occur at the sidelobes minima, thus yielding negative

group delay values (bottom panel) in a narrow frequency region around the reflection minima. Therefore, tunnelling of reflected pulses centred at the frequency minima is expected. As it was shown in section 4.4.2, if the number of HL bilayers (N) increases more minima will appear between the main reflection peaks by the rule $2N + 1$, which sharpens the reflection's minima and narrows the frequency region for negative group delay. Here, we focus on the possible propagation regime for pulses centred at the Bragg frequency. In this case, superluminal reflection with $\tau_r \sim 20$ ns is expected from Fig. 4.20. Superluminal reflection occurs if $\tau_r < 2L_T/c$, where L_T is the filter's total length (in this case $2L_T/c = 63.6$ ns). As N increases, simulations (not included here) indicate that τ_r finally saturates as a signal of the Hartman effect (see section 4.4.4).

A different situation is obtained when the mirror spacing d is not a quarter-wavelength layer. The structure is no longer a Bragg reflector, but a Fabry–Perot. The cases $d = \lambda/2$ and $3\lambda/2$ for the $(HL)H - L' - (HL)^2H$ and $(HL)H - L' - (HL)H$ assembled filters are shown in Fig. 4.21. The left column displays the reflection coefficient's magnitude $|r|$ and phase ϕ_r (top panel) and the group delay on reflection, τ_r , (bottom panel) of the asymmetrical FP filters, while the right column corresponds to the symmetrical ones. The coloured area highlights the spectral region in consideration. Several issues must be remarked.

In all cases (Fig. 4.21(a)–4.21(d)), the magnitude of the reflection coefficient shows an inverted peak at the Bragg frequency f_B , which (for the considered mirror spacings) coincides with a transmission resonance at the gap center. However, there are key differences in the phase function features around this frequency. In Fig. 4.21(a), the steep positive phase slope at the resonance leads to a marked peak in τ_r and signals subluminal reflection. Remarkably, the phase slope of the asymmetric FP filter flips its sign for $3\lambda/2$ mirror spacing (Fig. 4.21(c)), signalling tunnelling reflection. On the contrary, the symmetric structure in Fig. 4.21(b,d) does not sustain slow-fast light transition at f_B by adjusting d , since negative group delays are always obtained. Finally, these results show that the steeper the slope in ϕ_r , the deeper and sharper the group delay peak is. Hence, as in other SFL systems, large pulse delays (or advancements) occur at the expense of narrowband requirement. For instance, pulse peak advancements as large as 600 ns would be expected for narrowband pulses reflected on the asymmetric FP with $3\lambda/2$ mirror

spacing (Fig. 4.21(c)), where narrowband means that all the spectral components are comprised within the FWHM region centered at f_B . However, in the corresponding symmetric filter (Fig. 4.21(d)) the pulse bandwidth could be wider at the cost of reducing the pulse advancements to a maximum of -200 ns.

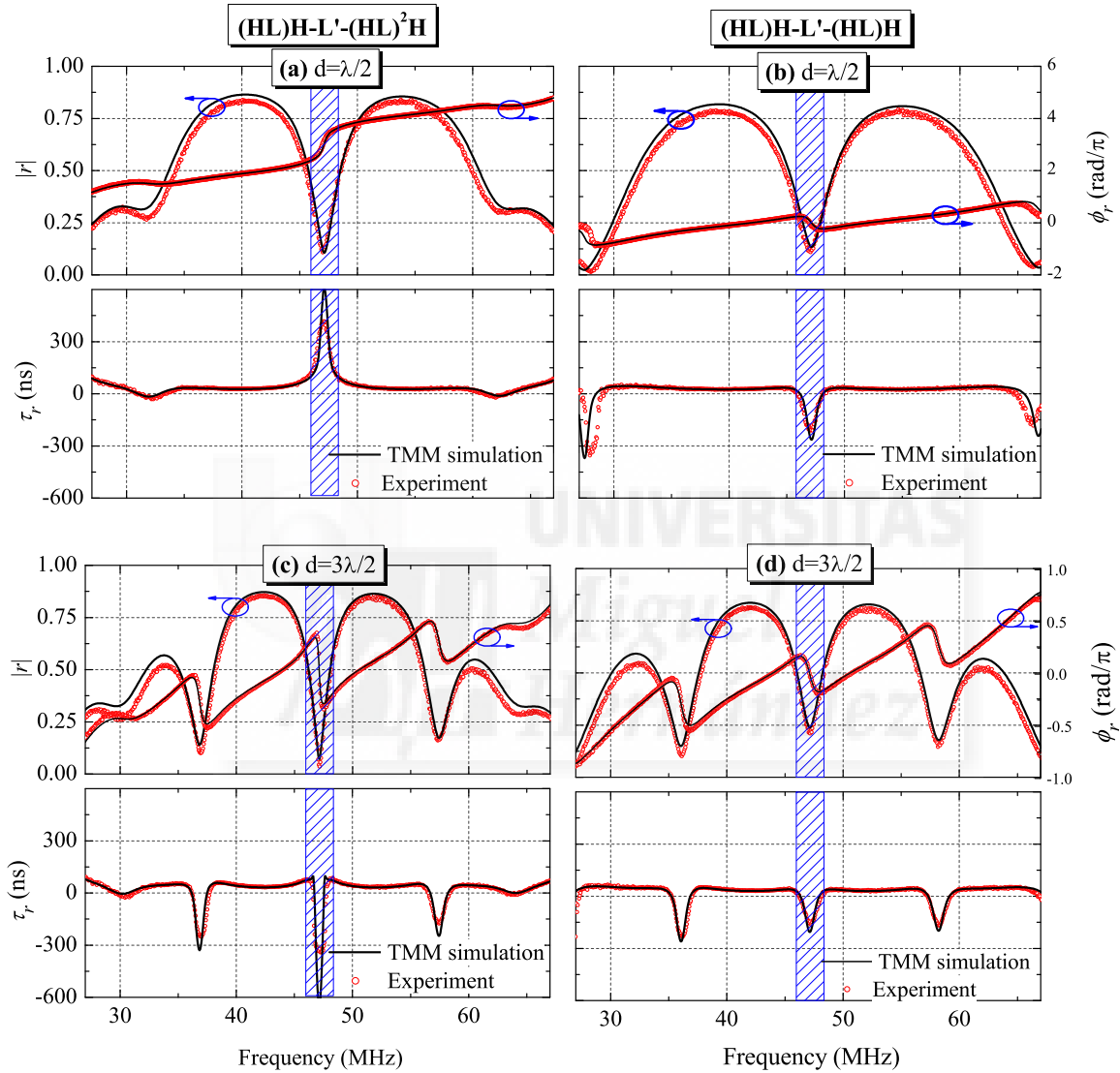


Figure 4.21: Experimental and theoretical results for the frequency-domain characterization of reflected pulses on asymmetric FP (left column) and symmetric FP (right column). Top panel shows the reflection's coefficient magnitude and phase, and bottom panel shows (17–point averaged) group delay for mirror spacing (a, b) $d = \lambda/2$, (c, d) $d = 3\lambda/2$.

To conclude, the results shown in Figs. 4.20 and 4.21 indicate that transition in the pulse reflection regime from superluminal to subluminal and furthermore to tunnelling, occurs in asymmetric FP filters by adjusting the mirror spacing from $d = \lambda/4$ to $d = \lambda/2$ and furthermore

to $d = 3\lambda/2$. This holds for narrowband pulses centered at the Bragg frequency of the multilayer mirrors in the FP. Similar results have been reported in asymmetric fiber Bragg gratings specially tailored to provide a double-Lorentzian spectral reflectivity [Lon-2002]. In that work, though, group delay tuning was probed versus frequency detuning from the Bragg resonance, i.e. by shifting the pulse carrier frequency along the band gap.

b. Attenuation-driven SFL transition in asymmetric FP filters

We analyze the role of the attenuation as the mechanism to drive the SFL transition in asymmetric FP when the mirror spacing is fixed to $\lambda/2$ or $3\lambda/2$. As an example, Fig. 4.22 displays $|r|$, ϕ_r , and τ_r in the case $N_1 = 1$, $N_2 = 2$ and $\lambda/2$ mirror spacing. The values of α indicated in the figure correspond to the total attenuation calculated at the Bragg frequency. For the typical attenuation in RG-58 and RG-59 cables the group delay at the Bragg frequency remains negative but a reduction in α by 0.5 leads from tunnelling to subluminal reflection. Similar results were obtained with $d = 3\lambda/2$ where in that case the attenuation must be reduced by 0.1. These results along with those of the previous sections, prove the feasibility of tuning the group delay in asymmetric FP filters by changing the mirror spacing and/or the attenuation.

Group delay tuning for reflected pulses have been reported in FP filters containing atomic absorbers [Rao-2004, Wan-2004]. Rao and Gupta considered a FP cavity with metallic mirrors filled with resonant absorbers and studied the propagation regimes for both transmitted and reflected pulses. Transition from subluminal to negative delay was achieved for pulses tuned at the cavity resonance by increasing the density of absorption atoms [Rao-2004]. Wang et al. report similar results for pulses reflected on a slab doped with absorptive two-level or three-level atoms, only the tuning mechanism consists in adjusting the slab's optical thickness to specific values which are even or odd multiples of $\lambda_0/4$, where λ_0 is the slab resonant wavelength [Wan-2004]. Interestingly, if the slab was doped with gain atoms no transition occurred, being the group delay on reflection subluminal (two-level atoms) or negative (three-level atoms). Active fiber Bragg gratings with an asymmetric profile have also been proposed for group delay tuning of reflected pulses [Lon-2005]. In that case the transition from tunnelling to subluminal regime is driven by gain and occurs through the passage of a local zero reflectivity condition.

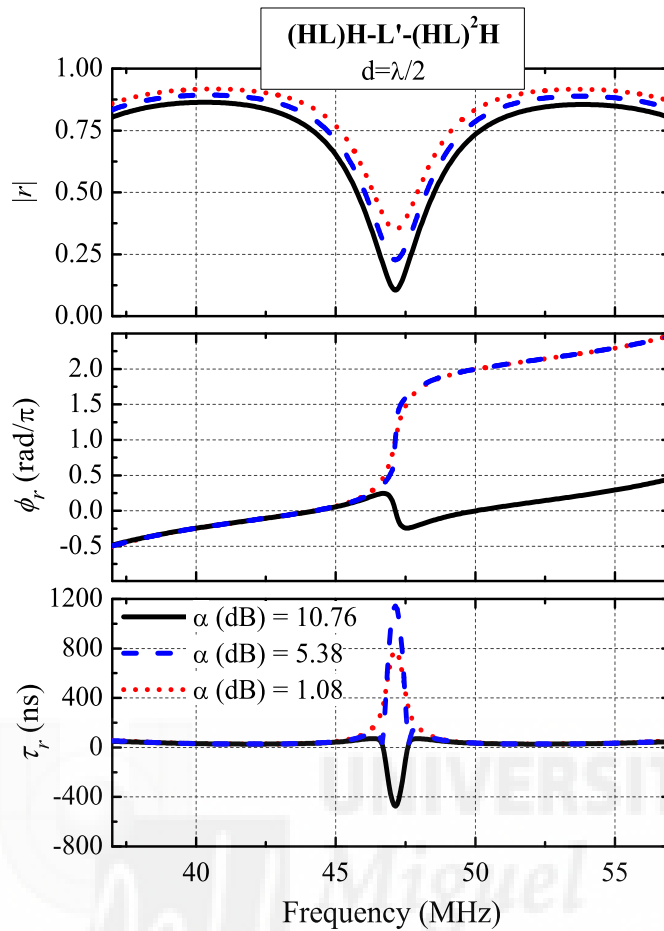


Figure 4.22: TMM simulations on the asymmetric FP filter $(HL)L - L' - (HL)^2H$ for mirror spacing $d = \lambda/2$ and three values of the total attenuation α at the Bragg frequency (47 MHz). Top panel shows magnitude of the reflection coefficient, middle panel shows phase of the reflection coefficient and bottom panel shows (17–point averaged) group delay.

As opposed to the systems cited above, we have shown the feasibility of group delay tuning in entirely passive asymmetric Fabry-Perot structures with multilayer mirrors.

4.5.3 Results and discussion in the time domain

Phase-time approach retrieval of the group delay values do not exactly correspond to the pulse delay measured in a time-domain experiment. Only for very narrowband pulses these delays coincide. Therefore, we probe in a time-domain experiment the feasibility of the proposed system for achieving group delay tuning of reflected pulses. As it was previously mentioned, a 3–dB 1×2 RF wave splitter is used to extract the reflected pulse in the time-domain experimental setup (see Appendix C.3). A certain distortion in the total reflection coefficient is

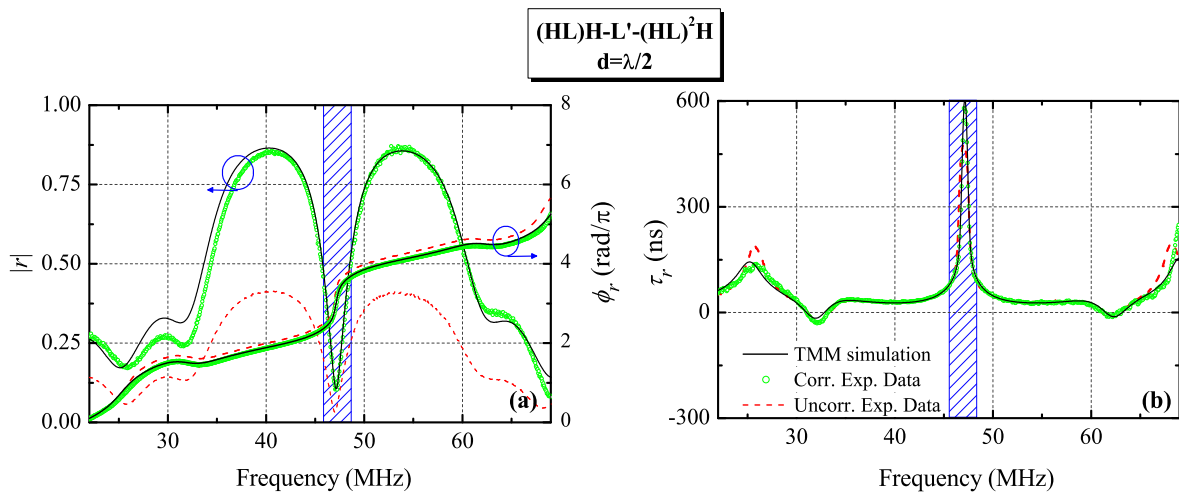


Figure 4.23: Frequency-domain characterization of reflected pulses on the system splitter + $(HL)H - L' - (HL)^2H$ ($d = \lambda/2$). Dashed red curves are the raw data. Green points are the experimental data after subtracting the effect of the splitter. Solid black line is the TMM simulation (without splitter). (a) Magnitude and phase of the reflection coefficient, (b) group delay.

thus expected. For this reason, prior to the time-domain characterization of our FP structures, it is necessary to determine the splitter's effect on the reflection coefficient and consequently on the group delay. This is done by measuring the S parameters of each splitter + FP system with the vector network analyzer.

As an example, Fig. 4.23 shows the frequency-domain characterization of the system formed by the splitter and the Fabry-Perot filter $(HL)H - L' - (HL)^2H$ with $d = \lambda/2$. In panel (a) we plot the magnitude and phase of the system's reflection coefficient, and in panel (b) the corresponding group delay obtained from the phase time approach (17-point smoothed). Three curves are shown. The dashed curve is the raw data of the splitter+FP system (labeled *uncorrected experimental data*), the green curve (labeled *corrected experimental data*) is the result of subtracting the effect of the splitters, and the solid curve corresponds to the TMM simulations (which do not consider the splitter). Simulations and corrected experimental data are in excellent agreement, thus assessing the accuracy of the procedure employed to subtract the effect of the splitters. The splitter's effect is deduced by comparing the uncorrected and corrected experimental data. Obviously, the splitter introduces losses and the amplitude of the pulse reflected on the system will be reduced. The splitter adds an additional phase (the raw

data phase function is above the numerical one) but since the features of the phase function are preserved, it has basically no effect on the group delay (note the perfect matching of the two experimental curves for τ_r). Therefore, the system exhibits the same features of the original Fabry–Perot filter, with a higher attenuation.

Let us now show in time domain the transitions in the propagation regime of reflected pulses that were predicted in the frequency-domain. Three structures are characterized: the $(HL)H - L' - (HL)^2H$ asymmetric Fabry-Perot with mirror spacing $d = \lambda/4, \lambda/2$ and $3\lambda/2$. The experimental setup is described in appendix C.3 (Fig. C.6). The modulating signal is a 300 kHz sinusoidal wave, which results in a $3.3 - \mu s$ wide pulse. This choice of the modulating frequency is a trade-off between narrow-enough bandwidth to avoid pulse distortion and large-enough bandwidth to get appreciable pulse peak advancements (or delays) in comparison to the pulse length. For each Fabry–Perot filter, the carrier frequency is tuned to the Bragg frequency ($f_B = 47$ MHz). Once again, because of the strong signal attenuation, a direct observation of the pulse peak on the oscilloscope was not accurate enough to measure the group delay. Hence, the pulse peak position was obtained by finding the best fit to the pulse envelope.

Figure 4.24 shows the pulse captures for the three asymmetric FP filters where each trace was normalized to its maximum value. The arrow indicates the envelope peak, whose delay is obtained as explained in appendix C.3. The transition in the pulse propagation regime is evident. The delay for the pulse reflected on the FP filter with $\lambda/4$ spacing between mirrors is 37 ns, which corresponds to superluminal reflection. By increasing the mirror spacing to $\lambda/2$, slow-light reflection with positive pulse delay of +679 ns is detected, this delay is about 12 times larger than that expected at the normal group speed. Eventually, a negative pulse delay of -485 ns is measured for $3\lambda/2$ mirror spacing. Negative delay means that the peak of the reflected pulse appears before the peak of the incident pulse has entered the structure (tunnelling regime). As it is clearly demonstrated in [Pev-2008], abnormal peak advancements and delays arise from the coherent interference of the pulse frequency components. Each component travels at the phase velocity $2/3c$ in the cables, but their relative phases are modified after the pulse's reflection on the system; as a result, the peak of the reflected pulse (where the

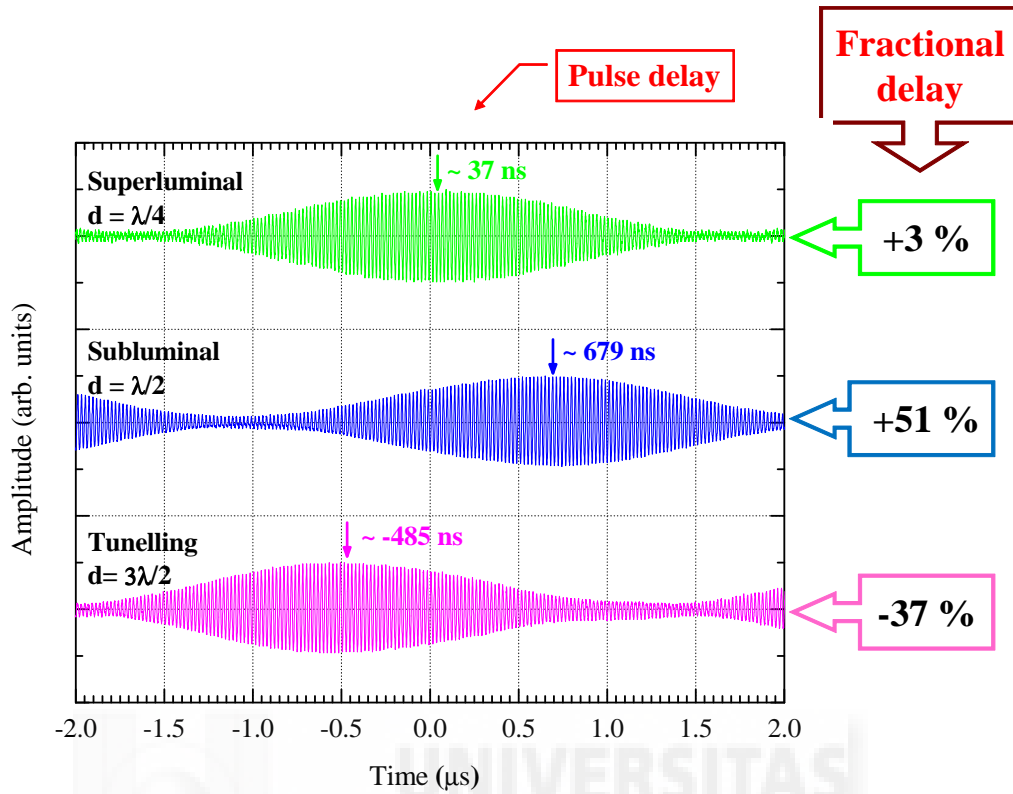


Figure 4.24: Wave-packet traces of $(HL)H - L' - (HL)^2H$ with mirror spacing $d = \lambda/4$, $d = \lambda/2$ and $d = 3\lambda/2$. The pulse carrier frequency is the Bragg frequency (47 MHz). The arrow indicates the envelope peak whose delay is obtained as mentioned in Appendix C.3. Each trace is normalized to its maximum value.

frequency components are all in phase) is shifted backwards (or forwards) and the pulse appears to travel at superluminal (or subluminal) speed. Because of the low modulating frequency, the pulses are hardly distorted.

A figure of merit of SFL systems is the fractional delay, defined as the ratio between the pulse delay and the duration of the incident pulse, T_{in} . Different definitions of the pulse duration are considered that lead to different estimations of the fractional delay. In our experiments, if we take T_{in} as the period of the modulating signal ($3.3\mu s$), the fractional delays obtained are: +1% ($d = \lambda/4$), +21% ($d = \lambda/2$) and -15% ($d = 3\lambda/2$). A common definition is to take T_{in} as the FWHM of the detected pulse; in our experiment that is the pulse *amplitude* signal. However, for a comparison with SFL systems in the optical range (where the optical *power* instead of the field envelope is detected) we must define T_{in} as the FWHM of the pulse power signal. In this case, the fractional delays become +3%, +51% and -37%. These values are comparable

to those encountered in active fiber Bragg gratings [Lon-2005], where gain-driven group delay tuning from slow to fast-light reflection was predicted with $\sim +50\%$ and $\sim -40\%$ fractional delays.

4.6 Conclusions

In this chapter the arising of slow and fast light for reflected pulses in linear and passive slabs and multilayer systems was studied. So far, SFL in reflection had only been reported for doped multilayer systems, and in left-handed media. The conclusions to be reached in this chapter are the following:

- I. We have provided experimental evidence of NGDs for reflected pulses on microstrip slabs, thus confirming previous reported theoretical predictions on optical dielectric slabs. Group delays as low as -9 ns were obtained by frequency-domain characterization of a weakly absorbing microstrip line at 2.5 GHz. This microwave operating device scales excellently to its corresponding structure in the optical range. The reflective group delay at the slab's design frequency verifies a simple scaling law, in the same way as that obtained for pulses transmitted on weakly attenuating MZIs.
 - II. We have also provided experimental evidence of NGDs for reflected pulses on microstrip Bragg reflectors, with group delays as low as -8 ns. As in the case of slabs, this phenomenon occurs in a very narrow frequency interval around the reflection minima and is a consequence of the steep negative slope of the reflection phase function at these frequencies.
 - III. We have also measured pulse delays directly in the time-domain. The results obtained for microstrip Bragg filters using a power splitter are in very good agreement with their frequency-domain characterization. An advancement of 2.2 ns was detected for a wave-packet of 1.95 GHz carrier frequency and 50 ns width.
 - IV. Also, relevant differences in the Hartman effect for reflected and transmitted pulses on Bragg reflectors have been shown in this work. Namely, the much faster saturation rate
-

of the group delay in reflection, which is hardly affected by the attenuation. We have provided a new interpretation of this effect in terms of the mirror's effective length. Slow light on reflection is shown to occur at some of the reflection minima in mismatched DBRs, where the length of one of its layers is changed in a very small fraction of the nominal length.

- V. We have shown that group delay tuning can be achieved in passive asymmetric Fabry-Perot filters with Bragg mirrors by adjusting the mirror spacing or the attenuation. This occurs for reflected narrowband pulses tuned at the Bragg frequency when the mirror spacing changes from $d = \lambda/4$ (superluminal) to $d = \lambda/2$ (subluminal) and finally to $d = 3\lambda/2$ (tunnelling). Fixing the mirror spacing to $d = \lambda/2$ or $d = 3\lambda/2$, a reduction in the attenuation coefficient yields a fast to slow light transition at the Bragg frequency.
 - VI. Experimental evidence of group delay tuning in passive asymmetric Fabry-Perot filters was obtained in the RF range by using 3.3μ -wide sinusoidal wave-packets that were reflected on Fabry-Perot filters based on high and low-impedance coaxial cables. Fractional delays from +51% (subluminal) to -37% (tunnelling) were measured upon increasing the mirror spacing. These values are similar to the fractional delays expected in active asymmetric fiber Bragg gratings upon changing the gain.
 - VII. Finally, the possibility of advancing or delaying pulses reflected on these linear and passive multilayered devices might be interesting for sensing purposes and for applications that require group delay control (like that discussed in the next chapter). Other applications include more efficient non-linear optical devices, enhancing the sensitivity of interferometers, switches and delay lines among others. These systems can be scaled to the optical range due to the universality of the wave interference phenomena, and are proposed as an alternative to SFL techniques based on active or non-linear media.
-

Chapter 5

Efficiency enhancement of feedforward amplifiers based on DBRs

In this chapter, an alternative topology for the feedforward amplifier based on a distributed Bragg reflector (DBR) is proposed and analyzed. Around its reflection minima, a DBR exhibits a negative group delay (NGD) in reflection, whereas it behaves normally in transmission, i.e., with positive group delay (PGD). We demonstrate that the length of the delay lines that are used to balance the loops in the conventional feedforward scheme can be reduced, or even eliminated, by employing a DBR as a NGD circuit in reflection and a PGD circuit in transmission. Firstly, feedforward linearization technique and general scheme of a feedforward amplifier are described. Secondly, we describe the concepts that must be considered when designing the DBR to be applied in the feedforward amplifier that is proposed in third section. The simulated performance of such feedforward amplifier is shown in the fourth section for a two-tone probe signal and a 2-channel wideband code-division multiple-access band (WCDMA). In both cases, a linearization improvement of at least 40 dB is obtained within a 10 MHz bandwidth. This DBR-based feedforward scheme provides a theoretical efficiency enhancement comparable to that achieved in feedforward architectures with a NGD circuit, and leads to a larger size reduction. A comparison of our results with those of previously reported feedforward topologies is given. Finally, the conclusions of this chapter are summarized.

5.1 Feedforward amplifier description

Feedforward is one of the preferred linearization techniques in actual digital communications and multicarrier systems, specially in base-station applications within the frame of modern wireless communications. This technique is well known for its ability of working with wideband signals and for its good performance in terms of linearization and stable operation [Cri-2002].

The general scheme of a feedforward amplifier based on delay lines consists of two loops, as shown in Fig. 5.1. The first one is the signal cancellation loop, where the intermodulation distortion (IMD) generated by the main power amplifier (MPA) is isolated by subtracting the input signal to the MPA output signal. The resulting error signal is an estimation of the distortion introduced by the amplifier. Since the power level of the error signal is small, it is necessary to use an error power amplifier (EPA) by means of a second loop (distortion cancellation loop) which hardly brings in distortion. By combining the signal at the output of the main amplifier with that of the error amplifier, the distortion generated by the former can be reduced. In order to compensate the time delay introduced by both the main and error amplifiers, delay elements in each loop are employed.

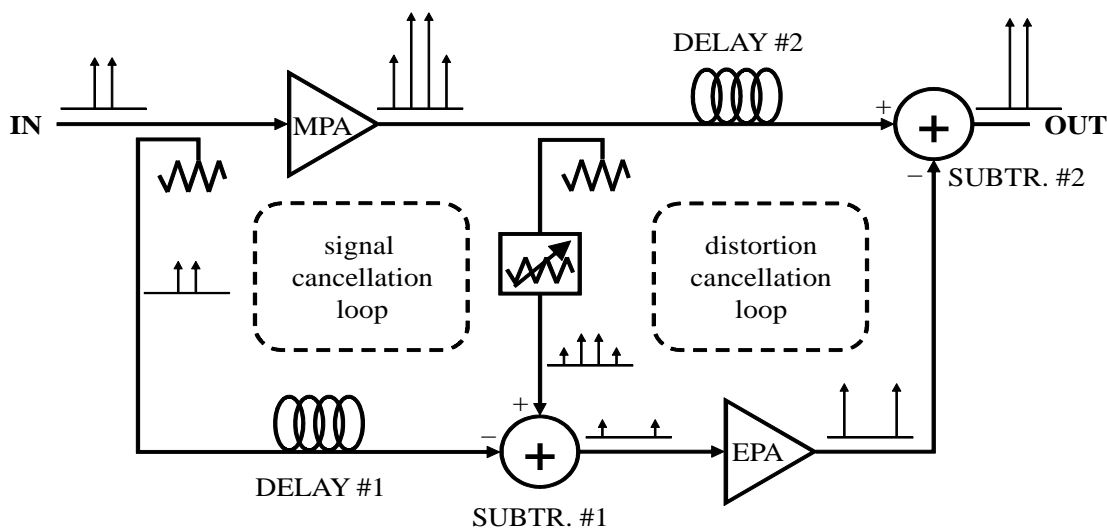


Figure 5.1: General scheme of a conventional feedforward amplifier with delay lines to compensate the delays introduced by the amplifiers.

The success of the feedforward linearization technique requires a high degree of amplitude and phase matching between the signals in the branches that are combined. Various techniques to compensate the amplitude and phase imbalances (that inevitably occur due to component tolerances, temperature drifts and operating changes) have been reported [Gar-2006, Kur-2007]. Most of them are based on an adaptive control of complex coupling factors that are introduced in the conventional feedforward topology by means of adjustable devices, like vector modulators.

Another key aspect is the power efficiency. The main sources of efficiency degradation are the power consumption of the EPA and the delay elements connected at the output of the MPA. To optimize the efficiency, the EPA power consumption can be minimized [Lar-2005]. But still the use of delay elements markedly degrades the efficiency because of their insertion losses [Par-1994]. Therefore, minimization of the delay elements is critical for high efficiency applications. Furthermore, a reduction in the size and cost of the feedforward amplifier would be achieved, because the delay elements are typically bulky and expensive high-power coaxial cables or delay-line filters.

In this context, the concept of negative group delay (NGD) has taken a prominent role and various applications with passive [Not-2007] and active [Cho-2010, Rav-2007] electronic circuits were proposed. As we have seen and analyzed in the previous chapters, in a NGD circuit, the time that takes the peak of the signal's envelope to be transmitted (or reflected) by the circuit is negative, i.e. the envelope's peak exits the circuit before the peak of the input pulse has entered it. This occurs for rather narrowband signals with carrier frequency where the circuit's transmission (or reflection) phase function $\phi(\omega)$ has a rapid decrease with frequency.

The NGD-circuit solution to the feedforward amplifier implies compensating the positive delay introduced by the amplifier's components, thus avoiding (or at least reducing) the use of delay lines. This modification of the conventional feedforward topology was, to our knowledge, first proposed in [Not-2007]. The NGD circuit consisted in three series RLC resonators arranged in π shape and connected at the driver stage of the EPA. A 40% reduction of the delay line in the distortion cancellation loop was reported. However, this system is not convenient to amplify wideband modulated waveforms such as wideband code-division multiple access (WCDMA) signals, where the bandwidth is about 5 MHz. A more adequate proposal was reported in

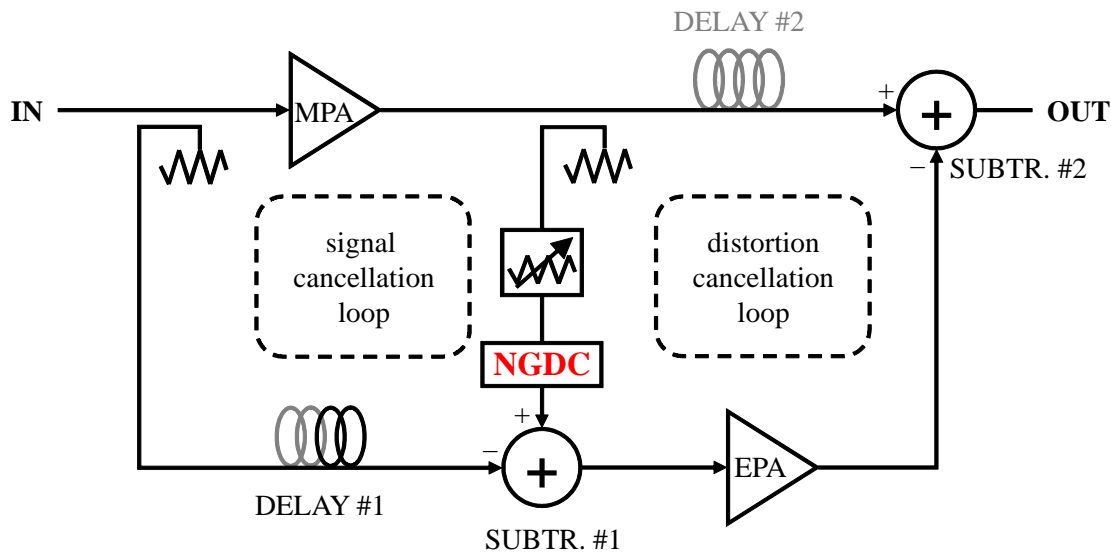


Figure 5.2: Scheme of a feedforward amplifier based on an NGD circuit.

[Cho-2010] and is illustrated in Fig. 5.2, where an active NGD circuit with distributed elements (transmission line resonators) in the common branch of the two loops is employed. As a consequence, the delay line in the second loop, which greatly contributes to the efficiency degradation, is almost completely reduced and that of the first loop is substantially shortened. Nevertheless, small signal high gain amplifiers had to be connected to compensate for the NGD-circuit loss [Cho-2010]. Although the dc power consumption of these small signal amplifiers is less than that consumed by the delay lines in the conventional feedforward scheme, an alternative solution might be interesting.

We have provided experimental evidence of negative group delays in distributed Bragg reflectors (DBR) fabricated with microstrip technology, for pulses centred at the frequencies of the reflection minima in chapter 4. Around these frequencies, it is possible to delay the transmitted pulse while advancing the pulse reflected on the DBR.

In this chapter, we set as our goal to demonstrate the viability of a new feedforward amplifier topology, where the delay elements in both loops are almost completely eliminated by using a microstrip DBR as delay compensation element. Such DBR is a simple, passive, compact and low-cost structure.

5.2 Bragg reflectors design

A Bragg reflector operative at microwave frequencies can be made by periodically connecting conventional microstrip transmission lines of different widths, all of them quarter-wavelength for a given design frequency, as it has been studied extensively in the previous chapter. We design $(LH)^N L$ structures, where L is a low impedance line (40Ω), H is a high impedance line (50Ω), and N is the number of unit cells (LH) . Fig. 5.3 gives an example of such a DBR structure with $N = 3\frac{1}{2}$ periods. The impedance and effective dielectric constant of each line is calculated using the Hammerstad-Jensen approximation [Ham-1980] for a high-frequency double-sided copper plated laminate of 60 mil thickness, a relative dielectric constant of 3.6 and 0.0013 loss tangent. These are the properties of the commercial RT/duroid 6035HTC laminate, which is a suitable choice for high power applications due to its high thermal conductivity.

The resulting impedance profile is the origin of the device's typical behaviour, which is depicted in Fig. 5.4 for a DBR structure of $3\frac{1}{2}$ periods, 40/50 impedance contrast and design frequency $f_0 = 3.23$ GHz. The transmission and reflection coefficients (panels (a) and (b)) were simulated using the transfer matrix method [Yeh-1988] adapted to microstrip structures (see chapter 4). The group delay curves in panel (c) were obtained by deriving the corresponding phase function with respect to frequency. The DBR exhibits a rejection band (or band gap) in transmission and a passband in reflection centred on the design frequency f_0 . Besides this principal band (which repeats at odd multiples of f_0), the reflection coefficient shows a number of local minima around which the group delay in reflection (τ_r) is negative: the smaller the value of the reflection minimum, the narrower and more pronounced is the corresponding peak in τ_r . Because of the attenuation, the magnitude of τ_r at the reflection minima gets smaller for higher frequencies.

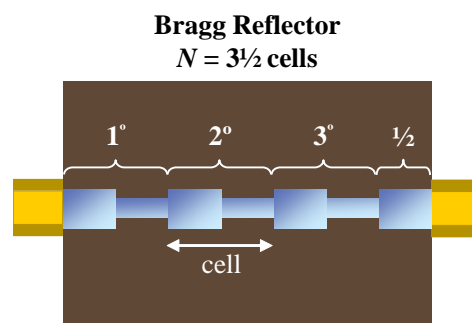


Figure 5.3: Microstrip Bragg reflector structure $(LH)^N L$ of $3\frac{1}{2}$ periods.

Interestingly for our purposes, at the reflection's local minima the group delay in transmission (τ_t) is positive. This situation is more remarkable at the frequencies on the band gap edge, which exhibit strong NGD in reflection and PGD in transmission. As it will be clear in the following sections, this feature is essential for applying the DBR to the feedforward amplifier.

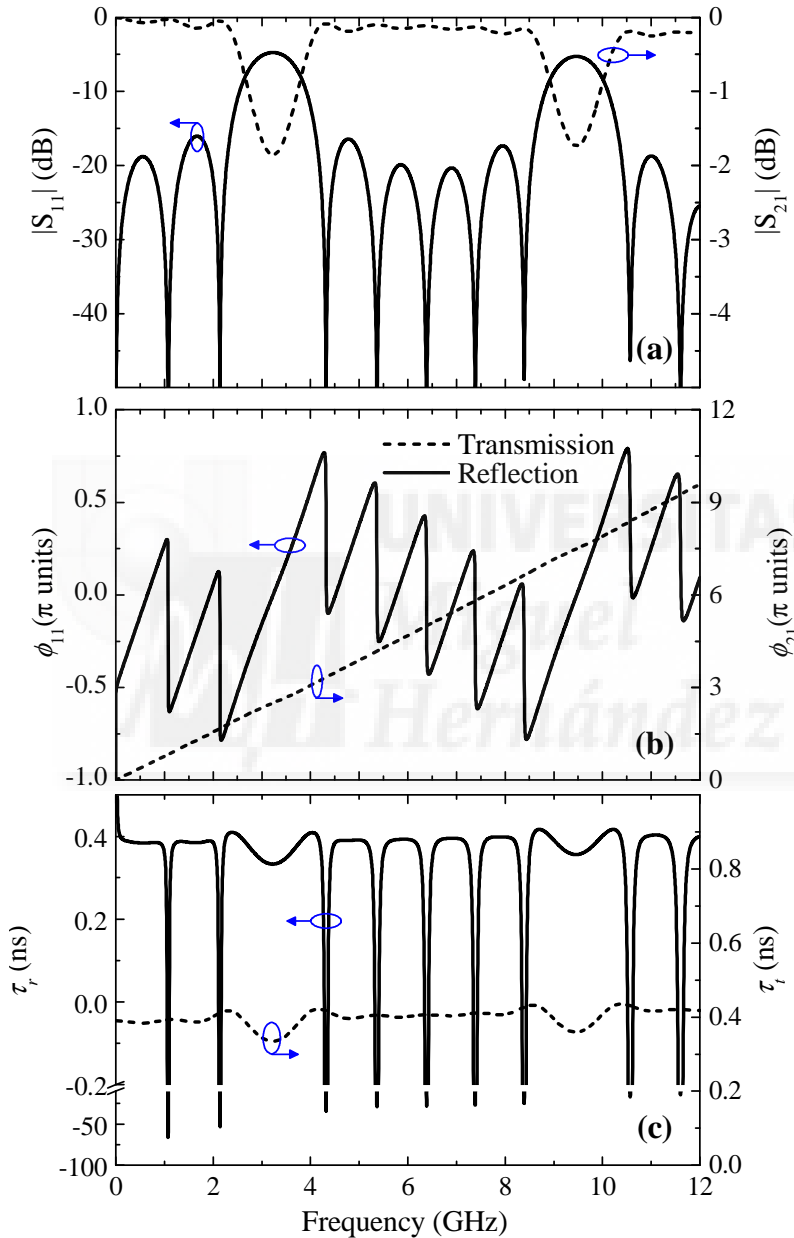


Figure 5.4: Simulated results of the (a) magnitude of the transmission coefficient S_{21} (dashed line) and of the reflection coefficient S_{11} (continuous line), (b) transmission and reflection phase functions (c) group delay of the DBR structure $(LH)^3L$ with impedance contrast 40/50.

Therefore, the starting condition in the design of the DBR is to set one of the reflection's local minimum (usually, but not necessary, the lower band edge) at the desired frequency value.

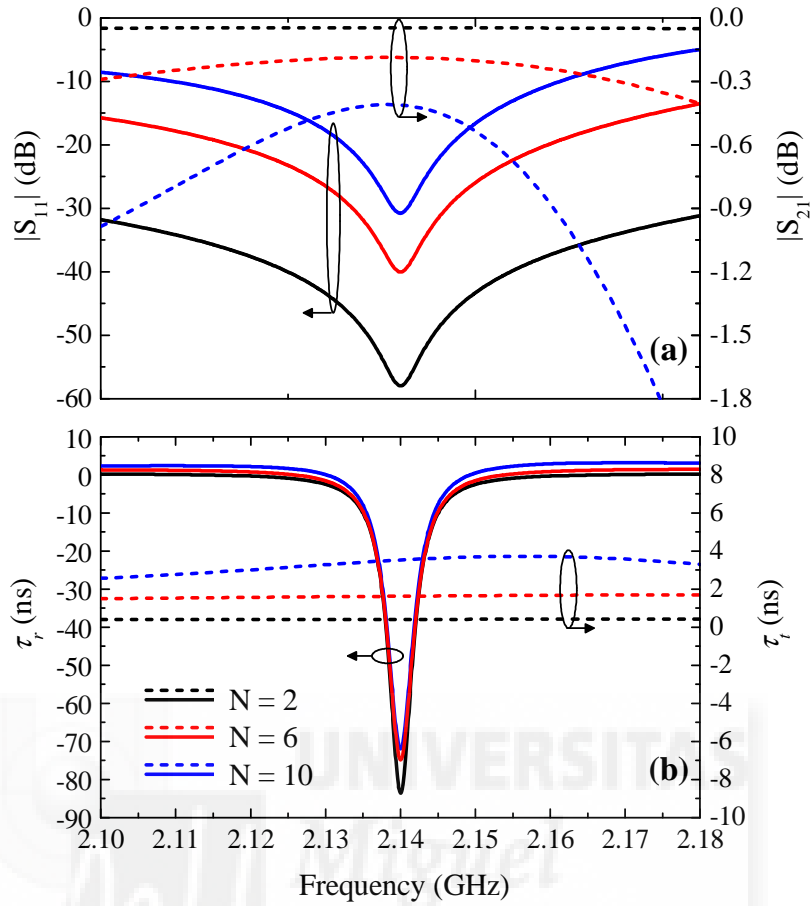


Figure 5.5: Simulation of (a) reflection (solid lines) and transmission (dashed lines) coefficients, and (b) group delay in reflection (solid lines) and in transmission (dashed lines) of $(LH)^N L$ Bragg reflectors with impedance contrast 40/50, for $N = 2$ (black), 6 (red) and 10 (blue).

Such target frequency corresponds to the main spectral component of the signal entering the feedforward amplifier. We need to know what determines the location of the minima. Numerical simulations show that the number of minima between principal bands increases as the number of periods N increases. The position of a minimum of the reflection coefficient is mainly linked to the design frequency (i.e., to the length of the elements in the unit cell) and to the number of periods. Although in a less drastic way, the position of the minima is also affected by the impedance contrast.

Let us analyze the degree of control of the NGD and PGD values at the reflection's minima, since the ability to design the DBR with the desired group delay values is necessary for the application proposed in this work. Fig. 5.5 shows the evolution of the reflection and transmission coefficients and group delays with the number of periods N in the frequency region

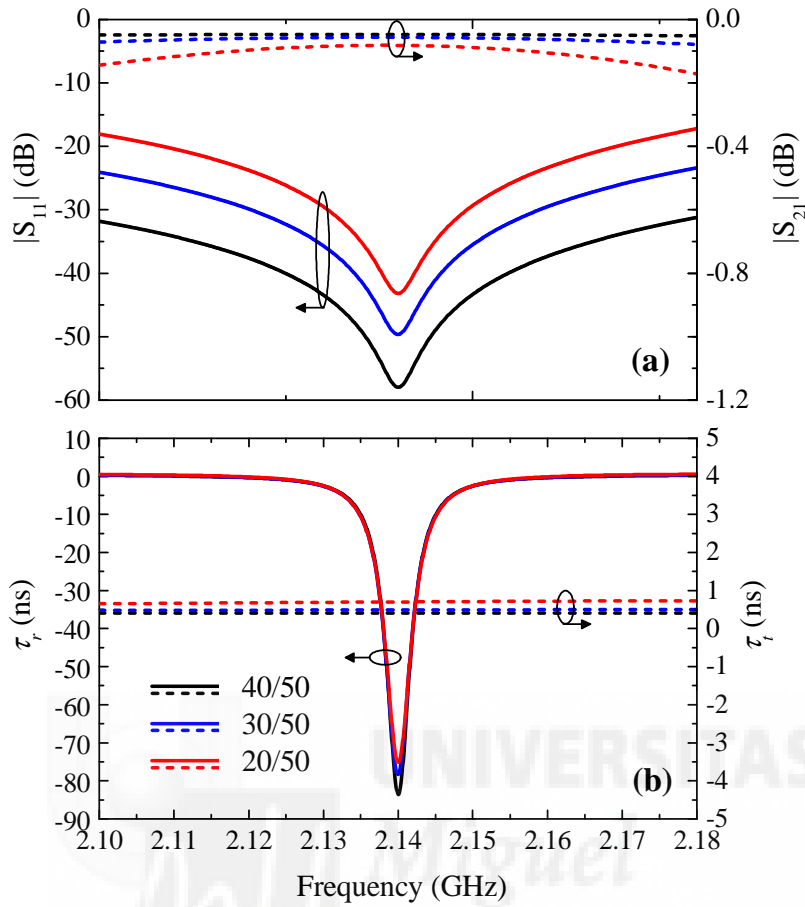


Figure 5.6: Simulation of (a) reflection (solid lines) and transmission (dashed lines) coefficients, and (b) group delay in reflection (solid lines) and in transmission (dashed lines) of $(LH)^2L$ Bragg reflectors with different impedance contrast: 40/50 (black), 30/50 (blue) and 20/50 (red).

centred on the lower band edge. Three structures $(LH)^N L$ with impedance contrast 40/50 and periods $N = 2, 6, 10$ are considered. As N increases from 2 to 10, the reflection coefficient increases more than 27 dB. At the same time, the absolute value of τ_r decreases in more than 11 ns. In turn, the transmission coefficient decreases in less than 0.4 dB, and τ_t increases in less than 3.2 ns. The effect of the impedance contrast on the group delay at the lower band edge is illustrated in Fig. 5.6. It shows simulations on the $(LH)^2L$ Bragg reflector for the following L/H values: 40/50, 30/50, 20/50. The position of the minimum is affected only slightly by the impedance contrast. As the impedance contrast increases from 40/50 to 20/50, the reflection coefficient increases more than 14 dB. At the same time, the absolute value of τ_r decreases in more than 8 ns. In turn, the transmission coefficient decreases in less than 0.04 dB, and τ_t increases in less than 0.3 ns.

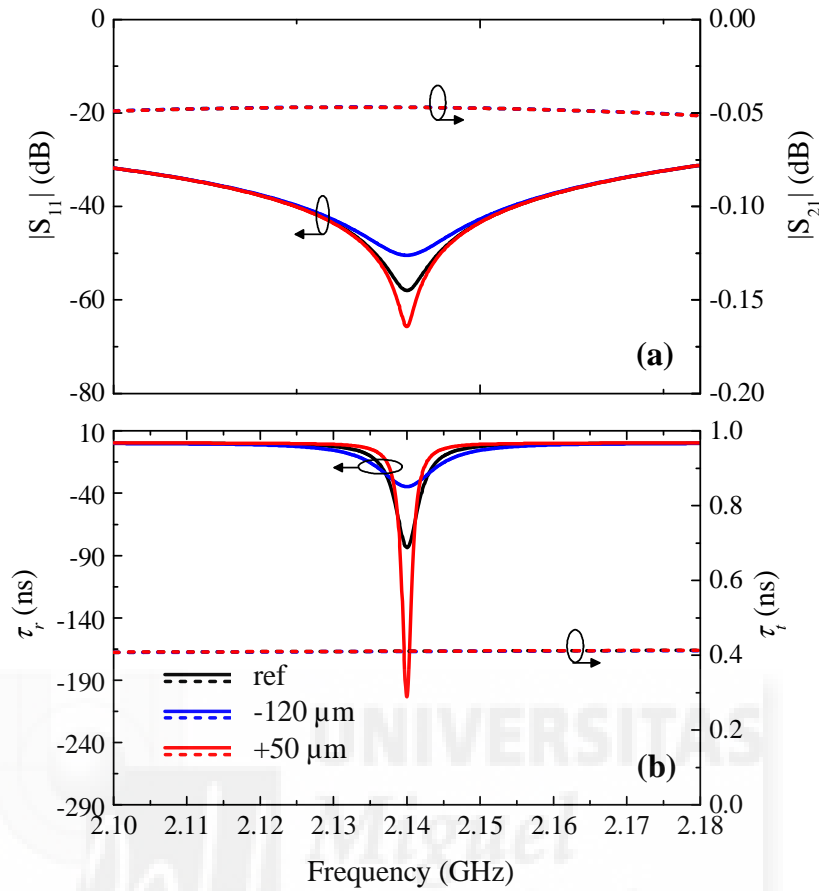


Figure 5.7: Evolution of the reflection and transmission coefficients (top panel) and group delays (bottom panel) when readjusting the length of the last element in a DBR with $2^{1/2}$ periods. Each period consists of a 40Ω and a 50Ω microstrip line with length designed to obtain the 2^{nd} minimum at 2.14 GHz.

Considering the range of group delay values displayed in these figures, we conclude that the group delay's absolute value at a given frequency close to a reflection minimum varies only very little with the impedance contrast or with the number of periods. Hence, the change of these two parameters within the fabrication practical limits makes it possible to modify the group delay in a few nanoseconds. Nevertheless, if a broader range of group delay values are required, action should be taken on another aspect of the structure.

With this idea, we have analyzed various DBRs where the length of one of its elements is slightly changed from its expected value. Fig. 5.7 shows the effect of diminishing or augmenting the length of the last element of a DBR of $2^{1/2}$ periods which was designed to obtain the 2^{nd} minimum (lower bandedge) at 2.14 GHz with elements of 13.5 mm approximate

length. Considering as starting point a reference structure with group delay at the minimum of about -84 ns, it is possible to reach -200 ns by only increasing in $50 \mu\text{m}$ the length of the last element, whereas -30 ns NGD would be achieved by only reducing the length in $120 \mu\text{m}$.

The typical delay magnitude required for these structures in order to linearize power amplifiers operative at microwave frequencies lies below 20 ns. Hence, the length reduction in the last element must be hundreds of microns. Besides, the rest of elements will have to be readjusted to avoid changing the frequency of the minimum. If the number of periods is increased, the effect of readjusting the last element is less severe, thus enabling a finer control over the group delay. Consequently, when designing the DBR, attention should be paid to the accuracy of the fabrication system in order to decide what number of periods leads to a good compromise between device size and degree of control on the delay.

Regarding the transmission coefficient, this passive device exhibits a relative flat response around the frequencies of the reflection minima. It can be easily designed to yield transmission values above 98% with group delays below 0.5 ns, as far as high frequency substrates are employed.

The design of the DBR that actually is used in our feedforward amplifier takes into account the above considerations. The number of periods is left low to reduce size. The impedance contrast is chosen so that the magnitude of S_{11} is appropriate for signal cancellation in the first loop. Finally, the length mismatch of the last element is adjusted to achieve the proper group delay on reflection.

5.3 Feedforward topology with DBR

We replace the NGD circuit proposed in in previous schemes [Not-2007] and [Cho-2010] by a microstrip DBR, with the aim of reducing the length, not just of the delay line in the distortion cancellation loop, but also of that in the main loop. This solution is based on the ability of DBRs to provide NGDs and PGDs for reflected and transmitted pulses, respectively, as well as on the

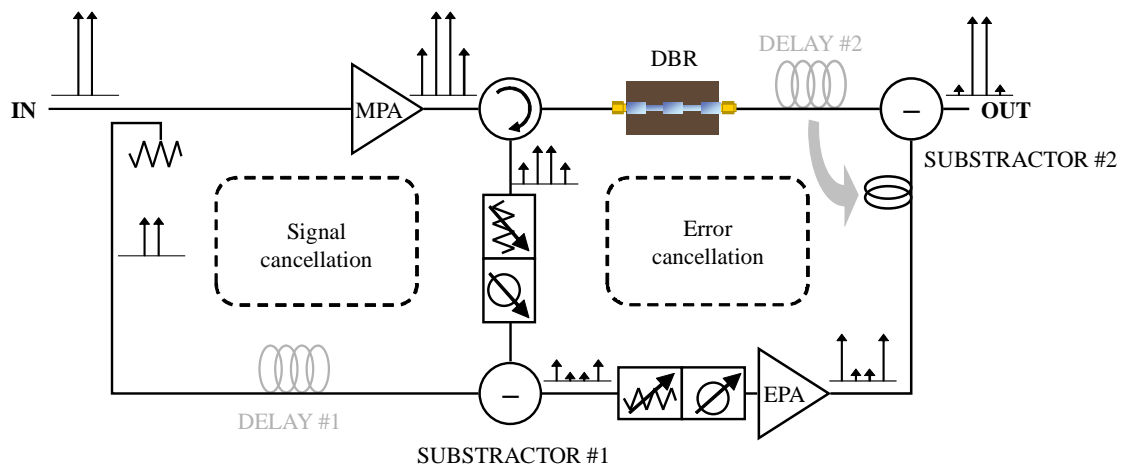


Figure 5.8: Topology of the feedforward amplifier proposed in this work, where a DBR that drives NGD on reflection and PGD on transmission is employed. The cancelled delay lines are shadowed.

control of such delays by modifying the DBR characteristics (number of periods, impedance contrast and length readjustment in one of the lines).

The amplifier's topology is illustrated in Fig. 5.8. A feedforward amplifier with a two-tone probe signal is considered. The output signal of the MPA (containing IMD and delayed) is sent to the DBR through a circulator which, in turn, sends the signal reflected on the DBR to the common branch of both loops. Let us point out that although the large signal attenuation in passive NGD circuits is usually a drawback of this kind of linearization technique, in our case, where the NGD comes in reflection, it is rather an advantage since only a little fraction of the signal amplified by the MPA is required to be brought to subtractor #1, while the rest of the signal is transmitted through the DBR with almost 100% transmission.

An appropriate design of the DBR reflection spectrum will compensate the delay brought in by the MPA, thus making delay line #1 unnecessary (note the shadowed delay symbol in the figure). Consequently, the reference signal that enters subtractor #1 will cancel the two principal tones, while only letting pass the error signal. This signal is then amplified by the EPA which, in turn, yields a time delay that is in general smaller than that introduced by the MPA. Therefore, at the entrance to subtractor #2, the error signal is expected to be advanced with respect to the signal that arrives through the DBR. For that reason, an extra delay line at the EPA output may be necessary, as the circuit in the figure shows. In addition, two vector modulators were included

for a correct fine balance of gain and phase in both loops [Cho-2010]. Note, too, that since the DBR drives a PGD on transmission, it is possible to reduce or even to completely eliminate delay line #2.

5.4 Results

Simulation results of the proposed DBR-based feedforward scheme were obtained by using Keysight's Advanced Design System (ADS) and they are given below. As MPA we selected a power amplifier of 45dB gain at 2.14 GHz that brings in 11.6 ns time delay with -45 dBc linearity (see Fig. 5.9), whereas an amplifier of 8.9 ns delay and gain of 42 dB was chosen for the EPA. This choice was made for an ulterior comparison of our results with those of [Cho-2010]. The DBR structure was designed to optimize the suppression of the third order IMD of a two-tone signal at 2.14 GHz and 10 MHz bandwidth. A structure of $2\frac{1}{2}$ periods with lines of 40Ω and 50Ω and a length readjustment of the last line of -3.5% was used. The DBR size is about $68 \times 50 \text{ mm}^2$. It is smaller than the NGD circuit ($180 \times 90 \text{ mm}^2$) employed in [Cho-2010].

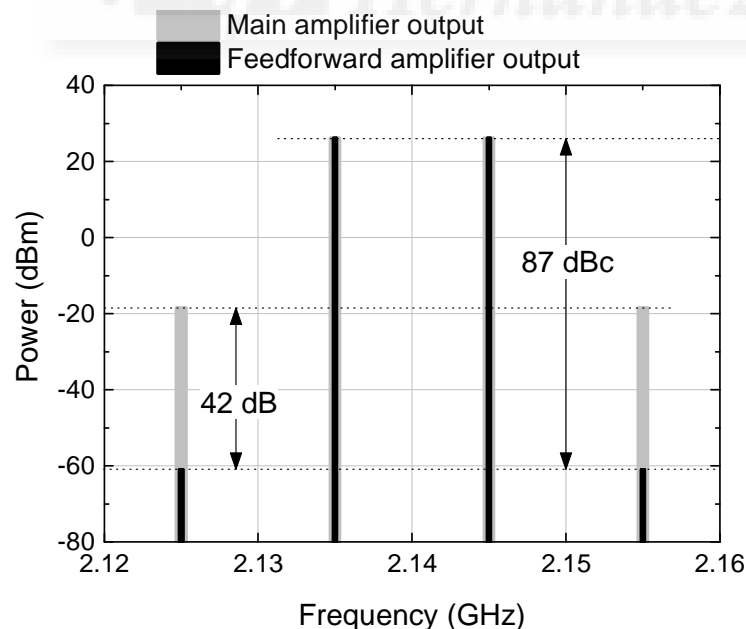


Figure 5.9: Power of the harmonics at the output of the main power amplifier without feedforward correction (grey bars) and with the feedforward correction (black bars) for a two-tone input signal.

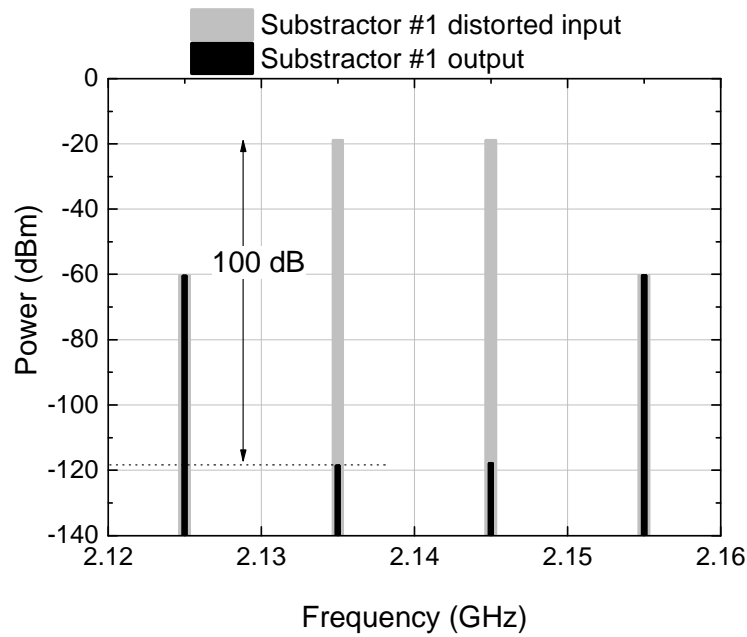


Figure 5.10: Balance of subtractor #1: cancellation of the principal signal for a two-tone input.

This structure exhibits a negative group delay on reflection of -11.6 ns for a signal with two tones at 2.135 and 2.145 GHz. Fig. 5.10 shows the suppression of the principal signal in subtractor #1: the comparison between the signal reflected from the DBR (which can be seen as a small fraction of the main amplifier output signal) and the subtractor's output signal yields a subtractor's efficiency of 100 dB. At the same time, the DBR presents a negative group delay on reflection of about -8.8 ns and about $+0.4$ ns on transmission for the IMD signal, thus, being necessary to introduce a delay line of 0.3 ns at the EPA output. The output signal of the feedforward amplifier is shown in Fig. 5.9, where a -87 dBc linearity is observed, thus improving in 42 dB the performance with respect to the non-linearized amplifier.

Table 5.1 gives a comparison of the delay lines considered in three different feedforward topologies that use amplifiers of the same delay level.

	Delay line #1 (ns)	Delay line #2 (ns)
Conventional	11.6	8.9
Ref [Cho-2010]	4.1	1.2
This work	0	0.3

Table 5.1: Comparison of the value of the delay lines used in different feedforward amplifier topologies.

	Type of results	BW (MHz)	Linearity (dBc)
Ref [Cho-2010]	Experimental	10	-53
Ref [Oga-2004]	Experimental	10	-55
This work	Simulated	10	-65

Table 5.2: Comparison of the linearity obtained in feedforward amplifiers with a WCDMA signal at 2.14 GHz.

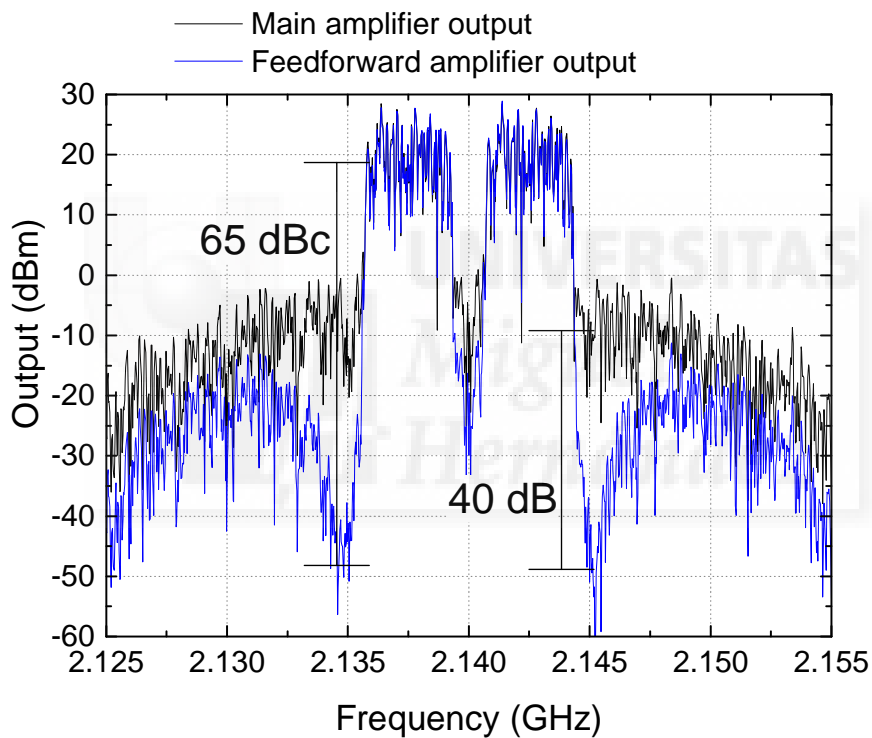


Figure 5.11: Power spectra at the output of the main amplifier without (black line) and with (blue line) the feedforward correction for a 2-channel WCDMA signal.

In addition, simulations of the proposed feedforward amplifier were run for a 2-channel WCDMA input signal at 2.14 GHz. Fig. 5.11 shows the output amplifier spectra, with and without feedforward linearization. Although this structure does not exhibit a flat response in reflection, our results represent an improvement of 40 dB in the linearity within a 10 MHz bandwidth. Table 5.2 compares the linearity achieved in this work with that obtained experimentally by other authors. These results indicate that a practical realization

of such amplifier may provide improvements comparable to those obtained in [Cho-2010] and [Oga-2004].

5.5 Conclusions

In this chapter an alternative topology for the feedforward amplifier based on a DBR is proposed. The conclusions to be reached in this chapter are the following:

- I. We have provided numerical evidence of the efficiency enhancement of feedforward amplifiers based on distributed Bragg reflectors. We have proposed a new amplifier topology that takes advantage of the simultaneous negative group delay on reflection, as well as positive group delay on transmission, of passive DBR structures implemented with microstrip technology. In this new feedforward amplifier scheme, the conventional delay elements are replaced, totally or partially, by a single DBR included in the distortion cancellation loop. Through a slight length readjustment of one of the microstrip lines in the DBR, this structure provides a substantial range of NGD values, running from a few nanoseconds to several tens of nanoseconds. Finer group delay adjustments can be achieved by changing the impedance contrast and the number of periods.
 - II. As an example, we have designed a DBR structure that compensates an MPA delay of 11.6 ns for a two-tone signal at 2.14 GHz and 10 MHz bandwidth. The linearity obtained at the output of the feedforward amplifier was -87 dBc, which involves an improvement of 42 dB with respect to the non-linearized amplifier. Thanks to this solution, only an extra delay line of 0.3 ns in the distortion cancellation loop was required. Additionally, we have also obtained a 40 dB linearization improvement for a 2-channel WCDMA signal of 10 MHz bandwidth. For larger bandwidths, more complex structures should be required, involving multistage DBRs, in order to obtain a flatter response in reflection. In that case, a reduction in the device size would be welcome and the use of meander shaped DBRs is an option to be considered.
-

Chapter 6

Conclusions and future work

6.1 Conclusions

This thesis has presented a theoretical and experimental investigation of slow- and fast-light effects in two kind of linear and passive structures: multiple-beam interferometers and mono- and multi-layer structures. The summary and detailed conclusions for each system, as well as for the proposed application in the microwave range, have been given at the end of their corresponding chapter. Here we provide an overall discussion of the main results.

In both the systems addressed in this work, the steep dispersion responsible for the abnormal group velocities has a structural origin, since it comes from the coupling between the pulse carrier frequency and the characteristic length of the system. Therefore, these SFL effects do not rely on electronic nor optical properties of the material in the branches of the interferometers or in the multilayers, as opposed to the case of media with gain or absorption resonances. As a consequence, the systems that have been studied here are scalable, and this provides easier experimental platforms where our theoretical models have been checked using the radiofrequency (RF) and microwave (MW) spectral range.

As a first main contribution of this thesis, a novel scheme to generate slow and fast light using multiple-beam interferometers has been proposed and investigated. Exact analytical

expressions for the transmission coefficient and group delay have been obtained as a function of frequency considering constant (dispersionless) attenuation and refractive index for the medium in the branches. An approximate analysis (valid for good fringe visibility and for frequencies around the transmission minima) has predicted the allowed propagation regimes in Mach–Zehnder and three–beam interferometers in terms of the system’s parameters (attenuation α , refractive index n , nominal length difference between branches Δ and length detuning ξ). For the first time, to our knowledge, it has been demonstrated that slow light cannot possibly be sustained if the length difference between adjacent branches of the interferometer is kept constant, like it is always the case of the MZI. If a small length detuning is allowed in one of the branches of the three–beam interferometer, slow light can arise at one of the two minima as long as ξ exceeds a critical value. This critical value that sets the slow to fast light transition has been obtained as a function of α , n and Δ . Simultaneously, tunneling, superluminal, or normal regime is sustained at the other minimum, depending on the system’s total attenuation.

The propagation of sinusoidally modulated wave packets through MZI and three–beam interferometers has been analytically obtained. The limitations of fast and slow light effects have been set as a function of the system’s and the pulse characteristics by quantifying typical figures of merit. Namely, fractional delay, pulse compression, expected Delay–Bandwidth Product and pulse break-up. These values, which are similar to those achieved in photonic band gap systems, are intrinsic to these interferometers and do not depend on the spectral range of operation whatsoever.

As a proof of model, RF experiments in the frequency and in the time domain have been performed on MZI and three–beam interferometers based on coaxial cables, yielding excellent agreement with the model predictions. Nonetheless, since most of the applications of slow and fast light are geared toward photonics, the model predictions have also been checked through numerical simulations in the optical range of a Si–based MZI and a Lithium Niobate three–beam interferometer, both operative at $1.55 \mu m$.

Regarding the potential application of these interferometers, typical values of their figures of merit are summarized in the Table 6.1 and compared with those of other SFL techniques. As it occurs in other techniques, the achievable pulse delays/advancements (provided pulse

compression is kept small) are always shorter than the pulse duration. This is a drawback for developing practical delay lines or optical buffers for signal processing. However, the very abrupt SFL transition when approaching the critical length detuning in three-beam interferometers opens the door for sensing applications. This suggests inducing the necessary phase shift not by a length detuning, but through a voltage which changes the refractive index on a branch of a Lithium Niobate interferometer, for example.

To conclude, the first part of this thesis provides a comprehensive study of the arising, capabilities and limitations of structural slow and fast light in a system other than a photonic band-gap structure. This is relevant since structural SFL effects had been only reported in systems exhibiting photonic band gaps, such as photonic crystals, Bragg gratings or coupled resonators.

The second main contribution of this thesis focuses on slow and fast light effects for pulses reflected on multilayer structures that are commonly used in actual photonic systems. While these effects have been widely studied for transmitted pulses, fewer results have been reported for pulses *reflected* on these structures. Our investigation here has run at a purely numerical and experimental level, where microstrip technology was applied to fabricate slabs and DBRs operative on the microwave range, Fabry–Perot filters were designed in the RF range and assembled using coaxial cables, and the transfer matrix method was used for the simulations.

With the above procedure, this thesis has provided experimental confirmation of a theoretical result reported by other authors on negative group delays for pulses reflected on weakly absorbing dielectric slabs. In addition, we have derived and demonstrated the scaling law that the group delay satisfies at the frequency of the reflection minima, where this behaviour occurs. We have found that the ratio of the real and imaginary part of the refractive index (n_r/n_i) sets the magnitude of the pulse advancement times the pulse center frequency. Our study has also made evident the analogy between such fast light effects and those described for narrowband pulses transmitted on low-loss MZI, which also verifies this simple scaling law and whose transmission spectrum is very similar to the reflection spectrum of a low-loss dielectric slab. Therefore, we can conclude that slow light on reflection cannot be supported on linear, passive low-loss dielectric slabs.

Results	$ FD $	DBP	n_g
3-beam int.	0.25	0.18	± 45
DBR	0.13	0.1	7
Asymm. FP	0.5	0.37	19
CPO [Geh-2006]	0.16	—	−4000
SBS [Son-2005]	0.3	1.05	7.6×10^{-4}
PBG [Bab-2008]	40	57	5.5
C-D [Oka-2007]	1200	42	1.8×10^{-4}

Table 6.1: Comparison between different systems: fractional delay (FD), delay-bandwidth product (DBP) and group index (n_g).

Remarkably, the characterization of SFL effects in DBRs with mismatched layer length and in asymmetric Fabry–Perot (FP) structures (with different number of layers in each mirror) has shown tunable slow to fast light regimes by changing either the mirror spacing or the attenuation (in the case of asymmetric FP) and by slightly modifying the length of one of the layers in the DBR. For example, by reflecting $3.3 \mu\text{m}$ -wide sinusoidal wave-packets on asymmetric FP based on high and low-impedance coaxial cables, fractional delays from +51% to −37% were measured. These values are similar to the fractional delays reported by other authors in active asymmetric fiber Bragg gratings.

The primary figures of merit of these multilayer structures are shown in the Table 6.1 and take values of the same order as those of multiple–beam interferometers. This should not be surprising because the physical origin of SFL effects in the two kinds of systems addressed in this work is the same. Namely, they are prompted by the interference of the pulse spectral components and are associated to Bragg–like conditions for total destructive interference of transmitted waves or total destructive interference of reflected waves, respectively. Therefore, a common disadvantage is the fact that these pulse delays/advancements occur around spectral minima and therefore, they are accompanied by a strong attenuation of the exiting pulse. Nevertheless, we believe it is worthwhile studying the application of these systems as sensors of strain, temperature or any magnitude that slightly changes the phase shift involved in this abrupt SFL transition. We can also envisage their application as group delay lines in cases where

delays/advancements are not required to be too large; an example is the application discussed in the third part of the Thesis.

As the third and last contribution, this Thesis has proposed the application of a DBR designed to operative in the MW range to enhance the efficiency of feedforward amplifiers, which use a standard linearization technique to eliminate the intermodulation products that arise in power amplifiers. This work proposes an alternative topology that enhances the efficiency and reduces the size of the conventional feedforward amplifier scheme by employing a microstrip DBR as a negative group delay (NGD) circuit on reflection and as a positive group delay (PGD) circuit on transmission. As an example, a DBR structure that compensates a delay of 11.6 ns in the power amplifier for a two-tone signal at 2.14 GHz and 10 MHz bandwidth was designed. A linearization improvement of 44 dB with respect to the non-linearized amplifier is obtained with the only requirement of an extra delay line of 0.4 ns in the distortion cancellation loop. Additionally, we have also obtained a 40 dB linearization improvement for a WCDMA signal of 10 MHz bandwidth. This DBR-based feedforward scheme provides an efficiency enhancement comparable to that achieved in feedforward architectures with a NGD circuit, and leads to a larger size reduction.

Finally, the possibility of advancing or delaying pulses on these linear and passive devices might be interesting for photonic applications such as sensing and group delay control, since these systems, which are proposed as an alternative to active or non-linear media, can be scaled to the optical range due to the universality of the wave interference phenomena.

6.2 Future work

Two main directions could be followed for future work based on this Thesis. Efforts toward the practical application of SFL based on these interferometers and multilayer structures might be a path worth exploring. In particular, their suitability for sensing applications and as group delay devices would improve if we are able to increase the operational bandwidth. Being a narrowband effect is a common problem to material-based and structural-based SFL that is addressed through different methods. For example, for material SFL systems, channelized

techniques have been proposed. It consists on creating separate narrowband SFL spectral channels for the different frequency components of a broadband signal and subsequently combine these outputs to achieve large fractional delays of broader signals.

Regarding applications based on group delay transitions, an important task would be to develop a full analytical description of SFL effects on asymmetric FPs as a function of the system parameters (mirror spacing d , number of layers in the mirrors, and attenuation coefficient), much in the same way as it has been done for multibeam interferometers. This complete description would allow to optimize designs for sensing applications.

A second path which we believe is interesting to follow focuses on achieving controlled group delay tunability. To achieve this, the use of liquid crystal-based interferometers and multilayer filters provides a way to perform this control by means of a voltage. For example, tunable SFL effects on liquid-crystal infiltrated Fabry-Perot filters and common-path polarization interferometers could be investigated by using the Jones matrix formalism for polarized light, since liquid crystals are highly anisotropic. The common-path polarization interferometer that consists in a waveplate placed between two polarizers is in many aspects similar to a MZI, where now instead of physically separating the two interfering beams, the two orthogonal polarization components travel through the same physical path but each of them “sees” a different refractive index. SFL effects are expected at the transmission minima and allowed group delay regimes could be analyzed in terms of the polarizers orientation and liquid-crystal birefringence.

Last, but not least, this Thesis has involved a lot of experimental work during the frequency and time domain characterization of multiple-beam and multilayer structures operative at the RF and MW range. Setting up these experiments in the optical range is an important scope in order to check new designs, like the use of liquid crystal-based structures, and further advance on this field.

Publications related to this thesis

Papers published in JCR journals

1. M. M. Sánchez-López, A. Sánchez-Meroño, J. Arias, J. A. Davis and I. Moreno, “Observation of superluminal and negative group velocities in a Mach-Zehnder interferometer”, *Appl. Phys. Lett.* **93**, 074102 (2008).
2. A. Sánchez-Meroño, J. Arias and M. M. Sánchez-López, “Negative group delay of reflected pulses on microstrip slabs and Bragg reflectors”, *IEEE J. Sel. Top. Quantum Electron* **46(4)**, 546-553 (2010).
3. J. Arias, A. Sánchez-Meroño, M. M. Sánchez-López and I. Moreno, “Slow and fast light in three beam interferometers: theory and experiment”, *Phys. Rev. A* **85(3)**, 033815 (2012).
4. A. Sánchez-Meroño, M. M. Sánchez-López and J. Arias, “Fast light in unbalanced low-loss Mach-Zehnder interferometers”, *Phys. Rev. A* **89(4)**, 043828 (2014).
5. E.Ávila, J. Arias, D. Carriazo-Rabadán, A. Sánchez-Meroño and M. M. Sánchez-López, “Feedforward amplifiers based on distributed Bragg reflectors” (submitted to *IEEE Transactions on Microwave Theory and Techniques*).

Other papers

1. A. Sánchez-Meroño, M. M. Sánchez-López, J. Arias and J.A. Davis, “Observación de pulsos superluminales y subluminales en interferómetros de multihaz y Mach-Zehnder”, *Óptica Pura y Aplicada* **42**, 215-220 (2009).

SPIE conference proceedings

1. A. Sánchez-Meroño, M. M. Sánchez-López, J. Arias, J. A. Davis and I. Moreno, “Group velocity control in multiple-beam and Mach-Zehnder interferometers”, *SPIE Photonics Europe*, 77161Y-77161Y (2010).
2. J. Arias, A. Sánchez-Meroño, M. M. Sánchez-López, E. Ávila-Navarro and I. Moreno, “Superluminal reflected pulses in microstrip slabs and photonic crystals”, *SPIE Photonics Europe*, 77130T-77130T (2010).
3. A. Sánchez-Meroño, M. M. Sánchez-López, J. Arias and I. Moreno. “Group-velocity control of reflected pulses on asymmetric Fabry-Perot filters”, *SPIE Photonics Europe* 84251S-84251S (2012).
4. J. Arias, A. Sánchez-Meroño, M. M. Sánchez-López, and I. Moreno. “Group delay tuning in three-beam interferometers: an alternative to photonic crystals for generating slow and fast light”, *SPIE Photonics Europe*, 84251O-84251O (2012).

Other conference communications

1. A. Sánchez-Meroño, M. M. Sánchez-López, J. Arias and J. A. Davis, “Observación de pulsos superluminales y subluminales en interferómetros de multihaz y Mach-Zehnder”, *Proc. VI OPTOEL* (2009).
 2. A. Sánchez-Meroño, E. Ávila-Navarro, J. Arias and M. M. Sánchez-López, “Control del retardo de grupo en reflectores de Bragg para amplificadores feedforward”, *Proc. XXV URSI* (2010).
 3. M. M. Sánchez-López, J. Arias, A. Sánchez-Meroño and I. Moreno, “Generación de luz lenta y luz rápida en interferómetros de tres haces”, *Proc. VII OPTOEL* (2011).
 4. D. Carriazo, E. Ávila, J. Arias, A. Sánchez-Meroño, G. Torregrosa and M. M. Sánchez-López, “Amplificador feedforward basado en reflector de Bragg”, *Proc. XXVI URSI* (2012).
 5. A. Sánchez-Meroño, J. Arias and M. M. Sánchez-López, “Luz rápida en interferómetros Mach-Zehnder de baja atenuación”, *Proc. VIII OPTOEL* (2013).
 6. A. Sánchez-Meroño, J. Arias and M. M. Sánchez-López, “Sintonización del retardo de grupo para pulsos reflejados en filtros Fabry-Perot asimétricos”, *Proc. VIII OPTOEL* (2013).
 7. J. Arias, A. Sánchez-Meroño, M. M. Sánchez-López and I. Moreno, “Fast light in lossy Mach-Zehnder interferometers”, *Proc. ICO* (2014).
-

Appendix A

Scattering parameters

At “low” frequencies, we can completely characterize a linear device or network using an impedance matrix, which relates the currents and voltages at each device terminal to the currents and voltages at all other terminals. But, at microwave frequencies, it is difficult to measure total currents and voltages. At high frequencies, S-parameters (scattering parameters) are commonly used to describe the performance of RF and microwave devices. These parameters can be used to completely describe the electrical behavior of the device (or network). In other words, we can determine the relationship between the incident and reflected wave at each device terminal to the incident and reflected waves at all other terminals.

The scattering matrix (S) describes the behavior of a multi-port network or device operating usually in the RF and microwave range. Its elements relate the incident and reflected waves at each port of the network [Riz-1988].

Fig. A.1 shows a linear network of N-ports with transmission lines connected to each port. Its characteristic impedances are denoted by Z_{01} , Z_{02} , ..., Z_{0N} and they are supposed real. Voltages and currents at the terminal planes, V_k and I_k , where k is the port number, are also displayed. In classical circuit theory, networks are typically characterized by an impedance (or admittance) matrix which relates these voltages and currents. This approach can be found in most of the literature on network theory. An alternative method, which is very useful in microwave analysis, is to describe the behavior of the network in terms of incident and scattered waves. These are shown in Figure A.1 and they are designated as a_k and b_k , respectively. Note that the outgoing

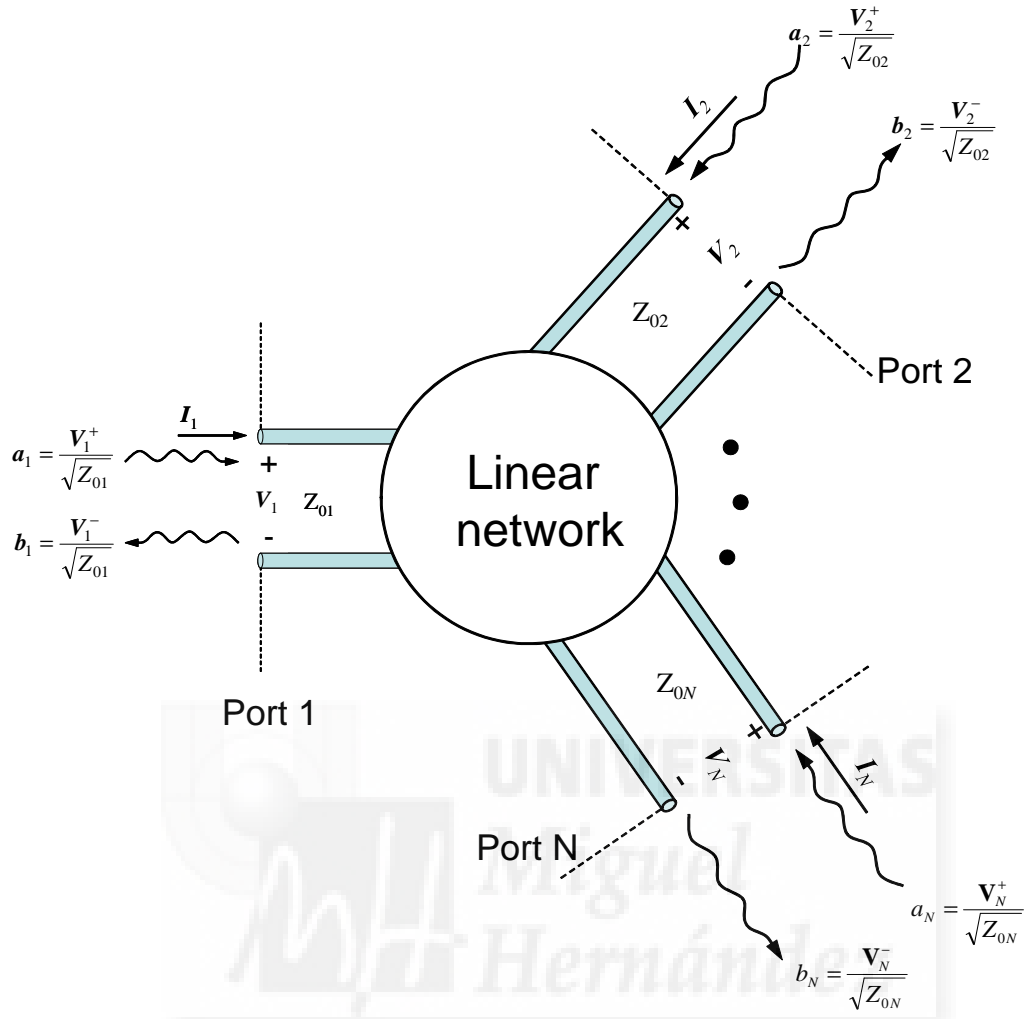


Figure A.1: Linear network of N -ports and their associated incident and scattered waves.

waves (b_k) are not labeled “*reflected*” as they are also associated to the transmission from other ports. These complex quantities are defined by the following equations:

$$a_k = \frac{V_k^+}{\sqrt{Z_{0k}}} = I_k^+ \sqrt{Z_{0k}} \quad (\text{A.1})$$

and

$$b_k = \frac{V_k^-}{\sqrt{Z_{0k}}} = I_k^- \sqrt{Z_{0k}} \quad (\text{A.2})$$

where V_k^+ , V_k^- , I_k^+ and I_k^- are the voltage and current waves, incident and scattered, Z_{0k} is the characteristic impedance of the line connected to the port k . Since Z_{0k} is real, the phase angle of a_k is the same as the waves V_k^+ and I_k^+ . Similarly, the phase of b_k is the same as the wave

V_k^- and I_k^- . The square of its rms value is equal to the power flow associated with the incident and scattered wave, i.e.,

$$\begin{aligned} P_k^+ &= a_k^2 \\ P_k^- &= b_k^2 \end{aligned} \quad (\text{A.3})$$

Although a_k and b_k are sometimes called wave power, they are actually standard voltage (or current). The net/total power input at port k is given by:

$$P_{k;n} = a_k^2 - b_k^2 \quad (\text{A.4})$$

Moreover, the power delivered to the load port k is:

$$P_{kL} = b_k^2 - a_k^2 = b_k^2[1 - |\Gamma_k|^2] \quad (\text{A.5})$$

where $|\Gamma_k|$ is the magnitude of the reflection coefficient at port k . You can see that $|\Gamma_k| = a_k/b_k$.

The voltage and current at any point along the transmission line can be expressed in terms of travelling waves in both directions. Denoting the input plane terminals of the lines in Fig. A.1 as $z = 0$, we have

$$V_k = V_k^+ + V_k^- = \sqrt{Z_{0k}}(a_k + b_k) \quad (\text{A.6})$$

and

$$I_k = I_k^+ - I_k^- = \sqrt{Z_{0k}}(a_k - b_k) \quad (\text{A.7})$$

where V_k and I_k represent the voltage and current phasors at the k_{th} input port.

The travelling wave variables a_k and b_k at port k are defined in terms of V_k and I_k and a real-value positive reference impedance Z_{0k} as follows:

$$a_k = \frac{1}{2} \left(\frac{V_k}{\sqrt{Z_{0k}}} + I_k \sqrt{Z_{0k}} \right) \quad (\text{A.8})$$

and

$$b_k = \frac{1}{2} \left(\frac{V_k}{\sqrt{Z_{0k}}} - I_k \sqrt{Z_{0k}} \right) \quad (\text{A.9})$$

These equations describe the relationship between the power wave and the voltages and currents. The scattering matrix of a N-port network (Fig. A.1) relates the outgoing waves b_N to the incoming waves a_N that are incident to the N-port:

$$\begin{aligned} b_1 &= S_{11}a_1 + S_{12}a_2 + \dots + S_{1N}a_N \\ b_2 &= S_{21}a_1 + S_{22}a_2 + \dots + S_{2N}a_N \\ &\dots \\ b_N &= S_{N1}a_1 + S_{N2}a_2 + \dots + S_{NN}a_N \end{aligned} \quad (\text{A.10})$$

The matrix elements S_{11}, S_{12}, \dots are referred to as the scattering parameters or the S-parameters and define the characteristics of the network. Written in matrix form, equation (A.10) is expressed as

$$b = [S]a \quad (\text{A.11})$$

where a and b are column matrices representing the incident and scattered waves. The S-matrix for N-ports is given by

$$[S] = \begin{bmatrix} S_{11} & S_{12} & \dots & S_{1N} \\ S_{21} & S_{22} & \dots & S_{2N} \\ \vdots & \vdots & \dots & \vdots \\ S_{N1} & S_{N2} & \dots & S_{NN} \end{bmatrix} \quad (\text{A.12})$$

S-matrix elements are generally complex and they are easily measurable. For example, S_{11} , S_{22} , ... and S_{NN} correspond to the reflection coefficients at the input ports 1, 2, ... and N, respectively, when all output ports end in their characteristic impedances. Thus, S_{11} can be determined by connecting a generator on port 1 and loads with tuning impedance in the other ports. Since a_2, a_3, \dots, a_N are zero, the ratio between the incident and the reflected voltage at port 1 is exactly S_{11} :

$$S_{11} = \frac{b_1}{a_1} \Big|_{a_k=0 \forall k \neq 1} = \frac{V_1^-}{V_1^+} \Big|_{a_k=0 \forall k \neq 1} \quad (\text{A.13})$$

The off-diagonal coefficients of the S-matrix represent transmission coefficients. For example, the wave $S_{21}a_1$ emerging from port 2 when a generator is connected to port 1, and impedances of equal value to the characteristic line of the port are connected to the other ports (i.e., $a_2, a_3, \dots, a_N = 0$). Under these conditions, S_{21} is the transmission coefficient from port 1 to 2:

$$S_{21} = \frac{b_2}{a_1} \Big|_{a_k=0 \forall k \neq 1} = \sqrt{\frac{Z_{01}}{Z_{02}}} \frac{V_2^-}{V_1^+} \Big|_{a_k=0 \forall k \neq 1} = \sqrt{\frac{Z_{02}}{Z_{01}}} \frac{I_2^-}{I_1^+} \Big|_{a_k=0 \forall k \neq 1} \quad (\text{A.14})$$

For reciprocal networks, the S-matrix is symmetrical. That is, $S_{11} = S_{22} = \dots = S_{NN}$. If the network is lossless, the transmitting power and the reflected power must be equal to the total incident power. The sum of the incident powers at all ports is equal to the sum of the reflected power at all ports. This implies that the S-parameter matrix is unitary, that is:

$$\begin{aligned}
|S_{11}|^2 + |S_{12}|^2 + \dots + |S_{1N}|^2 &= 1 \\
|S_{21}|^2 + |S_{22}|^2 + \dots + |S_{2N}|^2 &= 1 \\
&\dots \\
|S_{N1}|^2 + |S_{N2}|^2 + \dots + |S_{NN}|^2 &= 1
\end{aligned} \tag{A.15}$$

2-port networks are very common in microwave devices. In this case Eq. (A.10) reduces to:

$$\begin{aligned}
b_1 &= S_{11}a_1 + S_{12}a_2 \\
b_2 &= S_{21}a_1 + S_{22}a_2
\end{aligned} \tag{A.16}$$

In the case of a lossless transmission ($\alpha = 0$), of length l , characteristic impedance Z_{0k} , and group velocity v , the S-parameters are::

$$\begin{aligned}
S_{11} = S_{22} &= \frac{j(\bar{Z}_{0k}^2 - 1) \sin vl}{2\bar{Z}_{0k}^2 \cos vl + j(\bar{Z}_{0k}^2 + 1) \sin vl} \\
S_{21} = S_{12} &= \frac{2\bar{Z}_{0k}}{2\bar{Z}_{0k}^2 \cos vl + j(\bar{Z}_{0k}^2 + 1) \sin vl}
\end{aligned} \tag{A.17}$$

where $\bar{Z}_{0k} = Z_{0k}/Z_0$ is the line impedance normalized of the normalize line to the characteristic impedance of the lines connecting to the ports, Z_0 .

In the case of a lossy transmission line ($\alpha \neq 0$) of length l , characteristic impedance Z_{0k} and propagation constant $\gamma = \alpha + vj$, the S-parameters are:

$$\begin{aligned}
S_{11} = S_{22} &= \frac{j(\bar{Z}_{0k}^2 - 1) \sinh \gamma l}{2\bar{Z}_{0k}^2 \cosh \gamma l + j(\bar{Z}_{0k}^2 + 1) \sinh \gamma l} \\
S_{21} = S_{12} &= \frac{2\bar{Z}_{0k}}{2\bar{Z}_{0k}^2 \cosh \gamma l + j(\bar{Z}_{0k}^2 + 1) \sinh \gamma l}
\end{aligned} \tag{A.18}$$

It can be easily checked that the above equation converge to Eqs. (A.17) if non attenuation in the line ($\alpha = 0$) is considered.

Appendix B

Design of RF and MW structures

Waveguides are used to transfer electromagnetic power efficiently from one point in space to another. Some common guiding structures are shown in figure B.1. These include the typical coaxial transmission line, the two-wire and microstrip transmission lines, hollow conducting waveguides, and optical fibers. In practice, the choice of structure is dictated by: (a) the desired operating frequency band, (b) the amount of power to be transferred, and (c) the amount of transmission losses that can be tolerated.

In this appendix we describe the considerations required for the design and fabrication procedure of the two types of structures considered in this work: coaxial lines used to build multiple-beam interferometers operative in the RF range discussed in Chapter 3 and microstrip lines for the mono- and multi-layer structures discussed in Chapter 4 and operative in MW range.

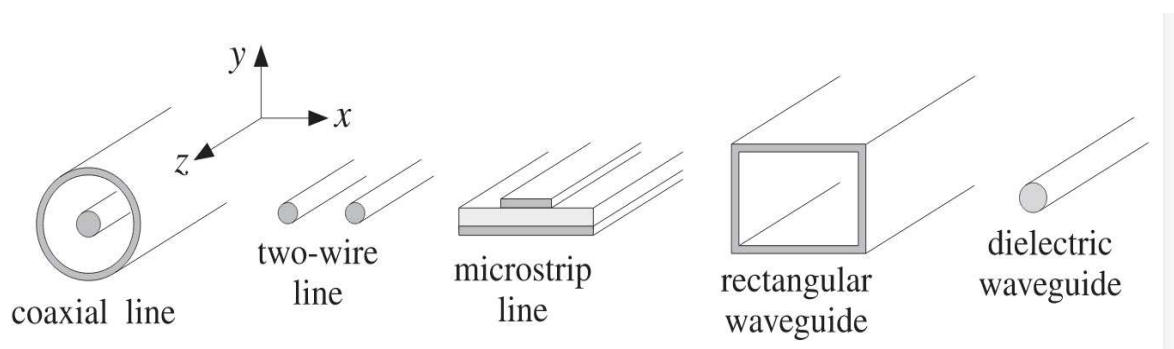


Figure B.1: (Extracted from [Orf-2002]). Typical waveguiding structures.

B.1 Coaxial transmission lines

A coaxial transmission line consists of two concentric conductors, the inner conductor being supported within the outer conductor through the use of a dielectric material.

B.1.1 Design

A basic principle in the design of most transmission lines is to find the optimum configuration of inner conductor to outer conductor dimensions where the power handling is maximized and the attenuation minimized. Each configuration will then determine a characteristic impedance for the line.

In this section, we described the considerations required for the characterization of coaxial lines. The electrical parameters of coaxial lines which are required for circuit design are impedance, attenuation and phase velocity.

Characteristic Impedance

We have used cables 50 and 75 Ohm (RG-58C/U and RG-59 respectively). The RG designation stands for Radio Guide; the U designation stands for Universal. Although the RG-series designations are common, there is no standard to guarantee their electrical and physical characteristics, so we should consult the fabrication handbook [Ariston].

Assuming the dielectric properties of the material inside the cable do not vary appreciably over the operating range of the cable, this impedance is frequency independent above about five times the shield cutoff frequency. For our coaxial cables, the shield cutoff frequency is 2000 Hz (RG-58C) and 1600 Hz (RG-59C)[Ott-2011].

Phase velocity

The vector network analyzer provides both the module and phase of the scattering parameters (see Appendix A). From the phase curve of parameter S_{21} (which is the transmission coefficient from port 1 to port 2) with respect to the frequency we get the phase velocity as,

	RG-58C/U	RG-59U
Manufacturer's $v(m/s)$ [Ariston]	$(2/3)c$	$(2/3)c$
Experimental $v(m/s)$	$(1.94/3)c$	$(1.97/3)c$

Table B.1: Theoretical and experimental phase velocity for cable RG-58C/U and RG-59U, where c is the light's speed in vacuum.

$$\phi_{S_{21}} = \frac{2\phi}{\lambda}nL = \frac{2\pi fL}{v} \Rightarrow v = \frac{\omega L}{\phi_{S_{21}}} \quad (\text{B.1})$$

The value thus obtained for v is shown in Table B.2 together with that provided by the manufacturer, which is obtained from the inductance (L) and capacitance (C) feature, using the following expression [Poz-2012]: $v = 1/\sqrt{LC}$.

Attenuation

Let us first recall the definition of this coefficient. The amplitude of a plane wave that propagates through a coaxial cable decreases exponentially due to the ohmic and dielectric losses [Poz-2012], we can write this as $V_M(z) = V_0 e^{-\alpha z}$, where z is a section of the cable and V_0 is the incident amplitude ($z = 0$). Therefore, the attenuation coefficient is obtained from the ratio between the amplitudes at the beginning and at the end of the cable, regarding:

$$\alpha = \frac{1}{L} \ln \left(\frac{V_0}{V_M(z=L)} \right) = \frac{1}{L} \ln \left(\frac{1}{|S_{21}|} \right) \quad (\text{B.2})$$

where L is the cable's length, and α is expressed in nepers per unit of length (nep/m). The above equation shows that the attenuation coefficient can be obtained directly by measuring the scattering parameter's magnitude $|S_{21}|$.

The attenuation of the line, which is normally expressed in terms of losses per unit length, in decibels per meter (dB/m), is due to dielectric losses and conductor losses. The dielectric material loss is directly proportional to frequency, whereas conductor losses are related to

Type of cable	α ($\frac{dB}{m}$)	α_0 ($\frac{dB}{m}$)	α_1 ($\frac{dB}{m\sqrt{MHz}}$)	α_2 ($\frac{dB}{m\cdot MHz}$)
50 Ω (RG-58C/U)	0.162	0.00635	0.01228	0.00033
75 Ω (RG-59U)	0.105	0.00037	0.01157	0.00014

Table B.2: Experimental attenuation for cable RG-58C/U and RG-59U at frequency $f = 100$ MHz.

the dimensions, permeability and conductivity of the material. Consequently, the losses are becoming higher as the frequency increases. We want consider not only the loss in the cable but also the loss in the connectors, so the frequency-dependent attenuation coefficient was measured over a frequency range from 0 to 200 MHz, in order to interpret the experimental transmission curves in this work.

For our work, the attenuation of the high and low impedance cables, RG-58C/U and RG-59U, respectively, was determined as a function of frequency by measuring the S_{21} scattering parameter for each kind of cable [Dav-2006]; the attenuation coefficients is described depends on the frequency through the following equation:

$$\alpha[dB/m] = \alpha_0 + \alpha_1\sqrt{f} + \alpha_2f \quad (\text{B.3})$$

where the frequency is given in MHz. Table B.2 contains the values of α_0 , α_1 and α_2 for each kind of cable.

The experimental value is considerably higher than the theoretical value (almost tenfold). This is because the cable used to measure $\alpha(\omega)$ is shorter than that used by the manufacturer (which implies a greater error), the effect of the connectors is considered and frequency characterization is lower than that used by the manufacturer. However, as we show in Chapter 3, the agreement between numerical simulations and the experimentally characterized transmission spectrum and group delay of the interferometer is excellent.

B.2 Microstrip lines

Microstrip is by far the most popular planar transmission line, especially for microwave integrated circuits and MMICs (Monolithic Microwave Integrated Circuits). Microstrip transmission lines consist of a conductive strip of width W and thickness t and a wider ground plane, separated by a dielectric layer (the “substrate”) of thickness h as shown in Fig. B.2.

The major advantage of microstrip over stripline is that all active components can be mounted on top of the board. The disadvantages are that when high isolation is required such as in a filter or switch, some external shielding may have to be considered. A minor issue with microstrip is that it is dispersive, meaning that signals of different frequencies travel at slightly different speeds.

B.2.1 Design

Samples were fabricated on a high-quality substrate using a LPKF Protomat 93s circuit board milling machine with $100 - \mu m$ resolution. The electrical parameters of microstrip lines which are required for circuit design are impedance, attenuation, wavelength and propagation constant. These parameters are interrelated assuming that the propagation mode is a transverse electromagnetic mode, or it can be approximated by a transverse electromagnetic mode. We have designed microstrip single lines following the Hammerstad and Jensen model [Ham-1980], which provides simple equations for characteristic impedance and effective dielectric constant as functions of the microstrip width, substrate thickness and dielectric constant.

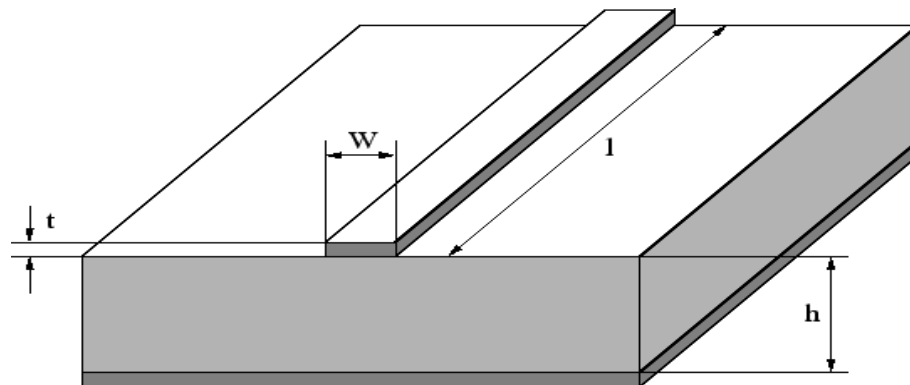


Figure B.2: Single microstrip line.

Appendix C

Experimental techniques for the frequency and time domain characterization.

The pulse propagation properties of the interferometers and multilayer structures discussed in this work are characterized in the frequency and in the time domain. A detailed description of these experimental techniques is here provided. Regarding the frequency-domain, the group delay regimes are closely linked to the spectral transmission (or reflection) features of the structure. Therefore, a vector network analyzer (VNA) is used to measure the scattering parameters and retrieve the experimental group delay function versus frequency. Since actual pulse delay values depend not only on the spectral characteristics of the system but also on the pulse shape, pulse propagation experiments are also included. The experimental setup and technique applied to measure the delay of pulses transmitted and reflected on our structures is here described. We show that in both the frequency- and time- domain characterization, an accurate procedure must be followed to get reliable high quality measurements.

C.1 Setup in the frequency domain

A two-port vector network analyzer (PNA series, Agilent model E8363B) has been used for characterizing our radio frequency and microwave structures. Through calibration, VNAs provide the highest level of accuracy for measuring RF components. Calibrating is so important

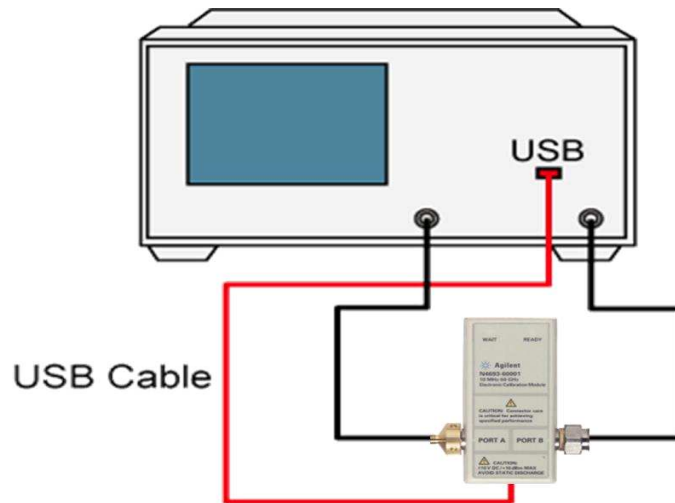


Figure C.1: Illustration of the use of ECal to calibrate our two-port vector network analyzer (Agilent, model E8363B)

to network analysis because it is impossible to make perfect test hardware, and too difficult and too expensive to make the network analyzer hardware so good that the need for error correction is entirely eliminated. An electronic calibration (ECal, see Fig.C.1) was used as a precision two-port calibration technique for our VNA. ECal replaces the traditional calibration technique, which uses mechanical standards. With mechanical standards it is required to make numerous connections to the test ports for a single calibration. With ECal, a full two-port calibration can be accomplished with a single connection to the ECal module and minimal operator interaction. This results in faster and more repeatable calibrations. Furthermore, it is necessary to indicate the presence of the adapters used to connect the structures, otherwise, it consider the adapters as part of the structure to be analyzed.

Measurements of the scattering (S) parameters and group delay were performed on a two-port vector network analyzer (Agilent, model E8363B). The parameters S_{11} and S_{21} , which correspond to the reflection and transmission coefficient, respectively, were recorded in the range of 1 to 9 GHz every 2.5 MHz. Experimental data contain a small amount of noise which is not very apparent in the S parameters themselves. To obtain the experimental group delay, the phase data curve is differentiated and this amplifies the noise leading to spurious effects [Moj-2000]. For this reason, network analyzer was configured to smooth the group delay by averaging 17 adjacent points. Although it is well known that smoothing is an arbitrary process

that may give results which vary critically with the smoothing parameters, we finally used a 17-point averaging algorithm, which does not essentially affect the group delay at the reflection (or transmission) maxima and is satisfactory enough to preserve the key features of the group delay trends at the reflection (or transmission) minima.

C.2 Smoothing of the phase function

In many experiments, as in our case, we are measuring a signal that changes rather slowly, whereas noise occurs as rapid, random changes in amplitude from point to point within the signal. It may be useful in some cases to attempt to reduce the noise by a process called smoothing. In smoothing, the data points of a signal are modified so that individual points that lay higher than the immediately adjacent points (presumably because of noise) are reduced, and points that lay lower than the adjacent points are increased. This naturally leads to a smoother signal. As long as the real underlying signal is actually smooth, the real signal will not be much distorted by smoothing, but the noise will be reduced.

In our case, we are interested in the phase function. At first sight the data dispersion of this function is not too apparent, but when it is differentiated versus frequency in order to obtain the group delay, a large spurious noise appears. Figure C.2 (top panel) shows the experimentally phase function measured with the vector network analyzer from 1 to 4 GHz for the structure $(HL)^4H$. Figure C.2 (bottom panel) shows the group delay obtained deriving the raw phase data function. As we see, the noise is such that masks the results.

C.2.1 Savitzky–Golay smoothing and differentiation filter

Most smoothing algorithms are based on the “shift and multiply” technique, in which a group of adjacent points in the original data are multiplied point-by-point by a set of numbers (coefficients) that defines the smooth shape, the products are added up to become one point of smoothed data, then the set of coefficients is shifted one point down the original data and the process is repeated. The simplest smoothing algorithm is the rectangular or unweighted sliding-average smooth; it simply replaces each point in the signal with the average of m adjacent

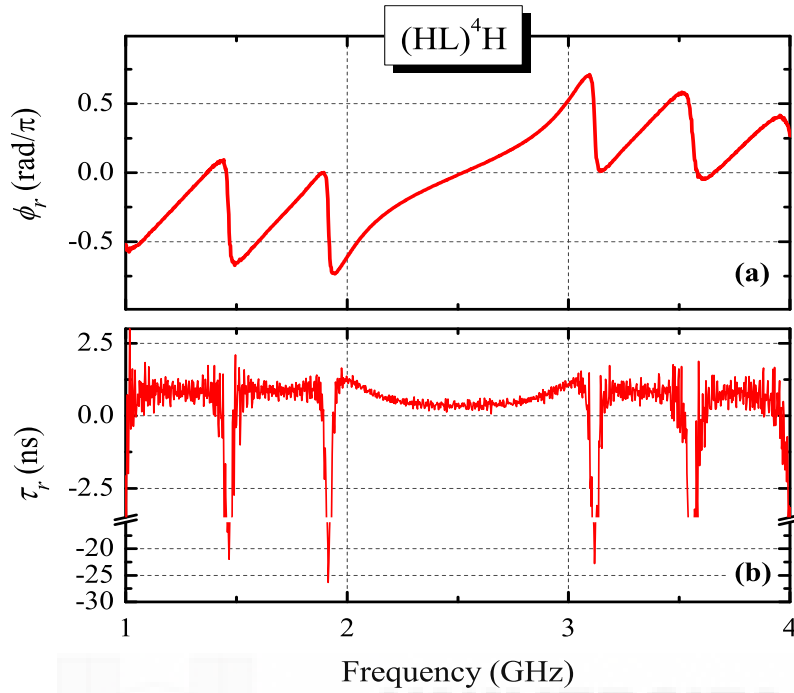


Figure C.2: Experimental results for the frequency characterization of reflected pulses on the $(HL)^4H$ Bragg reflector. Top panel shows the phase of the reflection coefficient, and bottom panel shows group delay without smoothing (i.e. obtained from deriving the raw phase data).

points, where m is a positive integer called the smooth width. For example, for a 3-point smooth ($m = 3$):

$$S_j = \frac{Y_{j-1} + Y_j + Y_{j+1}}{3} \quad (\text{C.1})$$

for $j = 2$ to $n - 1$, where S_j is the j^{th} point in the smoothed signal, Y_j the j^{th} point in the original signal, and n is the total number of points in the signal.

However, the Savitzky–Golay smoothing and differentiation filter optimally fits a set of data points to a polynomial in the least-squares sense, and it may be used with considerable improvement in the information obtained. The least squares calculations may be carried out in the computer by convolution of the data points with properly chosen sets of integers. If retaining the shape of the peak is more important than optimizing the signal-to-noise ratio, the Savitzky–Golay has the advantage over sliding-average smooths. It is capable of differentiation

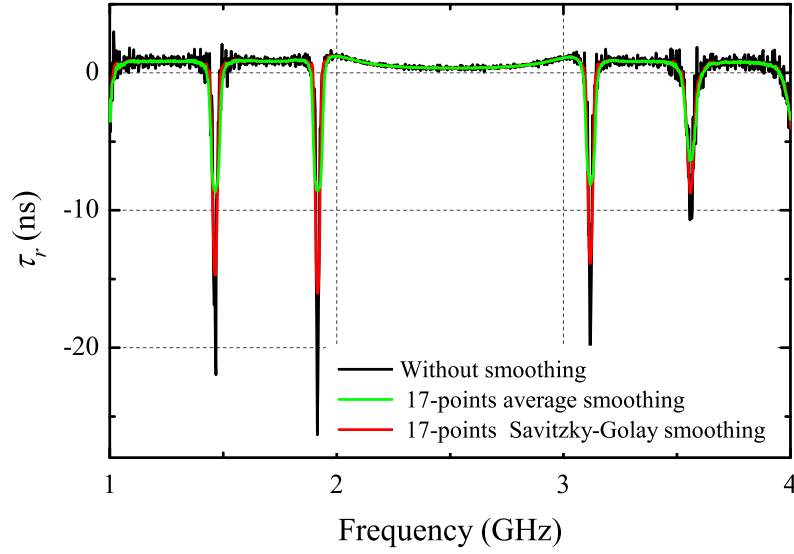


Figure C.3: Experimental group delay results retrieved from the phase function of a microstrip $(HL)^4H$ Bragg reflector. Without smoothing (black line), and with smoothing: 17-points average smooth (green line) and 17-points Savitzky-Golay smooth (red line) (smoothing of the raw phase data prior to differentiation).

as well as smoothing. Each data value f_i is replaced by a linear combination g_i of the same data and some neighbouring points.

$$g_i = \sum_{n=-n_L}^{n_R} c_n f_{i+n} \quad (\text{C.2})$$

where n_L is the number of points to the left of data i , and n_R is the number of points to the right. For each point f_i , a polynomial least-squares fits to $n_L + n_R + 1$ points, then g_i is obtained as the value of the polynomial at position i .

First, we thought about using an average algorithm to smooth the phase function that does not substantially affect the yielded group delay at the reflection/transmission maxima while preserving the key features of the group delay at the reflection/transmission minima. Finally, we decided to use the Savitzky-Golay algorithm with 17 points, because it is more effective at retaining the shape of the original signal. The same numerical treatment (phase smoothing prior differentiation) has been applied to the experimental and simulated data throughout this work.

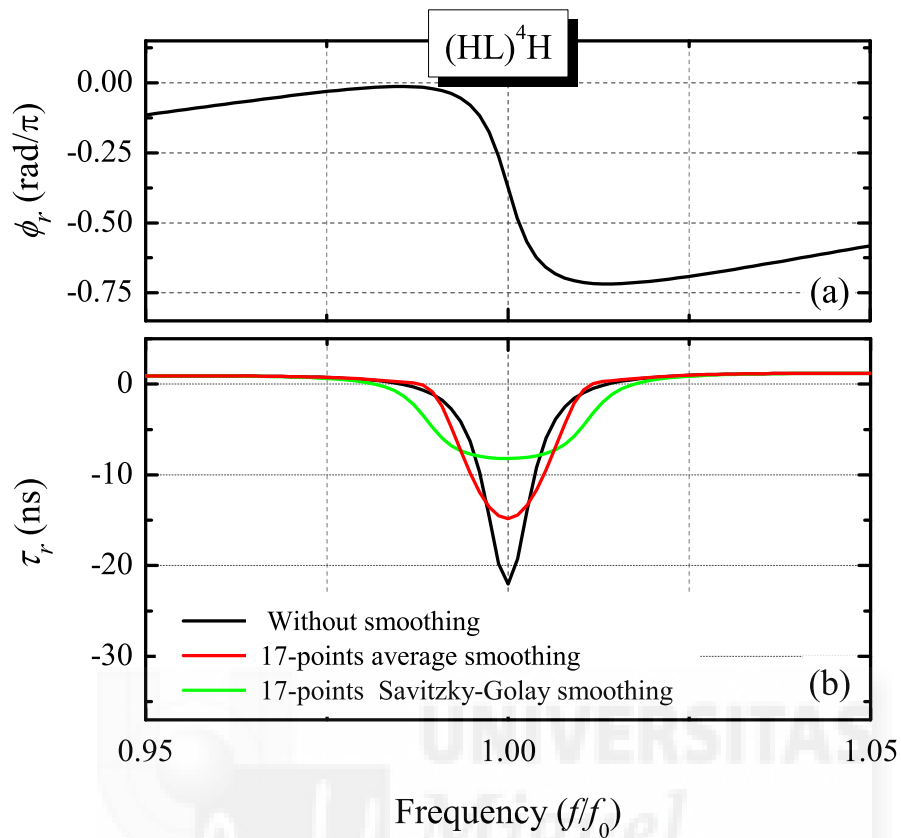


Figure C.4: TMM simulations for the frequency characterization of reflected pulses on a microstrip $(HL)^4H$ Bragg reflector. Top panel shows the phase of the reflection coefficient, and bottom panel shows the group delay without smoothing (black line), and smoothed: 17-points average smoothing (green line) and 17-points Savitzky-Golay smoothing (red line).

Figure C.3 shows the experimental group delays results of a microstrip $(HL)^4H$ Bragg reflector: without smoothing (black line), and with smoothing (17-points average smoothing (green line) and 17-points Savitzky-Golay smoothing (red line)). As we can see, both algorithms remove the spurious noise.

Figure C.4 presents the same results as the previous figure but for numerical simulations, and centered around the frequency of one of the reflection minima. For the simulations, it is not necessary to perform any filtering nor smoothing, since there is no noise in the calculated data, but in order to compare theory with experiment, these data must be treated equally and hence, the same type of smoothing is performed. As we see, smoothing the phase data in order to get the group delay curves has two negative effects: delay value (absolute value) is reduced and the group delay peaks become wider.

C.3 Setup in the time domain

There are several methods for generating pulses depending on the shape of the desired pulse. Generating a Gaussian envelope of a sinusoidal signal, the high pass filtering of a square wave or the amplitude modulation (AM) of a sine wave are some methods that could be employed.

We would need a programmable generator to create a Gaussian envelope, which was not available case. Concerning the high-pass filter method, it is based on generating a square signal and pass it through an RC filter, where the center frequency of the pulse is defined by the values of the resistor and the capacitor. Since we are interested in studying the propagation of pulses in a given frequency range, this method seems not the most efficient. However one can easily generate a train of pulses (or wave packets) by amplitude modulation of a sinusoidal wave. To do this, we only need one or two generators that allow amplitude modulation and we can directly tune the center frequency of the pulse in a certain range of frequencies.

We thus chose for the method of amplitude modulation to generate a pulse train due to the considerations mentioned above. Two sinusoidal waves are necessary: the carrier and the modulating signal. The former is modulated by the latter, which is the signal carrying the information [Pro-1998].

First, we focus on multiple-beam interferometers in the RF range to describe the experimental setup in transmission. Second, the experimental setup in reflection is described for mono- and multi-layer systems in the RF- and MW- range, noting the differences between both setups.

C.3.1 Transmission

The experimental configuration used for real-time pulse propagation is similar to the one proposed by Munday et al. [Mun-2002] and is shown schematically in Fig. C.5. Generator-1 (Tektronix CFG-253) is used to produce a sinusoidal signal at hundreds of kHz to amplitude modulate the much higher frequency sinusoidal signal of generator-2 (IntraAction VFE-604A4), whose frequency can be varied between 40-80 MHz. A train of 2-, 3.3- and 5- μ s wide sinusoidally modulated wave packets with carrier frequencies in the MHz range is thus produced for the MZ, the three- and the four-beam interferometers respectively. The choice of

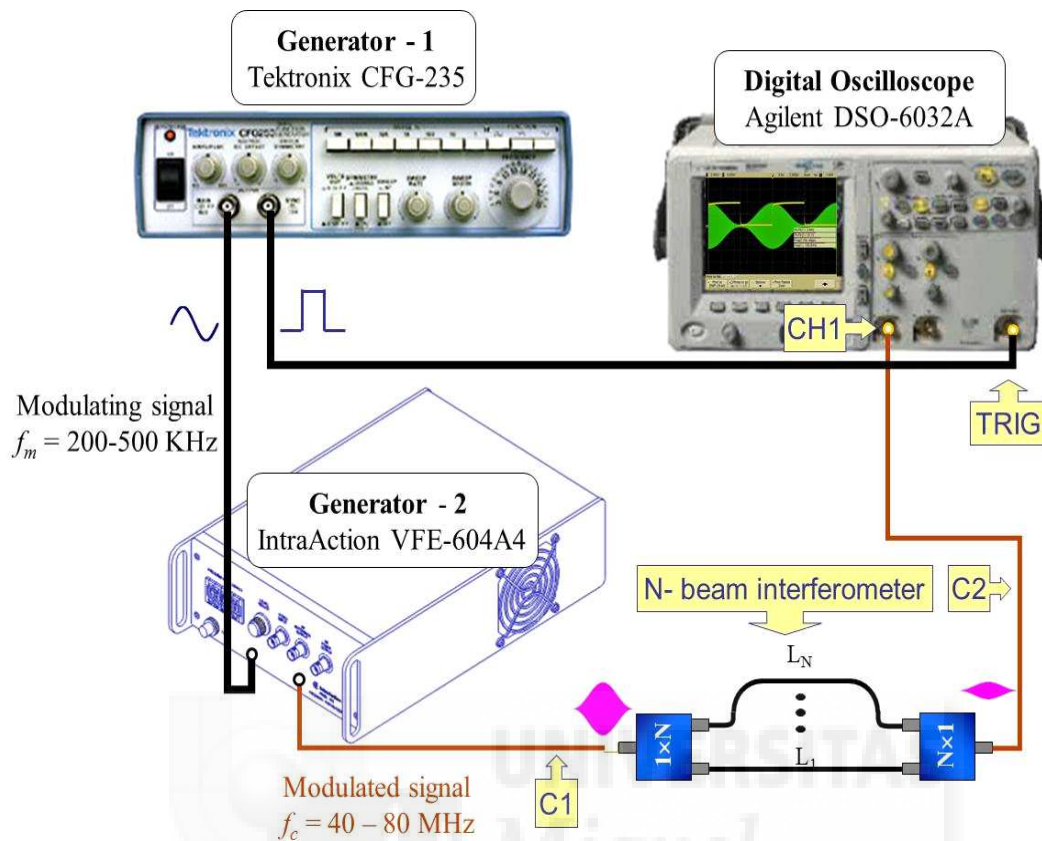


Figure C.5: Experimental setup for the time-domain pulse propagation measurements through the RF interferometers. The output sinusoidal signal from generator-2 is 100% amplitude modulated by the output signal from generator-1. C1 and C2 are 50Ω coaxial cables constituting the reference path (see text).

the modulating frequency must be a tradeoff between narrow-enough bandwidth to avoid pulse distortion, and large-enough bandwidth to get appreciable pulse delays in comparison to the pulse duration.

The pulse train transmitted through the interferometer is recorded at the oscilloscope (Agilent DSO-6032A) with a resolution of 0.5 ns (10 kSamples/5000 ns). The TTL signal from generator-1 is used to trigger the oscilloscope.

The pulse delay for each C1-interferometer-C2 system (see Fig. C.5) was obtained by the following procedure: first, a capture of the transmitted pulses was taken for a carrier frequency coinciding with the interferometer's first transmission minimum. Next, the interferometer was removed and cable C1 was connected to cable C2, and captures of transmitted pulses through this reference assembly were performed at the same carrier frequency than before. For each

interferometer, the pulse delay is then estimated as the time shift between the peak of the pulse transmitted by the system and the peak of the pulse travelling through the reference path. Let us recall that the pulse delay retrieved in this way will approach the group delay of Eq. (3.23) as the modulation frequency decreases. Since the signals were largely attenuated, a direct observation of the pulse peak on the oscilloscope was not accurate enough to measure the pulse delay. A systematic technique to determine the pulse center, which is less vulnerable to local fluctuations than the pulse peak, is more adequate. Hence, the pulse center is obtained from a numerical analysis of the data by finding the best fit to the pulse envelope.

A picture of the actual signal generators and digital oscilloscope used in the experimental device is displayed in Fig. C.5. The modulation (f_m) and carrier (f_c) frequency, and the amplitude of the modulating signal are set directly from the control panel of both generators. The modulation index m is selected by changing the power level (P_c) in generator-2.

C.3.2 Reflection

The experimental setup for the time-domain measurements of wave-packets reflected on a microwave DBR filter is shown in Fig. C.6. The 20-MHz sinusoidal output of generator-1 (Agilent 8648B) is used to amplitude modulate the sinusoidal signal of generator-2 (Agilent E4438C), whose frequency can be varied up to 6 GHz. This produces a train of sinusoidally modulated wave packets with carrier frequencies in the GHz range and 50 ns width that is reflected by the Bragg filter through a lowcost microwave power splitter. Although, a circulator should have been a more efficient way to extract the reflected wave, we decided to use a 3-dB splitter because of its simpler design and fabrication by microstrip technology. The reflected pulse train is recorded at the oscilloscope (Tektronix CSA8000 with only one available channel) with a resolution of 12.5 ps (4 kSamples/50 ns). Signal from generator 1 is used to trigger the oscilloscope.

In order to estimate the reflective pulse delay on reflection for the splitter-DBR system, the following procedure was observed: first, captures of the reflected pulses were performed for several carrier frequencies between 1 and 3.5 GHz using the experimental setup shown Fig. C.6. Next, the splitter-DBR system was removed and cable C1 was directly connected to cable C2,

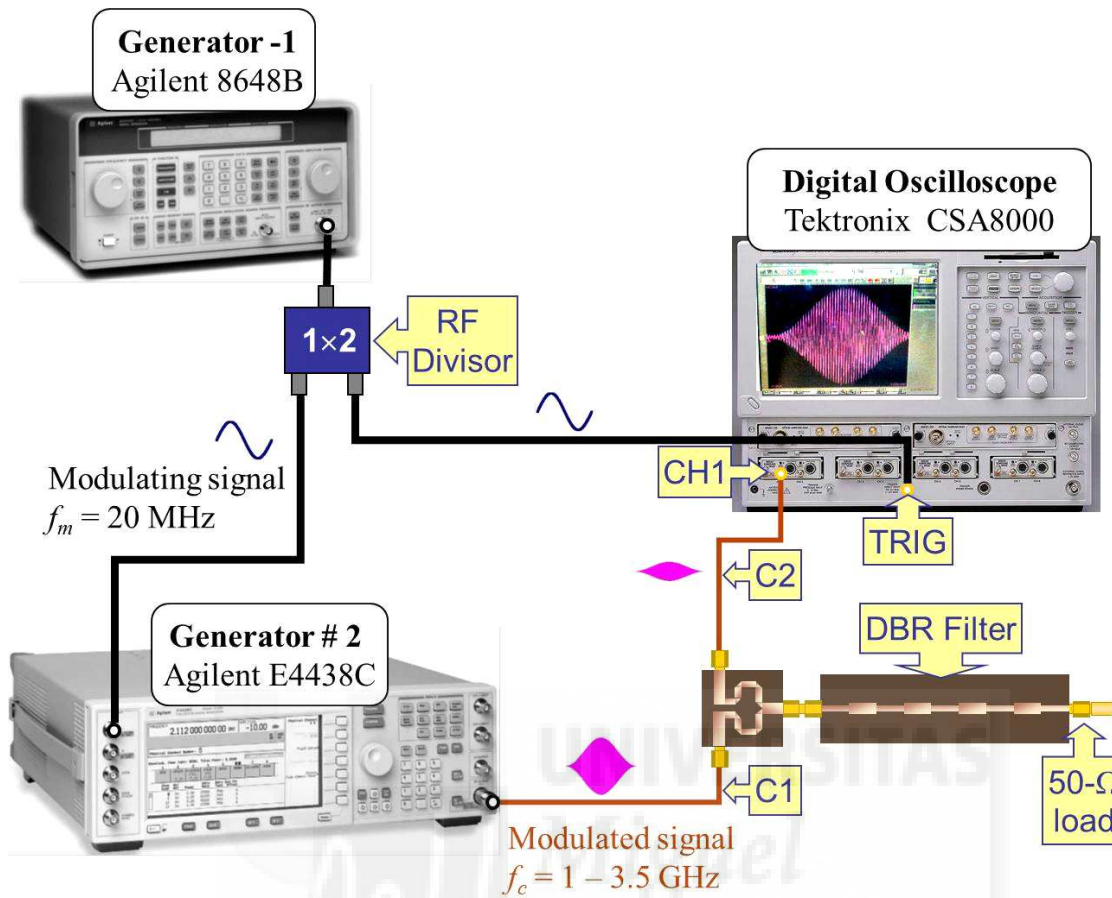


Figure C.6: Experimental setup for the time-domain wave-packet reflection measurements on a DBR filter. The output sinusoidal signal from generator-2 is 100% amplitude modulated by the output signal from generator-1. A microwave splitter to extract the reflected wave packets is used.

and captures of transmitted pulses through this reference assembly were performed at the same carrier frequencies than before. For each frequency, the pulse delay of the splitter-DBR system is then estimated as the time shift between the pulse reflected by this system and the pulse travelling through the reference path. The magnitude of the reflection coefficient is determined as the ratio between the amplitudes of these two pulses.

C.4 Design and fabrication of a 3-dB splitter

The design and fabrication by microstrip technology of a 3-dB splitter is described in this section. It is used to extract the reflected wave of the DBR in the time domain experiments (see section 4.4.3). The frequency characterization of the divider-DBR system is reported too.

Design and fabrication

In most circumstances, power dividers provide equal amplitude and equal phase splitting. In a resistive power divider, both output signals are 6 dB lower than the input signal, and they are in phase. In Wilkinson power dividers, the output signals are 3-dB below the input signal, and they are also in phase. The main differences between resistive power dividers and Wilkinson power dividers are that Wilkinson power dividers have 3-dB lower loss and possess the advantage of isolation between output. The purpose of the Wilkinson divider is to split the power of the input equally between two output ports, ideally without loss. Other properties of the Wilkinson power divider is that all ports are matched, the two output terminals are isolated from one another, and that it is reciprocal.

Three-port networks can not be reciprocal and matched without being lossy. The solution to this, in the Wilkinson power divider, is to add a resistor $2Z_0$ between the two outputs, where Z_0 is the line impedance. This resistor absorbs energy if there is a mismatch between the outputs. It also helps isolating the two outputs when the circuit functions as a power combiner. A quarter-wave transformers is used to match the input and output ports. We can see a scheme of our Wilkinson divider in Fig. C.7.

Fig. C.8 shows the fabricated sample on a low cost commercial substrate is shown. This substrate is a commercial microwave circuit board material with a dielectric constant of 4.6 and thickness of 1.5 mm [Taconic]. The nominal loss tangent of this substrate is 0.02. It was fabricated using a LPKF Protomat 93s circuit board milling machine with 100 μm resolution. The microstrip quarter wave line and characteristic impedance 70.7Ω ($\sqrt{2}Z_0$) has a length of

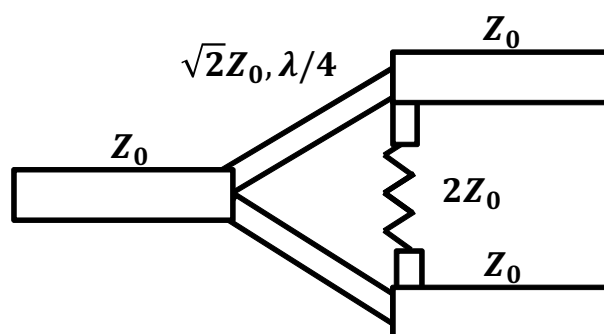


Figure C.7: Wilkinson power divider circuit scheme.

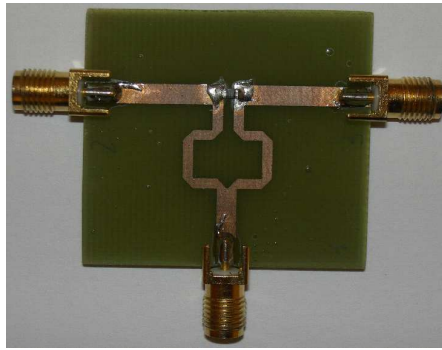


Figure C.8: Top view of fabricated microstrip Wilkinson divider.

16.92 mm and a width of 1.4 mm. This length corresponds to $\lambda/4$ (where λ is the wavelength in the medium) for a frequency $f_0 = 2.5$ GHz. The lines of characteristic impedance 50Ω have a width of 2.8 mm.

Frequency characterization

The following paragraphs detail some of the metrics that are often cited when designing.

The insertion loss and isolation are important parameters used to evaluate the quality of microwave dividers. The insertion loss refers to the additional loss above the nominal loss due to splitting. For example, in a 3 dB power divider the insertion loss might be specified as

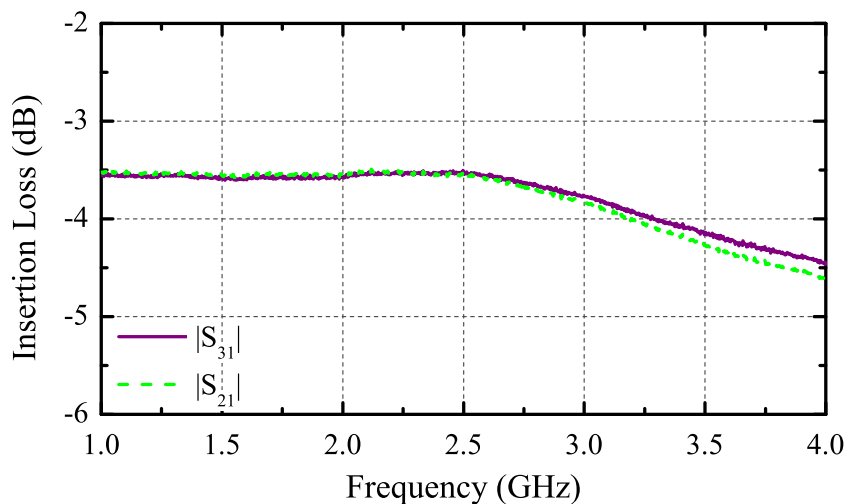


Figure C.9: Insertion loss of our Wilkinson divider.

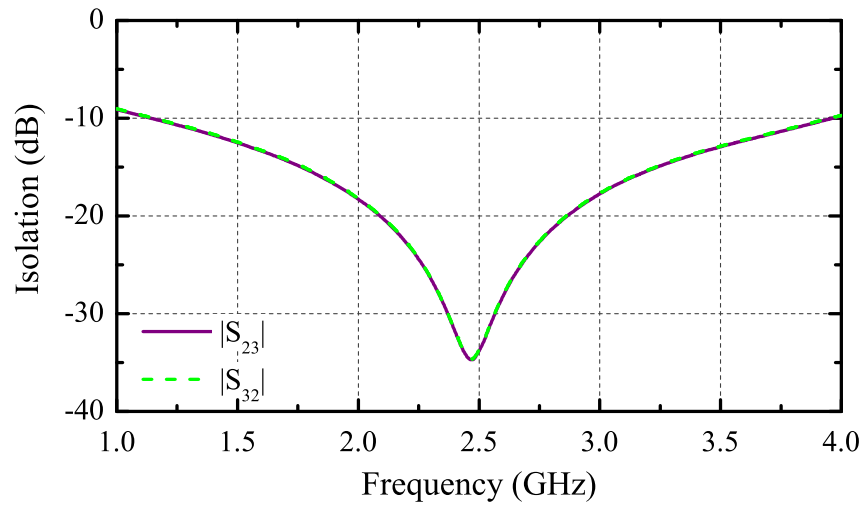


Figure C.10: Isolation between ports 2 and 3 ($|S_{23}|$ and $|S_{32}|$) of our Wilkinson divider.

0.5 dB. The additional losses are caused primarily by reflections, dielectric absorption, radiation effects, and conductor losses. Fig. C.9 shows the insertion loss, i.e., the scattering parameters' magnitude $|S_{21}|$ and $|S_{31}|$ measured with the vector network analyzer (Agilent E8363B). The experimental value (around 3.5 dB) is higher than the theoretical value (3 dB) as a result of not using a high frequency substrate.

In an ideal power divider the output ports are mutually isolated. In other words, a signal entering output 2 does not leak out of output 3. Isolation is defined as the ratio of a signal entering output-2 that is measured at output-3, assuming all ports are impedance matched. Fig. C.10 shows the isolation between ports 2 and 3 ($|S_{23}|$ and $|S_{32}|$).

Bibliography

- [Aga-2001] G. S. Agarwal, T. N. Dey, and S. Menon. “Knob for changing light propagation from subluminal to superluminal”. *Phys. Rev. A* **64**, 053809 (2001).
- [Agr-2004] G. Agrawal. *Lightwave Technology: Components and Devices*. Wiley (2004).
- [Aku-1999] A. M. Akulshin, S. Barreiro, and A. Lezama. “Steep Anomalous Dispersion in Coherently Prepared Rb Vapor”. *Phys. Rev. Lett.* **83**, 4277–4280 (1999).
- [Ariston] Ariston. www.ariston.es.
- [Ayn-2005] H. Aynaou, E. H. E. Boudouti, B. Djafari-Rouhani, A. Akjouj, and V. R. Velasco. “Propagation and localization of acoustic waves in Fibonacci phononic circuits”. *J. Phys: Condens. Matter* **17**, 4245 (2005).
- [Bab-2008] T. Baba. “Slow light in photonic crystals”. *Nature Photon.* **2** (8), 465–473 (2008).
- [Bal-1997] P. Balcou and L. Dutriaux. “Dual optical tunneling times in frustrated total internal Reflection”. *Phys. Rev. Lett.* **78**, 851–854 (1997).
- [Big-2003] M. S. Bigelow, N. N. Lepeshkin, and R. W. Boyd. “Superluminal and slow light propagation in a room-temperature solid”. *Science* **301**, 200–202 (2003).
- [Big-2003b] M. S. Bigelow, N. N. Lepeshkin, and R. W. Boyd. “Observation of Ultraslow Light Propagation in a Ruby Crystal at Room Temperature”. *Phys. Rev. Lett.* **90**, 113903 (2003).
- [Bol-1993] E. L. Bolda, R. Y. Chiao, and J. C. Garrison. “Two theorems for the group velocity in dispersive media”. *Phys. Rev. A* **48**, 3890–3894 (1993).
- [Bol-1994] E. L. Bolda, J. C. Garrison, and R. Y. Chiao. “Optical pulse propagation at negative group velocities due to a nearby gain line”. *Phys. Rev. A* **49**, 2938–2947 (1994).

- [Bor-2010] U. Bortolozzo, S. Residori, J. Huignard, and P. Pierre. “Slow and fast light: basic concepts and recent advancements based on nonlinear wave-mixing processes”. *Laser Photonics Rev.* **4**, 483–498 (2010).
- [Bor-2013] U. Bortolozzo, S. Residori, and J. C. Howell. “Precision Doppler measurements with steep dispersion”. *Opt. Lett.* **38**, 3107–3110 (2013).
- [Bou-2004] E. H. Boudouti, N. Fettouhi, A. Akjouj, B. Djafari-Rouhani, A. Mir, J. Vasseur, L. Dobrzynski, and J. Zemmouri. “Experimental and theoretical evidence for the existence of photonic bandgaps and selective transmissions in serial loop structures”. *J. Appl. Phys.* **95**, 1102–1113 (2004).
- [Boy-2003] R. W. Boyd. *Nonlinear Optics*. Elsevier Science (2003).
- [Boy-2007] R. W. Boyd and P. Narum. “Slow- and fast-light: fundamental limitations”. *J. Mod. Opt.* **54**, 2403–2411 (2007).
- [Boy-2009] R. W. Boyd. “Slow and fast light: fundamentals and applications”. *J. Mod. Opt.* **56**, 1908–1915 (2009).
- [Boy-2011] R. W. Boyd. “Material slow light and structural slow light: similarities and differences for nonlinear optics”. *J. Opt. Soc. Am. B* **29**, 2644–2645 (2012).
- [Bri-1960] L. Brillouin. *Wave Propagation and Group Velocity*. Academic Press New York and London (1960).
- [Cab-2002] J. M. Cabrera, F. J. López and F. A. López. *Óptica electromagnética*. Addison-Wesley Iberoamericana (2000).
- [Cab-2008] E. Cabrera-Granado and D. J. Gauthier. “Recent advancements in stimulated-Brillouin-scattering slow light”. *Opt. Pur. y Apl.* **41**, 313–323 (2008).
- [Cao-2004] H. Cao, A. Dogariu, and L. J. Wang. “Negative group delay and pulse compression in superluminal pulse propagation”. *IEEE J. Sel. Topics Quantum Electron.* **9**, 52–58 (2003).
- [Cen-1999] M. Centini, C. Sibilía, M. Scalora, G. D’aguanno, M. Bertolotti, M. Bloemer, C. Bowden, and I. Nefedov. “Dispersive properties of finite, one-dimensional photonic band gap structures: Applications to nonlinear quadratic interactions”. *Phys. Rev. E* **60**, 4891–4898 (1999).
-

- [Chi-1993] R. Y. Chiao. “Superluminal (but causal) propagation of wave packets in transparent media with inverted atomic populations”. *Phys. Rev. A* **48**, R34–R37 (1993).
- [Cho-2009] H. Choi, Y. Kim, Y. Jeong, and C.-D. Kim. “Synthesis of reflection type negative group delay circuit using transmission line resonator”. In “EuMC”, pages 902–905 (2009).
- [Cho-2010] H. Choi, Y. Jeong, C. D. Kim, and J. Kenney. “Efficiency enhancement of feedforward amplifiers by employing a negative group-delay circuit”. *IEEE Trans. Microw. Theory Techn.* **58**, 1116–1125 (2010).
- [Chu-1982] S. Chu and S. Wong. “Linear pulse propagation in an absorbing medium”. *Phys. Rev. Lett.* **48**, 738–741 (1982).
- [Cla-2014] J. B. Clark, R. T. Glasser, Q. Glorieux, U. Vogl, T. Li, and P. D. Lett. “Quantum mutual information of an entangled state propagating through a fast-light medium”. *Nature P* **8**, 515–519 (2014).
- [Col-1995] L. A. Coldren and S. W. Corzine. *Diode lasers and photonic integrated circuits*. John Wiley-Sons, New York, 475-480 (1995).
- [Cor-2009] B. Corcoran, C. Monat, C. Grillet, D. J. Moss, B. J. Eggleton, T. P. White, and T. F. O’Faolain, L. and Krauss. “Green light emission in silicon through slow-light enhanced third-harmonic generation in photonic-crystal waveguides”. *Nature Photon.* **3**, 206–210 (2009).
- [Cri-2002] S. C. Cripps. *Advanced Techniques in RF Power Amplifier Design*. Artech House. Artech House (2002).
- [Cua-2008] C. Cuadrado-Laborde. “All-optical ultrafast fractional differentiator”. *Opt. Quantum Electron.* **40** (13), 983–990 (2008).
- [D’Ag-2001] G. D’Aguanno, M. Centini, M. Scalora, C. Sibilìa, M. J. Bloemer, C. M. Bowden, J. W. Haus, and M. Bertolotti. “Group velocity, energy velocity, and superluminal propagation in finite photonic band-gap structures”. *Phys. Rev. E* **63**, 036610 (2001).
- [Dah-2005] D. Dahan and G. Eisenstein. “Tunable all optical delay via slow and fast light propagation in a Raman assisted fiber optical parametric amplifier: a route to all optical buffering”. *Optics* **13**, 6234–6249 (2005).
-

- [Dav-2006] J. A. Davis, D. A. Miller, M. D. M. Sánchez-López, and J. Cos. “Multiple-beam interference with coaxial cable analogs of optical arrays”. *Am. J. Phys.* **74**, 1066–1070 (2006).
- [Doi-2007] S. Doiron, A. Haché, and H. G. Winful. “Direct space-time observation of pulse tunneling in an electromagnetic band gap”. *Phys. Rev. A* **76**, 023823 (2007).
- [Elm-1969] W. Elmore, W. Elmore, and M. Heald. *Physics of Waves*. Dover Publications (1969).
- [Fao-2010] L. O. Faolain, S. A. Schulz, D. M. Beggs, T. P. White, M. Spasenović, L. Kuipers, F. Morichetti, A. Melloni, S. Mazoyer, J. P. Hugonin, P. Lalanne, and T. F. Krauss. “Loss engineered slow light waveguides”. *Opt. Express* **18**, 27627–27638 (2010).
- [Fle-2005] M. Fleischhauer, A. Imamoglu, and J. P. Marangos. “Electromagnetically induced transparency: Optics in coherent media”. *Rev. Mod. Phys.* **77**, 633–673 (2005).
- [Fra-2011] S. Franke-Arnold, G. Gibson, R. W. Boyd, and M. J. Padgett. “Rotary photon drag enhanced by a slow-light medium”. *Science* **333**, 65–67 (2011).
- [Fri-2012] M. Fridman, A. Farsi, Y. Okawachi, and A. L. Gaeta. “Demonstration of temporal cloaking”. *Nature* **481**, 62–65 (2012).
- [Gal-2007] J. F. Galisteo-López, M. Galli, A. Balestreri, M. Patrini, L. C. Andreani, and C. López. “Slow to superluminal light waves in thin 3D photonic crystals”. *Opt. Express* **15**, 15342–15350 (2007).
- [Gar-2006] P. Garcia-Ducar, J. de Mingo, and A. Valdovinos. “Misalignments feedforward transmitter correction design for nonlinear distortion cancellation in OFDM systems”. In “Veh. Tech. Conf., 1–5”, (2006).
- [Gar-1970] C. G. B. Garrett and D. E. McCumber. “Propagation of a gaussian light pulse through an anomalous dispersion medium”. *Phys. Rev. A* **1**, 305–313 (1970).
- [Gau-2006] D. J. Gauthier, A. L. Gaeta, and R. W. Boyd. “Slow light: From basics to future prospects”. *Photonics Spectra* **40**, 44–51 (2006).
- [Geh-2006] G. M. Gehring, A. Schweinsberg, C. Barsi, N. Kostinski, and R. W. Boyd. “Observation of backwards pulse propagation through a medium with a negative group velocity”. *Science* **312**, 895–897 (2006).
-

- [Geh-2008] G. Gehring, R. Boyd, A. Gaeta, D. Gauthier, and A. Willner. “Fiber-based slow-light technologies”. *J. Lightw. Technol.* **26**, 3752–3762 (2008).
- [Get-1973] W. J. Getsinger. “Microstrip dispersion model”. *IEEE Trans. Microw. Theory Techn.* **21**, 34–39 (1973).
- [Gho-2005] S. Ghosh, J. E. Sharping, D. G. Ouzounov, and A. L. Gaeta. “Resonant optical interactions with molecules confined in photonic band-gap fibers”. *Phys. Rev. Lett.* **94**, 093902 (2005).
- [Gho-2006] S. Ghosh, A. R. Bhagwat, C. K. Renshaw, S. Goh, A. L. Gaeta, and B. J. Kirby. “Low-light-level optical interactions with rubidium vapor in a photonic band-gap fiber”. *Phys. Rev. Lett.* **97**, 023603 (2006).
- [Gon-2005] M. González-Herráez, K.-Y. Song, and L. Thévenaz. “Optically controlled slow and fast light in optical fibers using stimulated Brillouin scattering”. *Appl. Phys. Lett.* **87**, 081113 (2005).
- [Gon-2010] M. Gonzalez-Herraez and L. Thévenaz. “Slow Light in stimulated Brillouin scattering: on the influence of the spectral width of pump radiation on the group index: Comment”. *Opt. Express* **18**, 8053–8054 (2010).
- [Gov-2006] A. A. Govyadinov and V. A. Podolskiy. “Gain-assisted slow to superluminal group velocity manipulation in nanowaveguides”. *Phys. Rev. Lett.* **97**, 223902 (2006).
- [Guo-2006] W. Guo. “Understanding subluminal and superluminal propagation through superposition of frequency components”. *Phys. Rev. E* **73**, 016605 (2006).
- [Hac-2002] A. Haché and L. Poirier. “Anomalous dispersion and superluminal group velocity in a coaxial photonic crystal: Theory and experiment”. *Phys. Rev. E* **65**, 036608 (2002).
- [Hac-2004] A. Haché and A. Slimani. “A model coaxial photonic crystal for studying band structures, dispersion, field localization, and superluminal effects”. *Am. J. Phys.* **72**, 916–921 (2004).
- [Ham-2009] Y. Hamachi, S. Kubo, and T. Baba. “Slow light with low dispersion and nonlinear enhancement in a lattice-shifted photonic crystal waveguide”. *Opt. Lett.* **34**, 1072–1074 (2009).
-

- [Ham-1980] E. Hammerstad and O. Jensen. “Accurate models for microstrip computer-aided design”. In “IEEE MTT-S”, pages 407–409 (1980).
- [Har-1997] S. E. Harris. “Electromagnetically induced transparency”. *Phys. Today* **50**, 36 (1997).
- [Har-1962] T. E. Hartman. “Tunneling of a wave packet”. *J. Appl. Phys.* **33**, 3427–3433 (1962).
- [Hau-1999] L. V. Hau, S. E. Harris, Z. Dutton, and C. H. Behroozi. “Light speed reduction to 17 meters per second in an ultracold atomic gas”. *Nature* **397**, 594–598 (1999).
- [Hec-2002] E. Hecht. *Optics*. Addison-Wesley (2002).
- [Hen-2010] R. Henker. *Investigation of the Slow- and Fast-Light Effect on the Basis of Stimulated Brillouin Scattering for Application in Optical Communication and Information Systems*. Ph.D. thesis, Dublin Institute of Technology (2010).
- [Ibr-2008] I. A. Ibraheem, J. Schoebel, and M. Koch. “Group delay characteristics in coplanar waveguide left-handed media”. *J. Appl. Phys.* **103**, 024903–024903–7 (2008).
- [Ish-2013] K. Ishizaki, M. Koumura, K. Suzuki, K. Gondaira, and S. Noda. “Realization of three-dimensional guiding of photon in photonic crystals”. *Nature Photon.* **7**, 133–137 (2013).
- [Jac-1998] J. Jackson. *Classical Electrodynamics*. John Wiley & Sons Inc., New York (1998).
- [Jar-2012] S. Jarabo, A. Schweinsberg, N. Lepshkin, M. Bigelow, and R. Boyd. “Theoretical model for superluminal and slow light in erbium-doped optical fibers: enhancement of the frequency response by pump modulation”. *Appl. Phys. B* **107**, 717–732 (2012).
- [Joa-2011] J. Joannopoulos, S. Johnson, J. Winn, and R. Meade. *Photonic Crystals: Molding the Flow of Light (Second Edition)*. Princeton University Press (2011).
- [Khu-2009] J. Khurgin and R. Tucker. *Slow Light: Science and Applications*. Taylor & Francis (2009).
-

- [Kit-2003] M. Kitano, T. Nakanishi, and K. Sugiyama. “Negative group delay and superluminal propagation: an electronic circuit approach”. *IEEE J. Quantum Electron.* **9**, 43–51 (2003).
- [Kni-1998] J. C. Knight, T. A. Birks, P. S. J. Russell, and J. P. de Sandro. “Properties of photonic crystal fiber and the effective index model”. *J. Opt. Soc. Am. A* **15**, 748–752 (1998).
- [Kra-2008] T. F. Krauss. “Why do we need slow light?” *Nature Photon.* **2**, 448–449 (2008).
- [Ku-2004] P. C. Ku, F. Sedgwick, C. J. Chang-Hasnain, P. Palinginis, T. Li, H. Wang, S. W. Chang, and S. L. Chuang. “Slow light in semiconductor quantum wells”. *Opt. Lett.* **29**, 2291–2293 (2004).
- [Kur-2007] E. Kurt and O. Palamutçuoğullari. “An adaptive feedforward amplifier application for 5.8 GHz”. *Turk. J. Electr. Eng. Co.* **14**, 437–443 (2006).
- [Lar-2005] C. L. Larose and F. M. Ghannouchi. “Optimal adaptation methods and class of operation: keys to improving feedforward amplifier power efficiency”. *IEEE Trans. Veh. Technol.* **54**, 456–467 (2005).
- [Lin-1998] S. Y. Lin, J. G. Fleming, D. L. Hetherington, B. K. Smith, R. Biswas, K. M. Ho, M. M. Sigalas, W. Zubrzycki, and S. R. Kurtz. “A three-dimensional photonic crystal operating at infrared wavelengths”. *Nature* **394**, 251–253 (1998).
- [Liu-2001] C. Liu, Z. Dutton, C. H. Behroozi, and L. Hau. “Observation of coherent optical information storage in an atomic medium using halted light pulses”. *Nature* **409**, 490–493 (2001).
- [Liu-2002] N. Liu, S. Zhu, H. Chen, and X. Wu. “Superluminal pulse propagation through one-dimensional photonic crystals with a dispersive defect”. *Phys. Rev. E* **65**, 046607 (2002).
- [Lon-2001] S. Longhi. “Superluminal pulse reflection in asymmetric one-dimensional photonic band gaps”. *Phys. Rev. E* **64**, 037601 (2001).
- [Lon-2002] S. Longhi, M. Marano, P. Laporta, M. Belmonte, and P. Crespi. “Experimental observation of superluminal pulse reflection in a double-Lorentzian photonic band gap”. *Phys. Rev. E* **65**, 045602 (2002).
-

- [Lon-2003] S. Longhi, M. Marano, M. Belmonte, and P. Laporta. “Superluminal pulse propagation in linear and nonlinear photonic grating structures”. *IEEE J. Sel. Topics Quantum Electron.* **9**, 4–16 (2003).
- [Lon-2005] S. Longhi. “Group delay tuning in active fiber Bragg gratings: From superluminal to subluminal pulse reflection”. *Phys. Rev. E* **72**, 056614 (2005).
- [Luc-1993] S. Lucyszyn, I. D. Robertson, and A. H. Aghvami. “Negative group delay synthesizer”. *Electronics Lett.* **29**, 798–800 (1993).
- [Lyo-2009] A. I. Lvovsky, B. C. Sanders, and W. Tittel. “Optical quantum memory”. *Nature Photon.* **3**, 706–714 (2009).
- [Mac-2001] H. Macleod. *Thin-Film Optical Filters*. Taylor & Francis (2001).
- [Mar-1992] T. Martin and R. Landauer. “Time delay of evanescent electromagnetic waves and the analogy to particle tunneling”. *Phys. Rev. A* **45**, 2611–2617 (1992).
- [McD-2001] K. T. McDonald. “Negative group velocity”. *Am. J. Phys.* **69**, 607–614 (2001).
- [Mit-1997] M. W. Mitchell and R. Chiao. “Negative group delay and ‘fronts’ in a causal system: An experiment with very low frequency bandpass amplifiers”. *Phys. Lett. A* **230**, 133–138 (1997).
- [Mit-1998] M. W. Mitchell and R. Chiao. “Causality and negative group delays in a simple bandpass amplifier”. *Am. J. Phys.* **66**, 14–19 (1998).
- [Moj-2000] M. Mojahedi, E. Schamiloglu, F. Hegeler, and K. J. Malloy. “Time-domain detection of superluminal group velocity for single microwave pulses”. *Phys. Rev. E* **62**, 5758–5766 (2000).
- [Moj-2003] M. Mojahedi, K. Malloy, G. Eleftheriades, J. Woodley, and R. Chiao. “Abnormal wave propagation in passive media”. *IEEE J. Sel. Top. Quantum Electron.* **9**, 30–39 (2003).
- [Mol-2004] F. Molina. *Realización de un programa de simulación de cristales fotónicos coaxiales y multicapas ópticas. Aplicaciones a reflectores de Bragg y filtros Fabry-Perot*. Master’s thesis, Universidad Miguel Hernandez (2004).
- [Mor-2005] J. Mørk, R. Kjøer, M. van der Poel, and K. Yvind. “Slow light in a semiconductor waveguide at gigahertz frequencies”. *Opt. Express* **13**, 8136–8145 (2005).
-

- [Mou-2013] A. Mouadili, E. H. El Boudouti, A. Soltani, A. Talbi, A. Akjouj, and B. Djafari-Rouhani. “Theoretical and experimental evidence of Fano-like resonances in simple monomode photonic circuits”. *J. Appl. Phys.* **113**, 164101 (2013).
- [Mug-2009] G. Muga, A. Ruschhaupt, and A. Campo. *Time in Quantum Mechanics*. Springer Berlin Heidelberg (2009).
- [Mun-2002] J. N. Munday and W. M. Robertson. “Negative group velocity pulse tunneling through a coaxial photonic crystal”. *Appl. Phys. Lett.* **81**, 2127–2129 (2002).
- [Mun-2003] J. N. Munday and W. M. Robertson. “Slow electromagnetic pulse propagation through a narrow transmission band in a coaxial photonic crystal”. *Appl. Phys. Lett.* **83**, 1053–1055 (2003).
- [Mun-2007] J. N. Munday and W. M. Robertson. “Observation of negative group delays within a coaxial photonic crystal using an impulse response method”. *Opt. Commun.* **273**, 32–36 (2007).
- [Mur-2012] S. Murugkar, I. León, Z. Shi, G. López-Galmiche, J. Salvail, E. Ma, B. Gao, A. C. Liapis, J. E. Vornehm, and R. W. Boyd. “Development of a slow-light spectrometer on a chip”. In “Proc. of SPIE”, volume 8264, pages 82640T 1–7 (2012).
- [Nak-2002] T. Nakanish, K. Sugiyama, and M. Kitano. “Demonstration of negative group delays in a simple electronic circuit”. *Am. J. Phys.* **70**, 1117–1121 (2002).
- [Nar-2010] F. B. Naranjo, P. K. Kandaswamy, S. Valdueza-Felip, L. Lahourcade, V. Calvo, M. González-Herráez, S. Martín-López, P. Corredera, and E. Monroy. “Novel InN/InGaN multiple quantum well structures for slow-light generation at telecommunication wavelengths”. *Phys Status Solidi* **7**, 100–103 (2010).
- [Nas-2012] Coalition of NASA, Army, Academic Researchers Wins Contract to Develop Innovative Flight Navigation Technology. *Fast Light Optical Gyroscopes for Precision Inertial Navigation* (2012).
- [Nim-2002] G. Nimtz, A. Haibel, and R. M. Vetter. “Pulse reflection by photonic barriers”. *Phys. Rev. E* **66**, 037602 (2002).
- [Nim-2003] G. Nimtz. “Superluminal signaling by photonic tunneling”. *IEEE J. Sel. Top. Quantum Electron.* **9**, 79–85 (2003).
-

- [Not-2007] H. Noto, K. Yamauchi, M. Nakayama, and Y. Isota. “Negative group delay circuit for feed-forward amplifier”. In “IEEE Microw. Symp.”, 1103-1106 (2007).
- [Oga-2004] T. Ogawa, T. Iwasaki, H. Maruyama, K. Horiguchi, M. Nakayama, Y. Ikeda, and H. Kurebayashi. “High efficiency feed-forward amplifier using RF predistortion linearizer and the modified Doherty amplifier”. In “IEEE Microw. Symp.”, (2004).
- [Ohm-2006] F. Öhman, K. Yvind, and J. Mørk. “Voltage-controlled slow light in an integrated semiconductor structure with net gain”. *Opt. Express* **14**, 9955–9962 (2006).
- [Oka-2007] Y. Okawachi, J. E. Sharping, C. Xu, and A. L. Gaeta. “Large tunable optical delays via self-phase modulation and dispersion”. In “CLEO Appl. Syst. Tech.”, OSA (2007).
- [Orf-2002] S. J. Orfanidis. *Electromagnetic Waves and Antennas*. Rutgers University New Brunswick, NJ (2002).
- [Ott-2011] H. Ott. *Electromagnetic Compatibility Engineering*. Wiley (2011).
- [Oug-2005] K. E. Oughstun and N. A. Cartwright. “Physical significance of the group velocity in dispersive, ultrashort gaussian pulse dynamics”. *J. Mod. Opt.* **52**, 1089–1104 (2005).
- [Par-1994] K. J. Parsons and P. B. Kenington. “The efficiency of a feedforward amplifier with delay loss”. *IEEE Trans. Veh. Technol.* **43**, 407–412 (1994).
- [Pev-2008] O. A. Peverini, R. Tascone, G. Addamo, G. Virone, and R. Orta. “On superluminal propagation”. *IEEE Antennas Propag. Mag.* **7**, 101–104 (2008).
- [Poi-2001] L. Poirier and A. Hache. “Nonlinear coaxial photonic crystal”. *Appl. Phys. Lett.* **78**, 2626–2628 (2001).
- [Poi-2005] L. Poirier, R. I. Thompson, and A. Hache. “Impossibility of negative group velocities in a periodic layer structure with or without loss”. *Opt. Commun.* **250**, 258 – 265 (2005).
- [Por-1999] H. Porte, V. Gorel, S. Kiryenko, J. P. Goedgebuer, W. Daniau, and P. Blind. “Imbalanced Mach-Zehnder interferometer integrated in micromachined silicon substrate for pressure sensor”. *J. Lightw. Technol.* **17**, 229–233 (1999).
-

- [Poz-2012] D. M. Pozar. *Microwave Engineering*. Wiley (2012).
- [Pro-1998] J. G. Proakis, D. G. Manolakis, and J. L. A. Castro. *Tratamiento Digital de Señales*. Prentice Hall (1998).
- [Qia-1999] Y. Qian, R. Coccioli, D. Sievenpiper, V. Radisic, E. Yablonovitch, and T. Itoh. “A microstrip patch antenna using novel photonic band-gap structures”. *Microw. J.* **42**, 66–76 (1999).
- [Rao-2004] V. S. C. M. Rao, S. Gupta, and G. S. Agarwal. “Atomic absorbers for controlling pulse propagation in resonators”. *Opt. Lett.* **29**, 307–309 (2004).
- [Rav-2007] B. Ravelo, A. Perennec, and M. Le Roy. “Synthesis of broadband negative group delay active circuits”. In “IEEE Microw. Symp.”, 2177-2180 (2007).
- [Rav-2007b] B. Ravelo, A. Perennec, and M. Le Roy. “Broadband balun using active negative group delay circuit”. In “Microw. Conf.”, 466-469 (2007).
- [Rav-2007c] B. Ravelo, A. Perennec, and M. L. Roy. “Active microwave circuit with negative group delay”. *IEEE Microw. Compon. Lett.* **17**, 861–863 (2007).
- [Rav-2008] B. Ravelo, M. Le Roy, and A. Pérennec. “Application of negative group delay active circuits to the design of broadband and constant phase shifters”. *Microw. Opt. Technol. Lett.* **50**, 3078–3080 (2008).
- [Rav-2010] B. Ravelo. *Study and Application of Microwave Active Circuits with Negative Group Delay*. Microwave and Millimeter Wave Technologies Modern UWB antennas and equipment abbreviation (2010).
- [Res-2008] S. Residori, U. Bortolozzo, and J. P. Huignard. “Slow and fast light in liquid crystal light valves”. *Phys. Rev. Lett.* **100**, 203603 (2008).
- [Riz-1988] P. A. Rizzi. *Microwave Engineering. Passive Circuits*. Prentice Hall (1988).
- [Rob-2002] W. M. Robertson, J. Ash, and J. M. McGaugh. “Breaking the sound barrier: Tunneling of acoustic waves through the forbidden transmission region of a one-dimensional acoustic band gap array”. *Am. J. Phys.* **70**, 689–693 (2002).
- [Saf-2011] A. H. Safavi-Naeini, T. P. M. Alegre, J. Chan, M. Eichenfield, M. Winger, Q. Lin, J. T. Hill, D. E. Chang, and O. Painter. “Electromagnetically induced transparency and slow light with optomechanics”. *Nature* **472**, 69–73 (2011).
-

- [Sal-1989] A. A. M. Saleh and J. Stone. “Two-stage Fabry-Perot filters as demultiplexers in optical FDMA LANs”. *J. Lightw. Technol.* **7**, 323–330 (1989).
- [Sal-2010] M. Salit and M. S. Shahriar. “Enhancement of sensitivity and bandwidth of gravitational wave detectors using fast-light-based white light cavities”. *J. Opt.* **12** (10), 104014 (2010).
- [Sav-1964] A. Savitzky and M. J. E. Golay. “Smoothing and differentiation of data by simplified least squares procedures.” *Anal. Chem.* **36**, 1627–1639 (1964).
- [Sch-2001] G. J. Schneider, S. Hanna, J. L. Davis, and G. H. Watson. “Defect modes in coaxial photonic crystals”. *J. Appl. Phys.* **90**, 2642–2649 (2001).
- [Sch-2006] A. Schweinsberg, N. N. Lepeshkin, M. S. Bigelow, R. W. Boyd, and S. Jarabo. “Observation of superluminal and slow light propagation in erbium-doped optical fiber”. *Europhysics Lett.* **73**, 218 (2006).
- [Sch-2012] A. Schweinsberg, Z. Shi, J. E. Vornehm, and R. W. Boyd. “A slow-light laser radar system with two-dimensional scanning”. *Opt. Lett.* **37**, 329–331 (2012).
- [Sha-2007] M. S. Shahriar, G. S. Pati, R. Tripathi, V. Gopal, M. Messall, and K. Salit. “Ultrahigh enhancement in absolute and relative rotation sensing using fast and slow light”. *Phys. Rev. A* **75**, 053807 (2007).
- [Sha-2014] S. M. Shahriar and F. A. Narducci. “Advances in slow and fast light VI”. In “Proc. SPIE”, volume 8998 (2014).
- [Sha-2005] J. Sharping, Y. Okawachi, J. van Howe, C. Xu, Y. Wang, A. Willner, and A. Gaeta. “All-optical, wavelength and bandwidth preserving, pulse delay based on parametric wavelength conversion and dispersion”. *Opt. Express* **13**, 7872–7877 (2005).
- [Shi-2007] H. Shin, A. Schweinsberg, G. Gehring, K. Schwertz, H. J. Chang, R. W. Boyd, Q.-H. Park, and D. J. Gauthier. “Reducing pulse distortion in fast-light pulse propagation through an erbium-doped fiber amplifier”. *Opt. Lett.* **32**, 906–908 (2007).
- [Sid-2003] O. Siddiqui, M. Mojahedi, and G. Eleftheriades. “Periodically loaded transmission line with effective negative refractive index and negative group velocity”. *IEEE Trans. Antennas Propag.* **51**, 2619–2625 (2003).
-

- [Sid-2004] O. Siddiqui, S. Erickson, G. Eleftheriades, and M. Mojahedi. “Time-domain measurement of negative group delay in negative-refractive-index transmission-line metamaterials”. *IEEE Trans. Microw. Theory Techn.* **52**, 1449–1454 (2004).
- [Sim-1981] G. R. Simpson. “A generalized n-port cascade connection”. In “IEEE Microw. Symp.”, pages 507–509 (June 1981).
- [Sin-2012] G. Singh, V. Janyani, and R. Yadav. “Modeling of a high performance Mach–Zehnder interferometer all optical switch”. *Opt. Applicata* **42**, 613–625 (2012).
- [Son-2005] K. Y. Song, M. G. Herráez, and L. Thévenaz. “Observation of pulse delaying and advancement in optical fibers using stimulated Brillouin scattering”. *Opt. Express* **13**, 82–88 (2005).
- [Spi-1994] C. Spielmann, R. Szipöcs, A. Stingl, and F. Krausz. “Tunneling of optical pulses through photonic band gaps”. *Phys. Rev. Lett.* **73**, 2308–2311 (1994).
- [Ste-1993] A. M. Steinberg, P. G. Kwiat, and R. Y. Chiao. “Measurement of the single-photon tunneling time”. *Phys. Rev. Lett.* **71**, 708–711 (1993).
- [Ste-2003] M. D. Stenner, D. J. Gauthier, and M. A. Neifeld. “The speed of information in a fast-light optical medium”. *Nature* **425**, 695698 (2003).
- [Su-2006] H. Su and S. L. Chuang. “Room temperature slow and fast light in quantum-dot semiconductor optical amplifiers”. *Appl. Phys. Lett.* **88**, 061102 (2006).
- [Taconic] Taconic Advanced Dielectric Division. www.taconic.com (Petersburgh, New York).
- [The-2008] L. Thévenaz. “Slow and fast light in optical fibres”. *Nature* **2**, 474–481 (2008).
- [Tir-1999] J. Tirapu, T. Lopetegui, M. A. G. Laso, M. J. Erro, F. Falcone, and M. Sorolla. “Study of the delay characteristics of 1-D photonic bandgap microstrip structures”. *Microw. Opt. Technol. Lett.* **23**, 346–349 (1999).
- [Tur-2001] A. V. Turukhin, V. S. Sudarshanam, M. S. Shahriar, J. A. Musser, B. S. Ham, and P. R. Hemmer. “Observation of ultraslow and stored light pulses in a solid”. *Phys. Rev. Lett.* **88**, 023602 (2001).
- [Wan-2000] L. J. Wang, A. Kuzmich, and A. Dogariu. “Gain-assisted superluminal light propagation”. *Nature* **406**, 277–279 (2000).
-

- [Wan-2004] L. G. Wang, H. Chen, and S. Y. Zhu. “Superluminal pulse reflection and transmission in a slab system doped with dispersive materials”. *Phys. Rev. E* **70**, 066602 (2004).
- [Wan-2006] L. G. Wang and S. Y. Zhu. “Superluminal pulse reflection from a weakly absorbing dielectric slab”. *Opt. Lett.* **31**, 2223–2225 (2006).
- [Wat-2005] K. Waters, J. Mobley, and J. Miller. “Causality-imposed (Kramers-Kronig) relationships between attenuation and dispersion”. *IEEE Trans. Ultrason., Ferroelectr., Freq. Control* **52**, 822–823 (2005).
- [Wen-2012] H. Wen, M. Terrel, S. Fan, and M. Digonnet. “Sensing with slow light in fiber bragg gratings”. *IEEE Sensors J.* **12**, 156–163 (2012).
- [Whe-1977] H. Wheeler. “Transmission-line properties of a strip line between parallel planes”. *IEEE Trans. Microw. Theory Techn.* **26**, 866–876 (1978).
- [Whe-2010] N. V. Wheeler, P. S. Light, F. Couny, and F. Benabid. “Slow and superluminal light pulses via EIT in a 20-m acetylene-filled photonic microcell”. *J. Lightw. Technol.* **28**, 870–875 (2010).
- [Whi-1996] J. Whitaker. *The Electronics Handbook*. Taylor & Francis (1996).
- [Wit-2010] W. Withayachumnankul, B. M. Fischer, B. Ferguson, B. R. Davis, and D. Abbott. “A systemized view of superluminal wave propagation”. *IEEE Proc.* **98**, 1775–1786 (2010).
- [Woo-2000] E. Wooten, K. Kissa, A. Yi-Yan, E. Murphy, D. Lafaw, P. Hallemeier, D. Maack, D. Attanasio, D. Fritz, G. McBrien, and D. Bossi. “A review of lithium niobate modulators for fiber-optic communications systems”. *IEEE J. Sel. Top. Quantum Electron.* **6**, 69–82 (2000).
- [Yeh-1988] P. Yeh. *Optical Waves in Layered Media*. John Wiley & Sons, New York (1988).
- [Yos-1982] T. Yoshino, K. Kurosawa, K. Itoh, and T. Ose. “Fiber-optic Fabry-Perot interferometer and its sensor applications”. *IEEE Trans. Microw. Theory Techn.* **30**, 1612–1621 (1982).
- [Zhu-2008] Z. Zhu, D. J. Gauthier, A. L. Gaeta, and R. W. Boyd. *Slow Light in Optical Waveguides, an invited chapter in Slow Light: Science and Applications*. Taylor & Francis (2008).
-

La presente tesis se ha presentado como compendio de las siguientes publicaciones:



Resumen global

Esta tesis se ubica dentro del campo de las tecnologías de luz lenta y luz rápida (SFL), cuya investigación se ha intensificado en los últimos años debido a sus interesantes aplicaciones, que van desde el procesado óptico de la información hasta la mejora de la precisión del senasado y la interferometría. Estas tecnologías se basan en sistemas que exhiben regiones de fuerte dispersión normal que permiten propagar pulsos a velocidades de grupo muy por debajo de la velocidad de la luz en el vacío (*luz lenta*) o fuerte dispersión negativa para lograr la propagación de pulsos a velocidades de grupo superlumínicas o incluso negativas (*luz rápida*). Estos regímenes anómalos de propagación tienen su origen en la interferencia de las componentes espectrales del pulso, así los efectos SFL se presentan en innumerables materiales que presentan resonancias espectrales. Los esfuerzos actuales en este campo se centran principalmente en la manipulación de medios activos (los cuales responden a la interacción con la luz generando estrechas bandas espectrales de ganancia o de absorción) o medios no lineales (*SFL material*) o en la optimización de medios microestructurados, sin fuerte dispersión del material, como cristales fotónicos, en los cuales la dispersión tiene un origen estructural y es debida al acoplamiento entre la longitud de onda incidente y la longitud característica del medio (*SFL estructural*).

Esta tesis se centra en el estudio, teórico y experimental, de la propagación del pulso electromagnéticos a velocidades de grupo anómalas en dos tipos de dispositivos lineales y pasivos. En la primera parte de la tesis se presenta un nuevo sistema que exhibe SFL

estructural, los interferómetros de multihaz. Se presenta un estudio exhaustivo de la aparición de SFL en este sistema carente de bandas de gap fotónico. Se desarrolla un modelo teórico que describe los regímenes de propagación de pulsos y sus limitaciones en términos tanto de las características del interferómetro como de las del propio pulso. Teniendo en cuenta los pulsos de amplitud modulada, las capacidades y limitaciones de los efectos SFL en este tipo de sistema se evalúan mediante la cuantificación de las figuras típicas de mérito como son: el retardo fraccional, la distorsión del pulso y producto retardo-ancho de banda. El marco teórico es válido para cualquier rango de frecuencia y las predicciones del modelo teórico se justifican mediante la realización de experimentos en el rango de radiofrecuencia y por medio de simulaciones numéricas exactas en el rango óptico. En primer lugar se considera el interferómetro más simple, con sólo dos ramas, ya que su uso es habitual en la tecnología actual de comunicaciones. Asimismo, se demuestra analíticamente que no es posible obtener luz lenta y que la atenuación total del sistema impulsa los cambios en los regímenes de propagación del pulso. Al aumentar el número de ramas, la transición de luz lenta a luz rápida se produce si la longitud óptica de una de las ramas se modifica ligeramente.

En la segunda parte de la tesis, la capacidad de las estructuras mono y multicapa para acelerar o frenar los pulsos electromagnéticos se investiga, con especial énfasis en sus propiedades de reflexión. Se estudian reflectores de Bragg y filtros Fabry-Pérot, usuales en los sistemas de comunicación de hoy en día. Estas estructuras han sido fabricadas para operar en el rango de microondas y en el rango de radiofrecuencia con el fin de confirmar las predicciones teóricas. Los resultados experimentales de su caracterización en frecuencia y en el dominio del tiempo se comparan con las simulaciones. La experimentación en estos rangos de frecuencia supone una importante ventaja sobre el rango óptico, ya que permite medir directamente la función de fase en transmisión (o en reflexión) de las estructuras empleando un analizador vectorial de redes de dos puertos vector. Esta caracterización es clave para identificar las distintas regiones de propagación (en transmisión o en reflexión) y evaluar posibles desviaciones sobre las predicciones teóricas. Además, se explora una posible aplicación de los reflectores de Bragg, haciendo uso del control de los retardos de grupo en transmisión y reflexión, para mejorar la eficiencia de los amplificadores feedforward, que se utilizan comúnmente para la cancelación de la distorsión inherente en amplificadores de microondas.

Conclusiones

Esta tesis presenta una investigación teórica y experimental de los efectos de luz lenta y luz rápida (SFL) en dos tipos de estructuras lineales y pasivas: interferómetros de multihaz, por un lado, y estructuras mono- y multi-capas, por otro. Las conclusiones resumidas y detalladas para cada sistema, así como para la aplicación propuesta en el rango de las microondas, se ha dado al final de su capítulo correspondiente. Aquí proporcionamos una discusión general de los principales resultados.

En los dos tipos de sistema abordados en este trabajo, la fuerte dispersión responsable de las velocidades de grupo anormales tiene un origen estructural, ya que se origina en el acoplamiento entre la frecuencia portadora del pulso y la longitud característica del sistema. Por lo tanto, estos efectos SFL no se basan en las propiedades electrónicas ni ópticas del material en las ramas de los interferómetros o en las multicapas, al contrario que ocurre en el caso de medios con resonancias de ganancia o absorción. Como consecuencia, los sistemas estudiados son escalables y esto proporciona plataformas experimentales más fáciles de implementar en donde nuestros modelos teóricos han podido ser comprobados, concretamente en el rango espectral de radiofrecuencia (RF) y de microondas (MW).

Como primera aportación principal de esta tesis, se ha propuesto e investigado un esquema novedoso para generar luz lenta y rápida utilizando interferómetros de múltiples haces. Se han obtenido expresiones analíticas exactas para el coeficiente de transmisión y para el retardo de

grupo en función de la frecuencia bajo condiciones de atenuación e índice de refracción constantes en el medio que forma las ramas. Con un análisis aproximado (válido a frecuencias en torno a los mínimos de la transmisión) se ha predicho los regímenes de propagación permitidos en interferómetros Mach-Zehnder (MZI) y en interferómetros de tres haces en términos de los parámetros del sistema (atenuación, índice de refracción, diferencia de longitud nominal entre las ramas y desajuste de longitud en una rama). Por primera vez, según creemos, se ha demostrado que no se puede obtener luz lenta si la diferencia de longitud entre las ramas adyacentes del interferómetro es constante, como siempre es el caso del MZI. Si se permite un pequeño desajuste de longitud en una de las ramas del interferómetro de tres haces, entonces puede aparecer luz lenta en uno de los dos mínimos, siempre y cuando ese desajuste supere un valor crítico. Este valor fundamental que establece la transición de luz lenta a luz rápida se ha obtenido como una función de la atenuación, del índice de refracción y de la diferencia de longitud nominal entre ramas adyacentes. Al mismo tiempo, se obtiene régimen de tunelado, superluminal, o régimen normal, en el otro mínimo, dependiendo de la atenuación total del sistema.

Se ha analizado la propagación de paquetes de onda sinusoidalmente modulados a través interferómetros MZI y tres de haces. Se han establecido las limitaciones de los efectos de luz lenta y rápida en función de las características del sistema y del pulso mediante el cálculo de las figuras de mérito típicas, es decir, retardo fraccional, compresión de pulso, producto retardo-ancho de banda y ruptura del pulso. Estos valores, que son similares a los obtenidos en sistemas de *gap* fotónico, son intrínsecos a estos interferómetros y no dependen del rango espectral de operación.

Como una prueba experimental del modelo, se han llevado a cabo experimentos de RF, en el dominio de la frecuencia y del tiempo, sobre interferómetros MZI y de tres haces construidos con cables coaxiales, obteniéndose un excelente acuerdo con las predicciones teóricas. Sin embargo, ya que la mayoría de las aplicaciones de luz lenta y rápida están orientadas hacia la fotónica, las predicciones de los modelos también se han comprobado a través de simulaciones numéricas en el rango óptico de un MZI basado en silicio y de un interferómetro de tres haces basado en niobato de litio, ambos operativos a 1,55 micras.

En cuanto a la posible aplicación de estos interferómetros, los valores típicos de sus figuras de mérito se resumen en la Tabla, en comparación con los de otras técnicas de SFL. Como ocurre en otras técnicas, los retardos/adelantos de pulso alcanzables (manteniendo la compresión de

pulso baja) son siempre más pequeños que la duración del pulso. Esto supone un inconveniente para el desarrollo de líneas de retardo prácticas para procesamiento de señales. Sin embargo, la abrupta transición SFL que aparece al acercarse al desajuste crítico en la longitud de una de las ramas del interferómetro de tres haces abre la puerta para aplicaciones de sensado.

Para concluir, destacar que la primera parte de esta tesis ofrece un estudio exhaustivo sobre el origen, capacidad y limitación de la luz lenta y rápida estructural en un sistema distinto a una estructura de *gap* fotónico. Esto es relevante ya que los efectos SFL estructurales habían sido sólo reportados en sistemas que exhiben *gaps* fotónicos, como cristales fotónicos, redes de Bragg (DBRs) o resonadores acoplados.

La segunda aportación principal de esta tesis se centra en los efectos de luz lenta y rápida de pulsos reflejos en estructuras multicapa, los cuales se utilizan comúnmente en los sistemas fotónicos reales. Mientras que estos efectos han sido ampliamente estudiados para pulsos transmitidos, en lo que se refiere a pulsos reflejados se han publicado menos resultados en estas estructuras. Nuestra investigación aquí se ha quedado en un nivel puramente numérico y experimental, aplicando tecnología microstrip para fabricar líneas y DBRs operativos en el rango de las microondas, y fabricando filtros Fabry-Perot para el rango de RF utilizando cables coaxiales. Para las simulaciones se usó el método de matriz de transferencia.

Resultados	$ FD $	DBP	n_g
Int. 3-haces	0.25	0.18	+45
DBR	0.13	0.1	7
FP Asimétrico	0.5	0.37	19
CPO [Geh-2006]	0.16	-	-4000
SBS [Son-2005]	0.3	1.05	7.6×10^{-4}
PBG [Bab-2008]	40	57	5.5
C-D [Oka-2007]	1200	42	1.8×10^{-4}

Tabla: Comparación entre diferentes sistemas en términos de retardo fraccional (FD), producto retardo-ancho de banda (DBP) e índice de grupo (n_g).

Esta tesis ha proporcionado la confirmación experimental de un resultado teórico publicado por otros autores sobre retardos de grupo negativos para pulsos reflejados en capas dieléctricas de baja absorción. Además, hemos deducido y demostrado la ley de escalado que el retardo de grupo satisface a la frecuencia de los mínimos de reflexión, donde se produce este comportamiento. Hemos encontrado que la relación de la parte real e imaginaria del índice de refracción n_r/n_i determina la magnitud del producto del tiempo de adelanto por la frecuencia central del pulso. Nuestro estudio también ha puesto de manifiesto la analogía entre tales efectos de luz rápida y aquellos descritos para pulsos de banda estrecha transmitidos en interferómetros MZI de baja atenuación, que también verifican esta ley de escalado simple y cuyo espectro de transmisión es muy similar a la del espectro de reflexión de una capa dieléctrica de bajas pérdidas. Podemos concluir asimismo que no puede sostenerse luz lenta en reflexión en capas dieléctricas pasivas.

Sorprendentemente, la caracterización de los efectos SFL en DBRs con el espesor de una de las capas desajustada y en estructuras Fabry-Perot (FP) con espejos asimétricos (con diferente número de capas en cada espejo) ha mostrado que se puede sintonizar de un régimen de luz lenta a luz rápida variando el espaciado entre espejos o la atenuación (en el caso de los FPs asimétricos) o modificando el espesor de una de las capas en el caso de un DBR. Por ejemplo, se han medido retardos fraccionales que van desde el +51% hasta el -37% en pulsos reflejados en estructuras FP construidas con cables coaxiales. Estos valores son similares a los retardos fraccionales publicados por otros autores en redes de Bragg activas y asimétricas.

Las principales figuras de mérito de estas estructuras multicapa se muestran en la Tabla y toman valores del mismo orden que las de los interferómetros de múltiples haces. Esto no debería ser sorprendente porque el origen físico de los efectos SFL en los dos tipos de sistemas es el mismo. Es decir, en los sistemas de multicapa, éstos están originados por la interferencia de las componentes espectrales del pulso y están asociados a condiciones del tipo Bragg para interferencia destructiva de ondas reflejadas. Por tanto, una desventaja común con los interferómetros es el hecho de que estos retardos/adelantos de pulso ocurren alrededor de los mínimos espectrales y por lo tanto, están acompañados por una fuerte atenuación del pulso de salida. Sin embargo, creemos que vale la pena estudiar la aplicación de estos sistemas como sensores de deformación, temperatura o cualquier magnitud que produzca un pequeño cambio en la fase, suficiente para producir la transición abrupta de SFL observada.

Como tercera y última contribución, esta Tesis ha propuesto la aplicación de un DBR diseñado y operativo en el rango de MW para mejorar la eficiencia de los amplificadores de feedforward, que utilizan una técnica de linealización estándar para eliminar los productos de intermodulación que surgen en los amplificadores de potencia. Este trabajo propone una topología alternativa que mejora la eficiencia y reduce el tamaño del amplificador convencional empleando un DBR como circuito de retardo de grupo negativo (NGD) en reflexión y como circuito con retardo de grupo positivo (PGD) en transmisión. Como ejemplo, se diseñó una estructura de DBR que compensa un retardo de 11,6 ns en el amplificador de potencia para una señal de dos tonos a 2,14 GHz y ancho de banda de 10 MHz. La mejora obtenida en la linealización es de 44 dB con respecto al amplificador no linealizado, con el único requisito de una línea de retardo extra de 0,3 ns en el bucle de cancelación de la distorsión. Además, hemos obtenido una mejora en la linealización de 40 dB para una señal WCDMA de 10 MHz de ancho de banda. Este esquema de amplificador *feedforward* basado en DBR proporciona una mejora de la linealización comparable al conseguido en otras arquitecturas *feedforward* publicadas en la literatura, pero con un menor tamaño y, presumiblemente, con un menor coste.

La posibilidad de adelantar o retrasar pulsos reflejados en estos dispositivos lineales y pasivos puede ser interesante para aplicaciones fotónicas, tales como la mejora de la precisión del sensado, ya que estos sistemas se proponen como una alternativa a los medios activos o no lineales. Las conclusiones y resultados de este trabajo son extensibles al rango óptico debido a la universalidad de los fenómenos de interferencia de ondas.

Observation of superluminal and negative group velocities in a Mach–Zehnder interferometer

M. M. Sánchez-López,^{1,a)} A. Sánchez-Meroño,¹ J. Arias,² J. A. Davis,³ and I. Moreno²

¹*Instituto de Bioingeniería, Universidad Miguel Hernández, 03202 Elche, Spain*

²*Departamento de Ciencia de Materiales, Óptica y Tecnología Electrónica, Universidad Miguel Hernández, 03202 Elche, Spain*

³*Department of Physics, San Diego State University, San Diego, California 92182-1233, USA*

(Received 13 June 2008; accepted 17 July 2008; published online 20 August 2008)

We demonstrate superluminal and negative group velocity regimes in a linear passive Mach–Zehnder interferometer. This phenomenon occurs in a narrow frequency region around the interferometer's transmission minima. Experiments are performed in the radio frequency range by using coaxial cables and 1×2 wave splitters. Group velocities of $2c$ and tunneling with a maximum fractional advancement of 0.12 were measured for electromagnetic sinusoidal wave packets of $2 \mu\text{s}$ width. These results agree with theoretical predictions using the interferometer's transmission phase function. This system is proposed as a simpler alternative to photonic crystals and active or microstructured multiple-beam interferometers for sustaining anomalous group velocities. © 2008 American Institute of Physics. [DOI: 10.1063/1.2969407]

Materials that exhibit large anomalous dispersion allow the wave group velocity to exceed c , the speed of light in vacuum, or even to become negative.¹ Anomalous dispersion occurs in media with sharp features in the transmission spectrum. Experimental evidence of this phenomenon has been so far provided in active systems with gain or absorption resonances (such as atomic vapors² and gain-assisted optical fibers,^{3,4} in nonlinear refractive index media,⁵ and in linear and passive periodic structures, such as photonic crystals⁶ and fiber Bragg gratings.⁷ Although most of this work was performed in the optical range, similar experimental results have been reported for microwave pulses⁸ and even at lower frequency ranges using electronic circuits.⁹

In this work, we demonstrate superluminal and negative group velocities in a linear and passive Mach–Zehnder interferometer (MZI). We show that the characteristic transmission pattern for this interferometer sustains these anomalous group velocity regimes over narrow frequency intervals within the interferometer's transmission minima, without the need of microstructuring or doping the arms of the interferometer. Tuning of the group velocity can be simply achieved by changing the length of one of the interferometer's arms. Our experiments are performed in the radio frequency (rf) range with a MZI using coaxial cables and 1×2 wave splitters. Because of their macroscopic dimensions, coaxial cable structures have been used in a variety of investigations, including the effects of impurity doping,¹⁰ the tunneling¹¹ and superluminal propagation of pulses¹² in photonic crystals, and the resonances of ultrathin Fabry–Pérot cavities.¹³ Implementation of the proposed MZI with optical fiber might be extended to all-optical signal processing applications where MZIs are widely used.

The expected group velocity of our MZI is calculated using the effective index approach,¹⁴ which ascribes the scattering loss of the electric field to an effective complex refractive index $n_{\text{eff}} = n + i\kappa$. The group velocity is related to the real part of n_{eff} by the well known expression¹

$$v_g = \frac{c}{n + \omega dn/d\omega}. \quad (1)$$

The real part of the refraction index is obtained from the overall phase shift on transmission (ϕ) through the structure of length L_{eff} , where L_{eff} is the average length of the cables that build the interferometer since the field amplitude in both arms is the same,

$$n = \frac{c\phi}{\omega L_{\text{eff}}}. \quad (2)$$

Substituting Eq. (2) into Eq. (1), the group velocity as a function of the total length and phase accumulated through the structure can be obtained as

$$v_g = \frac{L_{\text{eff}}}{d\phi/d\omega}. \quad (3)$$

We use this expression to predict the group velocity of our MZI, which consists of two coaxial cables (50 Ω , RG-58C/U), of 2 and 14 m length, respectively, connected to two 1×2 rf wave splitters (PE2000, Pasternack). The average length of the interferometer is thus $L_{\text{eff}} = 8$ m. The system's transmission spectrum (magnitude and phase) is calculated using a previously developed theory for the interference of N sinusoidal rf signals.¹⁵ It is also obtained experimentally by measuring the S_{21} scattering parameter with a two-port network analyzer (Agilent model E8363B). The transmission phase function $\phi(\omega)$ (theoretical and experimental) is then used in Eqs. (2) and (3) to obtain the interferometer's effective refractive index $n(\omega)$ and the expected group velocity $v_g(\omega)$.

These functions are shown in Fig. 1 in the frequency range where we will perform the experiments of pulse propagation. The transmission shows an oscillatory behavior at the frequencies of the transmission minima. The slope of the transmission phase function changes sign, and this causes the anomalous dispersion regions in the refraction index curve $n(\omega)$. These regions of negative slope of $n(\omega)$ lead to super-

^{a)}Electronic mail: mar.sanchez@umh.es.

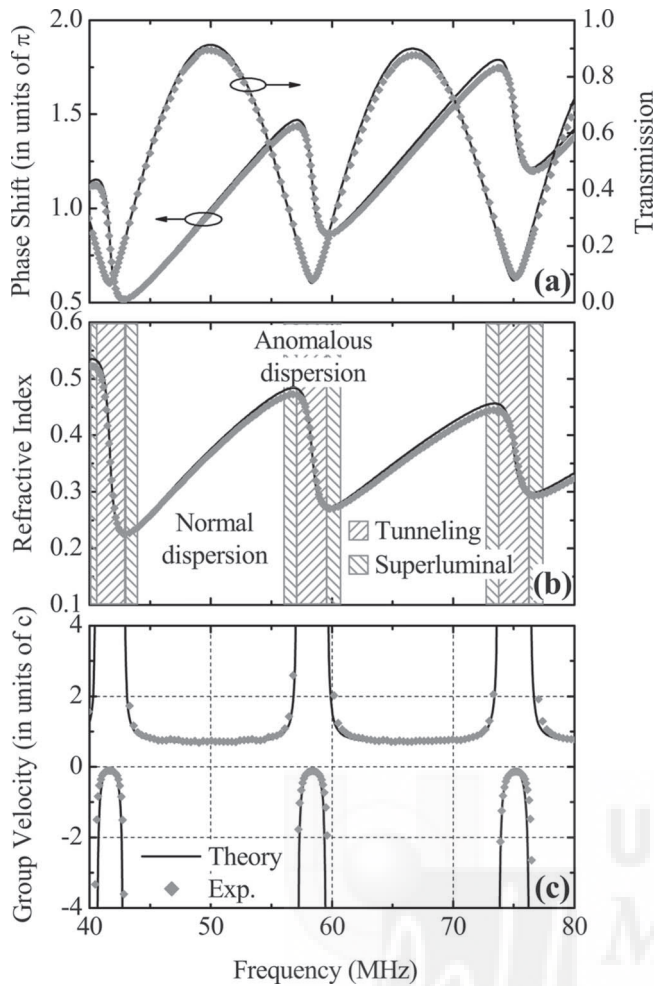


FIG. 1. Theoretical (lines) and experimental (symbols) results of (a) transmission coefficient magnitude and phase, (b) refractive index using Eq. (2), and (c) prediction of the group velocity using Eq. (3). Theoretical results use the calculated phase function $\phi(\omega)$, and experimental results use the measured $\phi(\omega)$. The interferometer arms have lengths of 2 and 14 m.

luminal or negative group velocities, depending on the magnitude of the slope. The anomalous dispersion is stronger at lower frequencies because of the lower attenuation in the cables. In the normal dispersion region, the group velocity equals the phase velocity in the cables ($0.67c$). Superluminal group velocities higher than $4c$ and negative group velocities as low as $-0.1c$ are expected for a signal with center frequency lying on a very narrow interval within the transmission minima. Comparison with a coaxial photonic crystal of the same effective length shows that our system achieves three times larger superluminal group velocities and presents regions of negative group velocity which are not expected in one-dimensional photonic crystals.¹⁶

We perform pulse propagation experiments in the frequency regions previously identified. The experimental setup is similar to the one proposed by Munday and Robertson¹¹ and shown in Fig. 2. The 500 kHz sinusoidal output of generator-1 (Tektronix CFG-253) is used to amplitude modulate the sinusoidal signal of generator-2 (IntraAction VFE-604A4), whose frequency can be varied between 40 and 80 MHz with a resolution of 10 kHz. This produces a train of sinusoidally modulated wave packets with carrier frequencies (f_c) in the megahertz range and $2 \mu\text{s}$ width that traverse the MZI and is recorded at the oscilloscope (Agilent DSO-

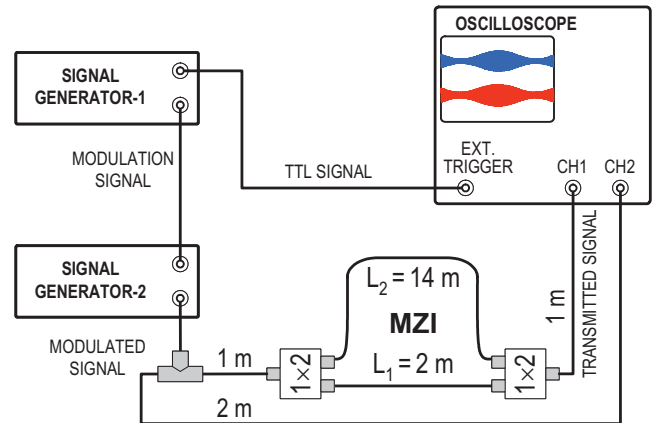


FIG. 2. (Color online) Experimental setup for the wave-packet propagation measurements through a MZI. The output signal from generator-2 is 100% amplitude modulated by the output signal from generator-1.

6032A). By means of a “T” connector at the output of generator-2, this wave packet is compared with that propagating along a single coaxial cable. The cable lengths indicated in Fig. 2 ensures that the time difference between these transmitted signals is equal to the propagation time through the interferometer (t_p).

Next, we perform accurate measurements of the group velocity by determining the pulse propagation time (t_p) through the interferometer, where $v_g = L_{\text{eff}}/t_p$. Since superluminal and mostly tunneling signals are largely attenuated, a direct observation of the pulse peak on the oscilloscope is not accurate enough. A systematic technique to determine the pulse center, which is less vulnerable to local fluctuations than the pulse peak, is more adequate. Different numerical methods have been suggested.¹² Here, the pulse center is obtained from a numerical analysis of the data by finding the best fit to the pulse envelope. The data is recorded with a resolution of 0.5 ns; however, the experimental error in the position of the pulse center is larger than 0.5 ns because the slightest pulse distortion makes the center of the top and bottom envelopes not coincident.

Figure 3 shows three wave-packet traces obtained at different carrier frequencies f_c . The size of the transmitted

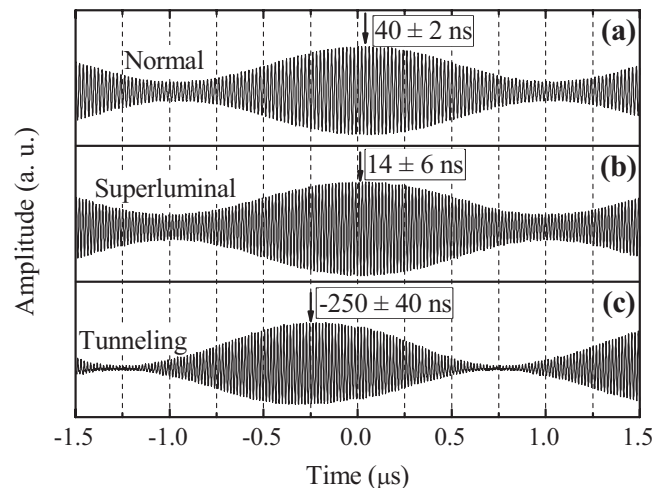


FIG. 3. Wave-packet traces at the three different propagation regimes, with carrier frequencies (a) 50 MHz (normal), (b) 56.5 MHz (superluminal), and (c) 58.3 MHz (tunneling). Each trace is normalized to its maximum amplitude.

signal (10 V in amplitude) decreases sharply as the frequency approaches the transmission minima. Accordingly, the amplitudes have been rescaled to make the analysis easier to discuss. The arrows indicate the time spent by the pulse center in propagating through the interferometer (t_p). Figure 3(a) shows the wave packet at a carrier frequency of $f_c = 50$ MHz corresponding to the normal dispersion region from Fig. 1. This signal is delayed by 40 ns as expected from the group velocity of $0.67c$.

This is also the time delay measured for this wave packet after propagating along a single coaxial cable of 8 m length (where the wave velocity is known to be $0.67c$), thus proving that the interferometer's effective length L_{eff} is indeed the average length of the two interferometer arms. Figure 3(b) shows the wave packet at a carrier frequency of $f_c = 56.5$ MHz corresponding to the superluminal region of Fig. 1. The amplitude of the signal was reduced to 4 V. The propagation time is reduced to 14 ± 6 ns denoting a superluminal group velocity of $1.9c \pm 0.8c$, close to the expected group velocity of $1.4c$. Figure 3(c) shows the wave packet at a carrier frequency of $f_c = 58.3$ MHz and is advanced to negative values of t_p . The amplitude of the signal was reduced to 1 V. Its center exits the MZI 250 ± 40 ns before the center of the input pulse has entered the structure, i.e., it tunnels through the interferometer with a negative group velocity of $-0.11c \pm 0.02c$, which is in good agreement with the expected group velocity ($-0.09c$). This counterintuitive effect is a direct result of the interference of the different frequency components and is not in conflict with relativistic causality.⁸ The fractional advancement achieved (advancement time/pulse width ratio) is of 0.12, the same value as the one reported with an erbium-doped optical fiber.³

To summarize, we have shown that plain MZIs can sustain superluminal and negative group velocities. Anomalous dispersion in a narrow frequency region around the interferometer's transmission minima is strong enough to hold these propagation regimes without the need of microstructuring, doping, or using nonlinear media in the interferometer's

arms. This anomalous dispersion is stronger than in one-dimensional photonic crystals, where negative group delays are not predicted. Experimental results have been obtained for sinusoidal wave packets propagating in a coaxial-cable MZI and are in good agreement with theoretical predictions using the effective refractive index approach. This system might be extended to the optical or microwave regimes for telecommunication applications.

Financial support from Ministerio de Educación y Ciencia through project FIS2006-13037-C02-02 is acknowledged.

- ¹L. Brillouin, *Wave Propagation and Group Velocity* (Academic, New York, 1960).
- ²L. J. Wang, A. Kuzmich, and A. Dogariu, *Nature (London)* **406**, 277 (2000).
- ³A. Schweinsberg, N. N. Lepeshkin, M. S. Bigelow, R. W. Boyd, and S. Jarabo, *Europhys. Lett.* **73**, 218 (2006).
- ⁴M. González-Herráez, K. Y. Song, and L. Thévenaz, *Appl. Phys. Lett.* **87**, 081113 (2005).
- ⁵Q. Yang, J. T. Seo, B. Tabibi, and H. Wang, *Phys. Rev. Lett.* **95**, 063902 (2005).
- ⁶A. M. Steinberg, P. G. Kwiat, and R. Y. Chiao, *Phys. Rev. Lett.* **71**, 708 (1993).
- ⁷S. Longhi, M. Marano, M. Belmonte, and P. Laporta, *IEEE J. Sel. Top. Quantum Electron.* **9**, 4 (2003).
- ⁸M. Mojahedi, E. Schamiloglu, F. Hegeler, and K. J. Malloy, *Phys. Rev. E* **62**, 5758 (2000).
- ⁹J. N. Munday and R. H. Henderson, *Appl. Phys. Lett.* **85**, 503 (2004).
- ¹⁰G. J. Schneider, S. Hanna, J. L. Davis, and G. H. Watson, *J. Appl. Phys.* **90**, 2642 (2001).
- ¹¹J. N. Munday and W. M. Robertson, *Appl. Phys. Lett.* **81**, 2127 (2002).
- ¹²A. Haché and L. Poirier, *Appl. Phys. Lett.* **80**, 518 (2002).
- ¹³J. A. Davis, M. M. Sánchez-López, J. Arias, M. Navarro, and I. Moreno, *Appl. Opt.* **46**, 3075 (2007).
- ¹⁴M. Centini, C. Sibilia, M. Scalora, G. D'Aguanno, M. Bertolotti, M. J. Bloemer, C. M. Bowden, and I. Nefedov, *Phys. Rev. E* **60**, 4891 (1999).
- ¹⁵J. A. Davis, D. A. Miller, M. M. Sánchez-López, and J. Cos, *Am. J. Phys.* **74**, 1066 (2006).
- ¹⁶L. Poirier, R. I. Thompson, and A. Haché, *Opt. Commun.* **250**, 258 (2005).

Negative Group Delay of Reflected Pulses on Microstrip Slabs and Bragg Reflectors

Aida Sánchez-Meroño, Julia Arias, and María del Mar Sánchez-López

Abstract—Experimental evidence of negative group delays (NGDs) for pulses reflected on microstrip dielectric slabs and Bragg reflectors is provided through frequency-domain characterization. This phenomenon occurs in a narrow frequency interval around the reflection minima, where the reflection phase function has a steep negative slope. Our results confirm recent theoretical predictions on weakly absorbing dielectric optical slabs, and a scaling law for the reflective group delay at the slab's design frequency is derived and probed. New interpretation of the Hartman effect (the saturation of the group delay with increasing structure length) is given in terms of the Bragg reflector's effective length.

Index Terms—Superluminal propagation, negative group delay, fast light, anomalous group velocity, Bragg reflectors, Hartman effect.

I. INTRODUCTION

SYSTEMS capable of sustaining superluminal and negative group velocities have attracted much interest in recent years because of their potential applications in communication networks [1], [2]. It is long known [3] that such propagation regimes occur in anomalous dispersive media, for narrow pulses with frequency components in the region where the frequency derivative of the refractive index is negative. Such anomalous pulse propagation regimes have been demonstrated experimentally in a wide range of optical systems including atomic vapors [4], doped optical fibers [5] and photonic band gap structures [6], [7]. Experimental evidence of this phenomenon has also been provided for lower frequency ranges, like microwave [2], [8], [9], radio-frequency [10], and even acoustic wave-packets [11].

When describing superluminal pulse propagation one often uses the more versatile concept of group delay, instead of group velocity, because it can be applied also to lumped systems, such as electronic circuits, where the device size is much smaller than the operating wavelength. In fact, such lumped systems have offered a clear insight on some controversial aspects of the superluminal phenomena, like the causality issue that arises for

negative group delays (NGDs) [12]. The group delay is the time delay of the pulse envelope as it propagates through a medium [3]. Following the usually adopted phase-time approach [2], [6], [9] the group delay of a transmitted, τ_t , (or reflected, τ_r) narrowband pulse, with center frequency ω_0 , is obtained from the frequency derivative of the transmission (or reflection) coefficient phase (ϕ) as

$$\tau_{t,r} = (\partial\phi_{t,r}/\partial\omega)_{\omega_0}. \quad (1)$$

NGDs are puzzling, since the peak of the output pulse precedes the peak of the input pulse. Although this phenomenon challenges common intuition, several works [4], [9], [12] demonstrate that it does not violate the causality principle.

Whereas most of the studies on superluminality deal with transmitted pulses, much fewer results have been reported concerning the superluminal propagation of *reflected* pulses. This topic is of interest since common devices in actual communication systems, like dielectric multilayer-based devices, host reflected waves and (not only) transmitted waves. In this context, reported studies on superluminal propagation of reflected pulses include Bragg gratings, Fabry–Pérot like photonic barriers and dielectric slabs.

Namely, superluminal peak advancement of reflected pulses was predicted in asymmetric photonic band gap structures where a transmission window inside the gap is opened [13]. These predictions were soon confirmed experimentally with the measurement of NGDs for picosecond optical pulses at 1.5 μm in fiber Bragg gratings adequately synthesized to have a double-Lorentzian spectral reflectivity function [14]. Also, superluminal reflection of microwave pulses in a Fabry–Pérot photonic tunneling barrier was reported in a time-domain experiment [15]. In this case, and although the reflected microwave pulse arrived earlier than the reference pulse, no NGDs were measured. An ulterior theoretical work [16] demonstrated that NGDs for reflected pulses in Fabry–Pérot barriers can be indeed achieved if the cavity contains resonant atomic absorbers. In a similar system, consisting of a dielectric slab doped with dispersive two-level or three-level atoms, superluminal reflected pulses with NGDs were obtained for specific slab thickness conditions [17]. Let us remark that in all the works cited above reporting NGDs in reflection [13], [14], [16], [17], the system is either asymmetric or doped with active or absorbing atoms.

Interestingly, a recent theoretical study has predicted large NGDs for reflected pulses in *symmetric, non-doped*, weakly absorbing dielectric slabs [18]. It shows that NGDs should occur for narrowband reflected pulses with center frequency in the minima of the slab's spectral reflective curve. The authors explicitly show that in these minima regions the reflective phase

Manuscript received September 04, 2009; revised October 23, 2009 and October 29, 2009. Current version published February 17, 2010. This work was supported by the Ministry of Education and Science in Spain under project FIS2009-13955-C02-02. The work of A. Sánchez-Meroño was supported by Generalitat Valenciana through the research program Gerónimo Forteza (FPA/2009/096).

A. Sánchez-Meroño and J. Arias are with the Department of Materials, Optics and Electronic Technology, Universidad Miguel Hernández, 03202 Elche, Spain (e-mail: aida.sanchez@umh.es; julia.arias@umh.es).

M. M. Sánchez-López is with the Department of Physics and the Institute of Bioengineering, Universidad Miguel Hernández, 03202 Elche, Spain (e-mail: mar.sanchez@umh.es).

Digital Object Identifier 10.1109/JQE.2009.2036744

function, $\phi_r(\omega)$, has a large negative slope, thus providing the NGD for reflected pulses according to (1). We have recently reported an analogous spectral curve in transmission, with steep negative slopes in the transmission phase function at the transmission minima, in an also linear and passive, but different system, consisting in a Mach–Zehnder interferometer, where NGDs of -250 ns were measured for transmitted electromagnetic sinusoidal wavepackets of $2 \mu\text{s}$ width [19].

In this paper we provide, for the first time to the best of our knowledge, experimental evidence of large NGDs in reflection for dielectric slabs, thus confirming the theoretical predictions in [18]. In addition, we show that such NGDs in reflection also occur for Bragg reflectors. Our experimental results are obtained in the microwave range by frequency-domain characterization of symmetric and passive microstrip dielectric slabs and Bragg reflectors. An advantage of operating in the microwave range is that we can measure the reflection phase function, $\phi_r(\omega)$, with a two-port vector network analyzer. Such a simple measurement of this key function that determines the pulse propagation regime cannot be directly performed in the optical range. We derive and probe a simple scaling law for the group delay at the design frequency, f_0 , of the dielectric slab. Scaling laws are useful in order to reproduce a specific device in another frequency range of operation.

Also, given that Bragg reflectors can be regarded as photonic barriers for pulses with their frequencies lying within the transmission gap, we investigate the differences in the Hartman effect for reflected and transmitted pulses on these periodic structures. The Hartman effect in such photonic barriers, i.e., the saturation of the group delay with barrier length, was reported long ago for transmitted pulses [20]. More recently, studies on photonic tunneling [15], [21] have shown that the saturation rate of the group delay is faster for reflected pulses than for transmitted pulses. As a remarkable result, we explain the saturation of group delay on reflection in terms of the Bragg reflector's effective length.

This paper is organized as follows. After this introduction, the fabrication of the microstrip devices and the experimental setup for their frequency-domain characterization is described in Section II. Section III presents the experimental results and their discussion. In Section IV, the main remarks and conclusions of this work are provided.

II. EXPERIMENT

In this section we describe the fabrication procedure of the two types of microstrip structures considered in this work. First, a high-impedance dielectric slab is fabricated to show experimentally the NGDs predicted by Wang and Zhu for optical dielectric slabs [18]. And second, Bragg reflectors are fabricated to analyze various aspects of their behavior for reflected pulses, such as the arising of NGDs and the Hartman effect.

We have designed microstrip single lines following the Hammerstad and Jensen model [22], which provides simple equations for characteristic impedance and effective dielectric constant as functions of microstrip width, substrate thickness and dielectric constant.

Samples were fabricated on a high-quality substrate using a LPKF Protomat 93s circuit board milling machine with $100\text{-}\mu\text{m}$ resolution. This substrate is a high-frequency double-sided

$35\text{-}\mu\text{m}$ copper plated laminate Taconic TLC, which is a commercial microwave circuit board material with a dielectric constant of 3.18 and thickness of 1.6 mm [23]. The nominal loss tangent of this substrate is 0.003. However, we found that experimental structures exhibit a larger overall attenuation than simulated structures with 0.003 loss tangent. A fitting procedure using the longest Bragg reflector (where attenuation effects are larger) led to 0.0045 as a more suitable value for the loss tangent and was used for the theoretical simulations presented in next section.

We have measured the actual values of every element width and length with an optical microscope of $100\text{-}\mu\text{m}$ resolution and checked that they lay within the experimental resolution of the milling machine.

Measurements of the scattering (S) parameters were performed on a two-port vector network analyzer (Agilent, model E8363B). The parameters S_{11} and S_{21} , which correspond to the reflection and transmission coefficient, respectively, were recorded in the range of 1 to 9 GHz either every 4.4 MHz (Bragg structures) or every 2.5 MHz (slab structure).

Experimental data contain a small amount of noise which is not very apparent in the S parameters themselves. To obtain the experimental group delay, the phase data curve must be differentiated and this amplifies the noise leading to spurious effects [24]. For this reason, in the calculations of the group delay following the phase-time approach in (1), the experimental phase data were smoothed prior differentiation. Although it is well known that smoothing is an arbitrary process that may give results which vary critically with the smoothing parameters, we finally used a 17-point Savitzky–Golay algorithm based on a second-degree polynomial fit [25], which does not essentially affect the slope of the phase at the reflection maxima and is satisfactory enough to preserve the key features of the group delay trends at the reflection minima.

A. High-Impedance Dielectric Slab

We have fabricated a microstrip slab of 1.377 mm nominal track width, which corresponds to a 86.6Ω characteristic impedance, and 39 mm nominal length. This length corresponds to $\lambda/2$ (where λ is the wavelength in the medium) for a frequency of $f_0 = 2.5$ GHz. The nominal impedance contrast between the $50\text{-}\Omega$ ports and the slab corresponds to the refractive index contrast ($1:\sqrt{3}$) of the optical dielectric slab considered by Wang and Zhu [18]. Fig. 1(a) shows the fabricated sample. Actual values of line width and length are 1.35 mm and 39.1 mm, respectively.

B. Bragg Reflectors

We have fabricated periodic $\lambda/4$ structures of the type $(\text{HL})^N\text{H}$ containing $N + 1/2$ unit cells, where H represents a high impedance (nominally 75Ω) line with length L_H and width w_H , and L represents a low impedance (nominally 50Ω) line with length L_L and width w_L . These Bragg reflectors were designed to have the first transmittance gap at a frequency of 2.5 GHz and were fabricated with $N = 2, 4, 6$, and 8 unit cells. As an example, Fig. 1(b) shows the $N = 2$ structure. The actual values of element width and length are $L_H = 19.25$ mm, $w_H = 1.75$ mm, $L_L = 18.75$ mm, and $w_L = 3.75$ mm in the

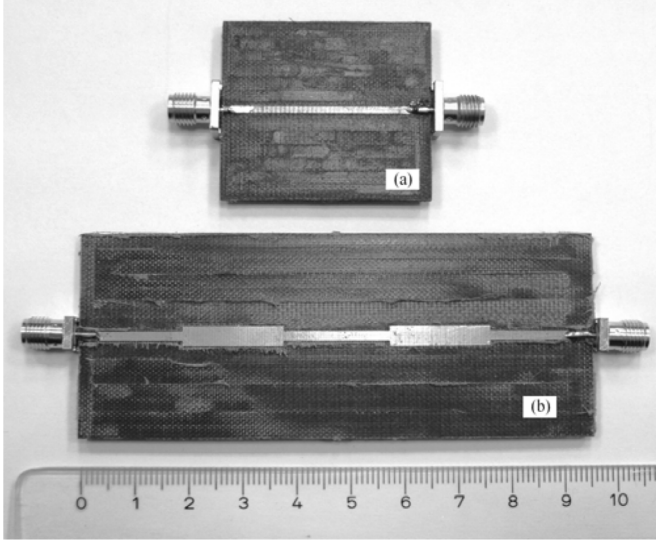


Fig. 1. Top view of fabricated microstrip structures: (a) 86.6 Ω dielectric slab, and (b) Bragg reflector with $2 + 1/2$ unit cells. SMA connectors have 50- Ω characteristic impedance.

case of the Bragg reflector with $N = 6$ layers. These values were similarly enough for the other structures and were the ones considered in the theoretical simulations presented in the next section.

III. RESULTS AND DISCUSSION

Let us first analyze the high-impedance microstrip dielectric slab. By means of the frequency-domain characterization performed with the vector network analyzer, we wish to compare the reflection of pulses on this microstrip slab with the behavior predicted by Wang and Zhu for a weakly absorbing optical dielectric slab [18].

For that purpose, we have selected one of the structures in [18], namely a dielectric slab with refractive indexes $1:\sqrt{3}:1$ and dielectric constant imaginary part $\varepsilon_i = 0.01$. In order to keep the frequency range shown in [18], with the first reflection minima at 129.9 THz, we have considered the thickness, d , of this optical slab to be $\lambda/2$ for a design frequency of $f_0 = 129.9$ THz, thus yielding $d \approx 0.66 \mu\text{m}$. Consequently, our microstrip line is a scaled version, in the microwave range, of this optical dielectric slab. A standard transfer-matrix method [26] (TMM) is then applied to calculate the reflection coefficient (magnitude $|r|$ and phase ϕ_r) of the optical slab as a function of frequency. For the microstrip line, these functions are measured using the network analyzer and they are also calculated numerically by TMM using the actual values of the microstrip line width and length. The corresponding group delay in reflection, τ_r , is then obtained from the frequency derivative of ϕ_r . In this calculation, the same numerical treatment (smoothing and differentiation) has been applied to the experimental and simulated phase functions. The results ($|r|$, ϕ_r and τ_r) are shown in Fig. 2, where the frequency axis has been normalized to the design frequency (2.5 GHz and 129.9 THz for the microstrip and optical slab, respectively) for better comparison.

The magnitude of the reflection coefficient in Fig. 2(a) shows the expected behavior of a dielectric slab, with minima at the

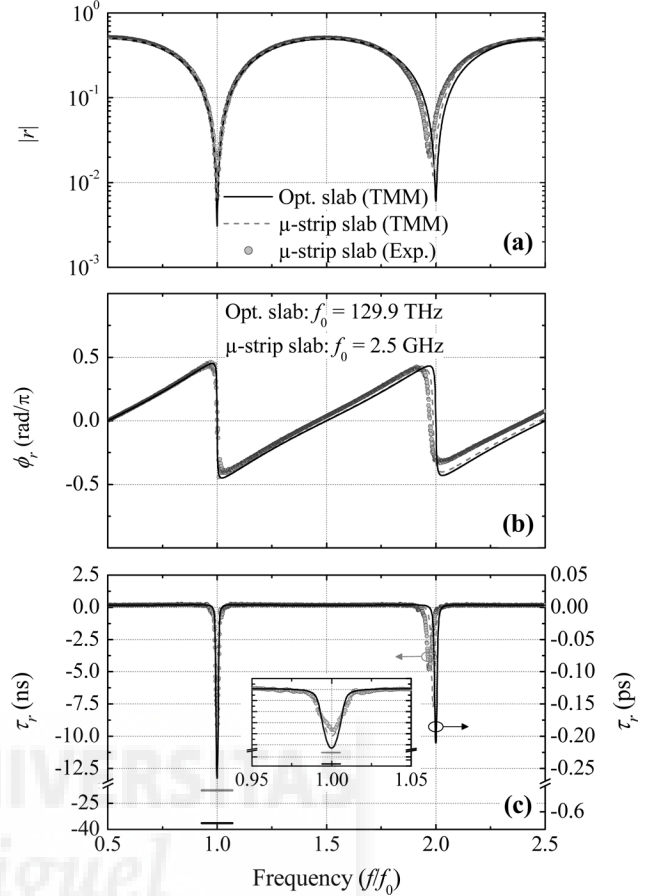


Fig. 2. Scaling of optical (in black) and microstrip (gray) slabs. TMM numerical simulation of a $\lambda/2$ optical dielectric slab for $f_0 = 129.9$ THz and thickness $d = 0.66 \mu\text{m}$ with $\varepsilon_r = 3$ and $\varepsilon_i = 0.01$ (black curve). TMM numerical simulation (dashed curve) and experimental frequency-domain characterization (circles) of a $\lambda/2$ microstrip slab for $f_0 = 2.5$ GHz and length $d = 39.1$ mm with loss tangent 0.0045. (a) Magnitude of the reflection coefficient in logarithmic scale, (b) phase of the reflection coefficient, and (c) group delay obtained using (1) after smoothing the phase function. The horizontal marks indicate the theoretical value of τ_r at f_0 when the phase data are not smoothed numerically. The inset figure shows the situation at f_0 in more detail.

resonant frequencies (f_0 and its multiples). These minima are more pronounced for the optical slab because of its weaker attenuation. The second resonance of the microstrip slab is slightly shifted from $2f_0$ because of the dispersion in the effective dielectric constant, which is indeed taken into account in the simulations [22]. The good agreement between the microstrip experimental and simulated curves probes the success of the microstrip design and fabrication. The reflection phase functions ϕ_r in Fig. 2(b) display a steep negative slope at the resonant frequencies, which lead to large and negative values of the group delay in Fig. 2(c). The results for the optical slab agree with those in [18]. The inset shows in detail the group delays at the design frequency. We attribute the difference in the experimental and simulated results for the microstrip to a higher attenuation of the actual slab. Group delay of $\tau_r \approx -9$ ns is expected for a microwave narrowband pulse of 2.5 GHz center frequency reflected on the fabricated microstrip slab. The corresponding situation for the optical slab and an optical pulse centered at 129.9 THz is $\tau_r \approx -0.25$ ps. Therefore, microwave pulses reflected on a microstrip slab show essentially the same

physics predicted in [18] for optical pulses reflected on the equivalent dielectric slab.

Now, let us make a closer comparison. Since this $\lambda/2$ microstrip slab is a scaled version, in the microwave range, of the $\lambda/2$ optical slab, a natural question arises: is there a scaling law for the NGD at the design frequency?

Using the analytical expressions of the group delays given by Wang and Zhu [18], it can be easily obtained that for small attenuation values, the reflective group delay at f_0 can be approximated as

$$\tau_r = -\frac{1}{2\pi f_0} \frac{n_r}{n_i} = -\frac{n_r}{f_0 c \alpha_0}. \quad (2)$$

where n_r and n_i are the real and imaginary part of the refractive index, respectively, c is the speed of light in vacuum, and α_0 is the attenuation per unit length and per design frequency f_0 . The ratio n_r/n_i is 600 for the optical slab, and 276 for the microstrip slab at f_0 . Therefore, according to (2) the expected group delay at f_0 for the optical slab is $\tau_r = -0.73$ ps, whereas for the microstrip slab it is $\tau_r = -17.57$ ns. These values are larger (absolute values) than the ones shown by the curves in Fig. 2(c) because of the smoothing of the phase functions. The horizontal marks in Fig. 2(c) indicate the values reached by τ_r at f_0 when the phase data are not smoothed numerically. As we can see, these latter values do agree with the scaling law in (2).

Finally, let us mention that in order to compare the group delays at the resonant frequencies, the limiting numbers of the time axes in Fig. 2(c) were selected such that, once multiplied by its corresponding f_0 , they take the same value for both slabs. In this way, the apparent difference in τ_r for the microstrip and optical slab is due to the ratio n_r/n_i .

We now discuss the frequency-domain characterization of our fabricated microstrip Bragg reflectors $(HL)^N H$. Considering the above results, and the typical reflectance spectrum of multilayer mirrors [26], NGDs in reflection should also be obtained in these structures.

Fig. 3 shows the reflection coefficient's magnitude, $|r|$, and phase, ϕ_r , (top and middle panels, respectively) and the group delay on reflection, τ_r , (bottom panel) obtained from (1). The experimental curves correspond to the scattering parameter data S_{11} , whereas the theoretical curves (solid line) have been obtained by applying the TMM [26], including the wave attenuation along the microstrip structure. The excellent agreement between theory and experiment is a consequence of considering the following issues.

First, for the numerical simulation of the structures, the actual values of the lengths and widths of the H and L layers are considered. The consideration of the actual values for L_H , w_H , L_L and w_L , rather than their design values, is important to avoid shifts in the positions of the resonant peaks between theory and experiment.

Second, in the calculation of the group delay, the same numerical treatment (explained in Section II) is given to the experimental and to the theoretical phase data.

Third, as explained before, instead of the nominal value of 0.003, a loss tangent of 0.0045 was considered in the TMM theoretical calculations for all the Bragg reflectors.

Let us now analyze the results. Fig. 3(a) corresponds to the microstrip structure $(HL)^2 H$. The function $|r|$ shows the typical oscillations in Bragg reflectors, with two main reflection peaks in the displayed frequency range. The first peak position agrees with its design value of 2.5 GHz, while the second peak is slightly shifted off 7.5 GHz in both the experimental and simulated curve because of the frequency dispersion of the microstrip effective dielectric constant. Between these peaks there are five reflection minima, and, as it occurs for the simpler microstrip slabs previously analyzed, these minima are associated to large negative slopes in the reflection phase function ϕ_r , and the consequent negative values of the group delay in a narrow frequency region around the reflection minima. For instance, at 1.6 GHz, group delays of -3 ns are reached and pulse peak advancements larger than 1 ns are expected for reflected pulses of 140 MHz bandwidth. These values of group delay and bandwidth are similar to the ones obtained in coplanar waveguide left-handed media [27].

As the number of layers (N) increases, the number of minima between the main reflection peaks increases by the rule $2N + 1$ [see Fig. 3(b), (c), and (d)] so that a larger number of minima must fit inside the same frequency interval. This sharpens the minima and makes narrower the frequency region of NGDs. Also, and due to the higher attenuation as N increases, less NGDs are reached. For instance, also at 1.6 GHz and for $N = 8$, the NGD is of only -1.5 ns and the pulse bandwidth is now limited to 90 MHz.

Experiments of superluminal reflection of optical pulses have reported [14] NGDs of -60 ps in fiber Bragg gratings specially apodized to provide a double-Lorentzian spectral reflectivity with a pronounced dip. The results of Fig. 3 show that NGDs should also occur for fiber Bragg gratings with an index profile like that of a quarter-wave dielectric structure. Interestingly, we found that our measured transmission coefficient data for the Bragg reflectors show that, as opposed to reflected pulses, NGDs do not occur for pulses transmitted in these linear and periodical structures. This issue is still controversial [28]–[30], and in this context, our S_{21} data agree with a previous theoretical work [29] which questioned experimental results reporting NGDs for transmitted pulses in coaxial cable photonic crystals [28].

The behavior of reflected pulses with their frequency components at the reflection's maxima (rather than at the minima) is now addressed. These frequency regions, where τ_r is positive, correspond to the transmission gaps. Therefore, Bragg reflectors behave as photonic barriers for pulses whose frequencies lie within the forbidden transmission regions. In this context, we investigate the origin of the differences observed in [15] and [21] on the Hartman effect for reflected and transmitted pulses. The Hartman effect is the saturation of the group delay of a pulse that propagates along a photonic barrier as the length of the barrier increases [31]. The frequency-domain characterization of our microstrip Bragg reflectors with increasing number of layers N makes possible to compare the Hartman effect for reflected and transmitted pulses.

For that purpose, we consider the frequencies of the transmission gaps (2.5 GHz and 7.5 GHz) and we plot, as a function of length, the corresponding values for the group delay on

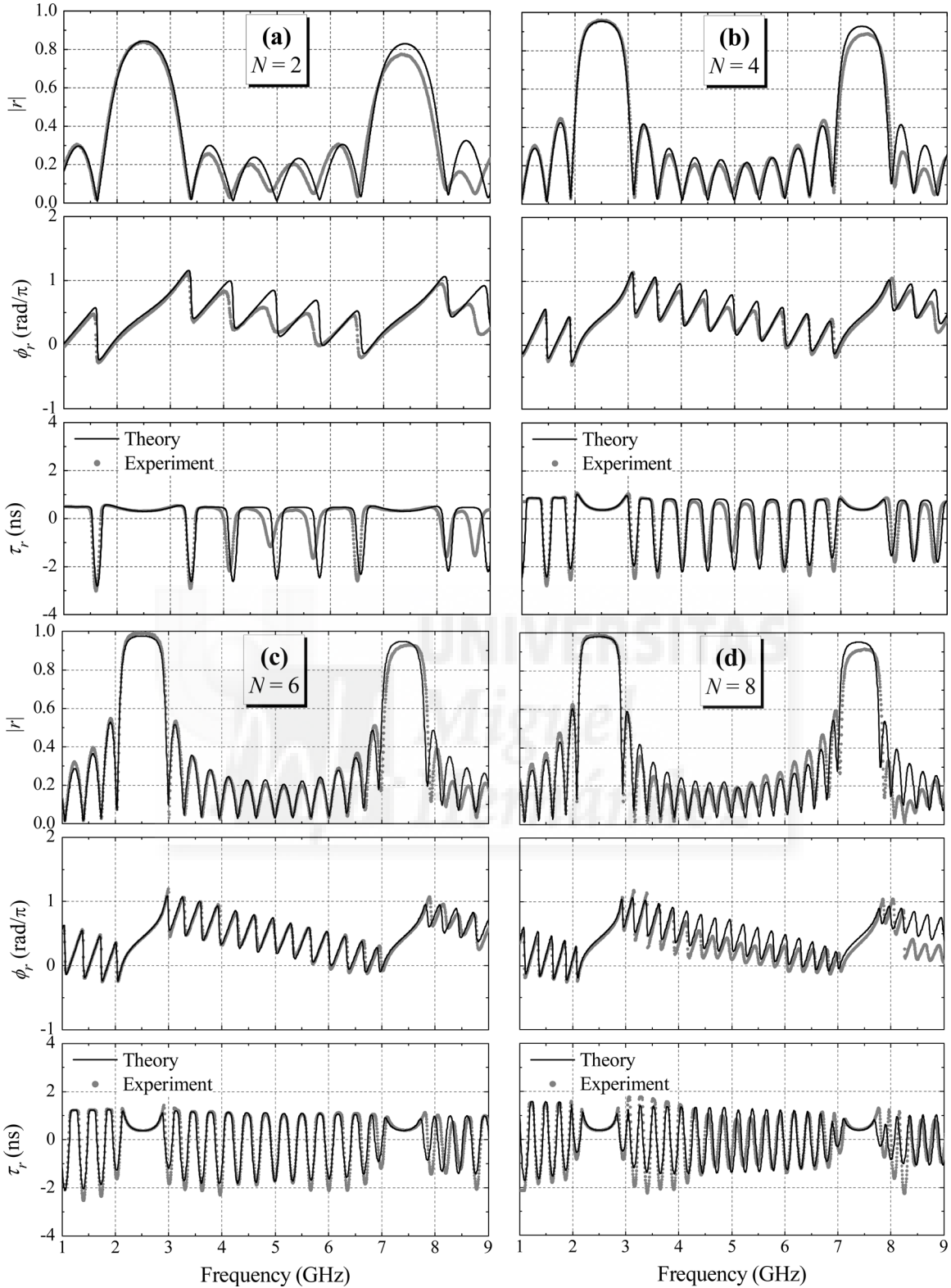


Fig. 3. Experimental and theoretical results for the frequency-domain characterization of reflected pulses on microstrip Bragg reflectors $(HL)^N H$. Top panel shows magnitude of the reflection coefficient, middle panel shows phase of the reflection coefficient, and bottom panel shows group delay (obtained using (1) after smoothing the phase function) for (a) $N = 2$, (b) $N = 4$, (c) $N = 6$, and (d) $N = 8$ unit cells.

reflection (τ_r) and on transmission (τ_t) obtained from Fig. 3 and from its analogous in transmission. The results are shown in Fig. 4. The filled points in the figure correspond to the experimental values and the crossed points join the TMM calcu-

lated values for the structures with $N = 1-8$. The agreement between theory and experiment is very good. Also included is the calculated group delay for a uniform microstrip waveguide, τ_0 , (dashed line).

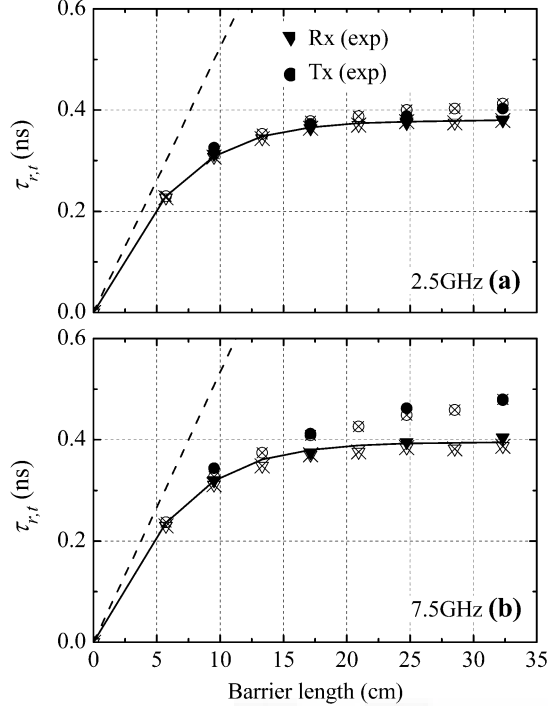


Fig. 4. Study of the Hartman effect in microstrip Bragg reflectors. Transmission and reflection group delays as functions of the length of the $(\text{HL})^N\text{H}$ structures at (a) 2.5 GHz, and (b) 7.5 GHz. Filled points are experimental data for $N = 2, 4, 6$, and 8, and crossed points are TMM theoretical results for $N = 1 - 8$. The solid line is obtained from (4), and the dashed line corresponds to a uniform microstrip waveguide.

Fig. 4(a) shows the group delays at 2.5 GHz. Reflection and transmission group delays coincide for short barriers, but as the barrier length increases, τ_r saturates for the structure with $N = 6$ layers (barrier length ~ 25 cm) whereas τ_t does not quite saturate yet. This different behavior is more evident at 7.5 GHz [see Fig. 4(b)], where τ_t clearly increases with barrier length (although at a slower rate than τ_0) while τ_r takes similar values as those in Fig. 4(a). This behavior was also observed in the tunnelling of radio frequency pulses through coaxial-cable band-gap structures [21]. It can be understood by closely examining the phase functions ϕ_r and ϕ_t as N increases. We found that the curves ϕ_r converge to the same linear function near the gap center frequency (thus yielding the same group delay), whereas the slopes of the ϕ_t curves increase slightly. This is due to the attenuation, which is higher for larger structures and smoothes the Bragg interference in the band gap region. As a consequence, the slope of ϕ_t tends to approach the value outside the gap region.

Therefore, the results of Fig. 4 clearly show that the role of attenuation is much weaker for τ_r , which rapidly saturates. This result was interpreted in [21] by regarding this kind of structures as a combination of a shortened lossless Bragg reflector and a uniform but absorptive waveguide. From this point of view, attenuation mainly affects the transmission wave and has negligible contribution to the reflected wave. Following this picture, one can attempt to estimate τ_t at f_0 for a given structure as a linear combination of τ_r and the group delay of a uniform microstrip line of the same length, τ_0 , with absorption-dependent

coefficients such that τ_r and τ_t coincide in the absence of attenuation. For our specific Bragg reflectors we found that a good approximation is

$$\tau_t \approx \left(1 - \frac{A}{\sqrt{2}}\right) \tau_r + \frac{A}{\sqrt{2}} \tau_0 \quad (3)$$

where $A = 1 - |r|^2 - |t|^2$ accounts for the total absorption through our Bragg structures at f_0 , which can be obtained by TMM numerical simulation. The values obtained from (3) exactly match the TMM calculated results of τ_t shown in Fig. 4. A generalization of this expression to any attenuation level is still under further investigation.

The above results point out that in the case of weak absorption, τ_r and τ_t approximately have the same value at f_0 , and a simple expression to estimate them can be very attractive. A reasonable approach considers the Bragg reflector as a discrete mirror with equal magnitude of the grating's reflection, $|r|$, but placed a distance L_{eff} away, such as it gives the proper mirror phase, ϕ_r . In this picture, τ_r can be estimated as the propagation delay of the incident wave traversing a distance equal to this effective mirror length L_{eff} and back:

$$\tau_r = \frac{2L_{\text{eff}}}{v_p} \quad (4)$$

The Appendix summarizes the main expressions used to calculate L_{eff} in terms of the mirror's characteristics. We consider a propagation velocity, v_p , as the average between the propagation velocities through 50- and 75- Ω elements, which gives a value of approximately $c/1.57$ at 2.5 GHz. Neglecting mirror losses, L_{eff} saturates with number of mirror periods to a value of approximately 38 mm. For $N = 6$, L_{eff} is 99% of the saturation value. The calculated values of τ_r for lossless Bragg reflectors using this simple approach (see solid curve in Fig. 4) are in excellent agreement with the theoretical values using TMM simulations.

IV. CONCLUSION

In this work, we have provided experimental evidence of NGDs for reflected pulses on microstrip slabs, thus confirming recent theoretical predictions on optical dielectric slabs. Group delays as low as -9 ns have been obtained by frequency-domain characterization of a weakly absorbing $\lambda/2$ microstrip line at 2.5 GHz. This microwave operating device scales excellently to its corresponding structure in the optical range. The reflective group delay at the slab's design frequency verifies a simple scaling law.

We have also provided experimental evidence of NGDs for reflected pulses on microstrip Bragg reflectors, with group delays of -3 ns for 140 MHz pulse bandwidth. As in the case of slabs, this phenomenon occurs in a very narrow frequency interval around the reflection minima and is a consequence of the steep negative slope of the reflection phase function at these frequencies. So far, NGDs in reflection had only been reported for asymmetric or doped multilayer systems, and in left-handed media.

Also, relevant differences in the Hartman effect for reflected and transmitted pulses on Bragg reflectors have been shown in this work. Namely, the much faster saturation rate of the group

delay in reflection, which is hardly affected by the attenuation. We have provided a new interpretation of this effect in terms of the mirror's effective length.

The possibility of advancing pulses reflected on these linear and passive multilayered microstrip devices might be interesting for applications in communication networks. This study is extensible to the optical range due to the universality of the wave interference phenomena.

APPENDIX

The mirror effective length of a lossless Bragg reflector can be calculated at the Bragg frequency as [32]

$$L_{\text{eff}} = \frac{1}{2} m_{\text{eff}} \Lambda \left(\frac{1}{1 + r_{\text{HL}}^2} - \frac{1}{2m_{\text{eff}}} \right) \quad (\text{A1})$$

where r_{HL} is the H-L interface reflectivity, Λ is the length of the mirror period, and m_{eff} is the effective number of mirror periods seen by the incident field at the Bragg frequency. This number can be calculated as

$$m_{\text{eff}} = \frac{\tanh \left[m \ln \left(\frac{1+r_{\text{HL}}}{1-r_{\text{HL}}} \right) \right]}{\tanh \left[\ln \left(\frac{1+r_{\text{HL}}}{1-r_{\text{HL}}} \right) \right]} \quad (\text{A2})$$

where m is the number of mirror periods, which is $N + 1$ in our structures.

ACKNOWLEDGMENT

The authors thank J. P. Espinosa for the fabrication of the microstrip filters.

REFERENCES

- [1] L. Thévenaz, "Slow and fast light in optical fibers," *Nat. Photonics*, vol. 2, pp. 474–481, Aug. 2008.
- [2] G. Nimtz, "Superluminal signalling by photonic tunneling," *IEEE J. Sel. Top. Quantum Electron.*, vol. 9, no. 1, pp. 79–85, Jan./Feb. 2003.
- [3] L. Brillouin, *Wave Propagation and Group Velocity*. New York: Academic Press, 1960, ch. 3.
- [4] L. J. Wang, A. Kuzmich, and A. Dogariu, "Gain-assisted superluminal light propagation," *Nature*, vol. 406, pp. 277–279, 2000.
- [5] A. Schweinsberg, N. N. Lepeshkin, M. S. Bigelow, R. W. Boyd, and S. Jarabo, "Observation of superluminal and slow light propagation in erbium-doped optical fiber," *Europhys. Lett.*, vol. 73, no. 2, pp. 218–224, 2006.
- [6] A. M. Steinberg, P. G. Kwiat, and R. Y. Chiao, "Measurement of the single-photon tunnelling time," *Phys. Rev. Lett.*, vol. 71, pp. 708–711, 1993.
- [7] S. Longhi, M. Marano, M. Belmonte, and P. Laporta, "Superluminal pulse propagation in linear and nonlinear photonic grating structures," *IEEE J. Sel. Top. Quantum Electron.*, vol. 9, no. 1, pp. 4–16, Jan./Feb. 2003.
- [8] J. Tirapu, T. Lopetegui, M. A. G. Laso, M. J. Erro, F. Falcone, and M. Sorolla, "Study of the delay characteristics of 1D photonic bandgap microstrip structures," *Microw. Opt. Technol. Lett.*, vol. 23, no. 6, pp. 346–349, Dec. 1999.
- [9] M. Mojahedi, K. J. Malloy, G. V. Eleftheriades, J. Woodley, and R. Y. Chiao, "Abnormal wave propagation in passive media," *IEEE J. Sel. Top. Quantum Electron.*, vol. 9, no. 1, pp. 30–39, Jan./Feb. 2003.

- [10] A. Haché and L. Poirier, "Anomalous dispersion and superluminal group velocity in a coaxial photonic crystal: Theory and experiment," *Phys. Rev. E*, vol. 65, pp. 036608 1–036608 6, 2002.
- [11] W. M. Robertson, J. Ash, and J. M. McGaugh, "Breaking the sound barrier: Tunneling of acoustic waves through the forbidden transmission region of a one-dimensional acoustic band gap array," *Am. J. Phys.*, vol. 70, no. 7, pp. 689–693, July 2002.
- [12] M. Kitano, T. Nakanishi, and K. Sugiyama, "Negative group delay and superluminal propagation: an electronic circuit approach," *IEEE J. Sel. Top. Quantum Electron.*, vol. 9, no. 1, pp. 43–51, Jan./Feb. 2003.
- [13] S. Longhi, "Superluminal pulse reflection in asymmetric one-dimensional photonic band gaps," *Phys. Rev. E*, vol. 64, pp. 037601 1–037601 4, Aug. 2001.
- [14] S. Longhi, M. Marano, P. Laporta, M. Belmonte, and P. Crespi, "Experimental observation of superluminal pulse reflection in a double-Lorentzian photonic band gap," *Phys. Rev. E*, vol. 65, pp. 045602(R) 1–045602(R) 4, Mar. 2002.
- [15] G. Nimtz, A. Haibel, and R. M. Vetter, "Pulse reflection by photonic barriers," *Phys. Rev. E*, vol. 66, pp. 037602 1–037602 4, Sept. 2002.
- [16] V. S. C. Manga Rao and S. Dutta Gupta, "Atomic absorbers for controlling pulse propagation in resonators," *Opt. Lett.*, vol. 29, no. 3, pp. 307–309, Feb. 2004.
- [17] L. G. Wang, H. Chen, and S. Y. Zhu, "Superluminal pulse reflection and transmission in a slab system doped with dispersive materials," *Phys. Rev. E*, vol. 70, pp. 066602 1–066602 6, Dec. 2004.
- [18] L. G. Wang and S. Y. Zhu, "Superluminal pulse reflection from a weakly absorbing dielectric slab," *Opt. Lett.*, vol. 31, no. 14, pp. 2223–2225, July 2006.
- [19] M. M. Sánchez-López, A. Sánchez-Meroño, J. Arias, J. A. Davis, and I. Moreno, "Observation of superluminal and negative group velocities in a Mach-Zehnder interferometer," *Appl. Phys. Lett.*, vol. 93, pp. 074102 1–074102 3, Aug. 2008.
- [20] Ch. Spielmann, R. Szipöcs, A. Stingl, and F. Krautzsch, "Tunneling of optical pulses through photonic band gaps," *Phys. Rev. Lett.*, vol. 73, pp. 2308–2311, 1994.
- [21] S. Doiron, A. Haché, and H. Winful, "Direct space-time observation of pulse tunnelling in an electromagnetic band gap," *Phys. Rev. A*, vol. 76, pp. 023823 1–023823 6, Aug. 2007.
- [22] E. Hammerstad and Ø. Jensen, "Accurate models for microstrip computer-aided design," in *IEEE MTT-S Int. Microwave Symp. Dig.*, 1980, vol. 80, pp. 407–409.
- [23] Taconic Advanced Dielectric Division, Petersburg, NY [Online]. Available: <http://www.taconic-add.com/>
- [24] M. Mojahedi, E. Schamiloglu, K. Agi, and K. J. Malloy, "Frequency-domain detection of superluminal group velocity in a distributed Bragg reflector," *IEEE J. Quantum Electron.*, vol. 36, no. 4, pp. 418–424, Apr. 2000.
- [25] A. Savitzky and M. J. E. Golay, "Smoothing and differentiation of data by simplified least squares procedures," *Analyt. Chem.*, vol. 36, no. 8, pp. 1627–1639, July 1964.
- [26] P. Yeh, *Optical Waves in Layered Media*. New York: Wiley, 1988, ch. 5 and 6.
- [27] I. A. Ibraheem, J. Schoebel, and M. Koch, "Group delay characteristics in coplanar waveguide left-handed media," *J. Appl. Phys.*, vol. 103, no. 2, pp. 024903–, 2008.
- [28] J. N. Munday and W. M. Robertson, "Negative group velocity pulse tunneling through a coaxial photonic crystal," *Appl. Phys. Lett.*, vol. 81, pp. 2127–2129, 2002.
- [29] L. Poirier, R. I. Thompson, and A. Haché, "Impossibility of negative group velocities in a periodic layer structure with or without loss," *Opt. Commun.*, vol. 250, pp. 258–265, 2005.
- [30] J. N. Munday and W. M. Robertson, "Observation of negative group delays within a coaxial photonic crystal using an impulse response method," *Opt. Comm.*, vol. 273, pp. 32–36, May 2007.
- [31] T. E. Hartman, "Tunneling of a wave packet," *J. Appl. Phys.*, vol. 33, pp. 3427–, 1962.
- [32] L. A. Coldren and S. W. Corzine, *Diode Lasers and Photonic Integrated Structures*. New York: Wiley, 1995, pp. 475–480.

Aida Sánchez-Meroño was born in Murcia, Spain, in 1984. She received the B.S. degree (with honors) in telecommunications engineering from the Universidad Miguel Hernández, Spain, in 2008. She is currently pursuing the Ph.D.

degree in industrial and telecommunications technologies in the Universidad Miguel Hernández, where she has been appointed with two research contracts for the formation of research personnel in September 2008 and 2009, respectively.

Her research interests are in the fields of wave propagation in anomalous dispersive media and group velocity control for communications applications.

Julia Arias was born in Zamora, Spain, in 1969. She received the M.S. degree in physics from the Universidad de Salamanca in 1993 and the Ph.D. degree from Universidad Politécnica de Madrid in 1998.

In 1999, she joined the Department of Materials, Optics and Electronic Technology of Universidad Miguel Hernández in Spain. Since 2001 she has been an Associate Professor in the area of Electronic Technology. Her research covers a wide range of both experimental and theoretical activities in the fields of semiconductor lasers, in particular, high-power lasers and vertical-cavity surface-emitting lasers, and in the field of multilayer dielectric optical filters, and wave propagation in anomalous dispersive media.

María del Mar Sánchez-López was born in Madrid, Spain, in 1969. She received the B.S., M.S., and Ph.D. degrees in physics from the Universitat Autònoma de Barcelona, Spain, in 1992, 1993, and 1997, respectively.

She held a one-year postdoctoral research grant with INFM, Salerno, Italy, where she conducted research in the field of high temperature superconductors and other strong-coupling systems. In October 1998, she joined the Department of Materials, Optics and Electronics Technology of Universidad Miguel Hernández in Spain. Since 2005 she has been an Associate Professor of Physics in the Physics Department of the Universidad Miguel Hernández. Her current research interests include both experimental and theoretical activities in the field of multilayer dielectric optical filters, wave propagation in anomalous dispersive media, and ferroelectric liquid crystal optical modulators. She has authored or coauthored more than 70 articles in peer-refereed journals and conference proceedings.

Dr. Sánchez-López is a member of the International Society of Optics and Photonics (SPIE) and the Real Sociedad Española de Física.



Slow and fast light in three-beam interferometers: Theory and experiment

J. Arias,¹ A. Sánchez-Meroño,¹ M. M. Sánchez-López,² and I. Moreno¹

¹*Departamento de Ciencia de Materiales, Óptica y Tecnología Electrónica, Universidad Miguel Hernández, 03202 Elche, Spain*

²*Instituto de Bioingeniería, Universidad Miguel Hernández, 03202 Elche, Spain*

(Received 8 November 2011; revised manuscript received 2 February 2012; published 16 March 2012)

We demonstrate the generation of slow and fast light (SFL) in a linear and passive three-beam interferometer. Such propagation regimes occur for narrowband pulses with center frequency close to the transmission minima. A model that fully describes SFL effects in this system is developed and an analytical approximate expression for the group delay at the minima is derived. We demonstrate that slow light is not possible if the length difference between adjacent branches of the interferometer is a constant. If a small length detuning (ξ) in one of the branches is introduced, slow light at one of the two minima can be obtained as long as ξ exceeds a critical value. Simultaneously, tunneling, superluminal, or normal regime is sustained at the other minimum, depending on the system's length. A proof-of-model experiment is performed in the radiofrequency range using coaxial cables and 1×3 power splitters. The possible realization and performance of such a system in the optical range is also discussed. This system is proposed as a simple alternative to active systems and photonic band-gap structures for sustaining both slow and fast light.

DOI: [10.1103/PhysRevA.85.033815](https://doi.org/10.1103/PhysRevA.85.033815)

PACS number(s): 42.25.Bs, 42.25.Hz, 73.40.Gk

I. INTRODUCTION

Research on slow and fast light (SFL) systems has increased in recent years in the photonics community. Although the possibility of propagating a light pulse in dispersive media at unusually slow or fast group velocity is been known for many decades [1], interest in this phenomena has been triggered by their promising applications in optical communications systems. In particular, the use of optical instead of electronic delay lines and the development of optical buffers, switches and synchronizers based on SFL systems have been suggested [2–4].

The group velocity of a pulse is the velocity at which the peak of its envelope propagates and is related to the frequency (ω) variation of the medium's refractive index n by

$$v_g = \frac{c}{n + \omega \frac{dn}{d\omega}}. \quad (1)$$

Thus, a steep positive spectral variation of the refractive index ($dn/d\omega > 0$) can lead to a very small group velocity ($v_g \ll c$) (*slow light* or subluminal pulse propagation), whereas in the case of steep anomalous dispersion ($dn/d\omega < 0$) the group velocity can be larger than the speed of light in vacuum c (superluminal pulse propagation) or even negative (pulse tunneling). These latter cases are known as *fast light*. Because of the Kramers-Kronig relations, such abnormal pulse propagation regimes are associated to sharp spectral features in the transmission spectrum [5].

Experimental evidence of SFL has been reported for a myriad of systems exhibiting material resonances (gain or absorption), like Bose-Einstein condensates [6], atomic vapors [7], solid crystals [8,9], semiconductor waveguides [10], semiconductor quantum wells and dots [11], and in optical fibers [12–14]. It has also been reported in systems exhibiting structural resonances (photonic band-gap systems, PBG), like photonic crystals [15] and fiber Bragg gratings [16,17], where the dispersion is due to coupling between the incident wavelength and the system's characteristic length. For such PBG

systems, experimental evidence of SFL has also been provided in the microwave [18–20] and radio-frequency (RF) [21,22] range. In fact, lower frequency setups have been relevant to clarify important issues, like the puzzling advancement of the outgoing pulse peak with respect to the incident pulse in tunneling experiments (negative v_g) [23], and have provided experimental evidence of a theoretically proposed structure exhibiting negative group delays in reflection [20]. They have been also used to explore quasiperiodic structures, such as Fibonacci or Thue-Morse, exhibiting strong normal and anomalous dispersion [24].

Regardless of the frequency range, let us note that all the aforementioned systems are either active (they respond to the interaction with light by generating narrow, gain, or absorption spectral bands) [6–11], exhibit nonlinear effects [12–14], or are periodically structured [15–22,24]. Unlike them, we have investigated the occurring of SFL effects in passive, linear, and nonperiodical structures. In a previous work [25], we demonstrated superluminal and negative group velocity in a linear and passive Mach-Zehnder interferometer (MZI) operative in the RF range. This behavior had also been outlined in Ref. [26] for an equivalent system consisting of a single asymmetric loop structure. We noted that anomalous dispersion in a narrow frequency region around the interferometer's transmission minima is strong enough to hold fast light without the need of microstructuring, doping, or using nonlinear media in the interferometer's arms. Slow light was, however, not observed in a MZI [25]. Slow light is particularly interesting since it improves the spectral sensitivity of interferometers [27] and enhances light-matter interaction and hence nonlinear effects [3].

Interestingly, the series loop structures studied by El Boudouti *et al.* [26] do present subluminal regime when defects are introduced. These structures may be regarded as MZIs (asymmetric loops) connected in series through segments. Like PBG systems, they exhibit bandgaps, and defect modes appear inside the transmission gaps if one of the segments connecting the loops is somehow changed (in length, for example). The

situation resembles that of a doped photonic crystal, with superluminal propagation for a pulse with center frequency in the bandgap and subluminal propagation for a pulse with center frequency at the defect mode. But unlike photonic crystals, an outstanding characteristic of this serial loop structure is the existence of bandgaps in a totally homogeneous material, without the need of refractive index contrast (or impedance contrast, if the system operates in the RF range as is the case in Ref. [26]).

With the aim of generating SFL regimes in a linear and passive interferometer, we have explored another alternative. Instead of connecting in series several MZIs, we increase the number of arms of a single interferometer. As a first attempt, we considered a four-beam interferometer with a nominal length difference (Δ) between adjacent arms [28,29]. The system was built with coaxial cables and measurements were performed for narrowband RF pulses centered at the transmission minima (the system exhibits three minima between two main transmission peaks). Simulations in the optical range for a Si-micromachined interferometer were also analyzed [29]. It was found that subluminal propagation only occurred if the length of any of the interferometer's arms was changed in a very small fraction (ξ) of the nominal length difference Δ ; otherwise, the pulse propagation regime was tunneling or superluminal.

These results look appealing but there remain open questions: Why is slow light not obtained for a constant length difference between the interferometer's arms? Why is a *small* length detuning ξ in one of the arms necessary to get a fast-slow light transition? Is there a critical value for such detuning? Can we predict, in terms of ξ , at which transmission minimum slow light will arise?

The present paper addresses these questions. Figure 1 shows a schematic that illustrates the concept of a lossless three-arm interferometer showing the typical transmission spectrum. We consider the simplest interferometer (least number of arms N) where a length detuning in a branch implies a change in the otherwise constant length difference between adjacent arms (Δ). Note that this condition holds only for $N \geq 3$ (this is why a MZI does not sustain slow light). We develop a model that fully describes SFL effects in such a three-beam interferometer. An exact expression of the group delay as a function of frequency, attenuation, and length detuning is derived. An approximate (but simpler) equation of the group

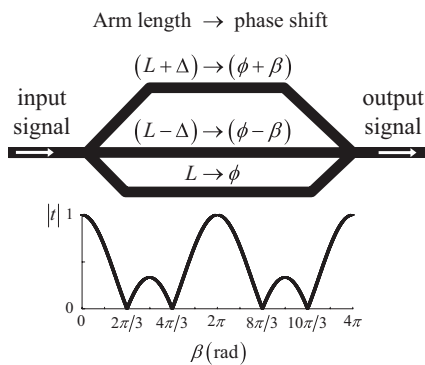


FIG. 1. Schematic of a lossless three-arm interferometer and its typical transmission spectrum.

delay at the transmission minima is given, and the critical length detuning needed to obtain slow light at each minimum is obtained. For the sake of generality, the theoretical results are presented using normalized frequencies and normalized group delays. A proof-of-model experiment is performed in the RF range by using coaxial cables and 1×3 wave splitters.

This work is outlined as follows. In Sec. II the analytical model is developed and its range of validity discussed. Section III describes the experimental techniques used in the proof-of-model experiments performed in the RF range. The results and discussion of such experiments are given in Sec. IV, where the frequency and time-domain characterization of several three-beam RF interferometers is reported and their agreement with theory is discussed. Basic figures of merit of the proposed SFL system and a design in the optical range are discussed. Finally, Sec. V contains the conclusions of this work.

II. ANALYTICAL MODEL

We consider a plane wave, with complex amplitude of 3, impinging on a three-arm interferometer. A 1×3 splitter divides the wave in three equal components that travel along each arm and then recombine by a 3×1 coupler. The transmitted complex amplitude at the end of the interferometer is:

$$t = \sum_{i=1}^3 e^{j\phi_i}, \quad (2)$$

where ϕ_i is the phase factor of the wave propagating along the i th branch, which, in turn, can be expressed as

$$\phi_i = \frac{\omega}{v} L_i + j\alpha L_i. \quad (3)$$

In Eq. (3) ω is the angular frequency, v is the phase velocity in the medium, L_i is the i th arm length, and α is the attenuation coefficient through the medium, which for simplicity is assumed to be constant over the whole frequency range. We define the length of each arm as:

$$L_1 = L - \Delta(1 - \xi), \quad L_2 = L, \quad \text{and} \quad L_3 = L + \Delta, \quad (4)$$

where Δ is the nominal length difference between adjacent arms. A small length detuning ($\xi \ll 1$) in the first arm is introduced to explore the induced transitions in the pulse propagation regimes at the transmission minima. The effective length of the interferometer is, thus [25],

$$L_{\text{eff}} = \frac{(L_1 + L_2 + L_3)}{3} = L + \frac{\xi \Delta}{3}. \quad (5)$$

By defining β as the phase associated to the nominal length difference, Δ , i.e., $\beta = \omega \Delta / v$, the real and imaginary parts of the transmission coefficient can be written as

$$\text{Re} = 1 + e^{-\alpha \Delta} \cos \beta + e^{\alpha \Delta(1-\xi)} \cos[\beta(1-\xi)], \quad (6a)$$

$$\text{Im} = e^{-\alpha \Delta} \sin \beta - e^{\alpha \Delta(1-\xi)} \sin[\beta(1-\xi)]. \quad (6b)$$

And the magnitude and phase of the transmission coefficient can be expressed as

$$|t| = e^{-\alpha L} \sqrt{\text{Re}^2 + \text{Im}^2}, \quad (7a)$$

$$\phi_t = \frac{\beta L}{\Delta} + \arctan \left(\frac{\text{Im}}{\text{Re}} \right). \quad (7b)$$

Let us note that the above quantities depend on ω through β .

We describe the propagation of an electromagnetic pulse through the interferometer in terms of the group delay, which is the time delay of the pulse envelope as it propagates through the system [1]. Following the usually adopted phase-time approach [18,23], the group delay is obtained from the frequency derivative of the transmission coefficient

phase:

$$\tau_g = \frac{\partial \phi_t}{\partial \omega} = \frac{L}{v} + \frac{\text{Re} \frac{\partial \text{Im}}{\partial \omega} - \text{Im} \frac{\partial \text{Re}}{\partial \omega}}{\text{Re}^2 + \text{Im}^2}. \quad (8)$$

Therefore, the exact expression of the group delay through the interferometer with constant attenuation α as a function of frequency (through β) and length detuning ξ is then

$$\frac{\tau_g}{\tau_p} = 1 + \frac{\Delta}{L} \frac{e^{-2\alpha\Delta} - (1-\xi)e^{2\alpha\Delta(1-\xi)} + e^{-\alpha\Delta} \cos \beta - (1-\xi)e^{\alpha\Delta(1-\xi)} \cos[\beta(1-\xi)] + \xi e^{-\alpha\Delta\xi} \cos[\beta(2-\xi)]}{1 + e^{-2\alpha\Delta} + e^{2\alpha\Delta(1-\xi)} + 2e^{-\alpha\Delta} \cos \beta + 2e^{\alpha\Delta(1-\xi)} \cos[\beta(1-\xi)] + 2e^{-\alpha\Delta\xi} \cos[\beta(2-\xi)]}. \quad (9)$$

In Eq. (9), the group delay has been normalized by $\tau_p = L/v$, that is, the phase delay in the medium over length L . Next, we analyze particular cases of attenuation and detuning.

A. Interferometer without detuning ($\xi = 0$)

Let us first consider the case where the length difference between adjacent arms is a constant ($\xi = 0$), and thus the interferometer effective length is $L_{\text{eff}} = L$.

1. Lossless media ($\alpha = 0$)

In this case, $\text{Re} = 1 + 2 \cos \beta$ and $\text{Im} = 0$. This implies that transmission minima are located where $\cos \beta = -1/2$; i.e., the first and second transmission minima after a principal maximum of order m lie at $\beta_1^0 = 2\pi(m + \frac{1}{3})$ and $\beta_2^0 = 2\pi(m + \frac{2}{3})$, respectively. From Eq. (8) it is then trivial to obtain the group delay at the minima as $\tau_g/\tau_p = 1$. The group delay is identical to the phase delay and, consequently, the group velocity equals the phase velocity. Therefore, a lossless interferometer with $\xi = 0$ cannot sustain anomalous propagation regimes. This is not surprising, since in a linear system with nothing altering the phase relation between the pulse components, the pulse peak cannot be shifted and, hence, it travels at the phase speed.

2. Lossy media ($\alpha > 0$)

If we consider a certain level of losses ($\alpha > 0$), the transmission minima are located where

$$\cos \beta = -\frac{\cosh(\alpha\Delta)}{2}. \quad (10)$$

Taking this into account, the group delay at the transmission minima according to Eq. (9) will be

$$\frac{\tau_g}{\tau_p} = 1 - \frac{\Delta}{L} \coth(\alpha\Delta). \quad (11)$$

As the \coth function is always positive for positive argument values, τ_g/τ_p is always smaller than 1 and, consequently, the system will never sustain subluminal regime. However, tunneling and superluminal regimes can arise at the minima by properly choosing the interferometer effective length for a given attenuation coefficient.

In order to go into more detail, we consider small values of $\alpha\Delta$, for which the transmission minima can be taken to lie at

$\beta_{1,2}^0$ (defined in Sec. II A 1) and Eq. (11) can be approximated by:

$$\frac{\tau_g}{\tau_p} \approx \left(1 - \frac{1}{\alpha L}\right). \quad (12)$$

The interferometer will therefore sustain tunneling at the minima ($\tau_g < 0$) if the effective length is chosen so that

$$\alpha L < 1, \quad (13)$$

whereas superluminal regime is possible at the minima ($0 < \tau_g < L/c$) if the effective length satisfies the condition

$$1 < \alpha L < \frac{n}{n-1}, \quad (14)$$

where n is the real part of the medium's refractive index. Two interesting points should be remarked. First, Eqs. (13) and (14) are restrictions on the values of the system's total attenuation. Hence, a proper change in the attenuation range (either by changing α and/or the interferometer's effective length L) could change the propagation regime at the transmission minima. Second, the former conditions do not depend on Δ ; the only role of Δ being that of determining the location of the minima.

The behavior discussed above is illustrated by numerical simulations on an interferometer with refractive index $n = 1.5$. Figure 2 shows the transmission coefficient magnitude calculated using Eq. (7a) and the group delay obtained from Eq. (9), for two attenuation values and $\Delta = L/2$. The transmission curve $|t|$ displays the typical three-beam interference pattern, with principal peaks at $\beta = 2\pi m$ (m is the order of the peak) and two minima located in between [30]. In agreement with our previous discussion, no abnormal propagation regimes occur in the lossless interferometer, while in the case of losses with $\alpha\Delta = 0.01$, tunneling appears around the two minima and negative group delays of almost $-50\tau_p$ can be reached.

The evolution of the pulse propagation regime at the minima, as a function of the total system's attenuation αL is described in Fig. 3. We consider $\alpha\Delta = 0.01$ and the τ_g curve obtained from Eq. (11) is plotted together with the straight line corresponding to the propagation phase delay through vacuum (L/c). Since the medium's refractive index is 1.5, $L/c = \tau_p/1.5$. As we can see, for small enough attenuation ($\alpha L < 1$) the system exhibits tunneling, in agreement with Eq. (13). For values of αL ranging between 1 and 3, superluminal propagation is sustained, in agreement with Eq. (14), and the system presents normal dispersion if $\alpha L > 3$. Hence, the total

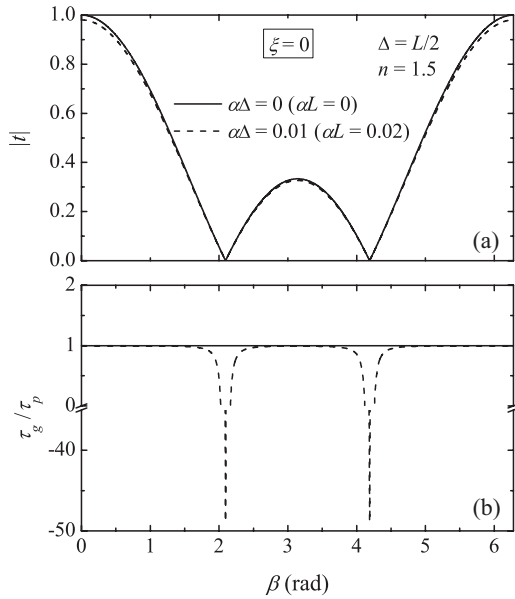


FIG. 2. (a) Transmission coefficient magnitude and (b) group delay Eq. (9) in units of the phase delay through the medium of a three-beam interferometer with length difference between adjacent arms $\Delta = L/2$, length detuning $\xi = 0$, and refractive index $n = 1.5$, for two values of the attenuation coefficient α .

attenuation in the system determines the pulse propagation regime. Fast light is achieved with small enough attenuation while it disappears if it is either too high ($\alpha L > \frac{n}{n-1}$) or zero.

B. Interferometer with detuning ($\xi \neq 0$)

We now consider the case where a small length detuning ($\xi \ll 1$) is introduced in the first branch of the interferometer. If $\alpha\Delta$ and $|\xi|$ are small, it can be shown that the transmission minima move with ξ according to

$$\beta_{1,2} \approx \beta_{1,2}^0 \left(1 + \frac{\xi}{2} \right), \quad (15)$$

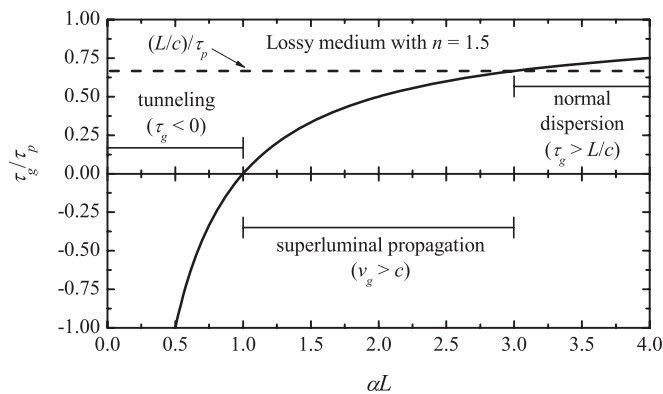


FIG. 3. Pulse propagation regimes at the transmission minima of a lossy three-beam interferometer without detuning ($\xi = 0$) as a function of the total system's attenuation αL . Group delay plotted from Eq. (11) (solid line) and phase delay through vacuum (dashed line). The delays are given in units of the phase delay through the medium.

where $\beta_{1,2}^0$ corresponds to the first and second minima when $\xi = 0$ and $\alpha = 0$.

1. Lossless media ($\alpha = 0$)

In a lossless medium, following Eq. (9), the group delay at the first and second transmission minima can be approximated by

$$\frac{\tau_{g1}}{\tau_p} \approx 1 - \frac{\Delta}{L} \frac{2\sqrt{3}}{\xi \beta_1^0}, \quad (16a)$$

$$\frac{\tau_{g2}}{\tau_p} \approx 1 + \frac{\Delta}{L} \frac{2\sqrt{3}}{\xi \beta_2^0}, \quad (16b)$$

respectively. Consequently, by setting $\xi \neq 0$, one can always obtain slow light at one of the minima. More specifically, these are the possible cases:

(i) If $\xi < 0$, the system sustains slow light at the 1st minimum. At the 2nd minimum, the possible pulse propagation regime is tunneling if

$$L < -\frac{2\sqrt{3}}{\beta_2^0 \xi} \Delta, \quad (17)$$

and superluminal ($0 < \tau_g < L_{\text{eff}}/c$) if

$$-\frac{2\sqrt{3}}{\beta_2^0 \xi} \Delta < L < -\left(\frac{n}{n-1} \right) \frac{2\sqrt{3}}{\beta_2^0 \xi} \Delta. \quad (18)$$

Otherwise, only normal propagation will be possible at the 2nd minimum.

(ii) If $\xi > 0$, slow light occurs at the 2nd minimum, whereas at the 1st minimum, the system will sustain tunneling if

$$L < \frac{2\sqrt{3}}{\beta_1^0 \xi} \Delta, \quad (19)$$

and superluminal propagation if

$$\frac{2\sqrt{3}}{\beta_1^0 \xi} \Delta < L < \left(\frac{n}{n-1} \right) \frac{2\sqrt{3}}{\beta_1^0 \xi} \Delta. \quad (20)$$

Otherwise, only normal propagation occurs at the 1st minimum. The above expressions set restrictions on the length L of the second branch, which is very close, but not equal, to the system's effective length [see Eq. (5)].

This behavior is observed in Fig. 4, for a three-arm interferometer, where its first branch has been increased or decreased according to $\xi = \pm 5\%$. Exact Eq. (9) was used to simulate the group delay as a function of β in a system with $\Delta = L/2$ and refractive index $n = 1.5$. The transmission's minima shift with ξ is manifest in the group delay curves. According to the approximation in Eq. (16), for a detuning of $+5\%$, the group delay should be $-15.5\tau_p$ and $9.3\tau_p$ at the first and second minima of zero-order, respectively. Whereas, if $\xi = -5\%$, the expected group delay at the zero-order first and second minimum is $17.5\tau_p$ and $-7.3\tau_p$, respectively. These approximate values of the group delay at the minima are in excellent agreement with the exact results shown in the figure.

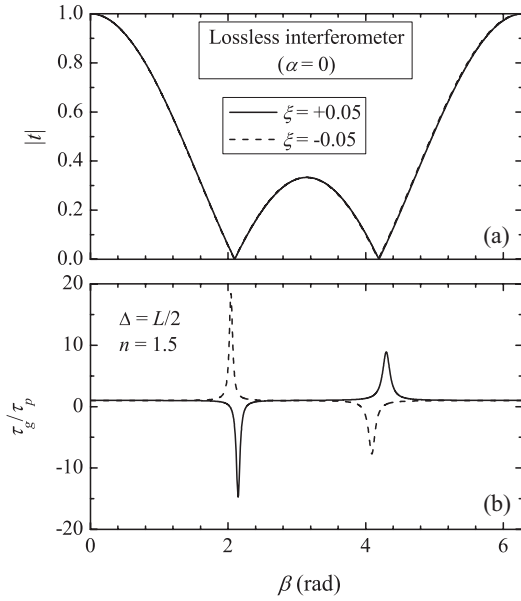


FIG. 4. (a) Transmission coefficient magnitude and (b) group delay of a lossless three-beam interferometer with nominal length difference between adjacent arms $\Delta = L/2$ and refractive index $n = 1.5$, for two values of length detuning ξ .

2. Lossy media ($\alpha > 0$)

In the most general case, where both detuning and a certain attenuation level are considered, and under the conditions of small $\alpha\Delta$ and $|\xi|$, Eq. (9) can be approximated at the transmission minima as

$$\frac{\tau_{g1}}{\tau_p} \approx 1 - \frac{\Delta}{L} \frac{2\sqrt{3}}{\beta_1^0(\xi - \xi_{c1})}, \quad (21a)$$

$$\frac{\tau_{g2}}{\tau_p} \approx 1 + \frac{\Delta}{L} \frac{2\sqrt{3}}{\beta_2^0(\xi - \xi_{c2})}, \quad (21b)$$

where the critical detuning lengths ξ_{c1} and ξ_{c2} are approximately

$$\xi_{c1} = -\frac{2\sqrt{3}\alpha\Delta}{\beta_1^0}, \quad (22a)$$

$$\xi_{c2} = +\frac{2\sqrt{3}\alpha\Delta}{\beta_2^0}. \quad (22b)$$

For lossless media, $\xi_{c1} = \xi_{c2} = 0$ and Eqs. (21) reduce to Eqs. (16); thus, recovering the situation discussed in Sec. II B 1. The role of the attenuation is then to increase the magnitude of the critical detuning needed to obtain slow light at the minima. Table I summarizes the possible propagation regimes at both minima. If $\xi < \xi_{c1}$, the system only sustains

TABLE II. Possible propagation regimes at the 1st transmission minimum.

Condition	$L < L_{t1}$	$L_{t1} < L < (\frac{n}{n-1})L_{t1}$	$L > (\frac{n}{n-1})L_{t1}$
$\xi < \xi_{c1}$	Slow	Slow	Slow
$\xi > \xi_{c1}$	Tunnel.	Superlum.	Normal

slow light at the 1st minimum. If $\xi > \xi_{c2}$, the system only sustains slow light at the 2nd minimum. For $\xi_{c1} < \xi < \xi_{c2}$ the allowed pulse propagation regimes at the minima can be tunneling, superluminal, or normal, depending on the length L . Table II summarizes the possible propagation regimes at the 1st minimum. If $\xi > \xi_{c1}$, there is a maximum value of L to obtain tunneling at the 1st minimum:

$$L_{t1} = \left(\alpha + \frac{\beta_1^0 \xi}{2\sqrt{3}\Delta} \right)^{-1}. \quad (23)$$

For lengths L greater than L_{t1} and smaller than $(\frac{n}{n-1})L_{t1}$, superluminal propagation is sustained at the 1st minimum. Finally, when L exceeds the value $(\frac{n}{n-1})L_{t1}$, the normal regime is attained.

Similarly, the possible propagation regimes at the 2nd minimum are shown in Table III. For $\xi < \xi_{c2}$, there is a maximum value of L to get tunneling at the 2nd minimum:

$$L_{t2} = \left(\alpha - \frac{\beta_2^0 \xi}{2\sqrt{3}\Delta} \right)^{-1}. \quad (24)$$

For lengths greater than L_{t2} and smaller than $(\frac{n}{n-1})L_{t2}$, superluminal propagation occurs at the 2nd minimum. Once again, when L exceeds the value $(\frac{n}{n-1})L_{t2}$ the normal regime is attained. In the case $\xi = 0$, lengths $L_{t1} = L_{t2} = 1/\alpha$, and Eqs. (13) and (14), for a lossy interferometer with a constant length difference Δ between adjacent branches, are recovered. Let us remark that, as opposed to that case, Δ does now influence the conditions that determine the propagation regime.

We have checked the validity of the approximated Eqs. (21) and (22) for estimating the group delay at the transmission minima. The approximated value has been compared with the exact result obtained from Eq. (9), as a function of the detuning ξ and for an attenuation level of $\alpha\Delta = 0.01$. The results in Fig. 5 reveal the following features: (i) the agreement between the approximated and the exact value of τ_g is excellent for ξ up to $\pm 5\%$; (ii) the group delay increases in magnitude as the detuning approaches the critical value; and (iii) the SFL transition when reaching the critical detuning is extremely abrupt. Namely, the absolute value of τ_g at each minimum approaches infinity when the length detuning equals exactly the corresponding ξ_c . This behavior is understood from

TABLE I. Possible propagation regimes at the transmission minima.

Condition	Regime at 1st min	Regime at 2nd min
$\xi < \xi_{c1}$	Slow	Tunnel., Superlum., and Normal
$\xi_{c1} < \xi < \xi_{c2}$	Tunnel., Superlum., and Normal	Tunnel., Superlum., and Normal
$\xi > \xi_{c2}$	Tunnel., Superlum., and Normal	Slow

TABLE III. Possible propagation regimes at the 2nd transmission minimum.

Condition	$L < L_{t2}$	$L_{t2} < L < (\frac{n}{n-1})L_{t2}$	$L > (\frac{n}{n-1})L_{t2}$
$\xi < \xi_{c2}$	Tunnel.	Superlum.	Normal
$\xi > \xi_{c2}$	Slow	Slow	Slow

Eqs. (6)–(8): for a given $\alpha\Delta$ value, the critical detuning is the one that makes $\text{Re}^2 + \text{Im}^2 = 0$ at the corresponding minimum. Therefore, this abrupt SFL transition is achieved through a passage from a zero transmission condition. We would like to draw attention here to the similarity of this mechanism with that reported by Longhi in active fiber Bragg gratings with asymmetric profile [17]. In that work, an abrupt superluminal to subluminal transition of reflected pulses near to a local minimum of the reflection spectrum is achieved by increasing the gain level.

III. EXPERIMENTAL TECHNIQUES

In this section, the experimental setup we have used for our proof-of-model experiment is described. We have designed a nominal interferometer consisting of a 1×3 RF power splitter, a 3×1 RF coupler (both PE2002, Pasternack), and three coaxial cables (50 Ω , RG-58C/U). The designed effective length of the system is 2 m and the intended length difference between adjacent cables is 1 m. In practice, every branch of the interferometer comprises the cable itself, the connectors between cable and splitters, and a small track inside the splitters. After measuring all these elements, the actual branch lengths of the starting interferometer were found to be $L_1 = 1.049$ m, $L_2 = 2.066$ m, and $L_3 = 3.088$ m, yielding $\Delta = 1.022$ m, and $\xi = +0.5\%$, according to our definitions in Eq. (4). In addition, four coaxial cables were prepared to substitute the L_1 cable of the starting interferometer. The actual first arm lengths are 0.989, 1.008, 1.086, and 1.103 m. Therefore, we have five interferometers to be characterized in frequency and time domain, each with $\Delta = 1.022$ m, and a set of values for ξ of -5.4% , -3.5% , $+0.5\%$, $+4.1\%$, and $+5.8\%$.

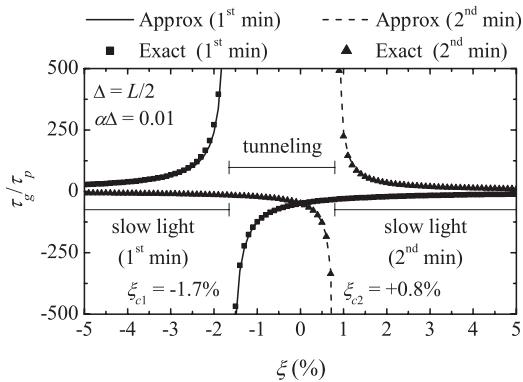


FIG. 5. Dependence with length detuning of the group delay at the minima for a three-beam interferometer with nominal length difference between adjacent arms $\Delta = L/2$ and attenuation $\alpha\Delta = 0.01$. The approach in Eqs. (21) (line) is compared to the exact result of Eq. (9) (symbols) for each minima.

TABLE IV. Fabricated three-beam RF interferometers with $L = 2.066$ m, $\Delta = 1.022$ m.

Interferometer	L_1 (m)	ξ (%)
L1-99	0.989	-5.4
L1-101	1.008	-3.5
L1-105	1.049	+0.5
L1-109	1.086	+4.1
L1-110	1.103	+5.8

This set of ξ values allows checking the evolution from fast to slow light at the minima as L_1 varies. All the cables available for the branches were cut out of the same long coaxial cable whose attenuation coefficient as a function of frequency, $\alpha(\omega)$, had been previously determined following the procedure in Ref. [30]. Knowing the system's attenuation was necessary in order to estimate the critical length detuning through Eq. (22) so that we could prepare the cables with adequate values of ξ to display the SFL transition. From the characterization of $\alpha(\omega)$ we obtained an attenuation of $\alpha = 0.015$ Np/m (0.13 dB/m) at 65.2 MHz (first transmission minimum of the nominal interferometer) and $\alpha = 0.022$ Np/m (0.19 dB/m) at 130.4 MHz (second transmission minimum of the nominal interferometer). These attenuation values yield a critical length detuning of $\xi_{c1} = -2.5\%$ and $\xi_{c2} = +1.9\%$ for the first and second minimum, respectively. The characteristics of the fabricated RF three-beam interferometers are summarized in Table IV.

The frequency characterization of these interferometers has been performed by means of a two-port vector network analyzer (PNA series, Agilent E8363B). The scattering parameter S_{21} (the transmission coefficient) was recorded in the 10–200 MHz range every 59.375 kHz with an average of 64 to help suppress the random noise. In addition, a full characterization of the splitters was carried out. We use this measurement to correct the interferometer experimental response for a proper comparison with simulation, which does not include the effect of the splitters. It was shown that both splitters directly interconnected introduce an overall group delay of 1.8 ns and an attenuation of 1 dB, approximately, in the transmission response.

The experimental data contain a small amount of noise, which is not very apparent in the S_{21} parameter itself. To obtain the experimental group delay, the phase data curve is differentiated and this amplifies the noise leading to spurious effects. For this reason, the network analyzer was configured to smooth the group delay by averaging 17 adjacent points. Although it is well known that smoothing may give results which vary critically with the smoothing parameters, the selected averaging algorithm preserves the key features of the group delay at the transmission minima.

Additionally, time-domain pulse propagation experiments have been performed on each interferometer. The experimental set-up is shown in Fig. 6. The 300 kHz sinusoidal output of generator-1 (Tektronix CFG-253) is used to amplitude modulate the sinusoidal signal of generator-2 (IntraAction VFE-604A4), whose frequency can be varied between 40 and 80 MHz. Therefore, only the first minimum can be observed. This produces a train of 3.3- μ s-wide sinusoidally modulated

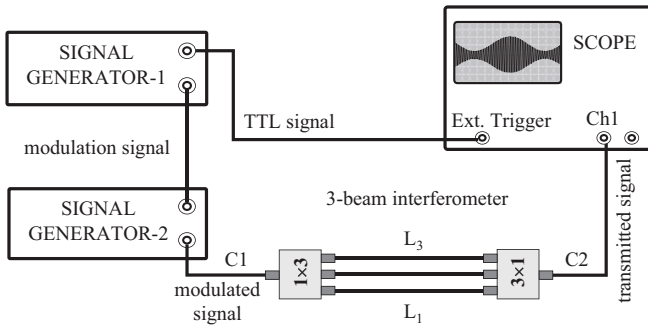


FIG. 6. Experimental set-up for the time-domain pulse propagation measurements through the RF interferometers. The output sinusoidal signal from generator-2 is 100% amplitude modulated by the output signal from generator-1. C1 and C2 are 50 Ω coaxial cables constituting the reference path (see text).

wave packets with carrier frequencies in the MHz range. The pulse train transmitted through the interferometer is recorded at the oscilloscope (Agilent DSO-6032A) with a resolution of 0.5 ns (10 kSamples/5000 ns). The TTL signal from generator-1 is used to trigger the oscilloscope.

The group delay for each C1-interferometer-C2 system (see Fig. 6) was estimated by the following procedure: first, a capture of the transmitted pulses was taken for a carrier frequency coinciding with the interferometer's 1st transmission minimum. Next, the interferometer was removed and cable C1 was connected to cable C2, and captures of transmitted pulses through this reference assembly were performed at the same carrier frequency than before. For each interferometer, the group delay is then estimated as the time shift between the peak of the pulse transmitted by the system and the peak of the pulse traveling through the reference path. Let us recall that the group delay estimated in this way will approach to the one retrieved from Eq. (8) as the modulation frequency decreases.

IV. RESULTS AND DISCUSSION

This section discusses the experimental results obtained for the fabricated RF interferometers described in Sec. III. Frequency and time-domain measurements were performed on these systems. The results are compared with the theoretical model developed in Sec. II. A design of such a device in the optical range is also proposed and discussed.

A. Results in the frequency domain

Figures 7 and 8 show the transmission (magnitude $|t|$ and phase ϕ_t) and group delay (τ_g) of our five three-beam RF interferometers whose parameters are summarized in Table IV. Experimental and simulation results are shown. Namely, we include two experimental curves. One corresponds to the whole system measured with the vector network analyzer (labeled *uncorrected experimental data*)—including the splitters—while the other (labeled *corrected experimental data*) is the result of subtracting the effect of the splitters in the way indicated in Sec. III. For each interferometer, the simulated $|t|$ and ϕ_t curves were obtained as in Ref. [30], by numerically calculating the interference of three sinusoidal RF

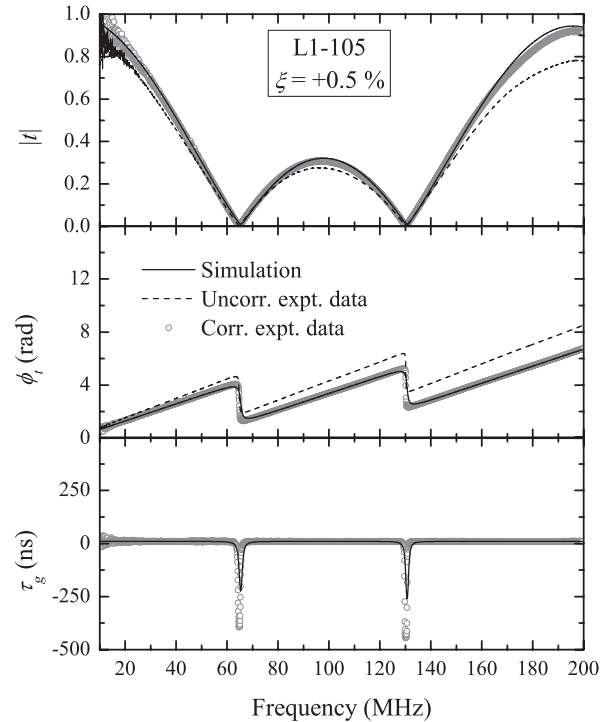


FIG. 7. Numerical simulation (solid curve) and experimental frequency-domain characterization of the starting interferometer L1-105. The dashed curve corresponds to the whole system measured with the vector network analyzer—including the splitters—and the symbols refer to the result of subtracting the effect of the splitters in the way indicated in Sec. III. (a) Magnitude of the transmission coefficient, (b) phase of the transmission coefficient, and (c) 17-point averaged group delay.

waves propagating through coaxial cables of the lengths given in Table IV, including the frequency-dependent attenuation in the cables. The τ_g curves were obtained by differentiating the corresponding numerical phase curve with respect to the frequency. The same 17-point smoothing algorithm as that applied to the measured τ_g curve was used for the simulated group delay. The agreement between simulations and the corrected experimental results is very good, thus assessing the accuracy of the procedure employed to subtract the effect of the splitters. From the figures, it is obvious that the splitters introduce losses (the peaks in transmission are less pronounced for the raw data) and also they add an additional phase (the raw data phase function is above the numerical one). Their effect on the group delay is hardly noticeable; for this reason only the corrected experimental τ_g curve is shown in the figures.

Let us first analyze the situation for the starting interferometer L1-105, which is displayed in Fig. 7. The $|t|$ curves exhibit absolute maxima every 200 MHz and two minima between the zero and the first-order principal peak that lie close to the expected positions $f_{01} = 65.4$ MHz and $f_{02} = 130.8$ MHz [see Eq. (15)]. Negative group delay around -400 ns are reached at both minima, accordingly to the steep negative slope of the phase function at these frequencies. These results agree with our model predictions, since the interferometer's length detuning ($+0.5\%$) satisfies the condition $\xi_{c1} < \xi < \xi_{c2}$ (with $\xi_{c1} = -2.5\%$, and $\xi_{c2} = +1.9\%$), and the length of the second

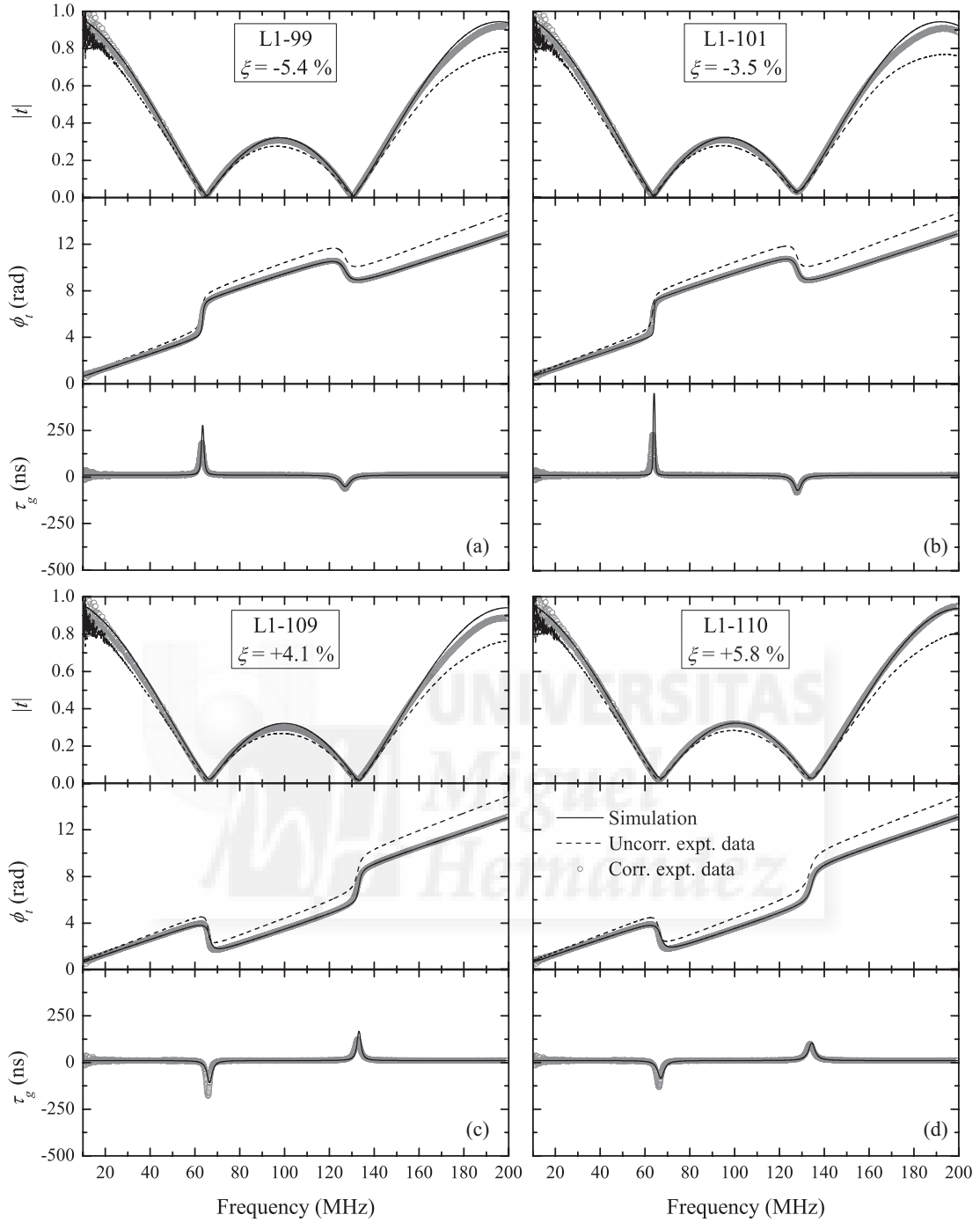


FIG. 8. Numerical simulations (solid curve), uncorrected (dashed curve), and corrected (symbols) experimental results for the frequency-domain characterization of three-beam RF interferometers. Top panel shows magnitude of the transmission coefficient, middle panel shows phase of the transmission coefficient, and bottom panel shows the 17-point averaged group delay for samples (a) L1-99, (b) L1-101, (c) L1-109, and (d) L1-110.

branch ($L = 2.066$ m) is well below the limiting values ($L_{t1} = 55.7$ m and $L_{t2} = 62.2$ m) above which tunneling regime disappears.

Figure 8 shows how the situation changes when the interferometer's length is slightly changed. According to theory, a reduction of at least $2.5\% \Delta$ in branch length L_1 fulfills the condition to generate slow light at the 1st minimum. On the contrary, an increase of at least $1.9\% \Delta$ would generate

slow light at the 2nd minimum. Figures 8(a)–8(d) correspond to samples L1-99, L1-101, L1-109, and L1-110, respectively. In the two samples with shorter L_1 , the system exhibits positive τ_g at the 1st minimum, while negative τ_g is retained at the 2nd minimum. The opposite situation occurs for samples L1-109 and L1-110. These results are justified within our model, considering the length detuning ξ of each sample (Table IV), the critical detuning lengths (ξ_{c1}, ξ_{c2}), and the model conditions

summarized in Tables II and III. Namely, $\xi < \xi_{c1} = -2.5\%$ for the system in Figs. 8(a) and 8(b) and $\xi > \xi_{c2} = +1.9\%$ for the system in Figs. 7(c) and 7(d), which explains the occurring of slow light at the 1st minimum in one case and at the 2nd minimum in the other. Also, a quick estimation using Eq. (24) shows that only tunneling can be sustained at the 2nd minimum for interferometers L1-99 and L1-101, since L (2.066 m) is for both systems smaller than L_{t2} (11.6 m and 15.8 m, respectively). A similar result occurs by using Eq. (23) to obtain the value of L_{t1} for systems L1-109 and L1-110; we find $L < L_{t1}$ (25.5 m, and 20.3 m, respectively), and this is why these samples exhibit tunneling at the 1st minimum.

From Fig. 8, the link between the strength of the group delay peaks and the steepness in the slope of the phase function is obvious. Such steepness is ultimately linked to the attenuation in the system (for higher attenuations the slopes are less pronounced) and to how much ξ approaches the critical detuning ξ_{c1} or ξ_{c2} . Samples L1-101 and L1-105 are the ones with ξ closer to one of the critical values, thus leading to the highest and narrowest τ_g peaks. Finally, the frequency shift of the minima as the length detuning varies is evident in Fig. 8. The minima move toward higher frequency as ξ increases, just like the theoretical model predicts.

B. Results in the time domain

Pulse propagation experiments were carried out using the experimental setup described in Sec. III (Fig. 6). The modulating signal was a 300 kHz sinusoidal wave, which results in a 3.3- μ s-wide pulse. This choice of the modulating frequency was a compromise between narrow-enough bandwidth to avoid pulse distortion and large-enough bandwidth to get appreciable pulse peak advancements (or delays) in comparison to the pulse length. For each interferometer, the carrier frequency was selected to coincide with the first transmission's minimum. Since the signals were largely attenuated, a direct observation of the pulse peak on the oscilloscope was not accurate enough to measure the group delay. Hence, the pulse peak position was obtained from a numerical analysis of the data by finding the best fit to the pulse envelope.

Figure 9 shows the pulse captures for the five RF interferometers. The arrow indicates the time spent by the pulse peak in propagating through the interferometers and it is obtained as explained in Sec. III. The SFL transition in the pulse propagation regime is evident in these captures. The τ_g values agree reasonably well with those found in the frequency-domain characterization. The pulse propagates with negative group delay of -302 , -147 , and -115 ns in samples L1-105, L1-109, and L1-110, respectively. Whereas positive group delays of $+248$ and $+308$ ns occur in samples L1-99, and L1-101, respectively. As it is clearly demonstrated in Refs. [31–33], such peak advancements and delays arise from the coherent interference of the pulse frequency components. Each component travels at phase velocity $2/3c$ in the cables, but their relative phases are modified after the pulse's transmission through the system; as a result, the peak of the output pulse (where the frequency components are all in phase) is shifted backward (or forward) and the pulse appears to travel at superluminal (or subluminal) speed. As it is argued in several works [32,33], these abnormal propagation regimes

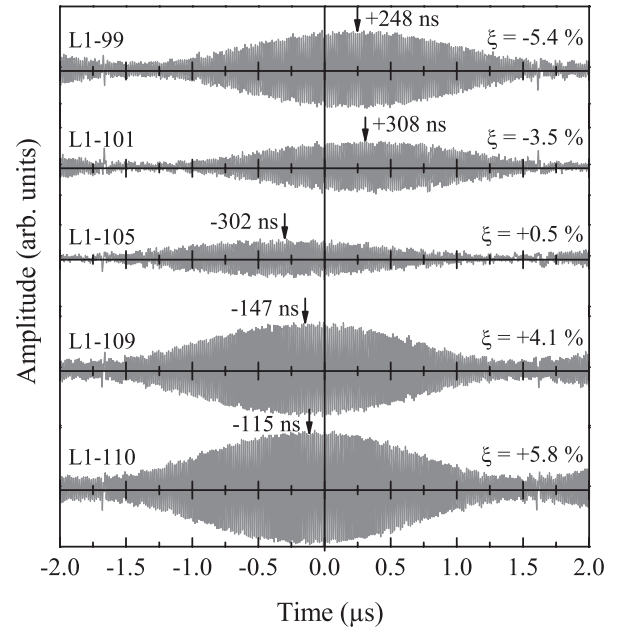


FIG. 9. Wave-packet traces of the RF interferometers (from top to bottom) L1-99, L1-101, L1-105, L1-109, and L1-110. In each case, the pulse carrier frequency is that of the 1st transmission minimum. The arrow indicates the pulse propagation time through the interferometer and it is obtained as mentioned in Sec. III.

occur only if the spatial length of the pulse (L_{pulse}) greatly exceeds that of the system. This condition is nicely satisfied here, since $L_{\text{pulse}} = 3.3 \mu\text{s} \times 2/3c = 400$ m is much longer than the interferometer's length ($L_{\text{eff}} \approx 2$ m).

C. Further discussion and operation in the optical range

Let us now discuss some figures of merit of the three-beam interferometer as an SFL system and its possible realization for delaying or advancing optical pulses. Considering an interferometer with a small length detuning, ξ , simulations show that the relative group delay $|\tau_{\text{del}}| = \tau_g - \tau_p$, which is the difference between the group delay and the phase delay in the medium over length L , matches a sequence of Lorentzian functions centered at each transmission minimum:

$$|\tau_{\text{del}}| = \frac{1}{2\pi} \frac{\frac{\Gamma}{2}}{(f - f_{\text{min}})^2 + (\frac{\Gamma}{2})^2}, \quad (25)$$

where f_{min} is the frequency of the considered transmission minimum and Γ is the full width at half maximum (FWHM) of the Lorentzian function at that minimum. The maximum relative group delay is then $|\tau_{\text{del}}|_{\text{peak}} = 1/\pi\Gamma$. Since the pulse delay (or advancement) will only be effective for signals centered at the transmission minima and with spectral components within these Lorentzian peaks, the product $|\tau_{\text{del}}|_{\text{peak}} \times \Gamma = 1/\pi \approx 32\%$ gives a rough estimation of the maximum delay-bandwidth product that can be achieved with this system. Let us note that this estimation is valid for any frequency range the interferometer may operate.

Another figure of merit in SFL systems is the fractional delay, defined as the ratio between the relative pulse delay, τ , and the pulse duration, T_0 . In our time-domain experiments, we have measured a maximum relative pulse delay of ~ 300 ns

($\tau_p \sim 10$ ns is almost negligible in comparison). Various measures of the pulse duration are considered by the authors. For our sinusoidally modulated wavepackets and by considering T_0 as the period of the modulating signal (3.3 μ s), we obtain a fractional delay of $\sim 9\%$. Instead, if we take T_0 as the FWHM of the pulse *amplitude* signal, this parameter becomes $\sim 18\%$. Furthermore, by regarding T_0 as the FWHM of the pulse *power* signal, then the measured fractional delay becomes $\sim 25\%$. For the rest of the discussion we will consider this last definition of T_0 since it is the optical power, and not the optical field envelope, which is detected in experiments performed in the optical range.

We have also performed numerical simulations on the propagation of sinusoidally modulated pulses through the interferometer. This study shows that the transmitted pulse width, T_{0t} , is smaller than T_0 , yielding a pulse compression b , given by $b = 1 - T_{0t}/T_0$. Either pulse delay or advancement is accompanied by a certain degree of pulse compression. The relation between pulse compression and fractional delay is roughly quadratic and for sinusoidally modulated pulses reads

$$b \approx 0.7 \left(\frac{|\tau|}{T_0} \right)^2. \quad (26)$$

This means that, in order to maintain the pulse compression below 5%, the fractional delay cannot exceed 27%, and to keep it below 10%, the fractional delay cannot exceed 38%. This explains the low pulse compression observed in our measurements with a 300 kHz modulating signal. Time-domain measurements with 500 kHz modulation frequency (not shown here) were carried out to confirm not only a high pulse compression but also a strong distortion.

The above discussion is entirely applicable to three-arm interferometers fabricated to operate at optical frequencies. Leaving the free-space configurations aside, there are several technologies to realize a wave-guided three-arm interferometer operating in the optical range, namely, all-fiber and channel waveguide structures. For practical purposes, it would be desirable to induce the SFL transitions by changing the optical path without affecting the physical length of the arms, i.e., by changing the refractive index. With this idea, lithium niobate (LN) is an excellent candidate material, being an established choice for electro-optic applications such as the realization of Mach-Zehnder optical modulators [34]. Optical waveguides can be fabricated, among other techniques, by in-diffusion of Titanium into an x- or z-cut LN crystal. A precise control of the phase shift in one arm can be achieved by applying an electric field through the metallic electrode above the corresponding

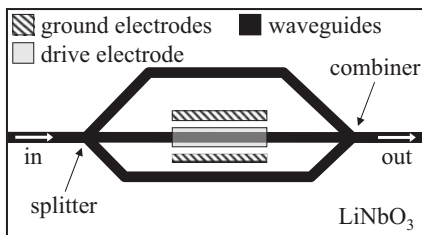


FIG. 10. Schematic of a lithium niobate three-arm interferometer.

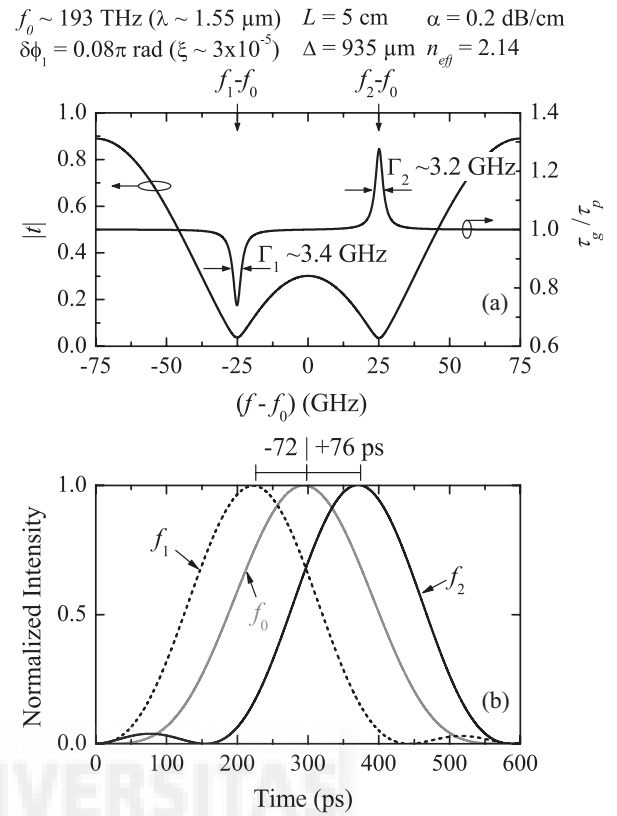


FIG. 11. Numerical simulation of a LN interferometer with the indicated parameters. (a) Magnitude of the transmission coefficient and group delay and (b) pulse traces of transmitted pulses with the indicated carrier frequencies corresponding to different propagation regimes.

waveguide, which induces a refractive index change due to the electro-optic properties of this material. Figure 10 shows a schematic of a z-cut LN unbalanced three-arm interferometer. Although it seems more adequate to place the drive electrode above one of the outer arms, the drive electrode has been placed above the middle arm in order to directly extrapolate our previous analysis with length detuning ξ . Therefore, an external voltage applied to the drive electrode will produce a phase shift, $\delta\phi_1$, in the shortest arm, which is equivalent to introducing a length detuning of $\xi = \frac{c}{n_{\text{eff}} 2\pi f} \frac{\delta\phi_1}{\Delta}$, where n_{eff} is the waveguide effective refractive index.

As an example, let us consider the case of a LN interferometer with $L = 5$ cm, nominal Δ of 935 μ m, and a phase shift $\delta\phi_1 \approx 0.08\pi$ rad (equivalent to a length detuning of $\xi = 3 \cdot 10^{-5}$). This value of Δ is chosen so that the separation between transmission minima of the same order is 50 GHz. Figure 11(a) shows the transmission coefficient and the group delay in a frequency range of 150 GHz centered at the middle frequency between a pair of minima of the same order at ~ 193 THz. Considering $n_{\text{eff}} = 2.14$, the phase delay in this system is $\tau_p \approx 356$ ps. Fast light regime is sustained at the first transmission minimum, whereas slow light appears at the second minimum. As indicated in the figure, pulses of bandwidth smaller than 3.4 and 3.2 GHz would be required to observe such peak advancement or delay, respectively. We have simulated the propagation of an optical pulse train through this

interferometer. An optical carrier of ~ 193 THz ($\lambda = 1.55 \mu\text{m}$) is sinusoidally modulated in order to produce a train of pulses with $T_0 = 214$ ps at a repetition rate of 1.7 GHz. Figure 11(b) shows the pulse traces corresponding to propagation at both transmission minima together with a pulse trace propagating at the central frequency, for which the group delay is τ_p . The relative pulse delays at the first and second minima are ~ -72 ps and $+76$ ps, respectively, yielding fractional delays of -34% and $+36\%$, with pulse compression of 8% and 9%, respectively. These values are larger than those reported in passive fiber Bragg gratings [16], where fractional delays and advancements of 17% were measured when tuning a picosecond optical pulse spectrum through the grating band gap. Our results are also similar to the ones reported in Ref. [17] for active fiber Bragg gratings when keeping the pulse compression in our system below 13%.

V. CONCLUSIONS

To summarize, we have demonstrated the arising of slow and fast light in linear and passive three-beam interferometers for frequencies close to the transmission minima. Transitions in the pulse propagation regime at these frequencies in terms of the system's characteristics (attenuation and length difference between adjacent arms) were theoretically analyzed. We have proved that slow light is not possible when the length difference between adjacent arms is a constant. In this case, fast light is achieved only if the system has attenuation. The total attenuation drives the group delay transitions at the transmission minima, where tunneling is the expected regime for low total attenuation, whereas superluminality and eventually normal propagation are attained as total attenuation further increases.

By introducing a small length detuning (ξ) in a branch, we have demonstrated that slow light can arise. Analytical expressions for the group delay τ_g at the transmission minima in the approximation of low attenuation and small length detuning were derived, and a critical length detuning (ξ_c) beyond which slow light appears was obtained. We found that in the case of lossless media ξ_c is zero, being the role of the attenuation to increase the magnitude of ξ_c . For every pair of minima located between absolute peaks of the transmission spectra, only one minimum may support slow light at a time, whereas the other minimum will sustain either tunneling, superluminal, or normal dispersion, depending on the system's length.

Let us remark that such length-detuning-driven SFL transition stems from a structural change in the system's dispersive properties at the transmission minima. This change is triggered by the passage through a local zero transmission when the critical detuning value is reached. This is in formal analogy to previously reported group delay tuning mechanism for pulses reflected on active Bragg gratings by changing the gain. But unlike it, here the SFL transition is attained in an entirely passive system.

An experimental demonstration of the model predictions on the pulse propagation regimes has been performed in the RF range by using 50- Ω coaxial cables and 1×3 power splitters to build five interferometers with ξ values ranging from -5.4 to $+5.8\%$. The structures were characterized in the frequency domain, and the group delay at the transmission minima showed the trends predicted by the analytical expressions. The same structures were used in a time-domain setup, where a group delay from less than -300 ns to more than $+300$ ns was measured for a train of 3.3- μs -wide sinusoidally modulated wavepacket with carrier frequency at the first minimum of each interferometer.

The maximum delay-bandwidth product of the system is estimated to be 32%. Numerical simulations on pulse propagation show that the achievable fractional group delays can reach 38% keeping pulse compression below 10%. These characteristics are intrinsic to the system; i.e., they are independent of its operational frequency range. Therefore, the achievable pulse advancements or delays for small pulse compression are shorter than the pulse duration. This would be a drawback for developing practical delay lines or optical buffers based on this system for signal processing. However, the very abrupt SFL transition when approaching the critical length detuning opens the door for sensing applications. With this sensing scope, let us note that similar phenomena would be expected by varying whatever changes the *optical path* in one of the arms. As an example, a lithium niobate interferometer operative at $1.55 \mu\text{m}$ was proposed where a fine control of the phase shift in a branch could be achieved by applying an electric field through a metallic electrode, which induces a refractive index change on the waveguide.

ACKNOWLEDGMENTS

Financial support from Ministerio de Educación y Ciencia through Project No. FIS2009-13955-C02-02 is acknowledged. The authors thank Guillermo Martínez de la Torre for the preparation of the coaxial cables.

[1] L. Brillouin, *Wave Propagation and Group Velocity* (Academic Press, New York, 1960).
 [2] L. Thévenaz, *Nat. Photonics* **2**, 474 (2008).
 [3] T. F. Krauss, *Nat. Photonics* **2**, 448 (2008).
 [4] E. Cabrera-Granado and D. J. Gauthier, *Opt. Pura Apl.* **41**, 313 (2008).
 [5] R. W. Boyd and P. Narum, *J. Mod. Opt.* **54**, 2403 (2007).
 [6] L. V. Hau, S. E. Harris, Z. Dutton, and C. H. Behroozi, *Nature (London)* **397**, 594 (1999).

[7] L. J. Wang, A. Kuzmich, and A. Dogariu, *Nature (London)* **406**, 277 (2000).
 [8] A. V. Turukhin, V. S. Sudarshanam, M. S. Shahriar, J. A. Musser, B. S. Ham, and P. R. Hemmer, *Phys. Rev. Lett.* **88**, 023602 (2001).
 [9] M. S. Bigelow, N. N. Lepeshkin, and R. W. Boyd, *Science* **301**, 200 (2003).
 [10] J. Mork, R. Kjaer, M. van der Poel, and K. Yvind, *Opt. Express* **13**, 8136 (2005).

- [11] H. Su and S. L. Chuang, *Appl. Phys. Lett.* **88**, 61102 (2006).
- [12] A. Schweinsberg, N. N. Lepeshkin, M. S. Bigelow, R. W. Boyd, and S. Jarabo, *Europhys. Lett.* **73**, 218 (2006).
- [13] M. González-Herráez, K. Y. Song, and L. Thévenaz, *Appl. Phys. Lett.* **87**, 081113 (2005).
- [14] D. Dahan and G. Eisenstein, *Opt. Express* **13**, 6234 (2005).
- [15] J. F. Galisteo-López, M. Galli, A. Balestreri, M. Patrini, L. C. Andreani, and C. López, *Opt. Express* **15**, 15342 (2007).
- [16] S. Longhi, M. Marano, P. Laporta, and M. Belmonte, *Phys. Rev. E* **64**, 055602(R) (2001).
- [17] S. Longhi, *Phys. Rev. E* **72**, 056614 (2005).
- [18] G. Nimtz, *IEEE J. Sel. Top. Quantum Electron.* **9**, 79 (2003).
- [19] M. Mojahedi, E. Schamiloglu, F. Hegeler, and K. J. Malloy, *Phys. Rev. E* **62**, 5758 (2000).
- [20] A. Sánchez-Meroño, J. Arias, and M. M. Sánchez-López, *IEEE J. Quantum Electron.* **46**, 546 (2010).
- [21] A. Haché and L. Poirier, *Phys. Rev. E* **65**, 036608 (2002).
- [22] J. N. Munday and W. M. Robertson, *Appl. Phys. Lett.* **83**, 1053 (2003).
- [23] M. Kitano, T. Nakanishi, and K. Sugiyama, *IEEE J. Sel. Top. Quantum Electron.* **9**, 43 (2003).
- [24] H. Aynaou, E. H. El Boudouti, Y. El Hassouani, A. Akjouj, B. Djafari-Rouhani, J. Vasseur, A. Benomar, and V. R. Velasco, *Phys. Rev. E* **72**, 056601 (2005).
- [25] M. M. Sánchez-López, A. Sánchez-Meroño, J. Arias, J. A. Davis, and I. Moreno, *Appl. Phys. Lett.* **93**, 074102 (2008).
- [26] E. H. El Boudouti, N. Fettouhi, A. Akjouj, B. Djafari-Rouhani, A. Mir, J. O. Vasseur, L. Dobrzynski, and J. Zemmouri, *J. Appl. Phys.* **95**, 1102 (2004).
- [27] Z. Shi, R. W. Boyd, D. J. Gauthier, and C. C. Dudley, *Opt. Lett.* **32**, 915 (2007).
- [28] A. Sánchez-Meroño, M. M. Sánchez-López, J. Arias, and J. A. Davis, *Opt. Pura Apl.* **42**, 215 (2009).
- [29] A. Sánchez-Meroño, M. M. Sánchez-López, J. Arias, J. A. Davis, and I. Moreno, *SPIE Proc.* **7716**, 77161Y 1-10 (2010).
- [30] J. A. Davis, D. A. Miller, M. M. Sánchez-López, and J. Cos, *Am. J. Phys.* **74**, 1066 (2006).
- [31] L. G. Wang, N. H. Liu, Q. Lin, and S. Y. Zhu, *Phys. Rev. E* **68**, 066606 (2003).
- [32] W. Guo, *Phys. Rev. E* **73**, 016605 (2006).
- [33] O. A. Peverini, R. Tascone, G. Addamo, G. Virone, and R. Orta, *IEEE Antennas Wirel. Propag. Lett.* **7**, 101 (2007).
- [34] E. L. Wooten, K. M. Kissa, A. Yi-Yan, E. J. Murphy, D. A. Lafaw, P. F. Hallemeier, D. Maack, D. V. Attanasio, D. J. Fritz, G. J. McBrien, and D. E. Bossi, *IEEE J. Sel. Top. Quantum Electron.* **6**, 69 (2000).



Fast light in unbalanced low-loss Mach-Zehnder interferometersAida Sánchez-Meroño,¹ María del Mar Sánchez-López,² and Julia Arias¹¹*Departamento de Ciencia de Materiales, Óptica y Tecnología Electrónica, Universidad Miguel Hernández, 03202, Elche, Spain*²*Instituto de Bioingeniería, Universidad Miguel Hernández, 03202, Elche, Spain*

(Received 31 January 2014; published 17 April 2014)

An analytical approach is reported that describes previously observed fast-light regimes in linear and passive Mach-Zehnder interferometers (MZI) where the optical path difference is due to a different length of the branches. Approximate expressions are developed for the transmission coefficient and group delay spectral functions valid for frequencies close to the transmission minima ω_{\min} , where these regimes occur. It is found that the group delay at ω_{\min} verifies a simple scaling law. We demonstrate that slow light cannot arise in this system, and that tunneling and superluminal regimes appear only for low-loss devices, where the attenuation drives the change in the propagation regimes. The propagation of a sinusoidally modulated pulse train through the MZI is described, and relevant figures of merit, which are intrinsic to the system and universal for any operative spectral range, are determined. The theoretical approach is illustrated by simulations of a silicon-based interferometer designed for advancing pulses at $1.55 \mu\text{m}$. Also, previously reported experimental results in the radiofrequency range are interpreted in the framework of the model.

DOI: [10.1103/PhysRevA.89.043828](https://doi.org/10.1103/PhysRevA.89.043828)

PACS number(s): 42.25.Bs, 42.25.Hz, 73.40.Gk, 07.60.Ly

I. INTRODUCTION

Slow and fast light (SFL) technologies are currently receiving much attention because of their interesting applications, ranging from optical information processing, with the realization of optical buffers, quantum memories, switches and synchronizers [1–3], to enhanced precision sensing [4,5] and interferometry [6].

These technologies are based on systems that exhibit steep positive dispersion to propagate a light pulse at unusually low group velocity (slow light, $v_g \ll c$) or steep negative dispersion to achieve pulse propagation at unusually fast group velocity (fast light, $v_g > c$ or negative) [7]. This is the case of materials with gain or absorption resonances [8,9] and of materials where a dip in the gain or in the absorption feature is induced by nonlinear optical processes, like electromagnetic [10] or photo-isomerization-induced [11] transparency, coherent population oscillations [12] or stimulated scattering [13–15]. SFL effects thus arise in a myriad of materials (atomic vapors, solid crystals, dye-doped liquid crystals, semiconductors, and optical fibers) because an abrupt variation of the real part of the complex refractive index (hereafter, simply the refractive index) n occurs in the narrow band around the resonance or dip due to the Kramers-Kronig relations that link the real and imaginary parts of the dielectric function.

Exotic pulse propagation regimes also occur in engineered media without substantial material dispersion, like photonic crystals [16,17] and Bragg gratings [18]. These systems consist of a periodic refractive index distribution and exhibit structural dispersion due to coupling between the incident wavelength and the characteristic length of the structure. The transmission spectrum has a forbidden region for certain directions and polarizations (photonic band gap), which sustains fast light, while slow light is generated at the photonic band edge and at the inside-gap resonance of doped photonic crystals or Bragg gratings. Contrary to the aforementioned systems with material resonances, SFL occurs here in entirely linear and passive structures. Because of the scaling properties of photonic

band-gap (PBG) systems, structural SFL has been detected not only in the optical range but also for lower frequencies, like microwave [19–21], radiofrequency (RF) [22,23], and even acoustic wave packets [24].

As an alternative to PBG systems, we recently demonstrated that structural SFL can be generated in multiple-beam interferometers of three or more branches [25,26], which are linear and passive systems not exhibiting photonic band gaps. The simplest interferometer of this kind, with only two branches, is the Mach-Zehnder interferometer. It is a common and versatile device in actual communication systems, widely used to build optical switches [27], modulators for optical signal multiplexing [28], sensors [29], and fractional optical differentiators for pulse-shaping applications and information processing [30]. Its typical interference pattern presents transmission peaks and valleys as a consequence of the phase shift between the two interfering beams, caused by either a difference in the length of the branches (unbalanced or asymmetric MZI), or by a refractive index difference between the branches of equal length (symmetric MZI).

This two-path interferometer has been shown to sustain fast-light propagation for frequencies close to the transmission minima [31–33]. In [31], frequency-domain characterization of an asymmetric loop structure (asymmetric MZI) built with coaxial cables showed negative phase jumps around the transmission minima. This led the authors to point out this structure as a good candidate for obtaining negative group velocity. Time domain experiments performed with Gaussian acoustic pulses [32] and sinusoidally modulated RF wave packets [33] corroborated these findings. By tuning the pulse carrier frequency slightly off the transmission minima, superluminal propagation was also detected [33]. No slow-light regimes were observed. Slow light in an MZI has only been obtained when the medium in one of the branches is microstructured [34] or exhibits a material-resonant feature [35].

The experimental results in [33] were interpreted in the framework of the effective index approach [36]. Within this picture, the scattering loss of the pulse spectral components is

ascribed to an effective complex refractive index whose real part is obtained from the overall phase shift on transmission $\phi_t(\omega)$ through the structure. The abrupt negative slope of $\phi_t(\omega)$ at the transmission minima [31–33] causes an anomalous effective dispersion whose origin is structural, i.e., it is not due to dispersion of the medium in the branches (which was, in fact, neglected), but to the features in the spectral transmission. This is also the situation in PBG systems.

In this work we bring these ideas further and develop a theoretical model that fully describes the arising of structural fast light in MZIs and its performance in terms of both the device parameters and the pulse characteristics. The medium in the branches is assumed to be linear and dispersionless in the frequency range of interest, which is a reasonable assumption for a medium exhibiting no gain or absorption peaks. To simplify the analysis, a constant attenuation coefficient is considered, and exact expressions for the complex transmission coefficient and group delay as a function of frequency are obtained. The conditions necessary to obtain appreciable fast light effects are discussed in terms of the fringe visibility, and the allowed propagation regimes are determined as a function of the device characteristics (size, refractive index, and attenuation coefficient of the medium in the branches). We show that the total attenuation is the mechanism that drives the change in the propagation regime for a given refractive index. A substantial difference regarding fast light effects is found between asymmetric and symmetric MZI.

The behavior of a pulse travelling through an SFL system depends not only on the characteristics of the system itself, but also on the pulse shape and duration. As a consequence, the group delay spectral function of the MZI will only be an estimation of the actual pulse delay measured in a time-domain experiment. This issue is addressed in this work by obtaining an approximate expression of the complex transmission coefficient, valid for frequencies close to the transmission minima, that is used to model the propagation of a sinusoidally modulated pulse train through the MZI. An analytic expression of the pulse delay, along with relevant figures of merit that quantify fast-light propagation, is determined. A comparison is made to recently reported SFL effects in three-beam interferometers [25]. The model predictions are illustrated with numerical simulations of a silicon-based MZI designed to operate at optical frequencies. Finally, the previously mentioned experimental results in the RF range [33] are revisited and interpreted in the framework of this model.

II. ANALYTICAL MODEL

We consider a plane wave of a unit complex amplitude impinging on a Mach-Zehnder interferometer. A 1×2 splitter divides the wave into two equal components that travel along each arm and then recombine by a 2×1 coupler. The transmitted complex amplitude at the end of the interferometer is

$$\hat{t} = \frac{1}{2} \sum_{i=1}^2 e^{j\phi_i}, \quad (1)$$

where ϕ_i is the phase of the wave propagating along the i th branch, which, in turn, can be expressed as

$$\phi_i = \frac{\omega}{v} L_i + j\alpha L_i. \quad (2)$$

In Eq. (2) ω is the angular frequency, v is the phase velocity in the medium, L_i is the i th arm length, and α is the attenuation coefficient of the medium. We define the length of each arm as

$$L_1 = L - \frac{\Delta}{2} \quad \text{and} \quad L_2 = L + \frac{\Delta}{2}, \quad (3)$$

where Δ is the length difference between arms. The effective length of the MZI is the average length of the branches since the input field amplitude is equally split between the two arms

$$L = \frac{(L_1 + L_2)}{2}. \quad (4)$$

Let us define β as the phase shift associated to the length difference Δ , i.e., $\beta = \omega\Delta/v$, and introduce the following quantities:

$$\mathcal{R} = \cosh(\alpha\Delta/2)\cos(\beta/2), \quad (5a)$$

$$\mathcal{I} = -\sinh(\alpha\Delta/2)\sin(\beta/2), \quad (5b)$$

which are related to the transmission coefficient according to $\hat{t} = e^{j(\omega/v+j\alpha)L}(\mathcal{R} + j\mathcal{I})$.

Therefore, the magnitude and phase of the transmission coefficient can be expressed as

$$|\hat{t}| = e^{-\alpha L} \sqrt{\mathcal{R}^2 + \mathcal{I}^2}, \quad (6a)$$

$$\phi_t = \frac{\beta L}{\Delta} + \arctan\left(\frac{\mathcal{I}}{\mathcal{R}}\right). \quad (6b)$$

The propagation of an electromagnetic pulse through the interferometer is often described in terms of the group delay, which is the time taken by the pulse envelope to propagate through the system [7]. Following the standard stationary phase approach for the plane waves constituting the pulse [19,20], the group delay is obtained from the frequency derivative of the transmission coefficient phase

$$\tau_g = \frac{\partial \phi_t}{\partial \omega} = \frac{L}{v} + \frac{\mathcal{R} \frac{\partial \mathcal{I}}{\partial \omega} - \mathcal{I} \frac{\partial \mathcal{R}}{\partial \omega}}{\mathcal{R}^2 + \mathcal{I}^2}. \quad (7)$$

Assuming that both the refractive index and attenuation coefficient of the medium in the branches are constant over the whole frequency range of interest, the following expression of the group delay as a function of frequency (through β) is retrieved

$$\tau_g = \tau_p \left(1 - \frac{\Delta}{2L} \frac{\sinh(\alpha\Delta/2)\cosh(\alpha\Delta/2)}{\cos^2(\beta/2) + \sinh^2(\alpha\Delta/2)} \right), \quad (8)$$

where $\tau_p (= L/v)$ is the phase delay over the system's effective length. The previous expressions are exact within the assumptions for the medium in the branches. In the following sections, easier to handle approximate equations will be derived with the aim of demonstrating anomalous propagation regimes as well as modeling the propagation of pulses through the MZI. The conditions considered for such a derivation are now discussed.

First, the analysis will be centered in a narrow frequency region around the transmission minima since it is where

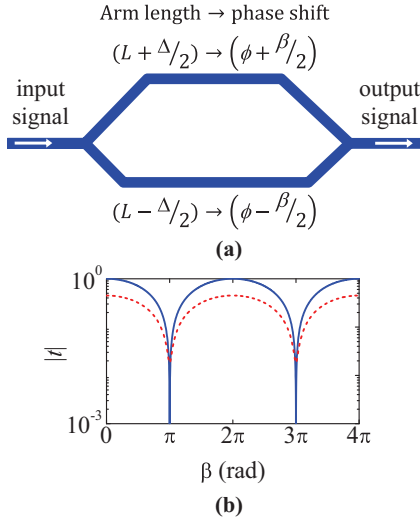


FIG. 1. (Color online) (a) Schematic of an unbalanced MZI and (b) its typical transmission spectrum with (dashed line) and without (solid line) attenuation.

fast light was experimentally observed [31–33]. An MZI has one minimum between two adjacent principal peaks on transmission. The extrema of the transmission function $|\hat{t}(\beta)|$ of Eq. (6a) lie at phase values $\beta_{\min} = (2m + 1)\pi$ (for minima) and $\beta_{\max} = 2\pi m$ (for maxima), where m is an integer number. The position of the minima does not change with attenuation, in contrast to the situation in a three-beam interferometer [25]. A schematic of the two-beam interferometer and its transmission spectrum with and without attenuation are displayed in Fig. 1.

Second, our analytical approach will be performed within the condition of high fringe contrast of the interference pattern (i.e., weak attenuation), which is necessary for the arising of anomalous pulse propagation regimes. In the absence of attenuation ($\alpha = 0$), Eq. (8) yields $\tau_g = \tau_p$, as it is expected in a linear and lossless system, where the phase relation between the pulse components remains unchanged and consequently the pulse peak travels at the phase velocity. On the opposite case, for very high attenuation, no anomalous pulse propagation regimes are observed. Since a high attenuation reduces the contrast of the interference pattern (as it can be appreciated in Fig. 1), the present analytical study will be performed within the condition of good visibility of the fringes. Such a condition corresponds to considering small $\alpha\Delta$ values, as it is demonstrated below.

The visibility of the interference pattern (or fringe contrast) is defined as [35]

$$\nu \equiv \frac{T_{\max} - T_{\min}}{T_{\max} + T_{\min}}, \quad (9)$$

where $T = |\hat{t}|^2$ is the transmittance and the subscript indicates its maximum or minimum value. Considering the phase values of the transmittance extrema (β_{\max} and β_{\min}) into Eqs. (5) and (6), the fringe contrast of the MZI is found to depend solely on the attenuation along the length difference between branches ($\alpha\Delta$)

$$\nu \equiv \frac{2e^{-\alpha\Delta}}{1 + e^{-2\alpha\Delta}}, \quad (10)$$

For a lossless interferometer ($\alpha = 0$) one gets $\nu = 1$, whereas the losses decrease the fringe visibility; the higher $\alpha\Delta$, the smaller is the fringe contrast. Since fast-light effects requires sharp spectral features, a visibility of at least $\nu = 0.65$ is required [35], and this requires that the amplitude ratio of the combining waves at the end of the MZI, $e^{-\alpha\Delta}$, should be less than $1/e$, that is, $\alpha\Delta < 1$. The analytical approximation in the next section will consider $\alpha\Delta < 0.5$ values, which assures a very good fringe visibility ($\nu \geq 0.9$) along with excellent agreement with the exact model developed above.

A. Transmission coefficient and group delay around the transmission minima

Let us derive approximate equations of the magnitude $|\hat{t}(\omega)|$ and phase $\phi_t(\omega)$ of the transmission coefficient, and the group delay $\tau_g(\omega)$, valid for frequencies close to a transmission minimum ω_{\min} . These expressions will be used in Sec. II C to study the propagation of narrowband sinusoidally modulated pulses through the MZI.

The transmission coefficient in Eq. (6) can be written in the terms of $(\beta - \beta_{\min})$. After some algebraic operations, the following expressions are obtained:

$$|\hat{t}| = e^{-\alpha L} \sqrt{\sin^2\left(\frac{\beta - \beta_{\min}}{2}\right) + \sinh^2\left(\frac{\alpha\Delta}{2}\right)} \approx e^{-\alpha L} \sqrt{\left(\frac{\beta - \beta_{\min}}{2}\right)^2 + \left(\frac{\alpha\Delta}{2}\right)^2}, \quad (11a)$$

$$\frac{\mathcal{I}}{\mathcal{R}} = \frac{\tanh(\alpha\Delta/2)}{\tan(\beta - \beta_{\min}/2)} \approx \frac{\alpha\Delta}{\beta - \beta_{\min}}, \quad (11b)$$

where the approximation valid for small angles ($\beta - \beta_{\min}$) and small $\alpha\Delta$ was considered. Recalling that $\beta = \omega\Delta/\nu$ and defining a new parameter $\gamma = -\alpha\nu$, this leads to the following approximate equations for the magnitude and phase of the transmission coefficient around the minima ω_{\min}

$$|\hat{t}(\omega)| \approx e^{-\alpha L} \frac{\alpha\Delta}{2} \sqrt{1 + \left(\frac{\omega - \omega_{\min}}{\gamma}\right)^2}, \quad (12a)$$

$$\phi_t(\omega) \approx \omega\tau_p + \arctan\left(\frac{\omega - \omega_{\min}}{\gamma}\right) + \frac{\pi}{2}. \quad (12b)$$

Note that the result of null transmission at the minima is recovered for the lossless case ($\alpha = 0$). Finally, the approximate expression for the group delay around each transmission minimum is retrieved through a ω derivation of the phase function in Eq. (12b)

$$\tau_g(\omega) \approx \tau_p + \frac{\gamma}{(\omega - \omega_{\min})^2 + \gamma^2}. \quad (13)$$

Equation (13) shows that the excess group delay ($\tau_g - \tau_p$) around the minima is a Lorentzian function, with $|\gamma|$ the half-width at half maximum (HWHM) and $1/\gamma$ the excess group delay at the transmission minima. Since γ is directly proportional to the attenuation coefficient for a given refractive index, one concludes that the larger the losses, the wider will be the group delay Lorentzian curve and the smaller will be the group delay absolute value at ω_{\min} . Hence, the softening

of the anomalous propagation regimes when the losses in the system are notable is proved.

B. Pulse propagation regimes at the transmission minima

In this section we provide theoretical proof that tunneling and superluminal regimes can arise at the transmission minima by properly choosing the interferometer's effective length for a given attenuation coefficient and refractive index. From Eq. (8) the exact group delay at the transmission minima β_{\min} reads

$$\tau_g = \tau_p \left[1 - \frac{\Delta}{2L} \coth \left(\frac{\alpha \Delta}{2} \right) \right], \quad (14a)$$

which can be approximated for small values of $\alpha \Delta$ as

$$\tau_g \approx \tau_p \left(1 - \frac{1}{\alpha L} \right) = \tau_p + \frac{1}{\gamma}. \quad (14b)$$

Alternatively, the above expression could also be obtained by evaluating Eq. (13) at ω_{\min} .

Interestingly, if we now apply the relationship between the attenuation coefficient and the imaginary part of the complex refractive index n_i ($\alpha = n_i \omega / c$) into Eq. (14b), the group delay at ω_{\min} can also be approximated as

$$\tau_g \approx \tau_p - \frac{n}{n_i} \frac{1}{\omega_{\min}}. \quad (14c)$$

The above expression brings two interesting points into attention. First, it sets a scaling law for the group delay since it indicates that the product $\omega_{\min} \times (\tau_g - \tau_p)$ does not depend on the interferometer's operative frequency range, but only on the ratio between the real and imaginary parts of the complex refractive index of the medium in the branches (n/n_i). Second, equivalent expressions were obtained for the group delay at the reflection minima of a weakly absorbing dielectric slab [21,37], which is indeed a multibeam interferometer. Therefore, it shows the resemblance between pulse transmission through an MZI and pulse reflection on a dielectric slab. This should not be unexpected since the MZI transmission spectrum is, in fact, very similar to the dielectric slab reflection spectrum.

Following the discussion, we now focus on a system with a given refractive index and take Eq. (14b) to analyze the possible propagation regimes at the minima. Equation (14b) shows that a lossy MZI cannot sustain slow light (τ_g cannot be larger than τ_p) because α is positive by definition. Only in the hypothetical case of an interferometer with gain ($\alpha < 0$) would the subluminal regime arise. Practical situations, like considering an MZI with a medium in one of the branches that exhibits a narrow gain resonance, are discussed in the literature [35].

The interferometer will sustain tunneling at the minima ($\tau_g < 0$) if the attenuation coefficient and the effective length are chosen so that

$$\alpha L < 1. \quad (15)$$

For larger αL , the superluminal regime will arise ($0 < \tau_g < L/c$) if the following condition is satisfied:

$$1 < \alpha L < \frac{n}{n-1}. \quad (16)$$

TABLE I. Possible propagation regimes at the transmission minima for a lossy MZI.

Condition	$\alpha L < 1$	$1 < \alpha L < \frac{n}{n-1}$	$\alpha L > \frac{n}{n-1}$
$\alpha > 0$	Tunneling	Superluminal	Normal

Therefore, the change in the pulse propagation regime is driven by the total attenuation of the interferometer αL , which can be modified by either changing the medium in the branches (i.e., α) and/or the interferometer's effective length L . The length difference between branches Δ plays no role in this issue, it only determines the frequency position of the minima, namely $\omega_{\min} = (2m+1)\pi\nu/\Delta$. Table I summarizes the possible propagation regimes at the minima as a function of αL .

The above analysis is illustrated by performing numerical simulations on a silicon-based MZI with refractive index $n = 3.48$. Figure 2 shows, for two attenuation values and $\Delta = L/10$ the magnitude of the transmission coefficient calculated using Eq. (6a) and the group delay as a function of β according to Eq. (8). As it was discussed, no anomalous propagation regimes occur in the lossless interferometer, while if losses with $\alpha \Delta = 0.015$ are considered, tunneling arises at each minimum with negative group delays close to $-6\tau_p$.

Figure 3 shows how the system's total attenuation drives the change in the pulse propagation regime. The group delay at the minima (normalized to the phase delay) is plotted as a function of αL for an interferometer with $\alpha \Delta = 0.015$. Together with the τ_g values obtained from Eq. (14a), the straight line $1/n$ corresponding to propagation over length L in a vacuum is represented. The system exhibits negative group delays for small-enough attenuation ($\alpha L < 1$). For values of αL ranging between 1 and 1.4, the propagation is superluminal,

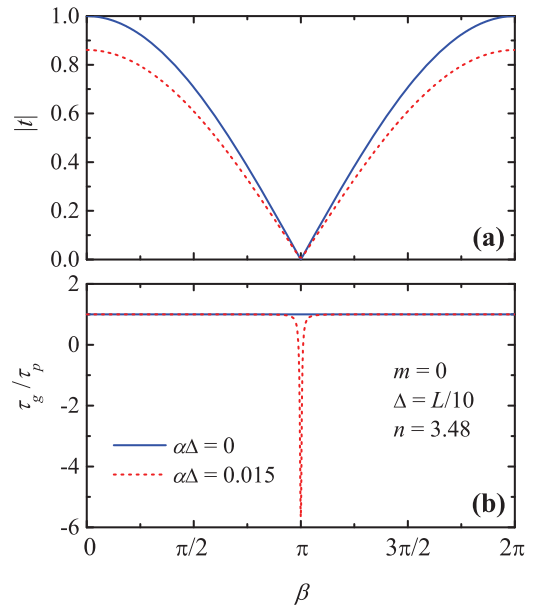


FIG. 2. (Color online) (a) Transmission coefficient magnitude and (b) group delay in units of phase delay through an Si-based MZI with length difference between arms $\Delta = L/10$ and refractive index $n = 3.48$ for two values of the attenuation coefficient α .

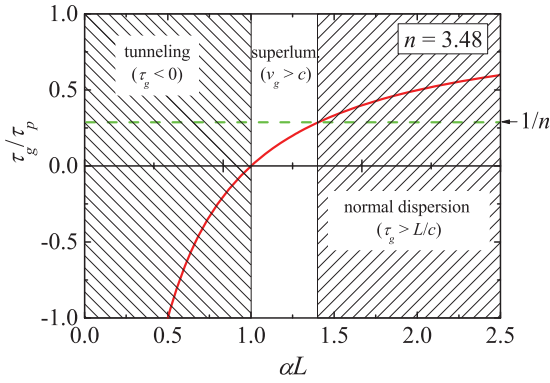


FIG. 3. (Color online) Pulse propagation regimes at the transmission minima of an Si-Based MZI with $\alpha\Delta = 0.015$ as a function of the total attenuation αL . Group delay plotted from Eq. (14a) (solid line) and phase delay through a vacuum (dashed line). The delays are given in units of the phase delay over the system's effective length.

in agreement with Eq. (16), while for too high attenuation $\alpha L > 1.4$ normal propagation is obtained. Therefore, fast light is achieved for weak-enough attenuation, while it disappears if it is either zero or too high ($> \frac{n}{n-1}$).

The fast-light conditions summarized in Table I and the impossibility of getting slow light coincide with those obtained for a three-beam interferometer with constant length difference Δ between adjacent arms [25]. In fact, the exact expression of the group delay at the transmission minima of this latter system is the same as the one derived here if Δ in Eq. (14a) is substituted by 2Δ , i.e., the length difference between the shortest and the longest arms of the three-beam interferometer. Therefore, a three-beam interferometer with constant Δ behaves, as far as SFL effects are concerned, as an MZI.

C. Propagation of sinusoidally modulated pulses

The propagation of a pulse train through the MZI is now modeled. A sinusoidally modulated wave packet with carrier frequency ω_c and modulation frequency ω_m is considered, $E_{\text{in}}(t) = E_c \sin(\omega_c t) [1 + M_{\text{in}} \cos(\omega_m t)]$, where the modulation index M_{in} is the amplitude ratio of the modulating and carrier signals. Together with the carrier component, this kind of modulation generates two side components of amplitude $E_{\pm s} = M_{\text{in}} E_c / 2$ and frequencies $\omega_{\pm s} = \omega_c \pm \omega_m$. By setting the carrier frequency at one of the minima ($\omega_c = \omega_{\text{min}}$) and using Eq. (12), the amplitude and phase of each spectral component after propagating through the system are obtained. Using Fourier theory, the envelope of the pulse transmitted through the interferometer reads

$$E_{\text{out}}(t) \propto 1 + M_{\text{out}} \cos[\omega_m(t - \tau_{\text{pulse}})], \quad (17)$$

with modulation index (M_{out}) and delay (τ_{pulse}) of the output pulse given by

$$M_{\text{out}} = M_{\text{in}} \sqrt{1 + \left(\frac{\omega_m}{\gamma}\right)^2}, \quad (18)$$

$$\tau_{\text{pulse}} = \tau_p + \frac{1}{\omega_m} \arctan\left(\frac{\omega_m}{\gamma}\right), \quad (19)$$

keeping in mind that $\tau_p = L/v$ and $\gamma = -\alpha v$.

The pulse delay in Eq. (19) is the time that a sinusoidally modulated pulse train of modulation frequency ω_m and a carrier frequency tuned at ω_{min} takes in travelling through the MZI. In the limit of extremely narrow pulse bandwidth $\omega_m \rightarrow 0$, $\tau_{\text{pulse}} \rightarrow \tau_p + 1/\gamma$, thus recovering the group delay value at ω_{min} which was discussed in Sec. II B. In other words, this analysis shows that the narrower the spectral pulse width, the more the *pulse delay* measured in a time-domain propagation experiment approaches the value of the *group delay* given by Eq. (14a).

An important figure of merit in SFL systems is the fractional delay [38], D_f , defined as the ratio between the excess pulse delay and the duration of the incident pulse T_{in} :

$$D_f = \frac{\tau_{\text{pulse}} - \tau_p}{T_{\text{in}}}. \quad (20)$$

This quantity is equal to the excess number of pulses that can be contained at any time within the system with respect to the number that would be contained if the pulses travelled at the phase velocity. It is hence a measure of how much the information storage capacity of the system is enhanced due to SFL effects. A common definition when dealing with optical pulses is to take the pulse duration as the FWHM of the pulse power. For sinusoidally modulated pulses of modulation index M , the pulse duration is $T = 2/\omega_m \arccos((1 - \sqrt{2} + M)/\sqrt{2}M)$ and consequently, D_f reads

$$D_f = \frac{\arctan\left(\frac{\omega_m}{\gamma}\right)}{2 \arccos\left(\frac{1 - \sqrt{2} + M_{\text{in}}}{\sqrt{2}M_{\text{in}}}\right)}. \quad (21)$$

Figure 4(a) shows that the fractional advancement $|D_f|$ (solid line) increases with modulation frequency. Also, Eq. (21) predicts $|D_f| = 34\%$ if modulation is performed with $M_{\text{in}} = 1$ and $\omega_m = |\gamma|$, i.e., the pulse spectral components lie within the FWHM of the group delay function in Eq. (13). For higher modulation frequencies, however, the pulse will undergo a certain degree of distortion, which is larger as ω_m increases. According to Eq. (18), the modulation index of the transmitted pulse is always larger than that of the input pulse, and consequently, the duration of the output pulse (T_{out}) will always be smaller, leading to a pulse compression b , whose value can be calculated by

$$b = 1 - \frac{T_{\text{out}}}{T_{\text{in}}} = 1 - \frac{\arccos\left(\frac{1 - \sqrt{2} + M_{\text{out}}}{\sqrt{2}M_{\text{out}}}\right)}{\arccos\left(\frac{1 - \sqrt{2} + M_{\text{in}}}{\sqrt{2}M_{\text{in}}}\right)}. \quad (22)$$

Figure 4(a) shows (dashed line) the relation between pulse compression and modulation frequency (normalized to $|\gamma|$). It is found that for not too high values of ω_m the compression factor goes roughly quadratic with the fractional delay $b \approx K D_f^2$. Considering $M_{\text{in}} = 1$, the proportionality constant K is 0.74 if $\omega_m \rightarrow 0$ and it is 0.71 if $\omega_m = |\gamma|$. This relation is illustrated in Fig. 4(b); it implies that, to keep the pulse compression below 5%, the fractional delay may not exceed 27%, and to keep it below 10% the fractional delay may not exceed 38%.

In addition to pulse compression, distortion of the pulse amplitude also appears, similarly to what is observed for fast light in systems with material resonances [39]. In the case of $M_{\text{in}} = 1$, this amplitude distortion acts as a pulse breakup, giving

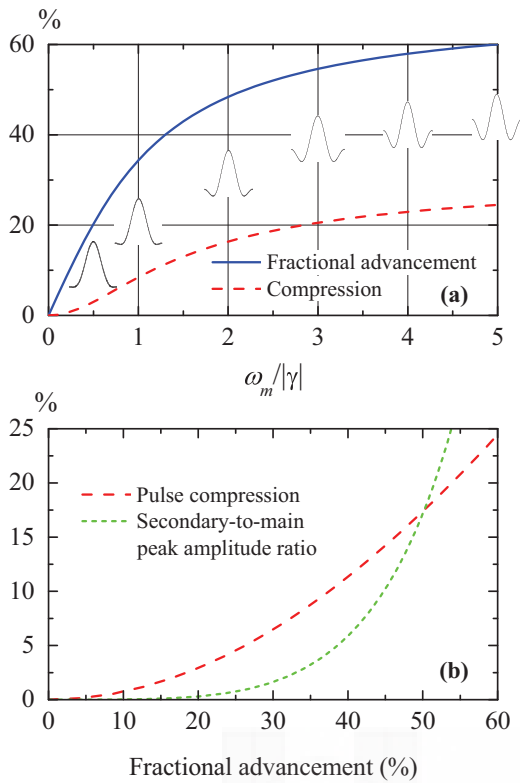


FIG. 4. (Color online) (a) Fractional advancement (solid line) and pulse compression (dashed line) versus normalized modulation frequency, and (b) pulse compression (dashed line) and secondary to main peak amplitude ratio (short-dashed line) as a function of the fractional advancement, for a 100% sinusoidally modulated pulse train with carrier frequency tuned at one of the transmission minima.

rise to a main peak (lying at $t = \tau_{\text{pulse}}$) and a secondary peak (lying at $t = \tau_{\text{pulse}} + \pi/\omega_m$). The secondary-to-main power amplitude ratio is given by $(1 - M_{\text{out}})^2/(1 + M_{\text{out}})^2$, which increases with increasing modulation frequency, or equivalently, with increasing fractional advancement, as shown in Fig. 4(b). Thus, to maintain the secondary peak amplitude below 10% of the main peak amplitude, the fractional delay may not exceed 45%.

Another relevant figure of merit of SFL systems is the delay-bandwidth product (DBP) [38], defined as the product of the delay and bandwidth of the signal transmitted through the system. This quantity can be estimated in various units depending on which magnitude the bandwidth is given. Choosing a modulation frequency $f_m = |\gamma|/2\pi$ so that the spectral components of the signal here considered lie within the FWHM of the Lorentzian group delay curve in Eq. (13), the expected DBP is $(\tau_{\text{pulse}} - \tau_p) \times 2f_m = 25\%$.

It is worth noticing that the above features and figures of merit are entirely applicable to MZIs operating at any frequency range. In this context, we shall recall the simple scaling law for the excess group delay at ω_{min} that was previously obtained [see Eq. (14c)], which is useful to transform a device originally designed to operate at a specific frequency range into another operative range. Finally, let us point out that the pulse propagation characteristics described above are equivalent to those derived for a three-beam interferometer [25].

III. RESULTS AND DISCUSSION

In this section, the model predictions are applied to Mach-Zehnder interferometers operative at two different spectral regions. First, a numerical simulation of the propagation of optical pulses centered at $1.55 \mu\text{m}$ is performed and second, our previous experimental results obtained in the RF range are revisited and interpreted in the framework of the model.

A. Simulation results in the optical range

A silicon-based MZI with an attenuation coefficient of 6.5 dB/cm and a refractive index of $n = 3.48$ is considered. It is designed to have a fixed branch length difference of $\Delta = 200 \mu\text{m}$ that sets the minima 430 GHz apart. Therefore, the model parameters take the values $\alpha\Delta = 0.015$ and $\gamma^{-1} = -155 \text{ ps}$. The conditions summarized in Table I yield the range of values that the system's effective length L must take to sustain tunneling, superluminal, or normal group delay at the minima. Consequently, three such MZIs of the following lengths are considered: $L = 2 \text{ mm}$ (tunneling), $L = 1.5 \text{ cm}$ (superluminal), and $L = 2 \text{ cm}$ (normal).

The transmission magnitude $|\hat{t}|$ and group delay τ_g of the three MZIs are calculated according to Eqs. (6a) and (8) in a frequency range of 450 GHz centered at the transmission minimum located at $f_{\text{min}} \approx 193 \text{ THz}$; the results are plotted in Fig. 5(a). As L increases, the attenuation of the transmission

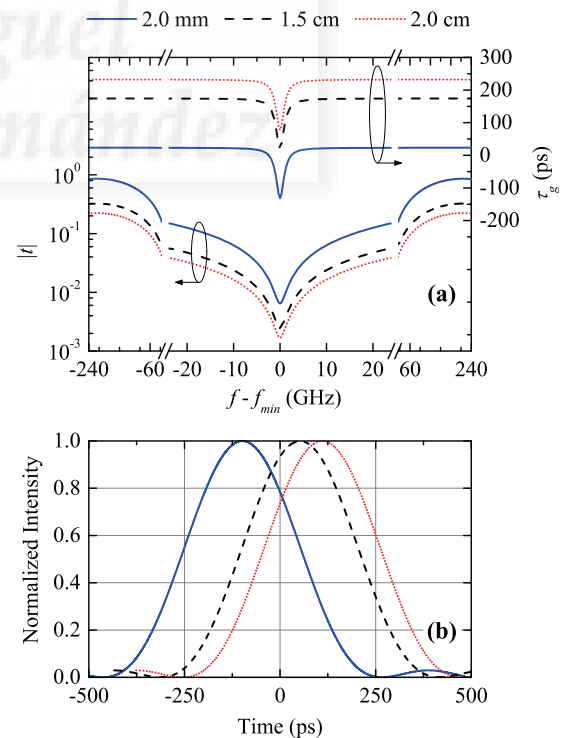


FIG. 5. (Color online) Numerical simulation of an Si-based MZI with parameters $\Delta = 200 \mu\text{m}$, $\alpha = 6.5 \text{ dB/cm}$, and $n = 3.48$ for three values of the effective length: $L = 2 \text{ mm}$ (solid line), $L = 1.5 \text{ cm}$ (dashed line), and $L = 2 \text{ cm}$ (dotted line). (a) Magnitude of the transmission coefficient and group delay. (b) Normalized traces of pulses with carrier frequency tuned at f_{min} and transmitted through each interferometer. The incident pulse has its peak at $t = 0$.

spectrum becomes stronger and the group delay curve shifts upwards because of the positive contribution of a larger phase delay. The group delay value at f_{\min} , namely $\tau_g \approx -131, 19$, and 77 ps, corresponds to the tunneling, superluminal, and normal regimes, respectively, in agreement with the model predictions. For each interferometer, the excess group delay curve $\tau_g(f) - \tau_p$ fits excellently to a Lorentzian function of HWHM $|\gamma|/2\pi \approx 1$ GHz and -155 ps excess delay at the minimum.

Now, an optical pulse train travelling through each interferometer is numerically simulated. The optical carrier is tuned at $f_{\min} \approx 193$ THz ($\lambda = 1.55 \mu\text{m}$) and it is 100% sinusoidally modulated at frequency $f_m = |\gamma|/2\pi$ to generate a train of pulses of width $T_{in} = 364$ ps at a repetition rate of 1 GHz. Figure 5(b) shows the pulse traces corresponding to a propagation through the interferometers of $L = 2$ mm (pulse 1), $L = 1.5$ cm (pulse 2), and $L = 2$ cm (pulse 3). All traces were normalized to its peak value for an easier comparison. The peak position of each envelope is the time that the pulse takes in travelling through the system, i.e., the pulse delay. These delays are, respectively, $\approx -98, 52$, and 110 ps and they agree very well with the values predicted by Eq. (19). Since the incident pulse (not depicted) has its peak at $t = 0$, pulse 1 clearly tunnels through the system, pulse 2 propagates almost superluminally (the superluminal delay should be less than $L/c = 50$ ps), whereas pulse 3 corresponds to a normal propagation. For the three pulses shown in the figure, a fractional advancement of $|D_f| = 34\%$ was observed, in agreement with Eq. (21).

The case of pulse 2 is a neat example that Table I provides an *estimation* of the propagation regime for narrowband pulses tuned at the minima. The pulse spectral width has indeed influence on the actual propagation regime, as it is reflected in Eq. (19) for τ_{pulse} . It was checked that by decreasing the modulation frequency slightly below 1 GHz, the resulting pulse does propagate superluminally through the MZI of $L = 1.5$ cm.

Figure 6 shows the normalized traces of two pulses transmitted through the shortest MZI ($L = 2$ mm, and phase delay $\tau_p = 23$ ps) and tuned at two frequencies: $f_{\min} \approx 193$ THz

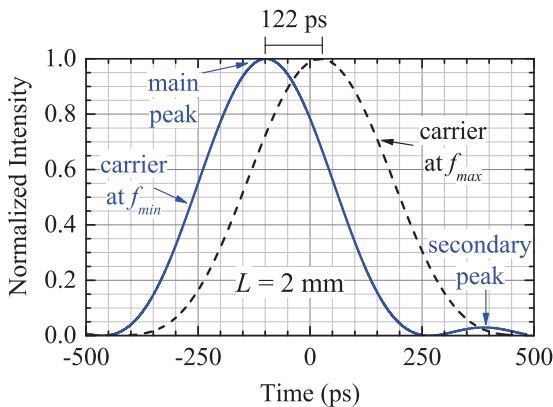


FIG. 6. (Color online) Normalized traces of pulses transmitted through the interferometer of $L = 2$ mm for two carrier frequencies: tuned at f_{\min} (solid line) and tuned at f_{\max} (dashed line). The incident pulse has its peak at $t = 0$.

(pulse 1) and the next transmission maximum $f_{\max} = f_{\min} + 215$ GHz. Since the pulse with carrier frequency at f_{\max} travels at the phase velocity, pulse 1 (main peak) is advanced 121 ps with respect to it. A slight compression of pulse 1 is revealed by measuring the widths of both pulses. Such a compression also occurs for pulse 2 and pulse 3 shown in the previous figure. In the three cases a compression factor of $b = 8\%$ is observed, in agreement with Eq. (22). In physical terms, this behavior can be ascribed to spectral reshaping of the input pulse due to the transmission feature at the minimum. Namely, the center pulse frequency is transmitted with less intensity than its side components, thus causing spectral broadening, and consequently, pulse shrinking in time. This situation has also been reported for fast light based on material resonances [39].

Figure 6 also shows the pulse 1 breakup, with a discernible secondary peak at 388 ps and power amplitude of 2.9% of the main peak power amplitude, in excellent agreement with the predicted values given that $M_{\text{out}} = \sqrt{2}$.

It is worth emphasizing that the above numerical simulations regard an *ideal* waveguide silicon-based MZI. Real waveguide-integrated interferometers usually have power imbalance on the nominal 3 dB couplers [27]. Interestingly, power imbalance can play the role of total losses αL in changing the propagation regime, as it can be deduced from the results found in [30]. In that work, the author analyzed the performance of an MZI with variable power splitting ratios. The softening of the phase jump in the phase spectral function for splitting ratios detuning from 3 dB is similar to the effect of total losses.

For practical purposes, one might consider the possibility of inducing the optical path difference in the MZI not by means of a physical length difference Δ , but through a difference in the refractive index of the branches Δ_n . We could then envisage an MZI with equal branch lengths and fabricated using an electro-optic material such as LiNbO_3 , where Δ_n is tuned upon the application of voltage [27]. It must be pointed out though that SFL effects cannot occur in such a device. More specifically, in an MZI with branches of equal length (and equal attenuation coefficient), the transmission is exactly zero at the minima for whatever attenuation coefficient. The plane-wave amplitude at the end of each branch is the same, and Δ_n makes the phase shift between each plane wave an odd multiple of π for certain frequencies, thus completely cancelling the transmission at those frequencies. No degree of freedom is left to yield an anomalous propagation regime. This situation is equivalent to that of the asymmetric and lossless MZI shown in Sec. II, which displays zero transmission at the minima and $\tau_g = \tau_p$. This physical discussion can be readily corroborated by a simple calculation for this hypothetical symmetric interferometer; it leads to a group delay that corresponds to a propagation at the average phase velocity, namely $\tau_g = \bar{n}L/c$, with \bar{n} being the average refractive index of the branches.

B. Revisiting experimental results in the RF range

The experimental results reported in our previous work [33] are now analyzed within the framework of the present model. The interferometer consists of two coaxial cables (50 Ω , RG-58C/U) of 2 and 14 m length, connected by a 1×2 RF power splitter and a 2×1 RF coupler (PE2000 Pasternack).

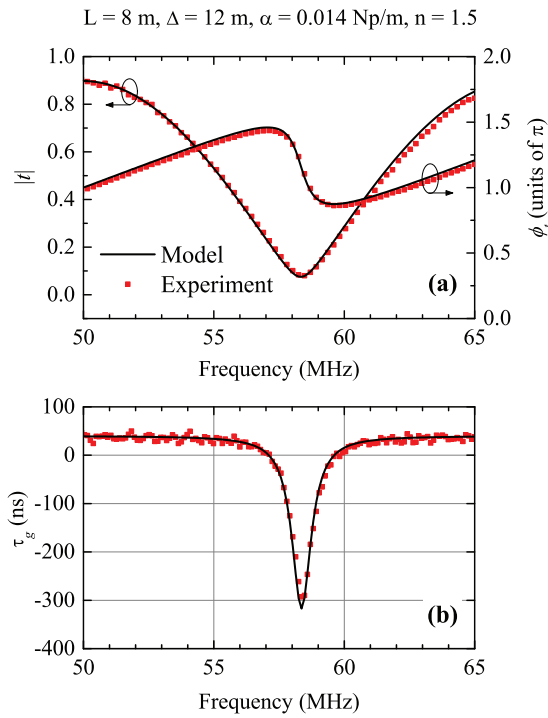


FIG. 7. (Color online) Experimental and model results of an RF MZI with the indicated parameters around a transmission minimum. (a) Magnitude and phase of the transmission coefficient and (b) group delay.

Hence, the system's effective length is $L = 8$ m and $\Delta = 12$ m is the length difference between branches. The phase velocity in the cables ($v = 2c/3$) corresponds to a refractive index of $n = 1.5$. The phase delay of the system is thus $\tau_p = 40$ ns. The cable attenuation coefficient was characterized as a function of frequency in the 20–100 MHz range yielding an average value of $\alpha = 0.014$ Np/m, which is considered as the constant coefficient loss in the model equations. Therefore, the model parameters take the values $\alpha\Delta = 0.168$ and $\gamma^{-1} = -1/\alpha v = -357.14$ ns. Considering Table I and the fact that $\alpha L = 0.112 < 1$, tunneling is the predicted group delay regime at the transmission minima. This regime should be clearly noticeable since the fringe visibility is $v = 99\%$.

The transmission magnitude, $|\hat{t}|$, the phase on transmission, ϕ_t , and the group delay τ_g of this MZI were calculated using Eqs. (6a), (6b), and (8). They are plotted in Fig. 7 together with previous experimental results [33] for comparison. The experimental $|\hat{t}|$ and ϕ_t curves correspond to the magnitude and phase of the S_{21} scattering parameter, which was recorded with a two-port vector network analyzer (Agilent E8363B) in the 20–100 MHz range every 112.5 kHz. The experimental τ_g curve was retrieved by numerical derivative of the experimental phase data with respect to the frequency. It should be remarked that in the experimental data shown here, the effects of the splitters (an overall attenuation of 1 dB and a delay of 2 ns) were subtracted since the splitters are not included in the model. As Fig. 7(a) shows, the constant loss coefficient $\alpha = 0.014$ Np/m considered in the model fits very well the experimental $|\hat{t}|$ and ϕ_t curves in the displayed frequency range. The experimental transmission minimum lies

at 58.3625 MHz, i.e., 62.5 kHz above the theoretical f_{\min} . The agreement was found to be also good in a broader spectral range (20–100 MHz), with the only effect of a lowering of the measured transmission peaks for larger frequencies because of the frequency dependence of the actual coefficient loss.

As shown in Fig. 7(b), the experimental group delay function is reasonably well accounted for by the theoretical model. The experimental and theoretical group delay at the minimum takes the values $\tau_g^{\text{expt}}(f_{\min}) = -292.81$ ns and $\tau_g^{\text{theor}}(f_{\min}) = -316.46$ ns, respectively. The error in the experimental value is estimated to be ± 30 ns, considering the data experimental dispersion and the frequency discretization. Let us note that the frequency derivative of the phase data amplifies the small amount of noise that is contained in the measured S_{21} parameter; this is why the experimental τ_g^{expt} curve exhibits significant data dispersion. The theoretical prediction of -316.46 ns lies within the experimental range $\tau_g^{\text{expt}}(f_{\min}) = -292.81 \pm 30$ ns. It is worth mentioning that the Lorentzian approximation of Eq. (13) with model parameter $\gamma^{-1} = -357.14$ ns almost perfectly fits the experimental function $\tau_g^{\text{expt}}(f)$.

The above results are now used to interpret the time-domain experiments reported in [33], where a train of sinusoidally modulated wave packets with carrier frequency in the megahertz range and 500 kHz modulation frequency was transmitted through the system. This modulation frequency is only by ≈ 50 kHz larger than $|\gamma|/2\pi$. Consequently, the side spectral components of the pulse lie only slightly beyond the FWHM of the Lorentzian group delay curve. Figure 8 shows the experimental pulse power traces (normalized to their maximum value) and their fitted envelopes for two different carrier frequencies f_c . A pulse delay of -250 ± 40 ns was reported for the wave packet with carrier frequency tuned at 58.3 MHz; i.e., it tunnels through the system since $t = 0$ is the peak position of the incident pulse. The pulse with

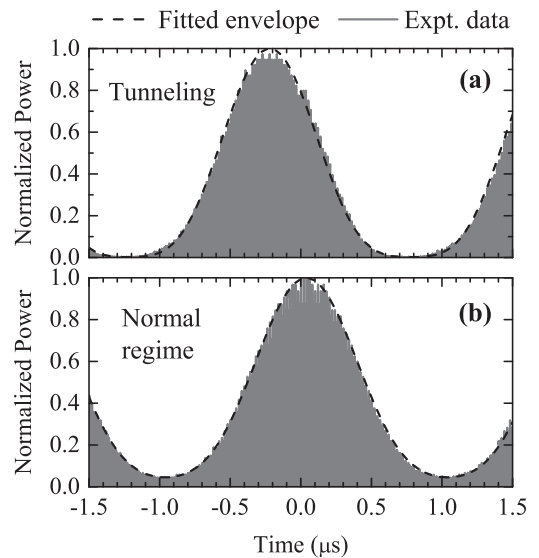


FIG. 8. Experimental pulse power traces and their fitted envelopes for two different carrier frequencies: (a) 58.3 MHz (tunneling) and (b) 50 MHz (normal regime). Each trace is normalized to its maximum amplitude. The fitted envelopes have modulation index (a) $M = 0.95$ and (b) $M = 0.65$.

TABLE II. Comparison between experimental and theoretical predictions for a tunnelled pulse in the RF MZI under analysis. The experimental data of Ref. [33] were used.

Results	M_{out}	$\tau_{\text{pulse}}(\text{ns})$	$ D_f $	$b\%$
Experiment	0.95 ± 0.05	-250 ± 40	0.35 ± 0.05	11.4 ± 1.3
Theory	0.98	-228	0.32	12.2

$f_c = 50$ MHz is delayed by 40 ns and undergoes neither distortion nor compression. This allows us to take the features of this pulse as those of the input pulse in our model. It also serves as the reference pulse for estimating the phase delay τ_p (40 ns) since its propagation is equivalent to that of a pulse traversing a single coaxial cable of 8 m (the MZI effective length). The envelopes that fit the experimental captures have modulation index $M_{\text{out}} = 0.95 \pm 0.05$ [Fig. 8(a)] and $M_{\text{in}} = 0.65$ [Fig. 8(b)]. Let us remark that because of the higher distortion of the tunnelled pulse (due to the sharp decrease of the transmitted signal at the minima) a rough error of ± 0.05 was estimated in its modulation index. Using the above values of the modulation index, the pulse duration (FWHM) for the tunnelled and input pulses is $T_{\text{out}} = 739.5 \pm 11.5$ ns and $T_{\text{in}} = 835$ ns.

Table II summarizes the comparison between the model predictions and the experimental results for the following quantities of the tunnelled pulse: output modulation index M_{out} , pulse delay τ_{pulse} , fractional delay D_f , and compression factor b . The theoretical predictions were obtained using $\omega_m = 2\pi \times 500$ kHz and the model parameter $\gamma^{-1} = -357.14$ ns into Eqs. (18), (19), (21), and (22). The experimental value of D_f was obtained from Eq. (20) using $\tau_{\text{pulse}}^{\text{expt}} = -250 \pm 40$ ns. The experimental figures of merit bear a good agreement with the model predictions. Since the output modulation index is $M_{\text{out}} \leq 1$ (as a consequence of having $M_{\text{in}} = 0.65$) no peak breakup is observed, in accordance to the theory.

IV. CONCLUSION

We have theoretically proved the arising of structural fast light in a linear, passive, weakly attenuating, unbalanced MZI. The interferometer is characterized by its branch length difference (Δ), its effective length (L), and the refractive index (n) and attenuation coefficient (α) of the medium in the branches, which are both considered constant.

An approximate analysis is performed within the condition of good fringe visibility (small $\alpha\Delta$) and in a narrow spectral region around the transmission minima, where anomalous regimes are observed. The intensity of fast-light regimes depends on how much the group delay differs from the phase delay, i.e., the *excess* group delay. It is highlighted that the magnitude of the excess group delay at the transmission minima scales with frequency by a proportionality constant, which is the ratio between the real and the imaginary parts of the complex refractive index of the branch media, in the same way as it has been reported for other interferometric systems; namely for pulses reflected on weakly absorbing slabs.

Keeping constant the refractive index, it is demonstrated that the total attenuation of the system αL drives the change in the group delay regimes at the minima, which range from tunneling, to superluminal, and finally, into normal regime as αL increases. Similar to other structural SFL systems, the obtained group delay spectral function is very well approximated by a Lorentzian curve in the frequency region around the transmission minima.

The propagation of amplitude-modulated sinusoidal pulses through an MZI is modeled and typical figures of merit intrinsic to the system have been obtained. Pulse advancement comes at the expense of pulse compression, and under certain modulation conditions, also peak-breakup. For a 100% modulated pulse with its entire spectrum within the Lorentzian group delay function the delay-bandwidth product is 25% and the fractional advancement 34%, with a pulse compression of 8% and a secondary-to-main peak amplitude ratio of about 3%.

The theoretical model here presented is valid for MZI operative at any frequency range. As an example, it has been applied to both the optical and RF ranges. In the first case, exact numerical simulations were performed in an MZI designed to advance a pulse centered at $1.55 \mu\text{m}$. In the second case, previously reported experimental results on a coaxial cable MZI have been successfully interpreted.

ACKNOWLEDGMENTS

Financial support from the Ministerio de Economía y Competitividad (Spain) and Fondos FEDER, through Project No. FIS2012-39158-C02-02, is acknowledged.

-
- [1] L. Thévenaz, *Nat. Photonics* **2**, 474 (2008).
 - [2] R. S. Tucker, P. C. Ku, and C. J. Chang-Hasnain, *J. Lightwave Technol.* **23**, 4046 (2005).
 - [3] H. N. Yum, M. E. Kim, Y. J. Jang, and M. S. Shahriar, *Opt. Express* **19**, 6705 (2011).
 - [4] M. S. Shahriar, G. S. Pati, R. Tripathi, V. Gopal, M. Messall, and K. Salit, *Phys. Rev. A* **75**, 053807 (2007).
 - [5] H. Wen, M. Terrel, S. Fan, and M. Digonnet, *IEEE Sensors J.* **12**, 156 (2012).
 - [6] Z. Shi, R. W. Boyd, D. J. Gauthier, and C. C. Dudley, *Opt. Lett.* **32**, 915 (2007).
 - [7] L. Brillouin, *Wave Propagation and Group Velocity* (Academic, New York, 1960).
 - [8] A. A. Goyadinov and V. A. Podolskiy, *Phys. Rev. Lett.* **97**, 223902 (2006).
 - [9] M. S. Bigelow, N. N. Lepeshkin, and R. W. Boyd, *Science* **301**, 200 (2003).
 - [10] L. V. Hau, S. E. Harris, Z. Dutton, and C. H. Behroozi, *Nature (London)* **397**, 594 (1999).
 - [11] D. Wei, U. Bortolozzo, J. P. Huignard, and S. Residori, *Opt. Express* **21**, 19544 (2013).
 - [12] A. Schweinsberg, N. N. Lepeshkin, M. S. Bigelow, R. W. Boyd, and S. Jarabo, *Europhys. Lett.* **73**, 218 (2006).
 - [13] M. González-Herráez, K. Y. Song, and L. Thévenaz, *Appl. Phys. Lett.* **87**, 081113 (2005).

- [14] J. Sharping, Y. Okawachi, and A. L. Gaeta, *Opt. Exp.* **13**, 6092 (2005).
- [15] E. Cabrera-Granado and D. J. Gauthier, *Opt. Pura Apl.* **41**, 313 (2008).
- [16] J. F. Galisteo-López, M. Galli, A. Balestreri, M. Patrini, L. C. Andreani, and C. López, *Opt. Express* **15**, 15342 (2007).
- [17] T. Baba, *Nat. Photonics* **2**, 465 (2008).
- [18] S. Longhi, M. Marano, P. Laporta, and M. Belmonte, *Phys. Rev. E* **64**, 055602(R) (2001).
- [19] G. Nimtz, *IEEE J. Sel. Top. Quantum Electron.* **9**, 79 (2003).
- [20] M. Mojahedi, K. J. Malloy, G. V. Eleftheriades, J. Woodley, and R. Y. Chiao, *IEEE J. Sel. Top. Quantum Electron.* **9**, 30 (2003).
- [21] A. Sánchez-Meroño, J. Arias, and M. M. Sánchez-López, *IEEE J. Quantum Electron.* **46**, 546 (2010).
- [22] A. Haché and L. Poirier, *Phys. Rev. E* **65**, 036608 (2002).
- [23] J. N. Munday and W. M. Robertson, *Appl. Phys. Lett.* **83**, 1053 (2003).
- [24] W. M. Robertson, J. Ash, and J. M. McGaugh, *Am. J. Phys.* **70**, 689 (2002).
- [25] J. Arias, A. Sánchez-Meroño, M. M. Sánchez-López, and I. Moreno, *Phys. Rev. A* **85**, 033815 (2012).
- [26] A. Sánchez-Meroño, M. M. Sánchez-López, J. Arias, J. A. Davis, and I. Moreno, *Proc. SPIE* **7716**, 77161Y (2010).
- [27] G. Singh, V. Janyani, and R. P. Yadav, *Optica Applicata* **42**, 613 (2012).
- [28] S. Khalfallah, P. Dubreuil, R. Legros, C. Fontaine, A. Munoz-Yagüe, B. Beche, H. Porte, R. Warno, and M. Karpierz, *Opt. Comm.* **167**, 67 (1999).
- [29] H. Porte, V. Gorel, S. Kiryenko, J. P. Goedgebuer, W. Daniau, and P. Blind, *J. Lightwave Technol.* **17**, 229 (1999).
- [30] C. Cuadrado-Laborde, *Opt. Quantum Electron.* **40**, 983 (2008).
- [31] E. H. Boudouti, N. Fettouhi, A. Akjouj, B. Djafari-Rouhani, A. Mir, J. O. Vasseur, L. Dobrzynski, and J. Zemmouri, *J. Appl. Phys.* **95**, 1102 (2004).
- [32] W. M. Robertson, J. Pappafotis, P. Flannigan, J. Cathey, B. Cathey, and C. Klaus, *Appl. Phys. Lett.* **90**, 014102 (2007).
- [33] M. M. Sánchez-López, A. Sánchez-Meroño, J. Arias, J. A. Davis, and I. Moreno, *Appl. Phys. Lett.* **93**, 074102 (2008).
- [34] A. Brimont, A. M. Gutierrez, M. Aamer, D. J. Thomson, F. Y. Gardes, J. M. Fedeli, G. T. Reed, J. Martí, and P. Sanchís, *IEEE Photon. J.* **4**, 1306 (2012).
- [35] Z. Shi and R. W. Boyd, *J. Opt. Soc. Am. B* **25**, 136 (2008).
- [36] M. Centini, C. Sibilina, M. Scalora, G. D'Aguanno, M. Bertolotti, M. J. Bloemer, C. M. Bowden, and I. Nefedov, *Phys. Rev. E* **60**, 4891 (1999).
- [37] L. G. Wang and S. Y. Zhu, *Opt. Lett.* **31**, 2223 (2006).
- [38] G. M. Gehring, R. W. Boyd, A. L. Gaeta, D. J. Gauthier, and A. E. Willner, *J. Lightwave Technol.* **26**, 3752 (2008).
- [39] R. W. Boyd and P. Narum, *J. Mod. Opt.* **54**, 2403 (2007).

